PAP-992

One copy of the manuscript submitted to
Department of Water Resources,
State of California

Field Testing of the Dynamic Stability of the Thermalito Diversion Dam Tainter-Gates

July 30, 2007

by

Noriaki Ishii
Professor, Osaka Electro-Communication University
18-8 Hatsu-Cho, Neyagawa, Osaka 572-8530, Japan
E-mail: ishii@isc.osakac.ac.jp

Keiko Anami
Assistant Professor, Ashikaga Institute of Technology
268-1 Omae-Cho, Ashikaga, Tochigi 326-8558, Japan
E-mail: anami@ashitech.ac.jp

Charles W. Knisely
Professor, Bucknell University
Lewisburg PA 17837, USA
E-mail: knisely@bucknell.edu

Mark G. Schultz
Supervising Engineer, California Department of Water Resources
2200 X Street, P.O.Box 942836, Sacramento, CA 95818, USA
E-mail: schultz@water.ca.gov

Stephen D. Slinkard
Chief of Mechanical/Electrical Design Section, US Army Corps of Engineers
1325 J Street, Sacramento, CA 95814-2922, USA
E-mail: Stephen.D.Slinkard@spk01.usace.army.mil

Robert V. Todd
Consultant

E-mail: rvtodd@comcast.net

HYDRAULIC INVESTIGATIONS
AND LABORATORY SERVICES
OFFICIAL FILE COPY

CONTENTS

1. INTRODUCTION 1

2. DETAILS OF FIELD TESTING 3
   2.1 Thermalito Diversion Dam Gates 3
   2.2 Instrumentation and Connection Flow-Chart 5
   2.3 Installation of Steel Rod and Selection of Diameter 13
   2.4 Testing Procedures 20
   2.5 Vibration Test Conditions and Gate Opening during Tests 26

3. MEASURED VIBRATION ACCELERATIONS 35

4. METHOD OF DATA ANALYSIS 76
   4.1 Software 76
   4.2 Window Selection for Frequency Power Spectrum Analysis 77

5. FREQUENCY POWER SPECTRUM OF VIBRATIONS 81

6. MEASURED IN-WATER NATURAL VIBRATIONS 122
   6.1 Natural Vibration Frequencies 122
   6.2 Amplitude and Phase-lag 123
   6.3 Vibration Modes 126
   6.4 Damping Ratio 134

7. EXAMINATION OF STEEL ROD DIAMETER FOR VIBRATION TESTS 136

8. FEM-SIMULATION OF IN-AIR NATURAL VIBRATIONS 138
   8.1 FEM Model Construction 138
   8.2 Dynamic Spring Constant of Wire Cables and Equivalent Modulus of Elasticity 140
   8.3 Natural Vibration Frequencies and Vibration Modes 141

9. THEORETICAL EXAMINATION OF DYNAMIC STABILITY AT TESTED BACK WATER LEVEL 147
   9.1 Confirmation of Theoretical Analyses with Calculations of In-Water Natural Vibration Frequency 147
   9.2 Self-Excitation Mechanism and Theoretical Analysis of Dynamic Stability 152
   9.3 Dynamic Stability of Gate #2 159
   9.4 Dynamic Stability of Gate #3 162

10. THEORETICAL EXAMINATION OF DYNAMIC STABILITY AT OTHER SUBMERGENCE LEVELS 164
   10.1 Dynamic Stability of Gate #2 164
   10.2 Dynamic Stability of Gate #3 170

11. TRIGGER LEVEL OF VIBRATION NEEDED TO INITIATE SELF-EXCITED VIBRATIONS 173

12. STRUCTURAL STRENGTH OF GATES TO SELF-EXCITED VIBRATION 180
12.1 Static Structural Deformation .....
12.2 Failure due to Stress Concentration .....
12.3 High Strength of Welded Joints against Tensile Force .....
12.4 Failure due to Buckling .....

13. OPERATIONAL MEASURES OF GATES FOR ITS ENTIRE DYNAMIC STABILITY .....

14. Concluding Remarks .....

Acknowledgements .....

References R-1

Appendix A-1

1. INTRODUCTION

On July 2, 1967 a 37-ton Tainter gate at the Wachi Dam in Japan failed. The photograph of the failed gate, shown in Figure 1.1a, was published by *Asahi Evening News* and *Asahi Newspaper* (with a Japanese caption and story) on July 3, 1967. The gate, along with the bridge over the gate, was swept at least 136 m downstream of the gate bay, leaving a giant hole in the gate bay. More than 28 years after the gate failure in Japan, on July 17, 1995, an 87-ton Tainter gate at the Folsom Dam near Sacramento, CA in the US failed. The photograph in Figure 1.1b, taken after the accident, was published by *The Japan Times* on July 19, 1995. Regarding the Folsom Dam gate failure, the dam manager at the time, Tom Aiken, in his press-conferences, and the gate operator, James Taylor, in his interviews, both presented repeated testimony that vibrations most certainly accompanied the gate failure,

In the ten years since gate failure in the US, spurred by both the Folsom Dam gate failure as well as that at the Wachi Dam in Japan, Ishii and Anami have persistently conducted intensive research utilizing laboratory testing of two- and three-dimensional model gates, full-scale field tests on operational gates tests as well as theoretical analyses (see References [1]-[39]), leading them to the conclusion that the underlying mechanism behind the failure of these two gates was an essential dynamic instability mechanism that all Tainter gates may possess. More precisely this dynamic instability has been termed "coupled-mode self-excited vibration instability," and is summarized in a final report entitled "Lessons from Folsom Dam Tainter-Gate Failure and Future Work for Subsequent Generations" (refer to [1]), which was presented to the Mid-Pacific Region of USBR, US Department of the Interior on Dec. 8, 2005 in an effort to inform and to educate current and future generations of gate engineers all over the world. In the cited final report, a complete picture of the Folsom Dam gate failure is presented. The report contains results from model tests on a large-scale three-dimensional model of the failed Folsom Dam Tainter-gate which fairly conclusively confirms the susceptibility of the failed Folsom Tainter gate to the proposed dynamic instability mechanism leading to very

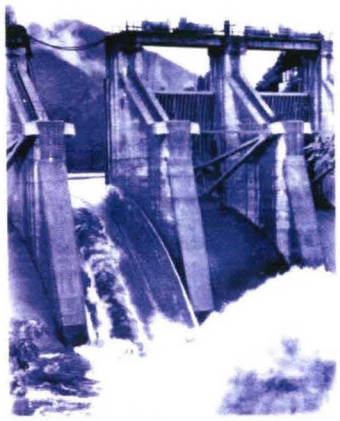

(a) failure of a 37-ton gate at the Wachi Dam in Japan on July 3, 1967 (courtesy of the Asahi Newspaper Co. Ltd.)

(b) failure of an 87-ton gate at the Folsom Dam in California (US) on July 17, 1995

Figure 1.1: Two examples of Tainter-gate failure.

2. DETAILS OF FIELD TESTING

2.1 Thermalito Diversion Dam Gates

Photos of the Thermalito Diversion Dam and the installed Tainter (radial) gates are shown in Figure 2.1. Vibration testing was conducted on gates #2 and #3 from the right side as viewed from upstream. The configuration and major dimensions of the gates are shown in Figure 2.2, where the top, upstream and side views are presented. The skinplate has a height of 6.65 m and a spanwise length of about 12 m. The length of radial arm is 9.14 m. The whole gate's mass is about 24 tons. The skinplate with 17 vertical T-beams and 2 horizontal girders is uniquely reinforced to reduce bending deformation with 8 tension rods, as shown by the photo in Figure 2.2. The radial arm structure has 2 struts strengthened with a truss structure. The side view of the gate on the dam crest is shown in Figure 2.3, in which a comparison image of the size of gate and a human is additionally presented. The gate is raised with 4 wire cables each with a diameter of 35 mm attached to both spanwise ends of the skinplate. The full length of the wire cables is 8.99 m, with a free length of about 5.27 m. The skinplate position is downstream from the top of the dam crest.

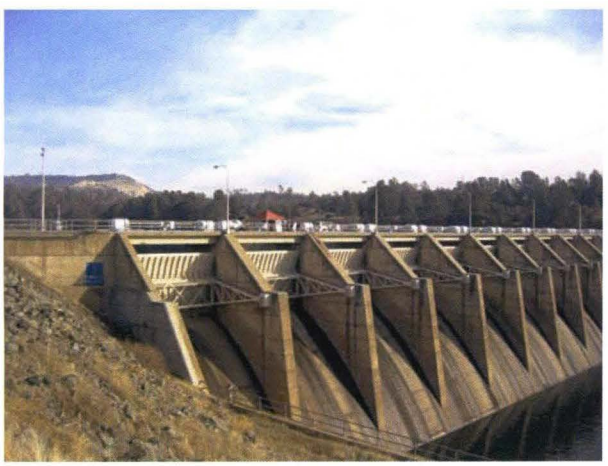

(a) Distant view of the dam from right bank.

(b) Distant view of the dam from left bank.

(c) Enlarged view of the gate.

Figure 2.1: Thermalito Diversion Dam and Tainter gate

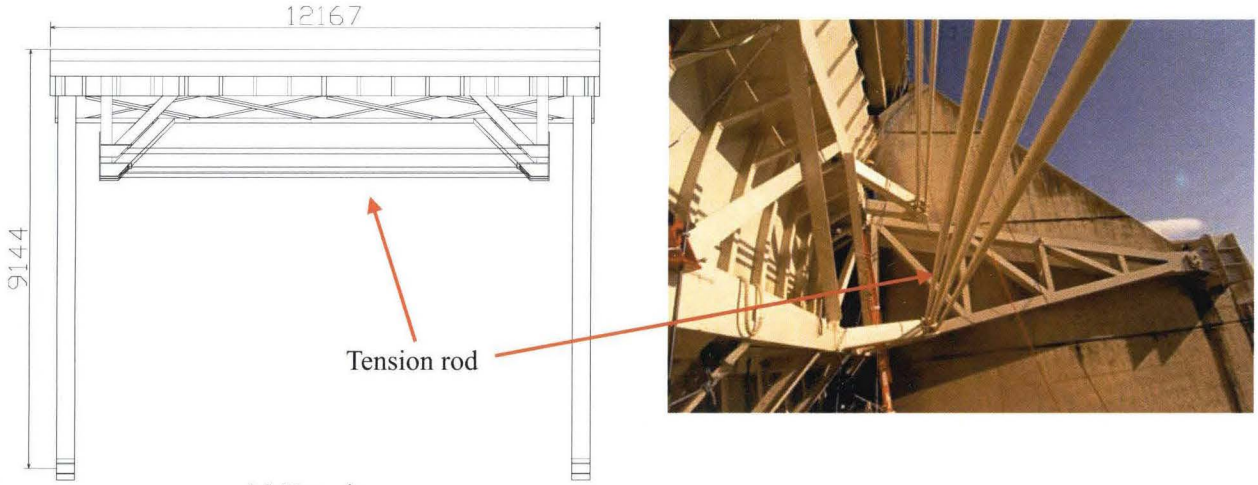

(a) Top view

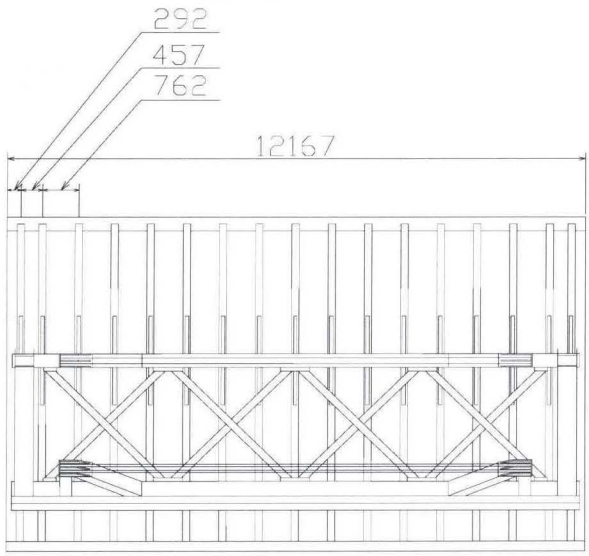

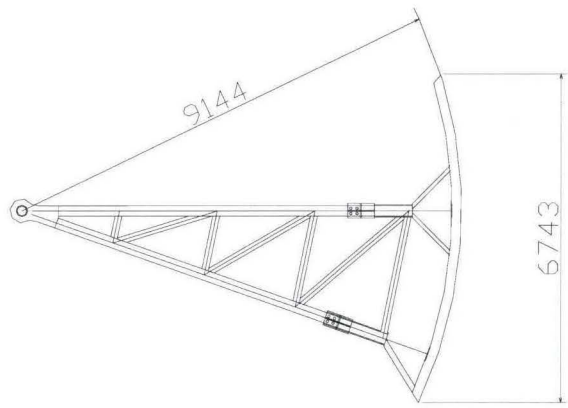

(b) Upstream view

(c) Side view

Figure 2.2: Drawings of Thermalito Diversion Dam Tainter gate.

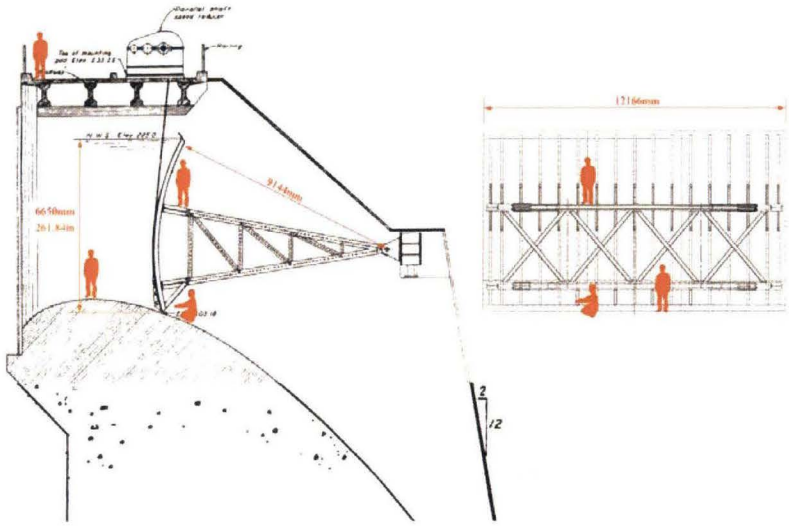

Figure 2.3: Side view of the gate on the dam crest, showing wire cables for raising the gate.

2.2 Instrumentation and Connection Flow-Chart

Major instrumentation for the present field tests are listed in Table 2.1 and shown in Figure 2.4, where a digital data recorder, a lap top computer, a FFT analyzer, high-quality servo-type accelerometers with accompanying amplifiers, and a gate opening sensor with its amplifier are presented. All instrumentation was carried on the flight from Japan to San Francisco and by car from San Francisco to the Thermalito Diversion Dam via Sacramento by our staff members, who are listed in Appendix A.

Table 2.1: Major instruments for field tests.

Article	Company	Type	Number of Article
Digital Data Recorder	TEAC	LX-10	2
Lap Top Computer	TOSHIBA	Dynabook G9	2
FFT Analyzer	A and D	AD3525	1
Servo type Accelerometer	Rion	LS-20C	15
Servo type Accelerometer	Rion	LS-10C	3
Pressure transducer	TOYODA	PMS-5M-1M	2
DC amplifier for Pressure transducer	TOYODA	AA6200	1
Dynamic strain amplifier	KYOWA	DTP-05MDS	1
Gate opening sensor with strain gauge	KYOWA		2
Power supply amplifier for Accelerometer	Rion	LF-20	6
Extended connecting cable for Accelerometer	Rion	EC-40D	18
Impact Hammer with force gauge	PCB	GK-086B50	1
Power supply amplifier for Hammer	PCB	GK-480M106	2

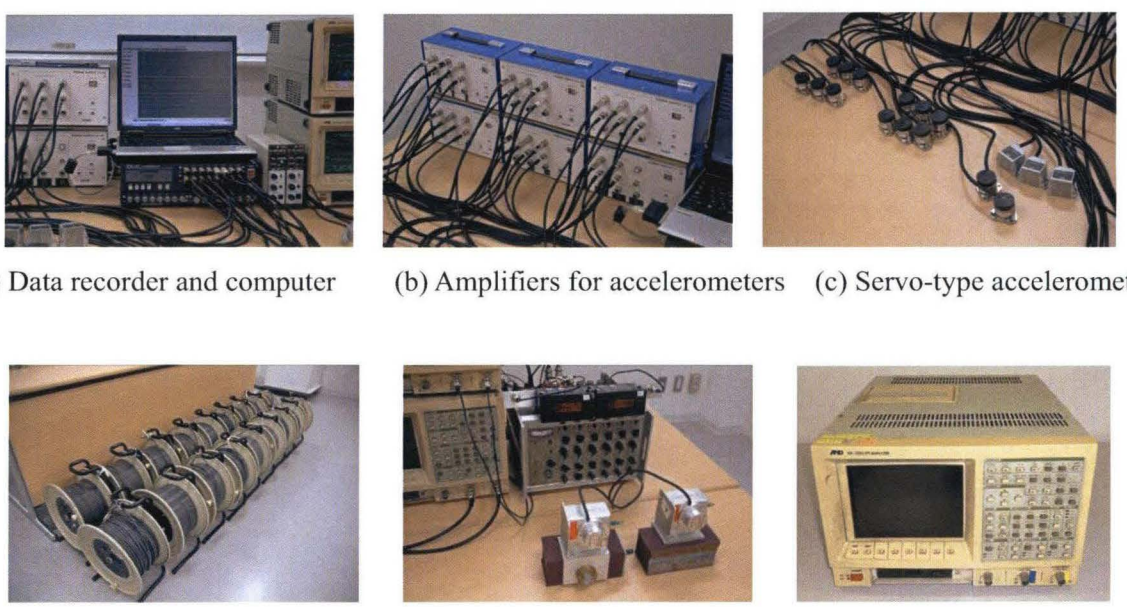

(a) Data recorder and computer (b) Amplifiers for accelerometers (c) Servo-type accelerometers

(d) 50 m-long cables for accelerometers (e) Gate-opening gauges (f) FFT analyzer

Figure 2.4: Photos of major instruments for field tests.

As shown by small red and blue circles in Figures 2.5, the vibrational acceleration of the gate was measured at 11 points on the vertical ribs along the skinplate and at 2 points on the radial arm, where the measurement positions are denoted "A" to "F" along the skinplate bottom, "E1" to E6" along the skinplate center and "L1" and "L2" along the radial arm. On the skinplate, radial vibrations were measured, as shown by the red arrows, In addition, tangential vibrations were also measured at "A", "E3" and "E6", as shown by the blue arrows. On the radial arm, the tangential and spanwise vibrations were measured, as shown by blue arrows. A total of 18 servo-type accelerometers (Lion Co.: LS-20C, LS-10C) were used. The accelerometers were attached to the gate, with strong magnet bases. The directions and positions of measurement were carefully determined on the basis of our previous experiences of field testing of Tainter gates, in order to correctly reveal the structural vibration modes of Thermalito gate. Figure 2.6 presents photos of the accelerometers on their magnetic bases, attached on the skinplate and the radial arm.

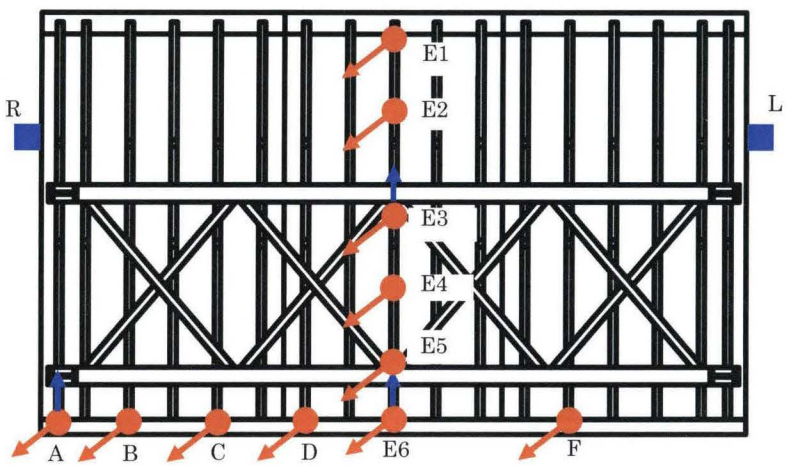

(a) Upstream view of skinplate

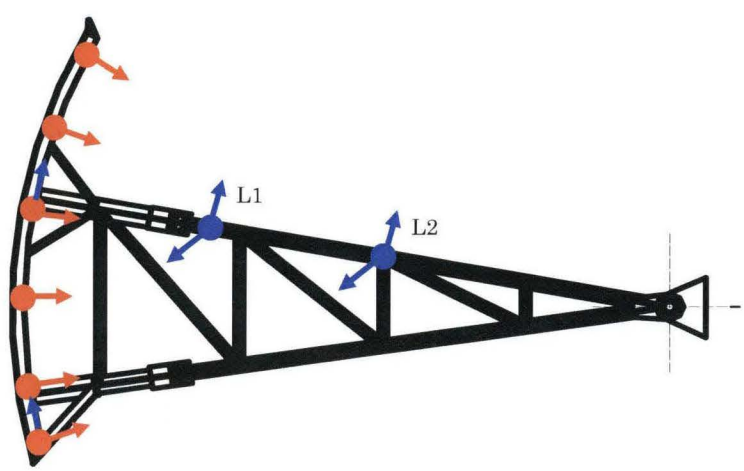

(b) Side view

Figure 2.5: Measurement positions of accelerations and gate-opening.

(a) Position A

(b) Position B

(c) Position C

(d) Position D

(e) Position E6

(f) Position F

(g) Positions E1 and E2

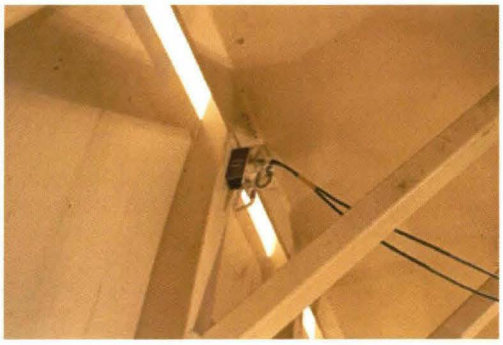

(h) Position E3

Figure 2.6: Accelerometers attached on skinplate and radial arm. (continues on the next page)

(i) Position E4

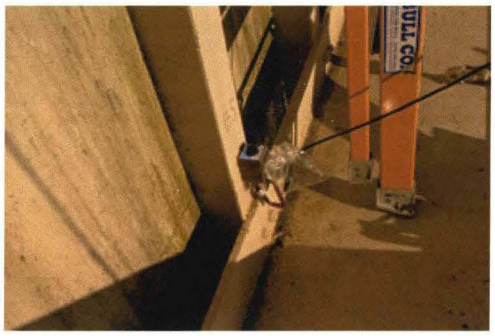

(j) Position E5

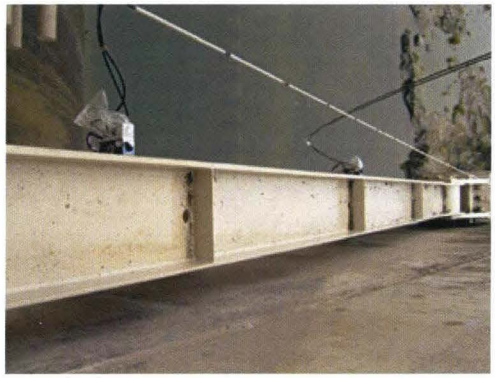

(k) Positions L1 and L2

Figure 2.6: Accelerometers attached on skinplate and radial arm.

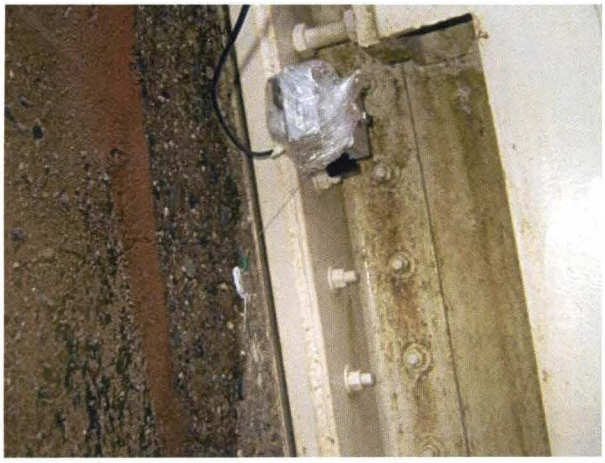

(a) Position R

(b) Position L

Figure 2.7: Gate-opening gauges attached to each side of the skinplate.

In addition, two gate-opening gauges (Kyowa co.: DPT-05MDS; see Figure 2.7) were attached with strong magnetic bases to each side of the skinplate, as shown by the small blue squares in Figure 2.5a. The gate-opening gauge has a thin wire cable, the tip of which was fixed with special adhesive to the concrete pier, as seen in the photos in Figure 2.7.

As shown in Figure 2.8, long cables connected the accelerometers and the gate-opening gauges to their respective amplifiers which were contained in a van parked on the bridge. The van served as the measurement station, as shown in Figure 2.9. The accelerometers (LION LS-20C, LS-10C) were connected to their respective power supplies and amplifiers (LION LF-20) in the measurement station through 50 m-long co-axial cables (LION EC-40D; see Figure 2.8b). A connection flow-chart diagram of the instrumentation is shown in Figure 2.10. All data were recorded on 2 digital data recorders with A/D converters (TEAC LX10) and monitored with 2 laptop computers (Toshiba: Dynabook G7/U24 PDDW) and an FFT analyzer (A&D: AD3525), to permit careful adjustment of the input level to the data recorders for optimum recording, as seen in Figure 2.9a. The impact hammer (PCB: GK-480M106) was used for checking the proper functioning of all accelerometers.

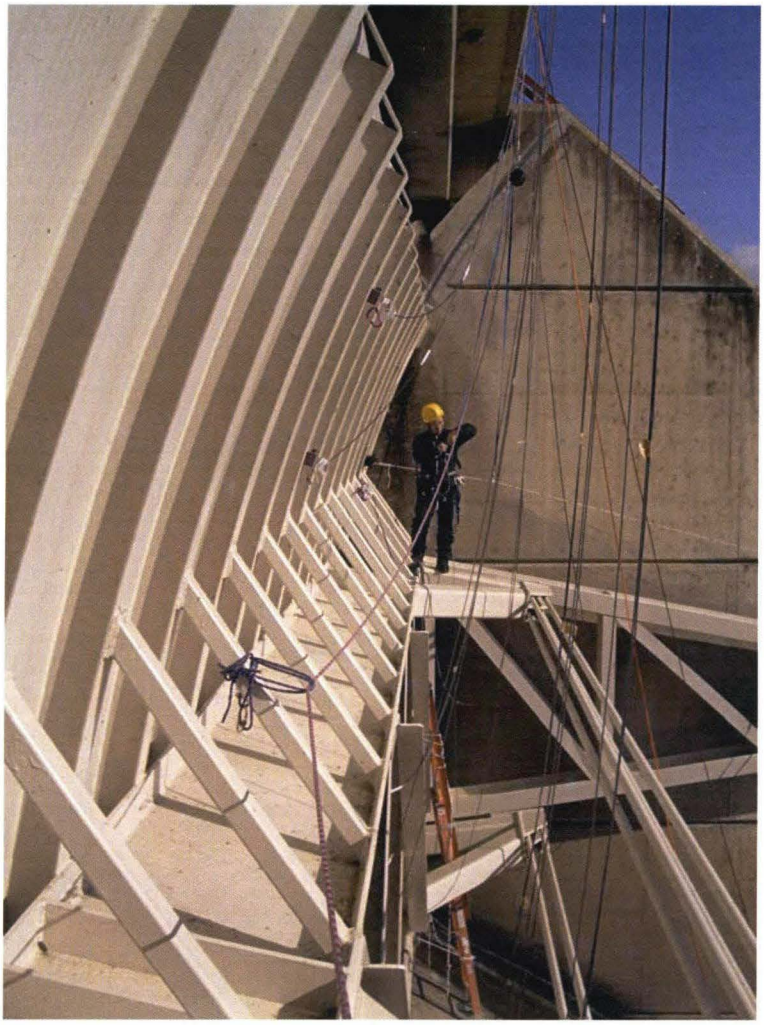

Figure 2.8: Long cables pulled up onto the bridge

(a) Amplifiers, digital data recorders, laptop computers and FFT analyzer for monitoring.

(b) Wiring for accelerometers.

Figure 2.9: Measurement station on bridge.

After amplification, the measurements of gate discharge opening at each side of the skinplate were recorded on the data recorder and monitored using digital display meters, which were set-up on the switch board of the gate operation, as shown in Figure 2.11.

The present field vibration testing was undertaken using the steel-rod breaking method as excitation. In this method, the gate was gradually raised in a step-wise fashion until the steel-rod fixed between the skinplate bottom and the dam crest was loaded past its capacity and broke suddenly. For correct testing, it was essential that the raising of the gate stop immediately as soon as the steel rod broke. In addition to the digital display meter showing gate opening height, a display monitor screen connected to a digital video camera mounted on the trunnion pier (see Figure 2.12) was positioned on the gate switch board, as shown in Figure 2.11, to further assist the gate operator in making fine adjustments of the gate opening. The digital video camera provided images of the steel rod at the bottom center of the skinplate. Figure 2.13 shows staff members taking measurements and monitoring the output of the instruments on the dam bridge.

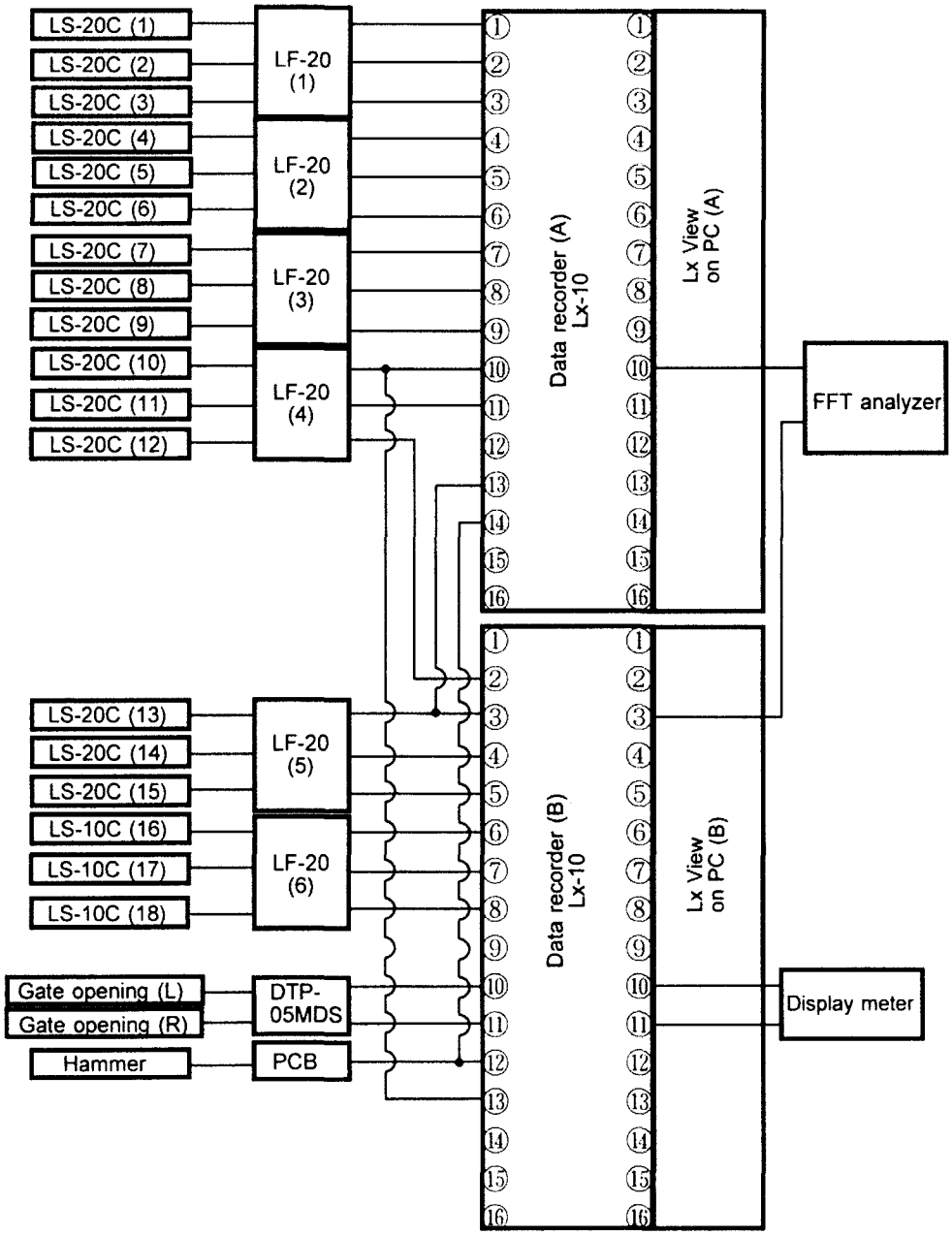

Figure 2.10: Connection flow-chart of the instrumentation.

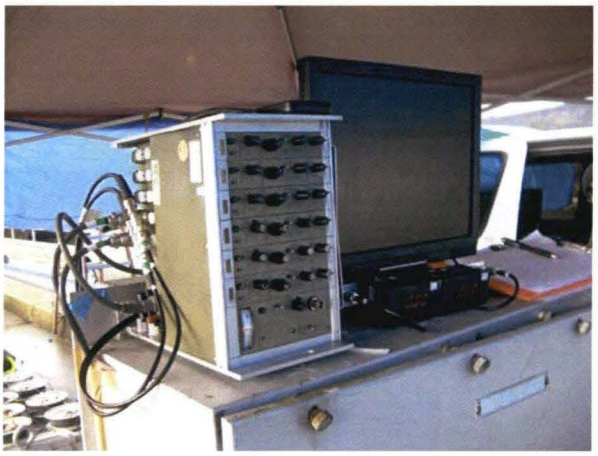

Figure 2.11: Gate opening gauge amplifier, the digital display meter and the monitor screen for the steel-rod breaking test.

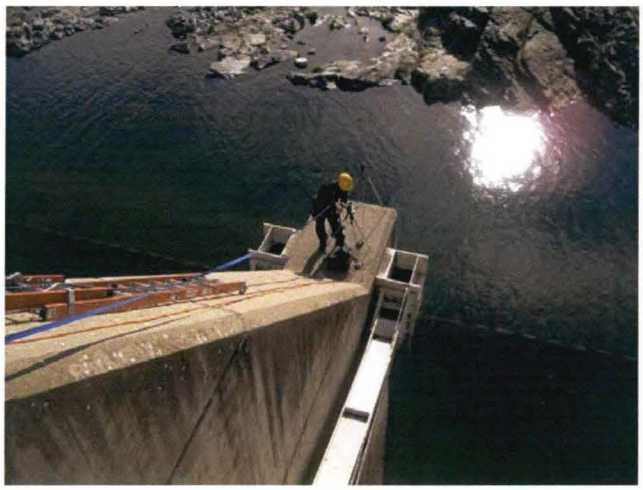

Figure 2.12: Digital video camera set-up on the trunnion pier.

Figure 2.13: Team members conducting measurements.

2.3 Installation of Steel Rod and Selection of Diameter

To provide a small initial impact force on the gate, a machined steel rod with a small diameter (much like a tensile test specimen) was installed between the bottom center of the skinplate and the spillway concrete, as shown in Figure 2.14. No drilling of the skinplate was needed because the L-bracket to which the steel rod was attached was, itself, fastened to the spanwise center of the lower horizontal girder flange with a pair of C-clamps. At the other end of the steel rod, a base plate was anchored to the spillway concrete just beneath the skinplate. The steel rod was connected to the L-bracket by a long threaded rod and a long nut, while the lower end of the steel rod was connected to the base plate using an eye bolt.

Initially, the steel rod was clamped to the downstream flange of the horizontal girder, as shown in Figure 2.14(a). However, initial vibration data, monitored on the bridge, was somewhat anomalous and not acceptable. For this reason, the position of the steel rod installation was immediately changed from the downstream flange to the upstream flange, closer to the skinplate, as shown in Figures 2.14(b) and 2.17(d). The Thermalito gate has a comparatively flexible horizontal girder, and because of the flexibility of the girder flange, an effective impact force could not be directly given on the skinplate when the rod was attached on the downstream flange. The upstream flange is directly welded to the skinplate ribs. Thus, the installation on the upstream-side, shown in Figure 2.17(d), resulted in a very effective impact force acting on the whole gate to initiate gate vibrations.

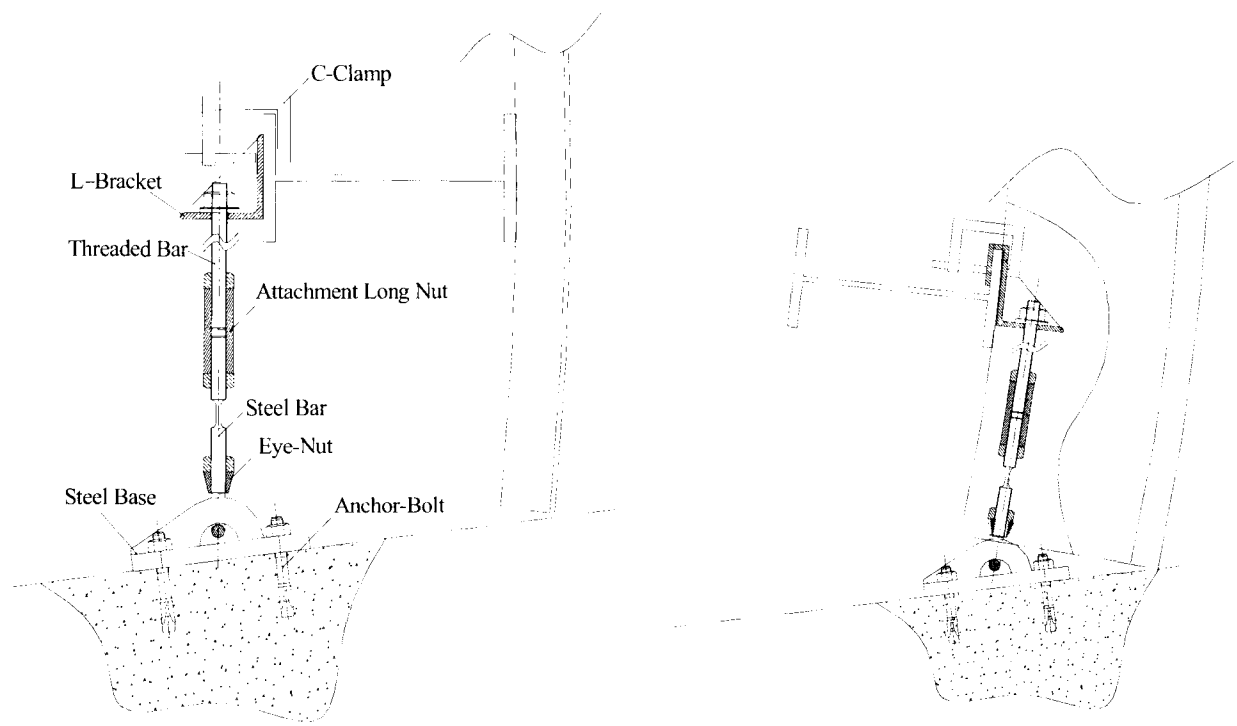

(a) Steel rod fixed on the downstream flange of girder. (b) Steel rod on the upstream flange.

Figure 2.14: Installation of steel rod between the skinplate rib and spillway concrete.

Blueprints of steel rod attachments are shown in detail in Figure 2.15. Photos of attachment L-bracket and plate are shown in Figure 2.16. The L-bracket is tightly clamped with two C-clamps to the horizontal girder flange, as shown in Figures 2.17(d) and (e), while the attachment base plate is fixed to the spillway concrete, with four anchor bolts with a diameter of 12 mm. An electric hammer drill with special drilling tool (manufactured by HILTI) was used to drill anchor holes, as shown in Figure 2.17(c). Upon completion of the testing, the anchor bolt holes were completely back-filled with concrete mortar.

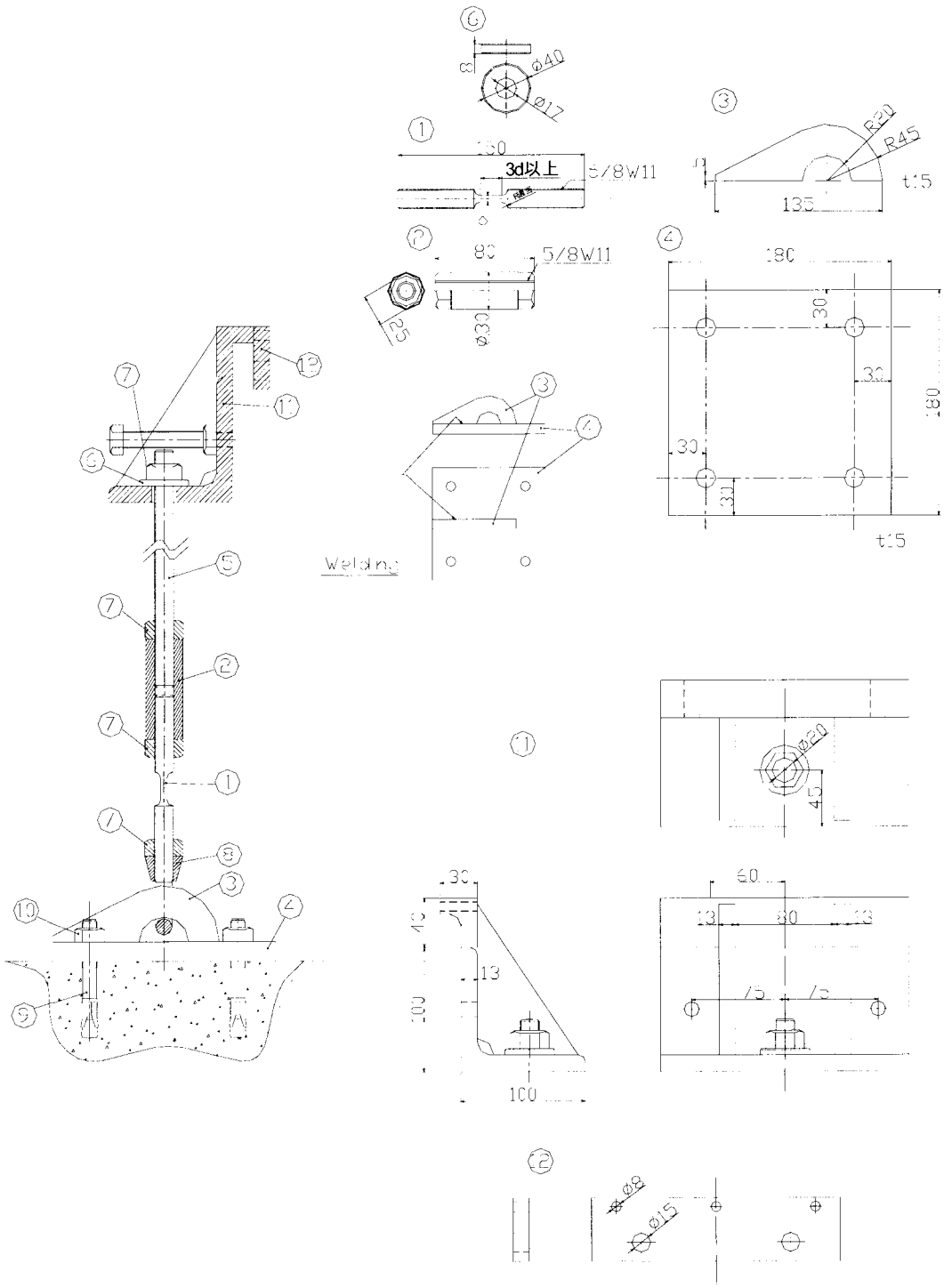

Figure 2.15: Blueprints for steel rod and attachment plates.

(a) L-bracket for clamping to the skinplate.

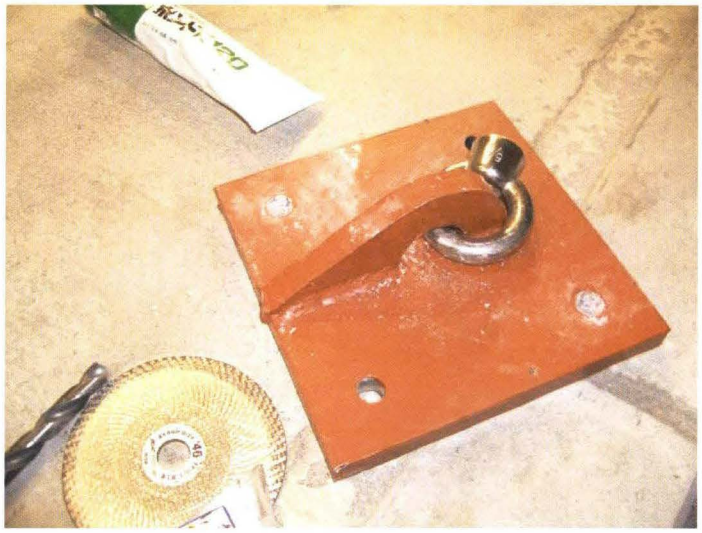

(b) Base plate to be anchored to the spillway concrete.

Figure 2.16: L-bracket and base plate for steel rod.

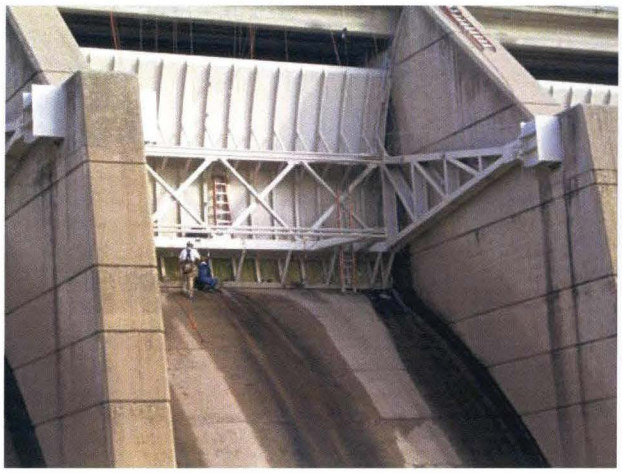

(a) Distant view of attachment.

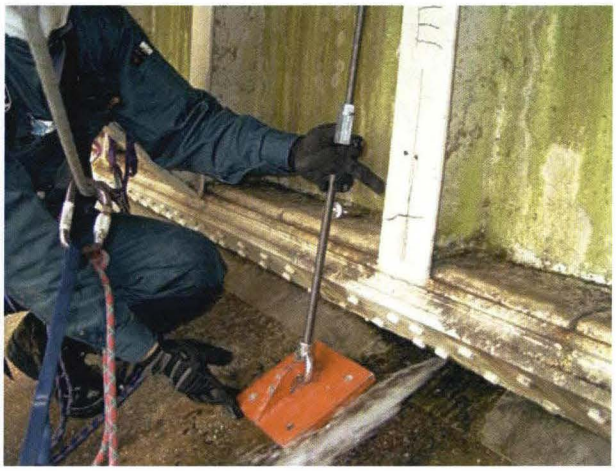

(b) Base plate attached to the spillway concrete.

(c) Drilling of anchor bolt holes.

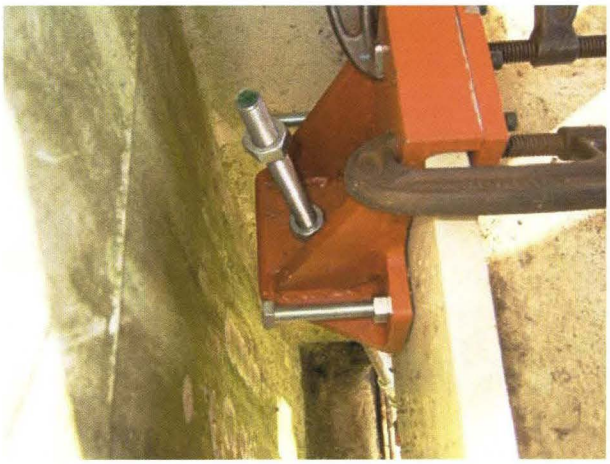

(d) L-bracket clamped to the upstream flange of the horizontal girder (from top).

(e) L-bracket clamped to the downstream flange of the horizontal girder (from bottom)

Figure 2.17: Installation of the steel rod.

Common dimensions and a photo of the machined steel rod are shown in Figure 2.18, where *d* represents the diameter of the neck of the steel rod. Prior to conducting the field tests, the material to be used for the steel rod was carefully considered. Tensile strength tests were conducted for both SS400 and S45C samples, as shown in Figure 2.19. The SS400 steel rod with a diameter of d = 9 mm broke at a lower tensile load of 18 kN (see the curve on the left in Figure 2.19(a)) after elongation of the neck, as clearly shown in Figure 2.19(b), because of its high ductility. Thus, SS400 was not suitable to provide an effective impacting force on the gate. On the other hand, the S45C steel rod with the same diameter of d = 9 mm broke at a higher tensile load of 48 kN (see the curve on the right in Figure 2.19(a)) when the neck was barely elongated at all, as shown in Figure 2.19(c), thus giving an effective impacting force on the gate. As a result, S45C was adopted for the steel rod in material.

The diameter of the steel rod, *d*, should be carefully determined using the elongation-to-tension-load characteristics of the gate lifting wire cables. Figure 2.20 represents the tensile load ΔF versus the steel rod diameter *d* and the elongation-to-tension-load characteristics of the lifting wire cables, estimated for the Thermalito Diversion Dam gate. The wire ropes of the Thermalito gate were specified as 6×19 IWRC which has an area A of 321 mm^2 and a modulus of elasticity, M_s, of 93.08 GPa, as shown in Tables 2.2 and 2.3. This modulus of elasticity is about 0.45 times the value of 206 GPa, which is the modulus of elasticity for the original material of wire cables. With these data in addition to the full length of wire ropes, L = 8.99 m, the elongation ΔL resulting from a tension load ΔF can be calculated by the following expression:

$$\Delta L = \frac{\Delta F \cdot L}{A \cdot M_s}$$

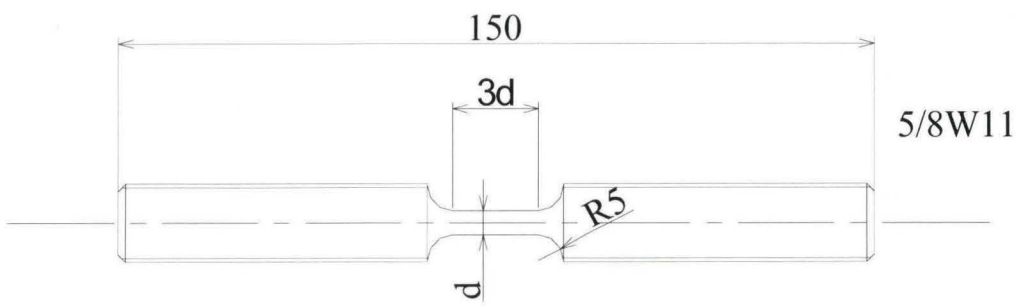

(a) Dimensions.

(b) Photo.

Figure 2.18: Threaded steel rod for breaking.

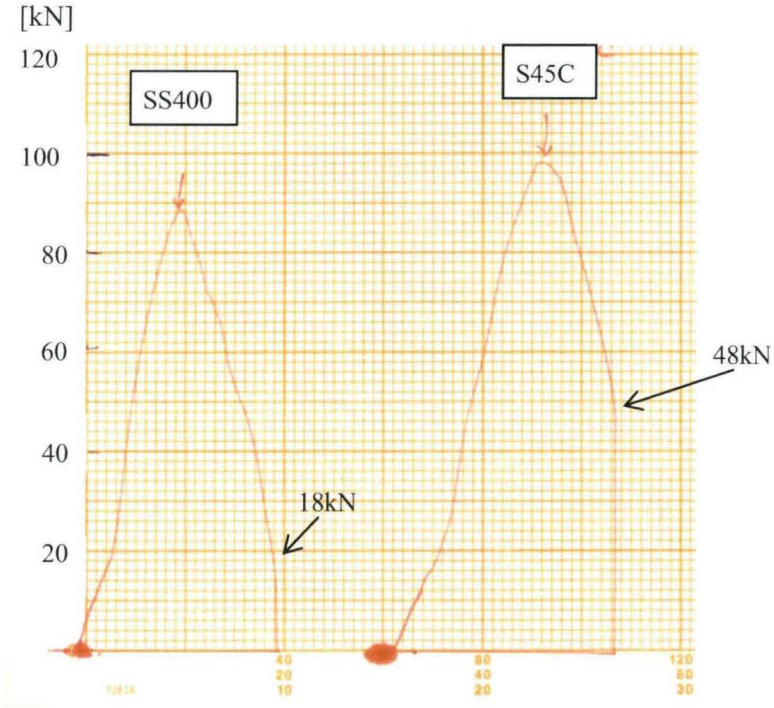

(a) Tensile strength test curve.

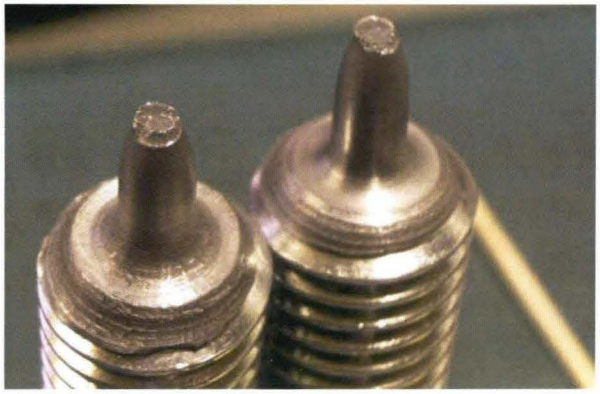

(b) SS400.

(c) S45C.

Figure 2.19: Tensile strength test results and photos of fracture section for SS400 and S45C steel rods with 9 mm diameters.

Based on the elongation-to-tension-load characteristics of the gate lifting wire cables, shown in Figure 2.20, a maximum diameter of 8 mm was specified for the steel rod so that the elongation of the lifting wires would not exceed about 1 mm, based on our expertise, assuring the complete safety of the gate.

About 50 steel rods with diameters ranging from 3 mm to 12 mm were made in Japan transported by our staff members to the USA.

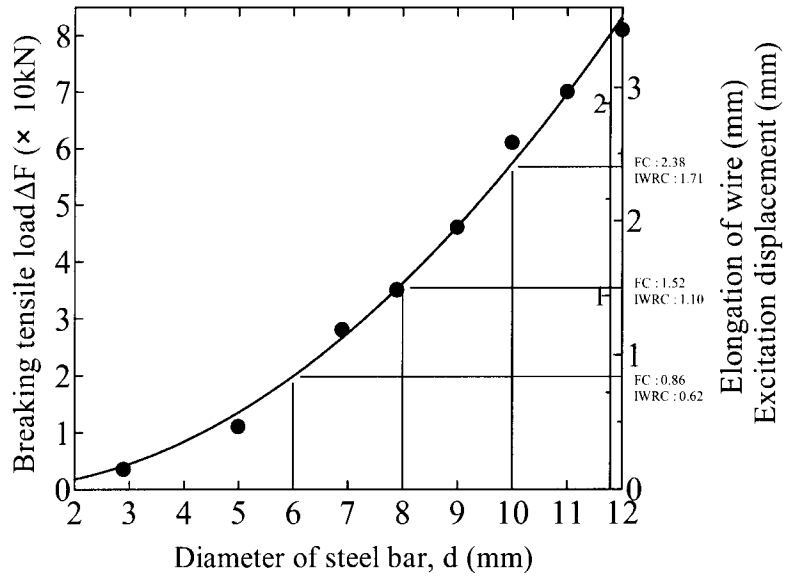

Figure 2.20: Tensile load on lifting wire cables and its elongation versus diameter of the steel rod.

Table 2.2: Approximate metal areas *A* of 26 mm (1-in.) wire rope of various specifications.

Rope Classification	Area	
	SQ. IN.	SQ. MM
6 x 7 FC	.384	258
6 X 37 FC	.410	276
6 X 19 FC	.427	289
8 X 19 FC	.360	243
6 X 19 IWRC	.475	321
6 X 37 IWRC	.493	333

Table 2.3: Approximate modulus of elasticity, M_s, for various wire rope specifications.

Rope Classification	0% to 20% Loading		21% to 65% Loading	
	PSI	MPa	PSI	MPa
6 x 7 FC	11,700,000	80,670	13,000,000	89,670
6 x 19 FC	10,800,000	74,470	12,000,000	82,740
6 x 37 FC	9,900,000	68,260	11,000,000	75,850
8 x 19 FC	8,100,000	55,850	9,000,000	62,080
6 x 19 IWRC	13,500,000	93,080	15,000,000	103,430
6 x 37 IWRC	12,600,000	86,880	14,000,000	96,530

2.4 Testing Procedures

Procedures used for vibration and stability field testing of the Thermalito Diversion Dam gates are as follows:

13 Nov. 2006 (Monday):

(1) In the afternoon, a face-to-face meeting with the dam owners at their office near the Thermalito Diversion Dam was held.

(2) In the evening, our field testing team visited the Thermalito Diversion Dam to check conditions around the gates.

14 Nov. 2006 (Tuesday):

(1) Preparations for field testing were undertaken from the morning through mid-afternoon and involved mounting instrumentation on various surfaces of Gate #2, as well as setting up and testing the recording and monitoring instrumentation in the measurement center contained in the van parked on the bridge road just over Gate #2.

(2) Once preparations were complete, and before leaving the dam site in the evening, an ambient excitation test and as well as the steel rod breaking excitation test using a small diameter sample were conducted to ensure that all instrumentation and procedures for the steel rod breaking were functional.

15 Nov. 2006 (Wednesday):

(1) The first task in the morning was the installation of the L-bracket and the base plate on the upstream-side of the horizontal girder closer to the skinplate to achieve a more effective impact excitation of the whole gate in the rod breaking excitation test.

(2) Subsequently, in the course of the morning, four steel rod breaking excitation tests were conducted on Gate #2.

(3) In the afternoon, all instrumentation was moved to Gate #3.

16 Nov. 2006 (Thursday):

(1) In the morning, four steel rod breaking excitation tests as well as an additional ambient excitation test were conducted on Gate #3. The field testing was completed.

(2) In the afternoon, all instrumentation was removed and packed. The test team left the Thermalito Dam.

Details of our work procedures are presented in Figure 2.21, where the roles assigned to each team member are described in detail with the time schedule. Further, from 14 Nov. to the morning of 15 Nov., a climbing expert, Mr. Sam Plank, was kind enough to assist us in mounting the instrumentation and steel rod

fixtures on the gate. For the entire duration of our field tests, Mr. Bill Pennington was kind enough to assist in many aspects of the testing.

Work Procedure for Staff Members
for
Field Test of Thermalito Diversion Dam

Nov. 13 (Mon) 13: 30 Face-to-face meeting

Noriaki Ishii	Mark Schultz	Linda Sue Solomon
Keiko Anami	Stephen Slinkard	Bill Pennington
Tatsuya Oku	Robert Todd	Trudy Payne
Satoshi Sasaki		Peter Setzchen
Yukio Matsumoto		

14:30 Visited Thermalito Diversion Dam gates to check conditions around gates

19:00 Attachment of accelerometers and gate opening gauges to magnetic base blocks and covering the iinstruments with plastic bags (in the hotel room)

Tatsuya Oku Satoshi Sasaki

The gate (use safety belts & lanyards

on the bridge

accelerometer

gate opening gauge

Figure 2.21(a): Work procedures of Nov. 13th for field test of the Thermalito Diversion Dam gate.

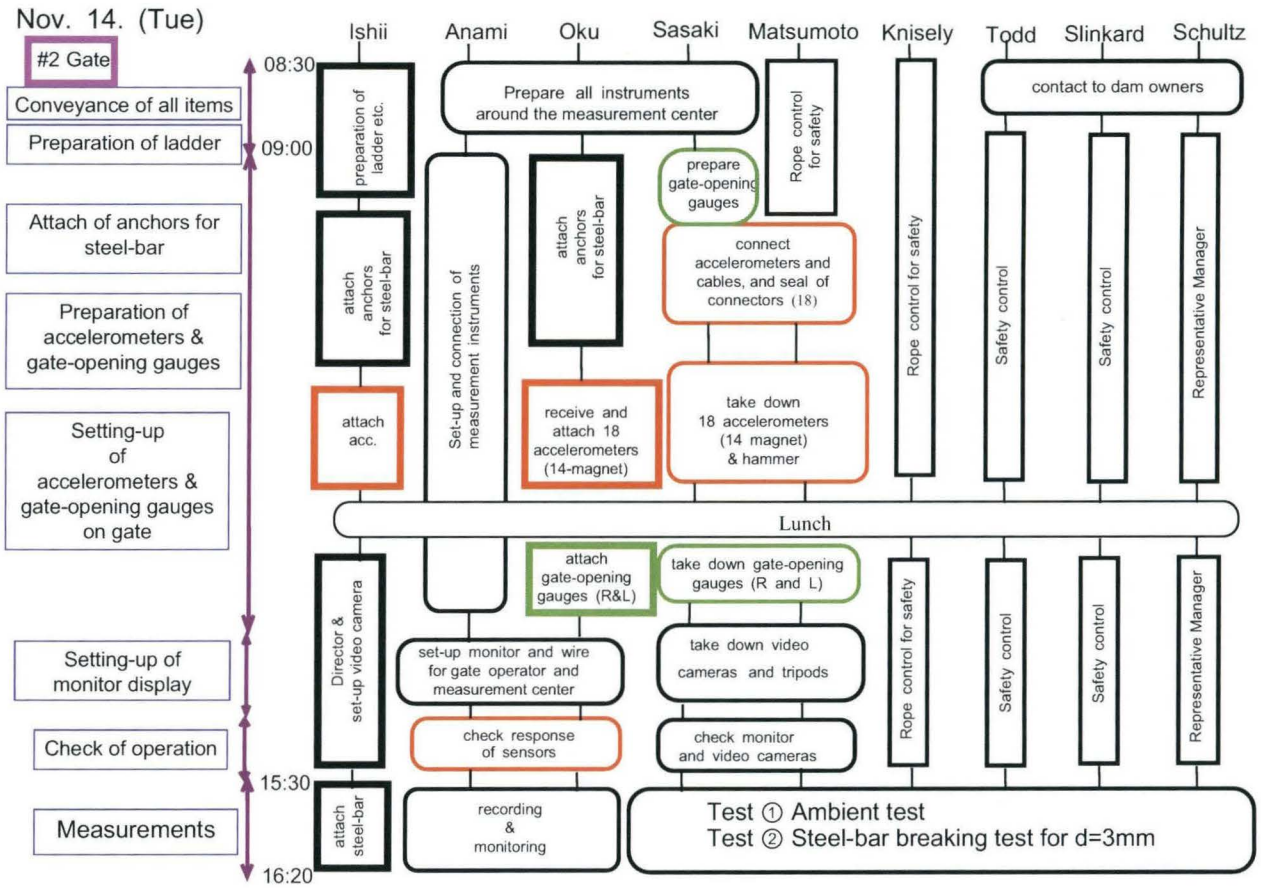

Figure 2.21(b): Work procedures of Nov. 14th for field test of the Thermalito Diversion Dam gate.

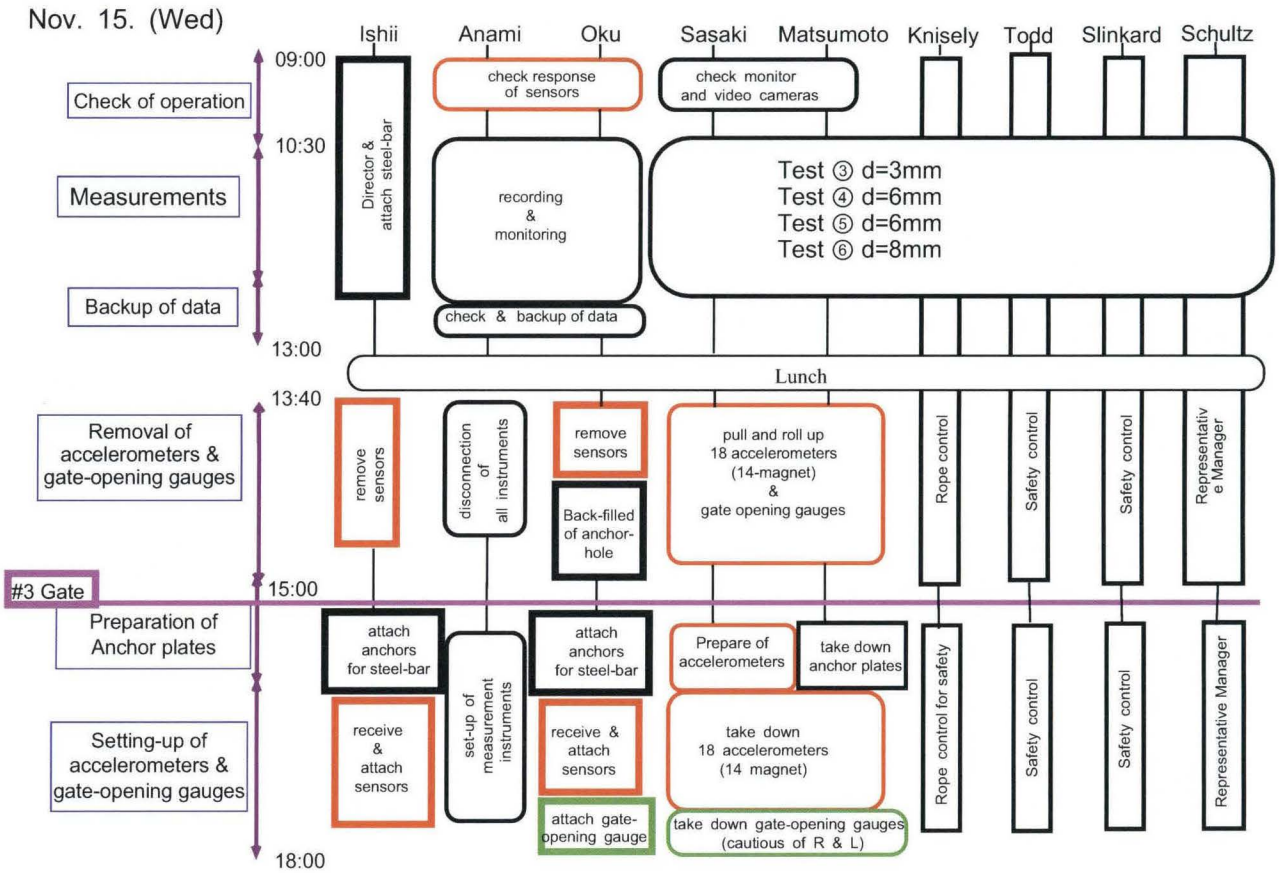

Figure 2.21(c): Work procedures of Nov. 15th for field test of the Thermalito Diversion Dam gate.

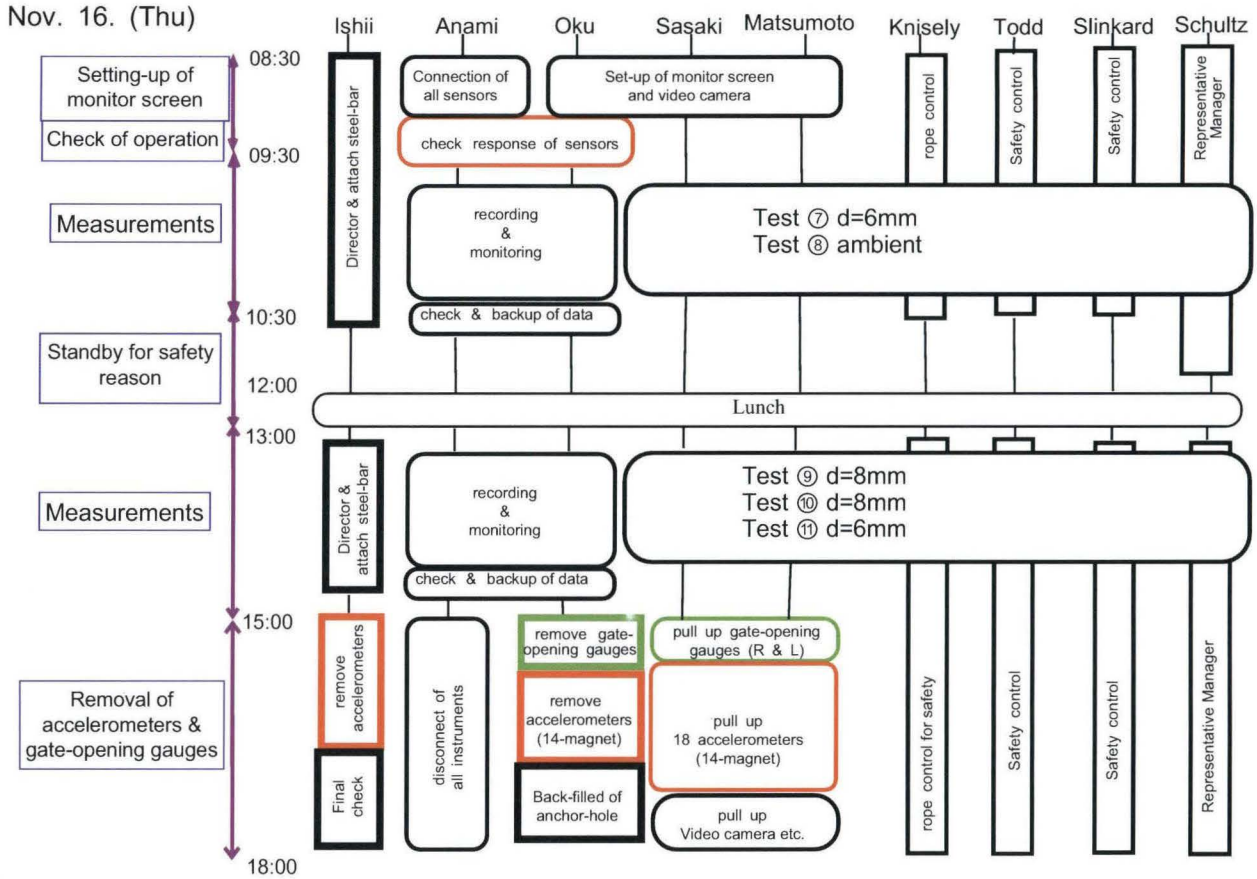

Figure 2.21(d): Work procedures of Nov. 16th for field test of the Thermalito Diversion Dam gate.

2.5 Vibration Test Conditions and Gate Opening during Tests

In the present field vibration testing, eleven tests were conducted, as listed in Table 2.4, which shows the test number, the gate number, the steel rod diameter, and the date and time. The water depth of upstream reservoir during tests is shown in Figure 2.22, in which the numbers correspond to the test numbers given in Table 2.4. The gate is installed downstream of the top of the dam crest, such that the bottom end of the skinplate is 0.5 m lower than the top of the dam crest. Therefore, the gate submergence depth was 0.5 m larger than the water level over the dam crest. The average gate submergence depth was 6.38 m.

Tests numbered 1 to 6 are for Gate #2 while the tests numbered 7 to 11 are for Gate #3. Tests 1 and 8 are ambient excitation tests, while all other tests used the steel rod breaking excitation, in which the diameter of steel rod was selected from 3 mm to 8 mm. Only in the test 2 was the steel rod installed on the downstream flange of horizontal girder. Figure 2.23(a) shows test 2 in which the steel rod with a diameter of 3 mm is installed using two long threaded bolts on the gate and the spillway concrete. However, as previously discussed, an effective impulsive excitation force sufficient to vibrate the gate could not be generated in test 2 due to the low rigidity of the horizontal girder. In all subsequent tests, the steel rod was installed on the upstream flange of the horizontal girder which is closer to the skinplate. Figure 2.23(b) shows this upstream mounting in which a steel rod with a diameter of 8 mm is installed through comparatively short threaded bolts. An effective impulsive excitation force sufficient to vibrate the whole gate was generated with this arrangement. Photos of the failed steel rod after testing are shown in Figures 2.24, with the upper side of the failed steel rod shown in Fig 2.24(a), while bottom portion of the rod is shown in Fig 2.24 (b).

Table 2.4: Test conditions.

Test No.	Gate No.	Diameter	Date	Time
1	2	ambient	Nov. 14, 2006	15:40
2		d=3mm		16:10
3	2	d=3mm	Nov. 15, 2006	10:55
4		d=6mm		11:17
5		d=6mm		11:35
6		d=8mm		12:16
7	3	d=6mm	Nov. 16, 2006	9:53
8		ambient		9:57
9		d=8mm		13:15
10		d=8mm		14:23
11		d=6mm		14:46

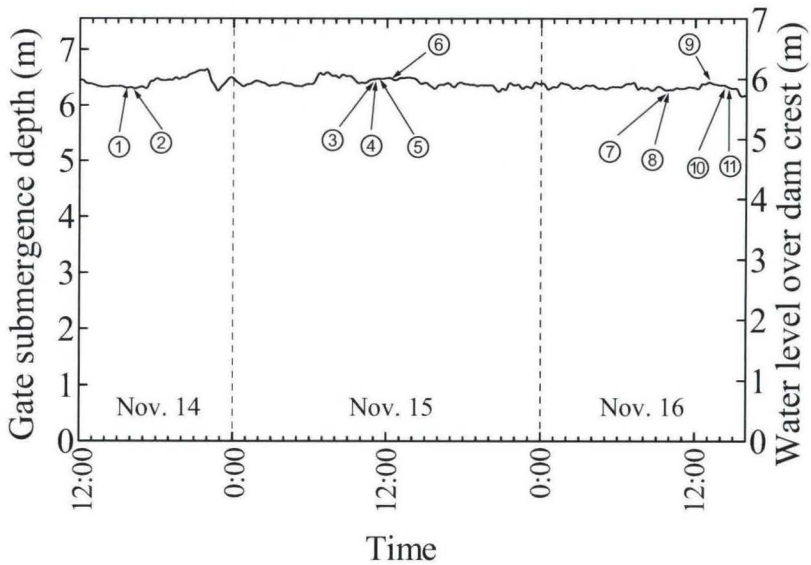

Figure 2.22: Water depth of upstream reservoir during field testing.

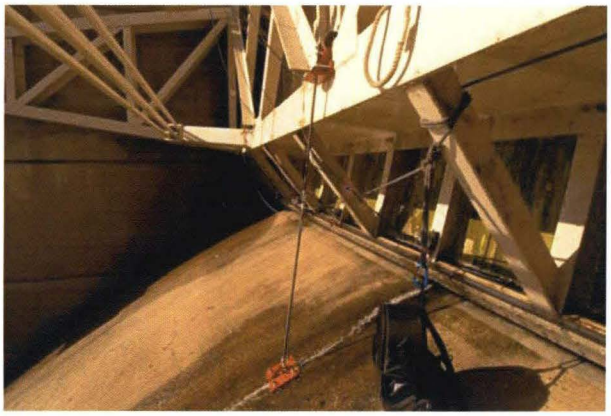

(a) On the downstream girder.

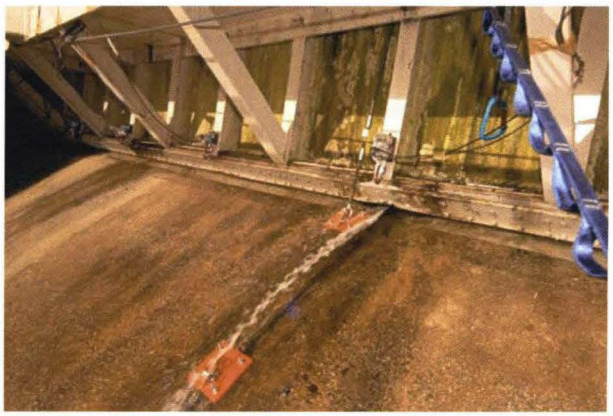

(b) On the upstream girder.

Figure 2.23: Photos of steel rod installations on the gate and the spillway concrete.

(a) Upper side.

(b) Lower side.

Figure 2.24: Photos of steel rod with a diameter of 8mm, after tested.

The gate openings during the tests are shown in Figure 2.21 to Figure 2.35. In each figure, part (a) shows the data for the full time length of gate operation during the test, with an indication of the steel rod breaking time, while parts (b) and (c) show enlarged views of the data near the steel rod breaking time, measured at the right and left hand sides (from upstream) of the skinplate, respectively. The solid line represents the gate opening on the right hand side while the broken line is that for the left-hand side.

A careful attention was taken to gradually open the gate, so that the gate could be stopped immediately after the steel rod fails. In all cases, the gate opening suddenly changes in the interval from 0.1 (sec) to 0.17 (sec) after the steel rod failed. This sudden change in the gate opening is denoted as the "excited displacement" of the skinplate and the corresponding data are plotted by small open circles in Figure 2.36, labeled with the corresponding test number.

These measured excited displacements are about twice as large as the estimated elongation of the wire, shown by the filled circles. This is an expected result, since the gate was dynamically released from the constraint of the bolt and experienced the unbalanced load of the elastic strain of the wire. Thus, the gate would have naturally exceeded its equilibrium position.

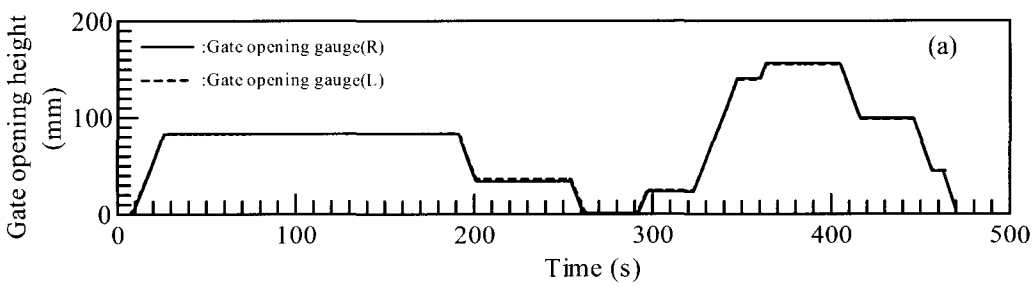

Figure 2.25: Gate opening during Test No.1 (ambient).

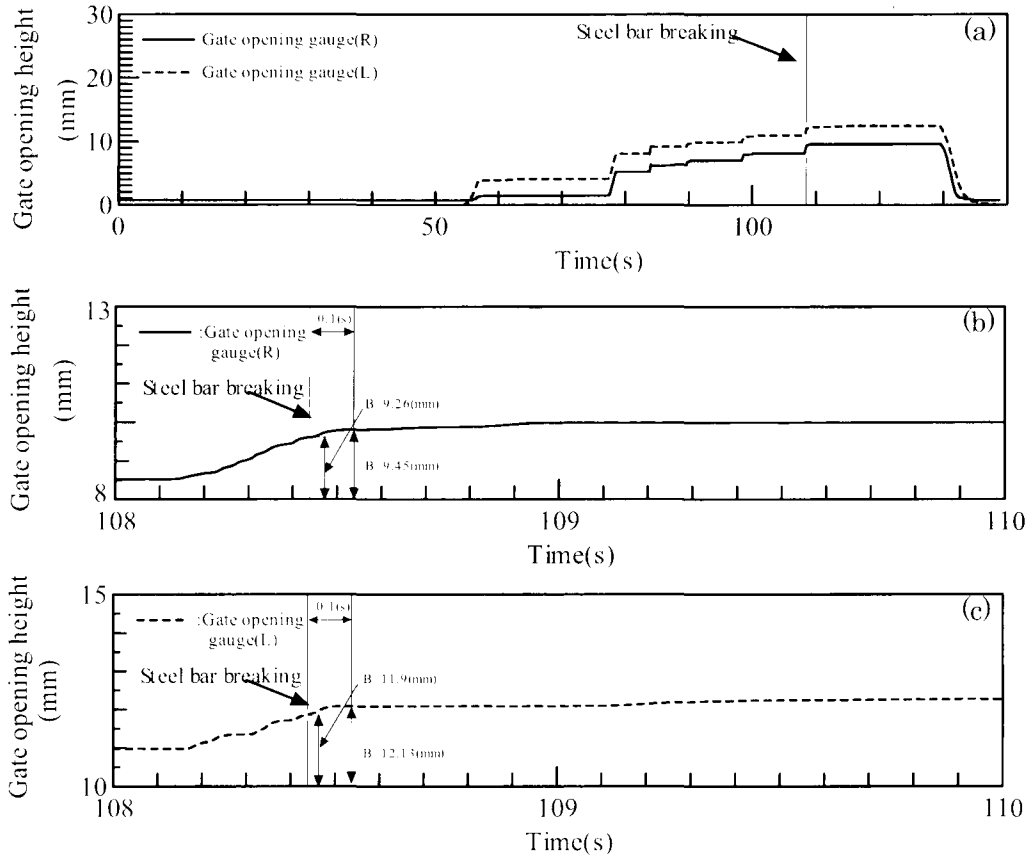

Figure 2.26: Gate opening during Test No.2 (d=3mm).

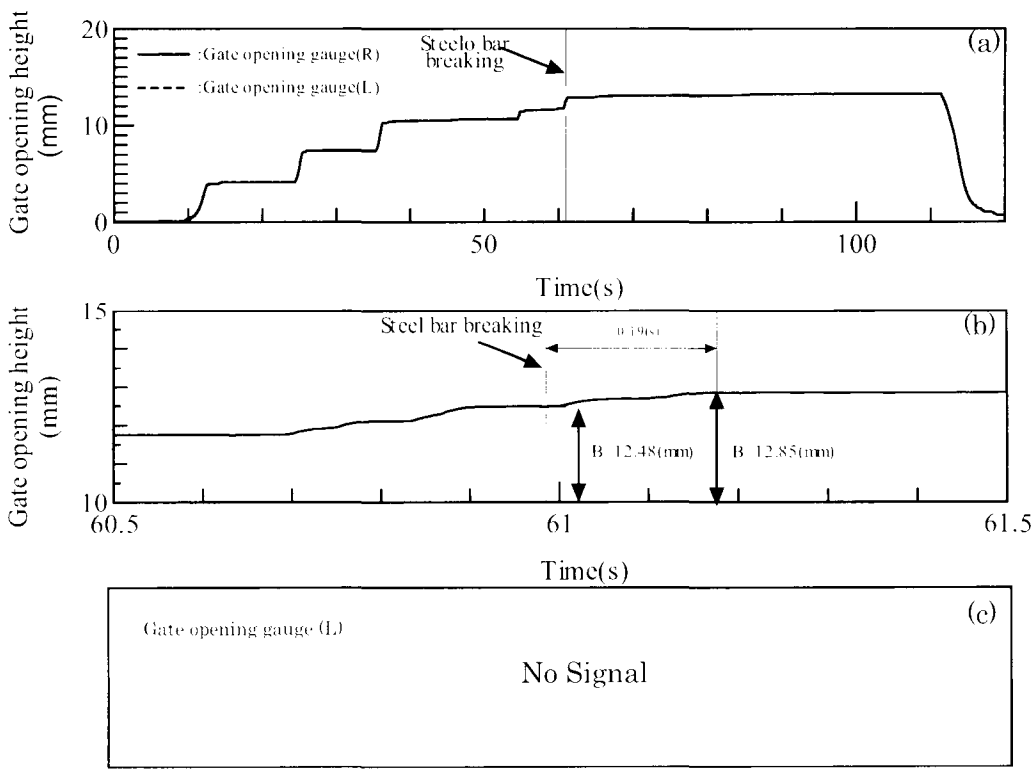

Figure 2.27: Gate opening during Test No.3 (d = 3 mm).

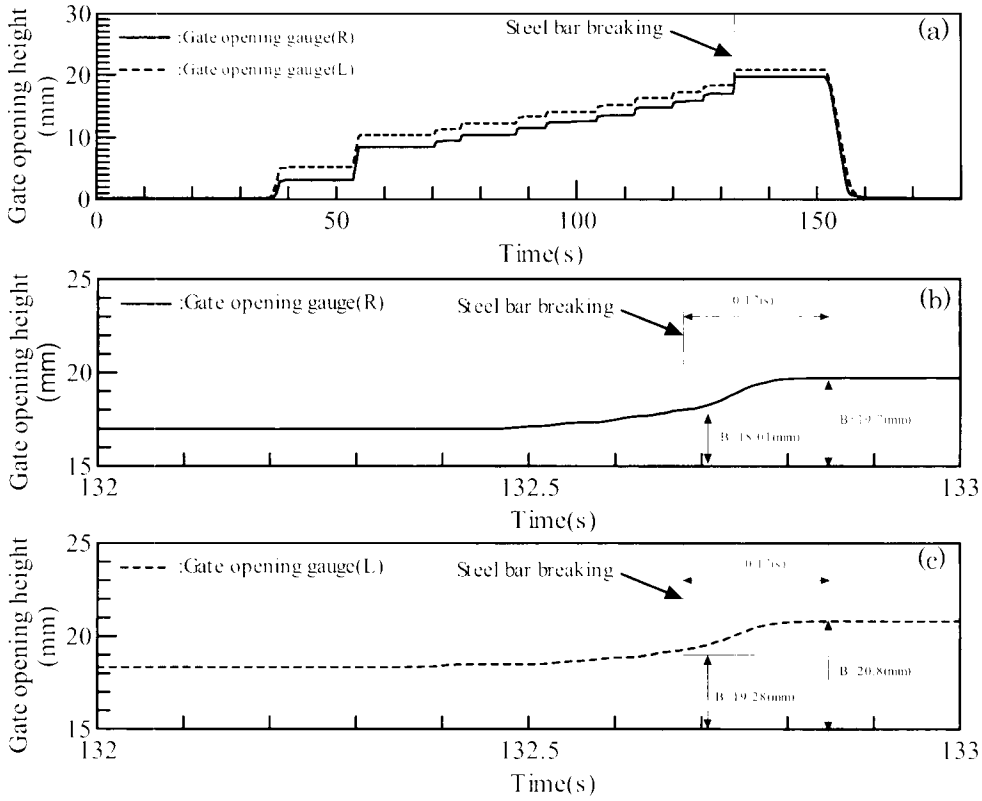

Figure 2.28: Gate opening during Test No.4 (d = 6 mm).

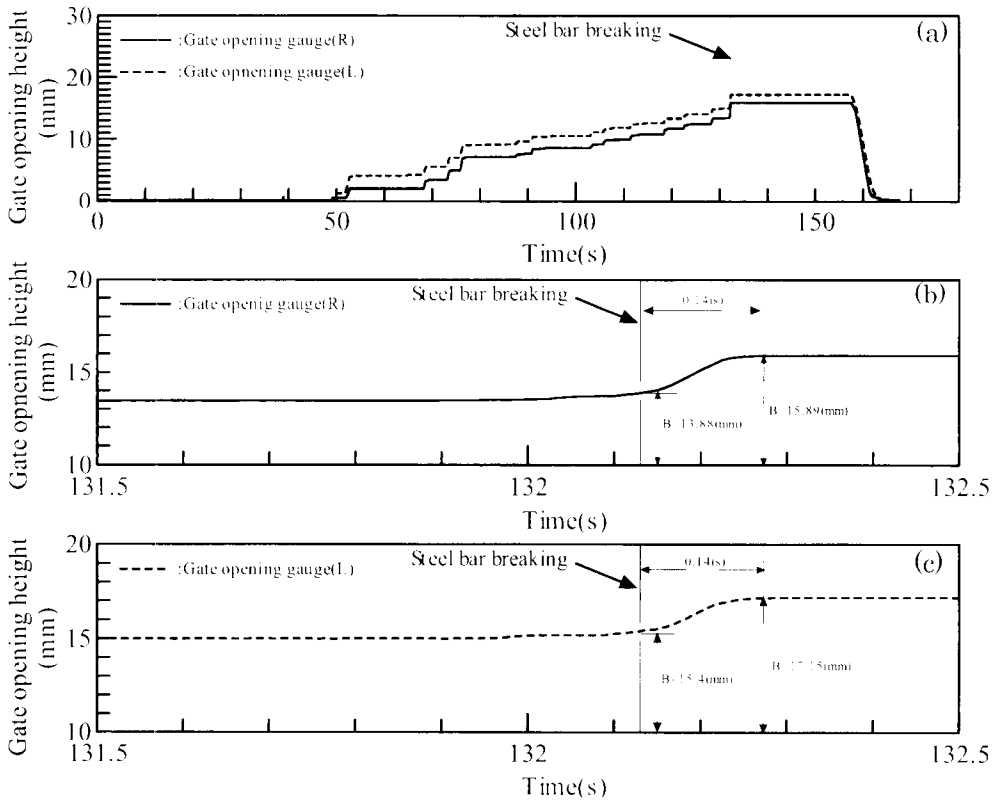

Figure 2.29: Gate opening during Test No.5 (d = 6 mm).

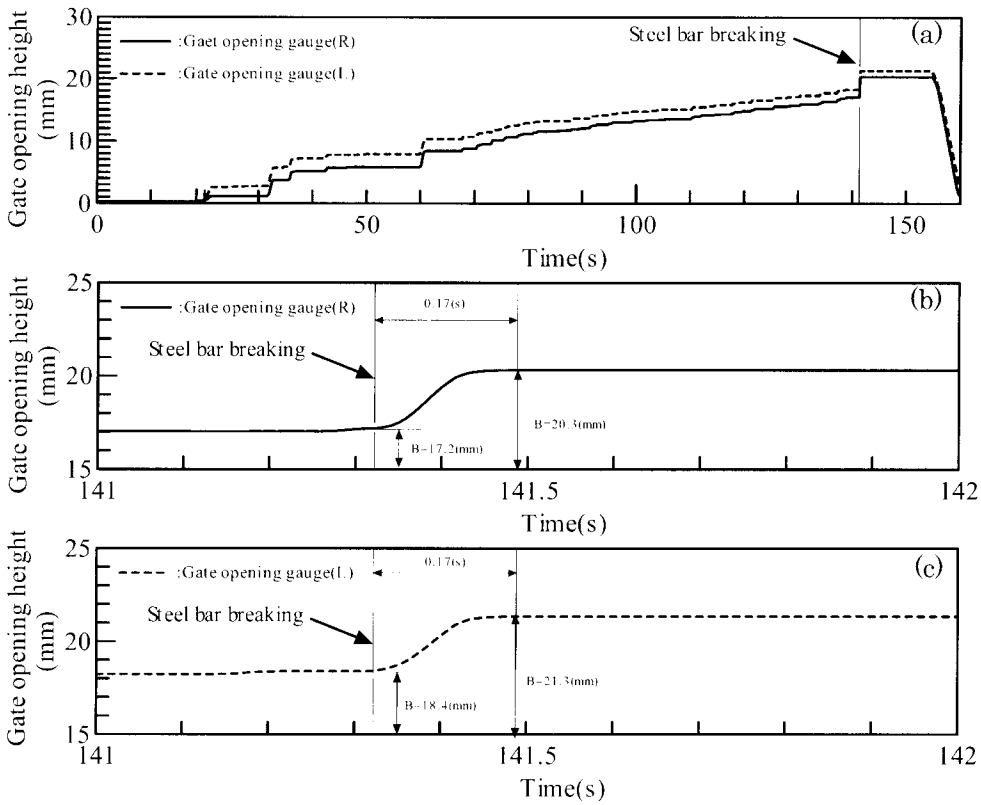

Figure 2.30: Gate opening during Test No.6 (d = 8 mm).

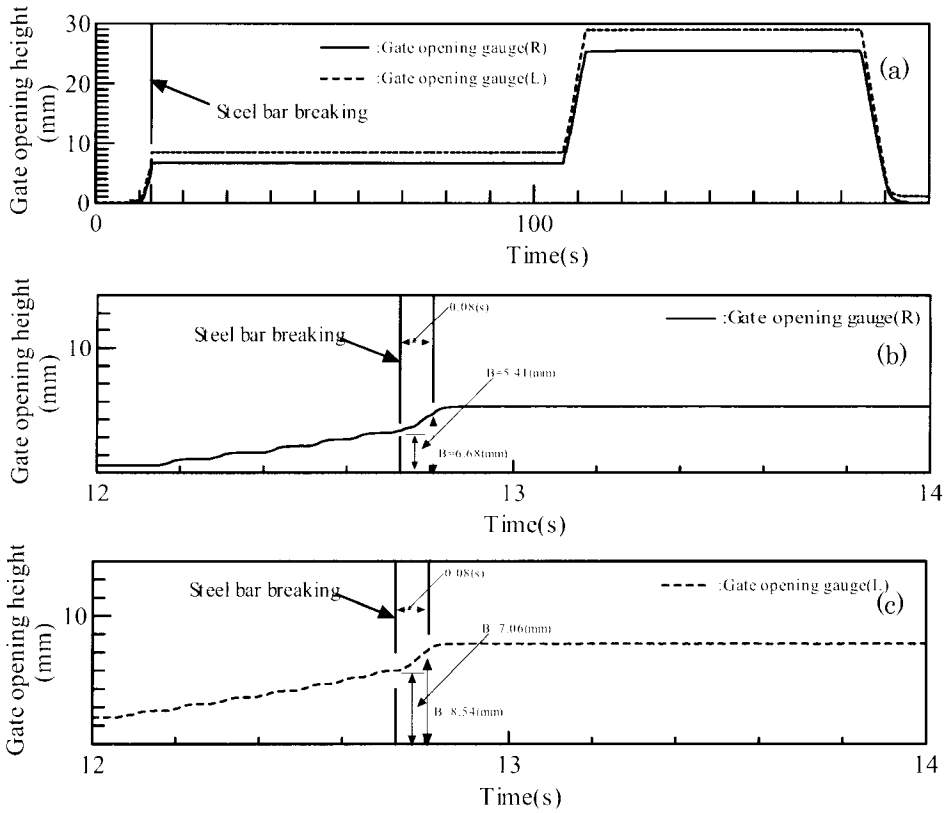

Figure 2.31: Gate opening during Test No.7 (d = 6 mm).

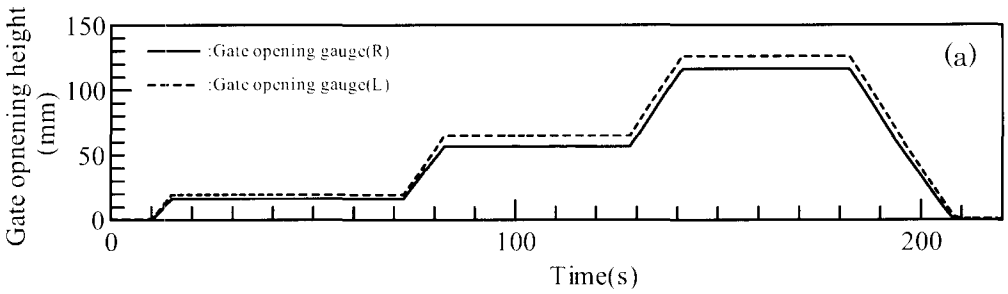

Figure 2.32: Gate opening during Test No.8 (ambient).

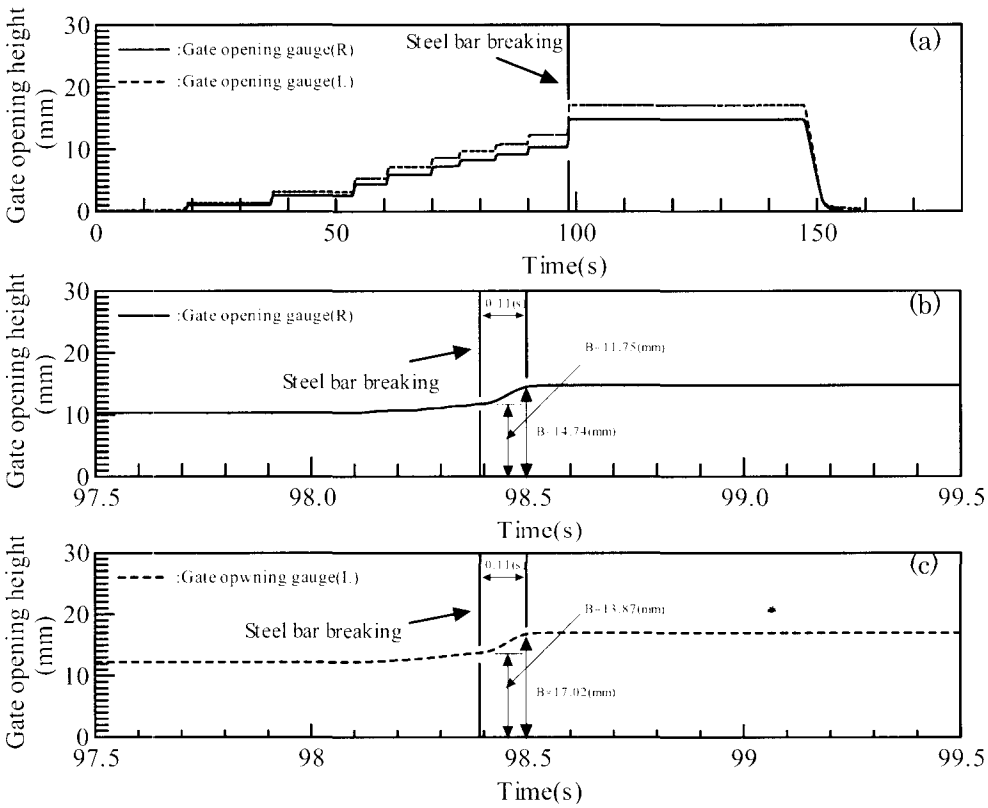

Figure 2.33 Gate opening during Test No.9 (d = 8 mm).

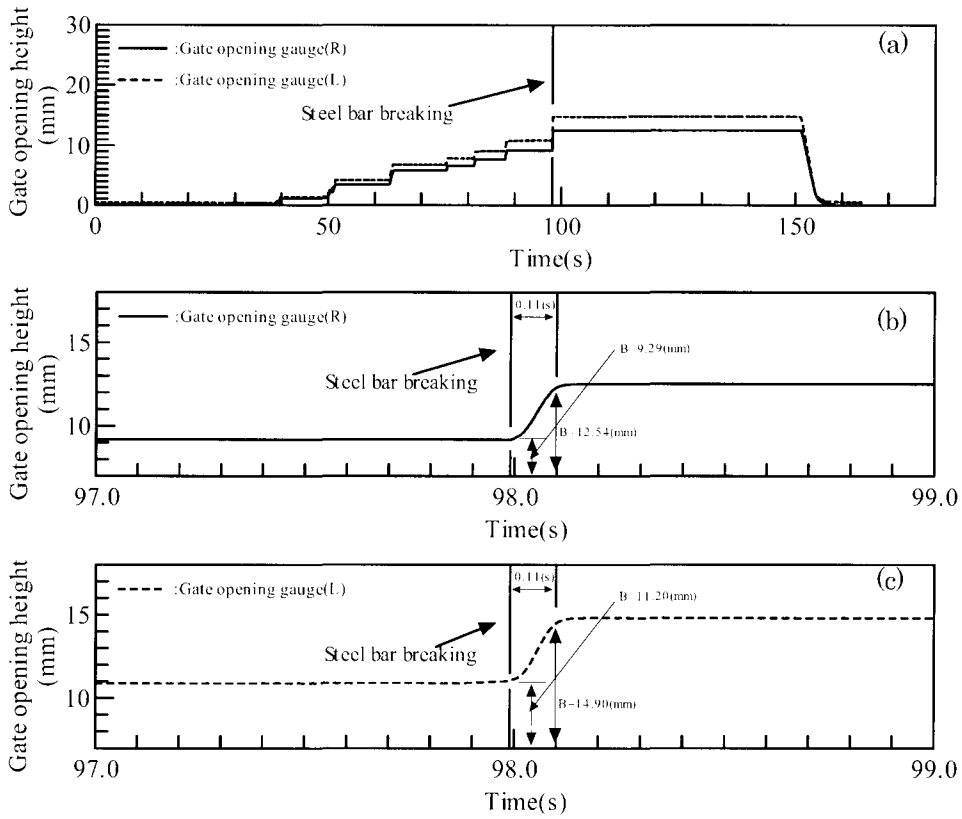

Figure 2.34: Gate opening during Test No.10 (d = 8 mm).

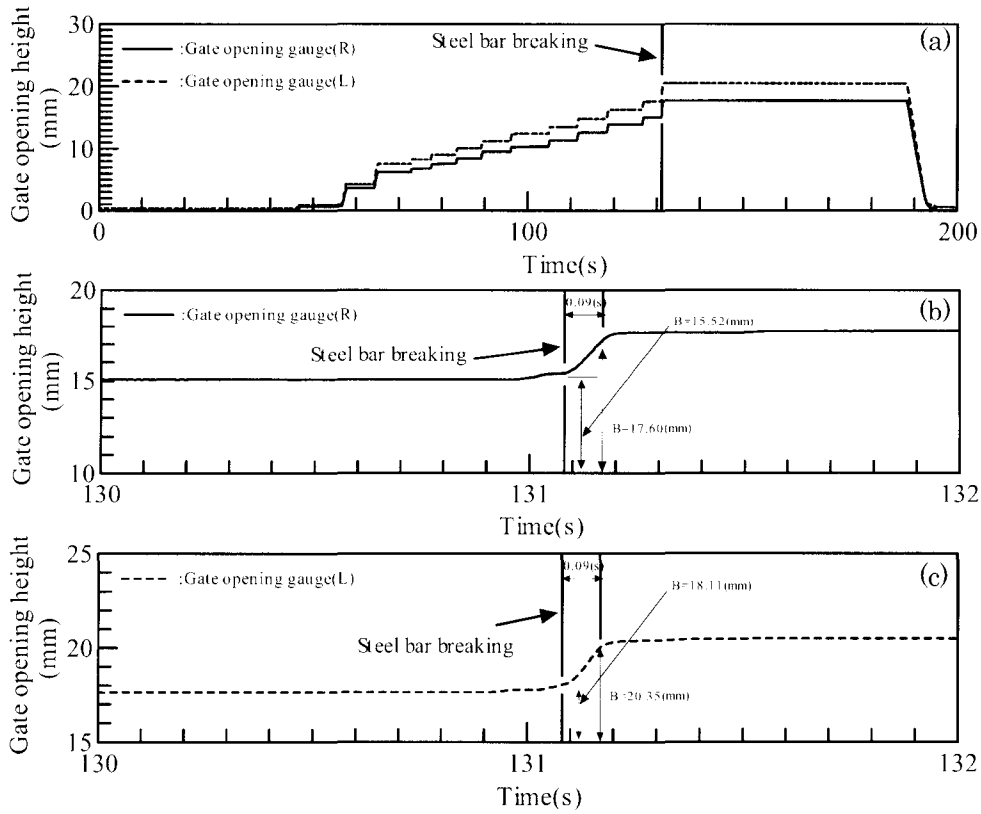

Figure 2.35: Gate opening during Test No.11 (d = 6 mm).

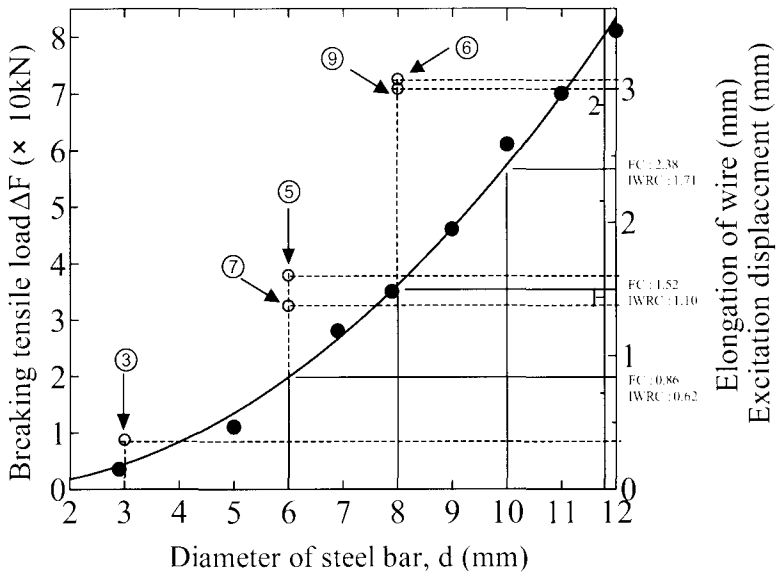

Figure 2.36: Initial vertical displacement of the skinplate due to steel rod breaking.

3. MEASURED VIBRATION ACCELERATIONS

Sequential pictures the of steel rod breaking, taken with a digital video camera, are shown in Figure 3.1. In Figure 3.1 9(a), the gate is closed, just prior to beginning the test. In Figures 3.1(b) to (d), the gate opening is increasing in a stepwise fashion, with a corresponding increase in the water flow rate. Finally, as shown in Figure 3.1(e), the steel rod breaks and upper portion rapidly accelerates away from the lower portion.

Vibration accelerations of the whole gate, in response to the input energy from the breaking of the steel rod, were recorded on computers through A/D Converters (see Figure 2.10), in which the data sampling was set at 12 kHz. Measured vibration accelerations for each of the tests listed in Table 2.2 are sequentially displayed as real time waveforms in Figures 3.2 to 3.8 for Gate #2 and in Figures 3.9 to 3.14 for Gate #3. Measurement positions and directions are schematically shown in the upper portion of each figure. In each figure (Figures 3.2 to 3.14), the trace labeled (a) shows accelerations in the radial direction, measured at the skinplate bottom, trace (b) shows accelerations in the radial direction, measured at the skinplate center, trace (c) shows accelerations in the tangential and spanwise directions, measured at the skinplate center and on the right-hand side upper radial arm. The alphanumerics shown in the upper right portion of each waveform show the measurement positions and directions, where "V" represents the vertical direction, (which should rigorously be denoted as the tangential direction), while "R" represents the radial direction (or as it is often called, the streamwise direction), and "S" represents the spanwise direction. For example, E6-R represents the streamwise acceleration measured at Point E6 at the skinplate bottom center, as previously defined in Figure 2.5.

For the ambient excitation in Test No.1 for Gate #2, representative data traces are shown in Figures 3.2 at a small gate opening of B = 23 mm and in Figure 3.3 at a larger gate opening B = 166 mm, For the ambient excitation in Test No.8 for Gate #3, representative data traces are shown in Figures 3.10 with a gate opening of B = 19 mm and in Figure 3.11 for a gate opening of B = 126 mm.

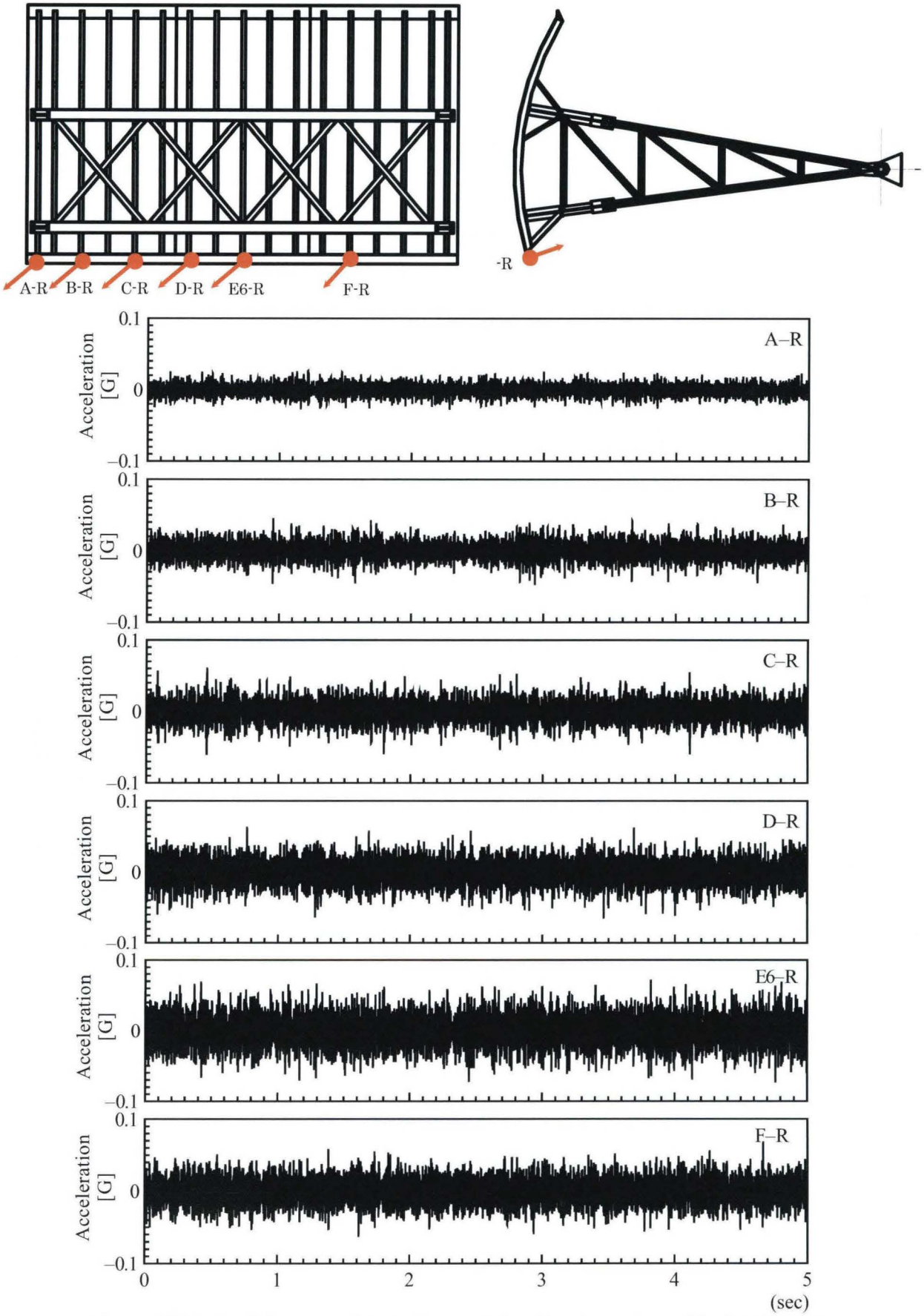

Figure 3.2(a): Real time waveforms of streamwise vibrations at the skinplate bottom (Test No.1: ambient, B = 23 mm).

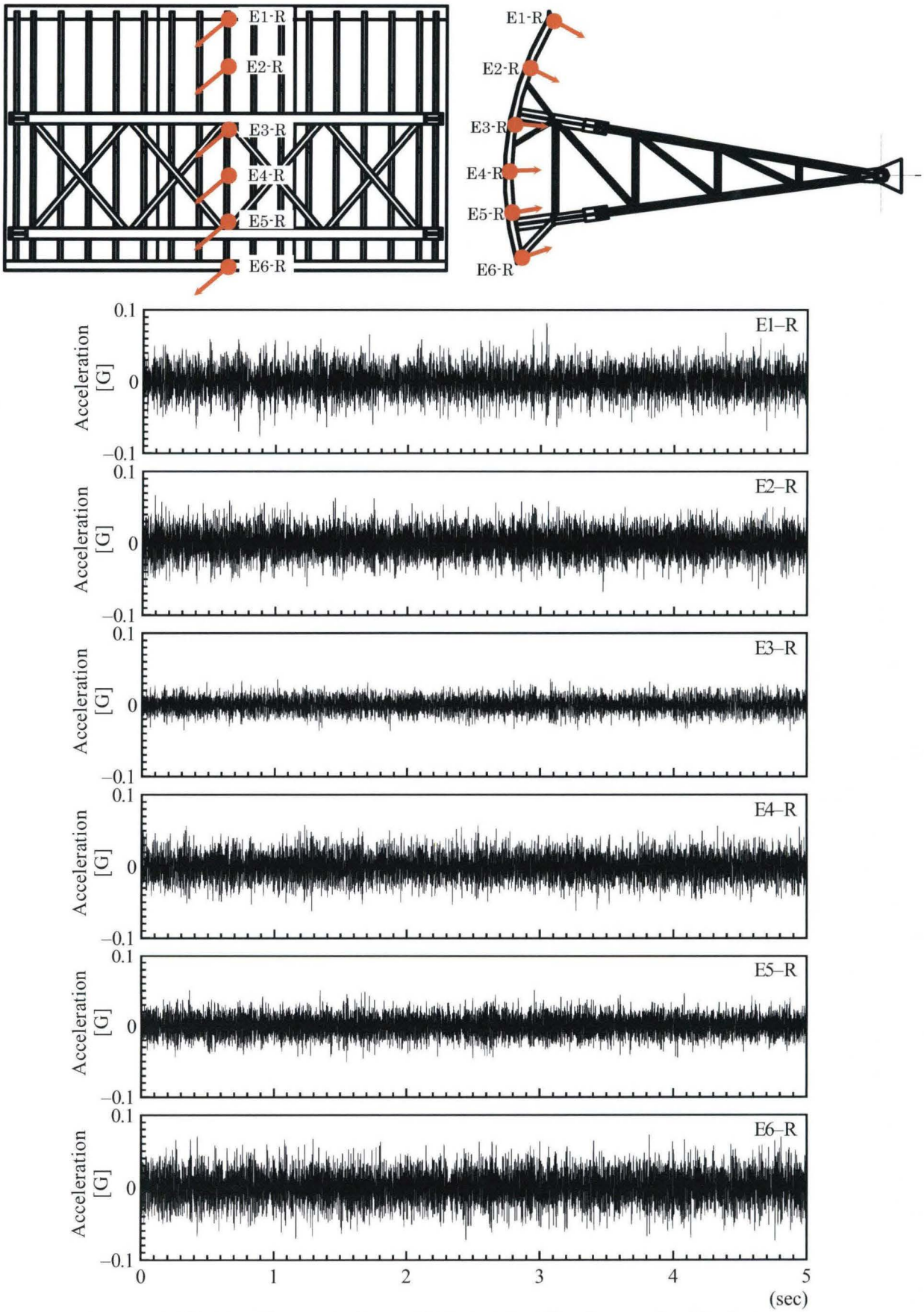

Figure 3.2(b): Real time waveforms of streamwise vibrations at the skinplate center (Test No.1: ambient, B = 23 mm).

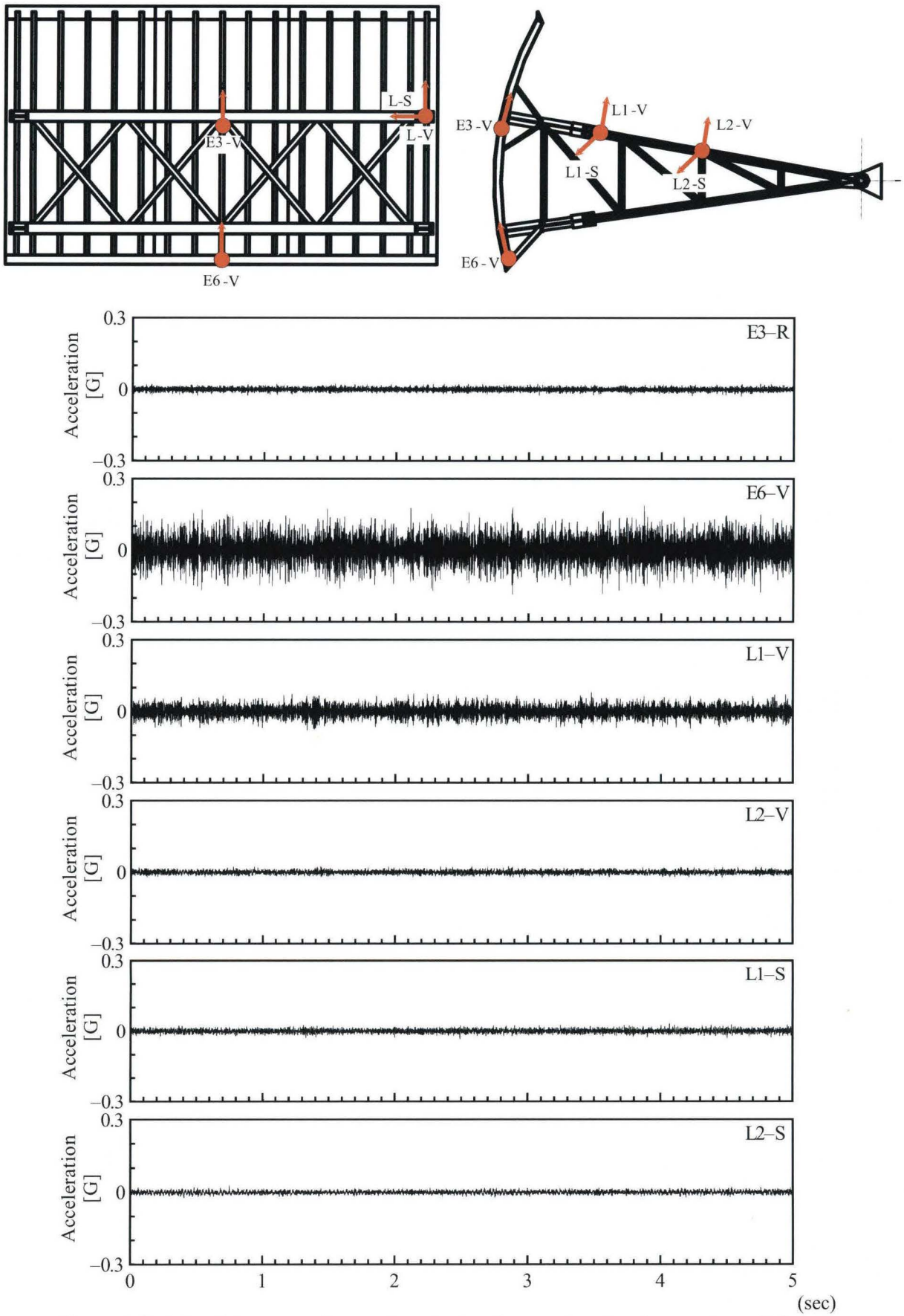

Figure 3.2(c): Real time waveforms of vertical and spanwise vibrations at the radial arm (Test No.1: ambient, B = 23 mm)

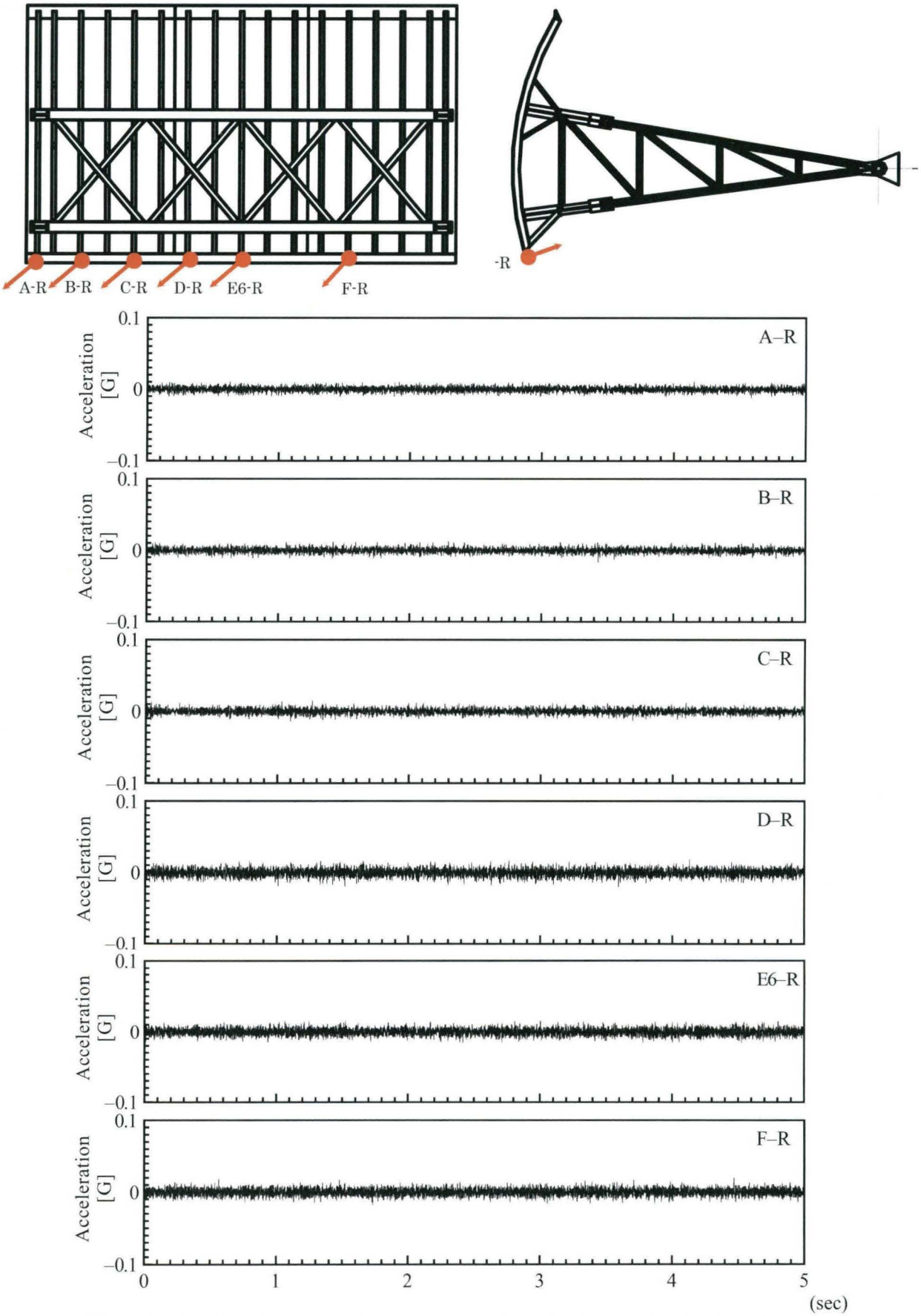

Figure 3.3(a): Real time waveforms of streamwise vibrations at the skinplate bottom (Test No.1: ambient, B = 156 mm).

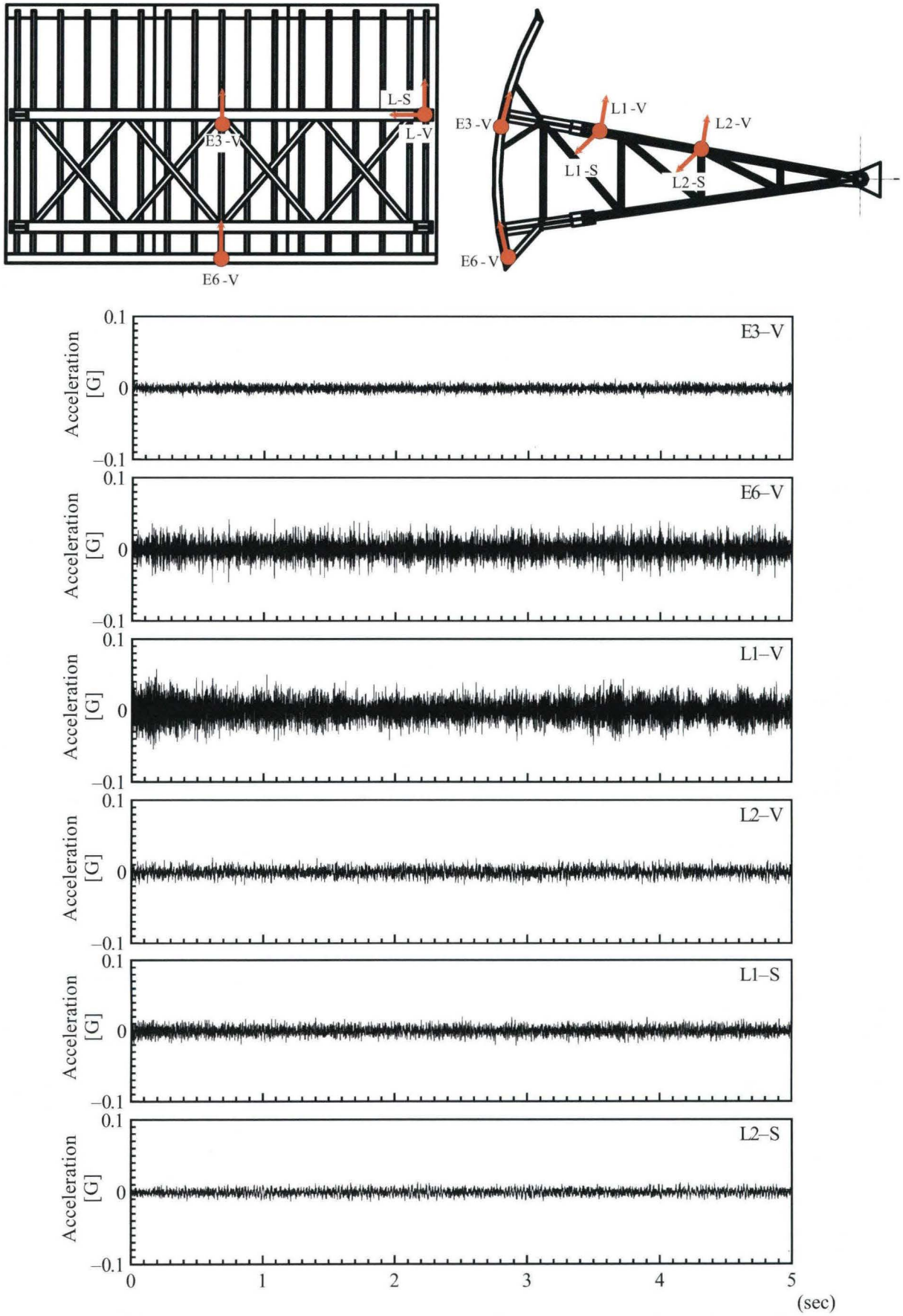

Figure 3.3(c): Real time waveforms of vertical and spanwise vibrations at the radial arm (Test No.1: ambient, B = 156 mm).

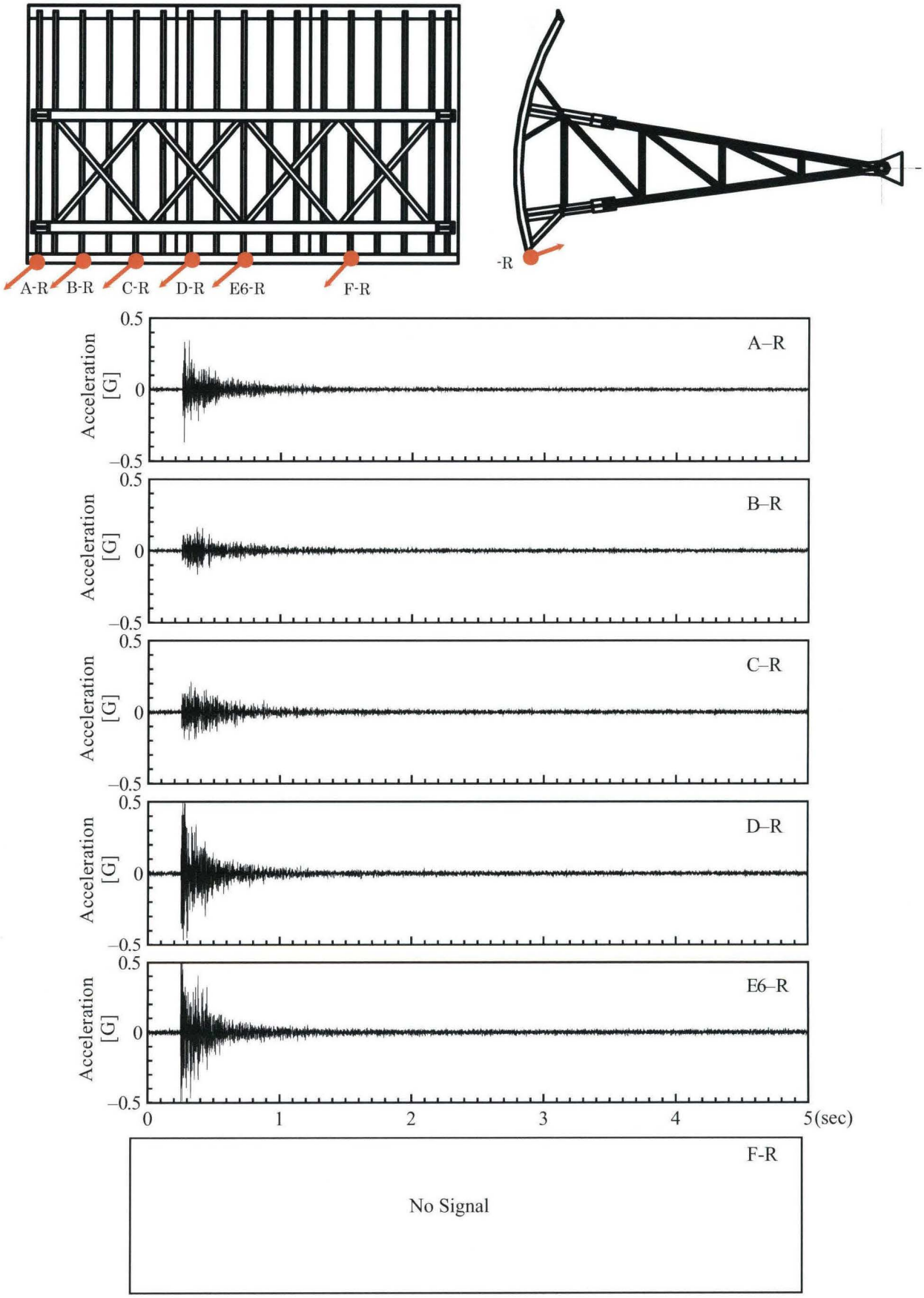

Figure 3.4(a): Real time waveforms of streamwise vibrations at the skinplate bottom (Test No.2: steel rod breaking, d = 3 mm).

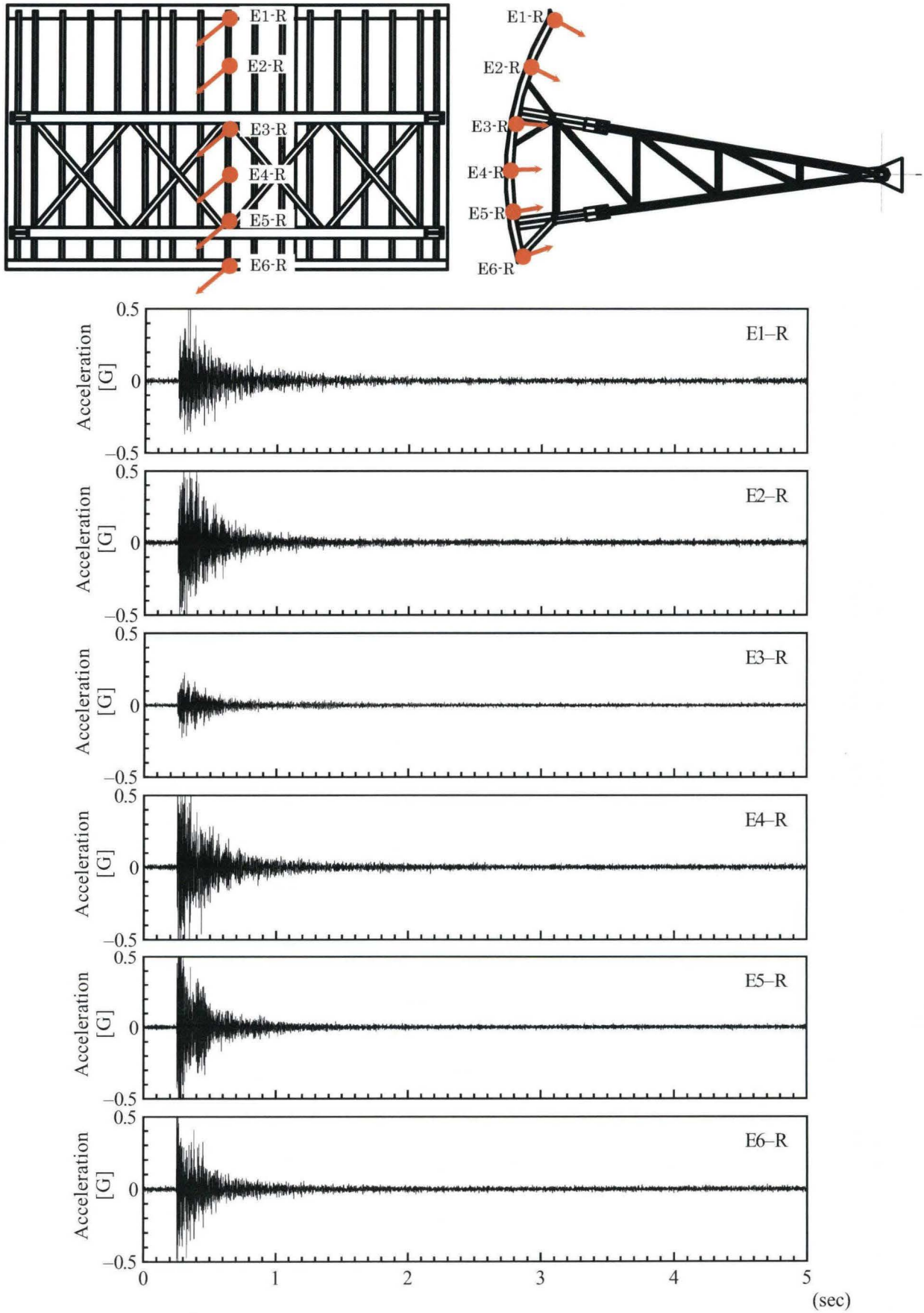

Figure 3.4(b): Real time waveforms of streamwise vibrations at the skinplate center (Test No.2: steel rod breaking, d = 3 mm).

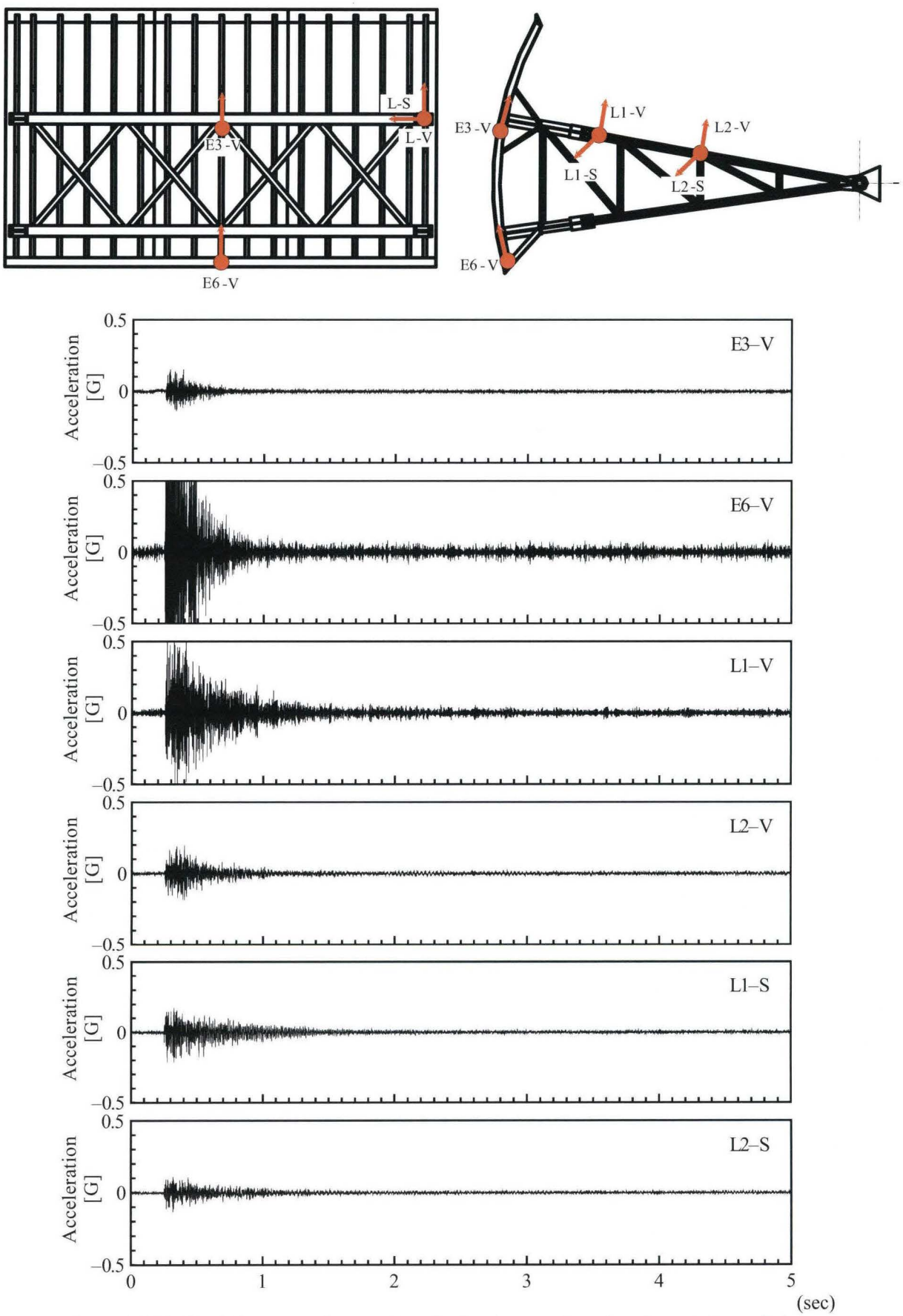

Figure 3.4(c): Real time waveforms of vertical and spanwise vibrations at the radial arm (Test No.2: steel rod breaking, d = 3 mm).

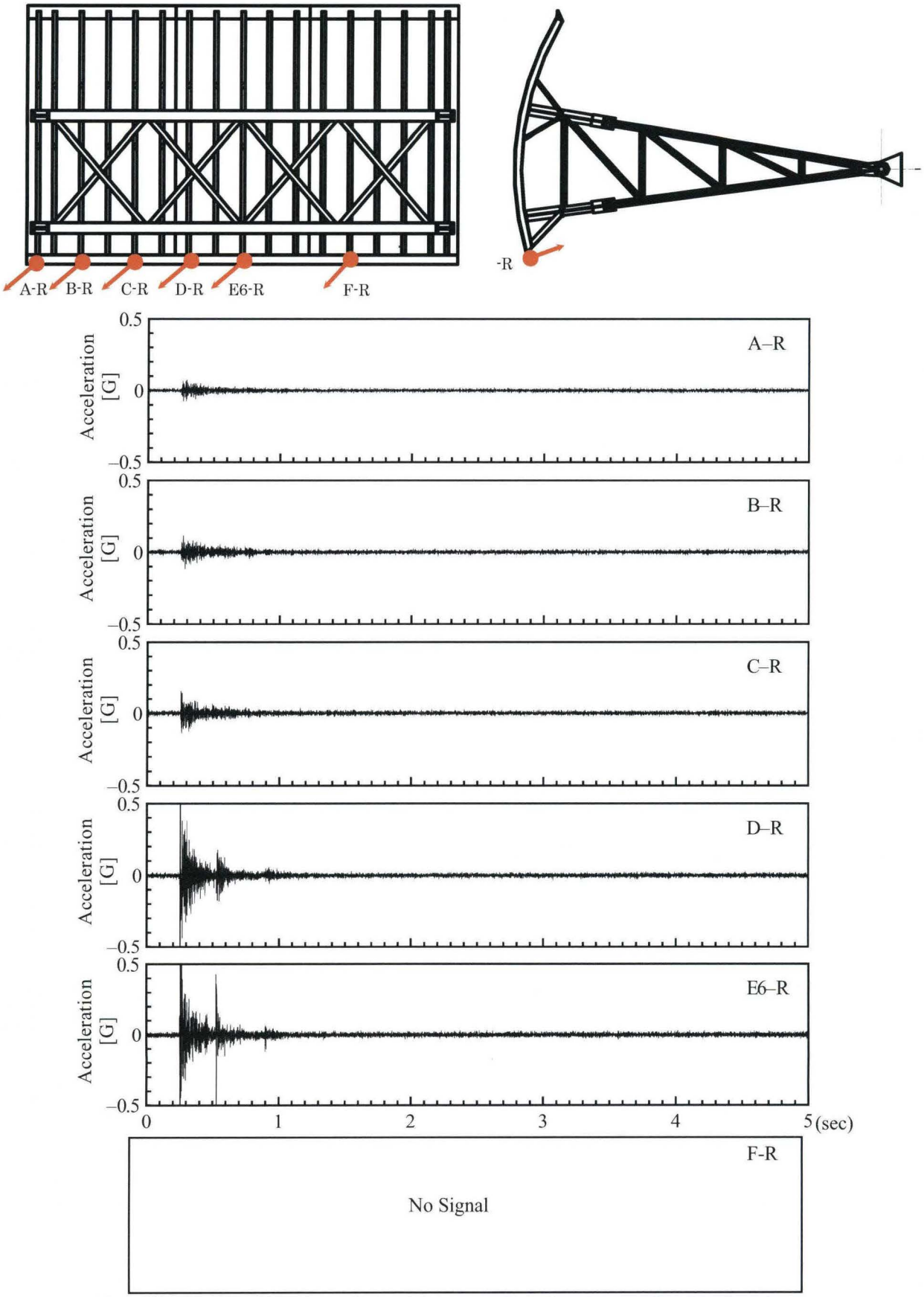

Figure 3.5(a): Real time waveforms of streamwise vibrations at the skinplate bottom (Test No.3: steel rod breaking, d = 3 mm).

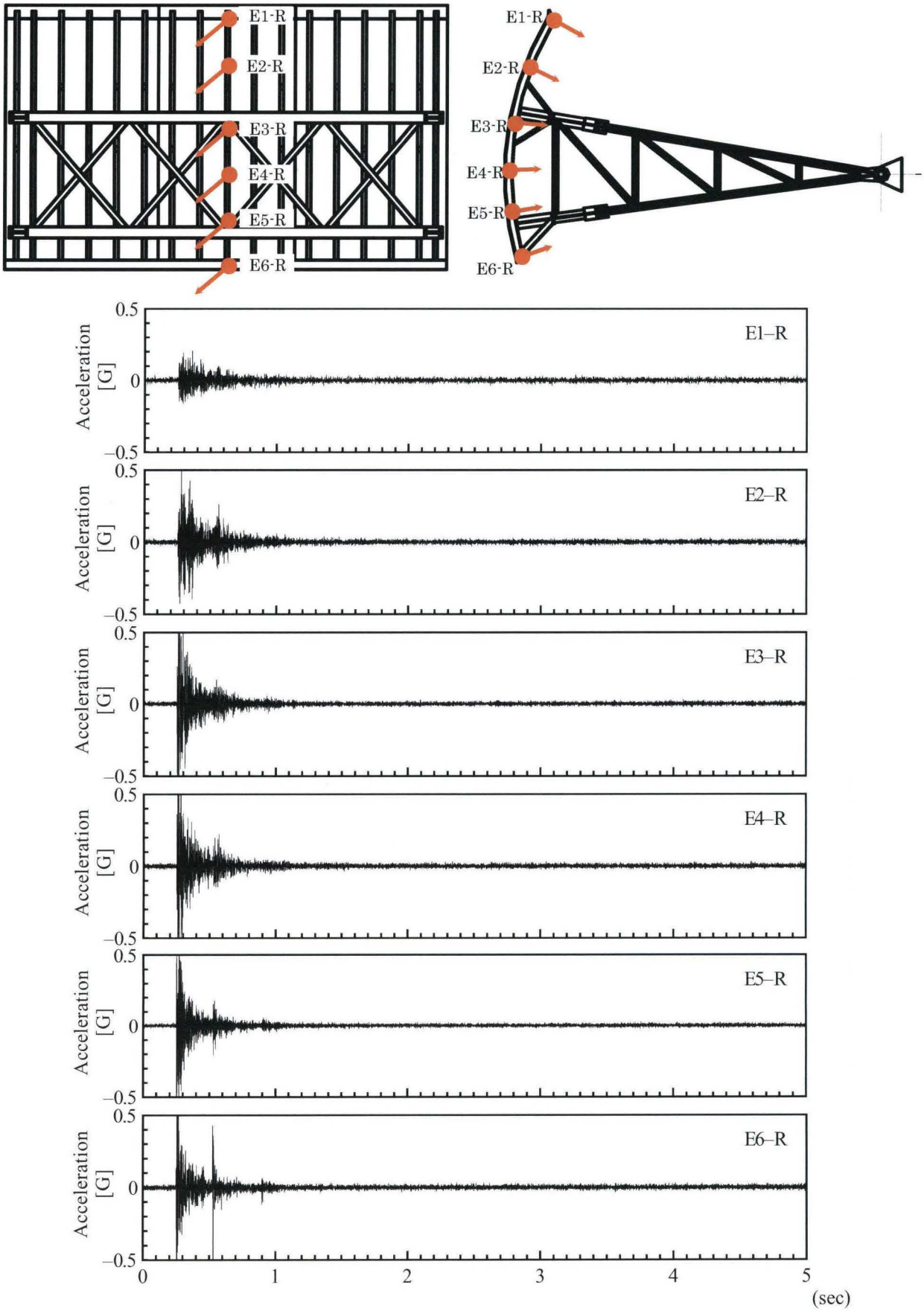

Figure 3.5(b): Real time waveforms of streamwise vibrations at the skinplate center (Test No.3: steel rod breaking, d = 3 mm).

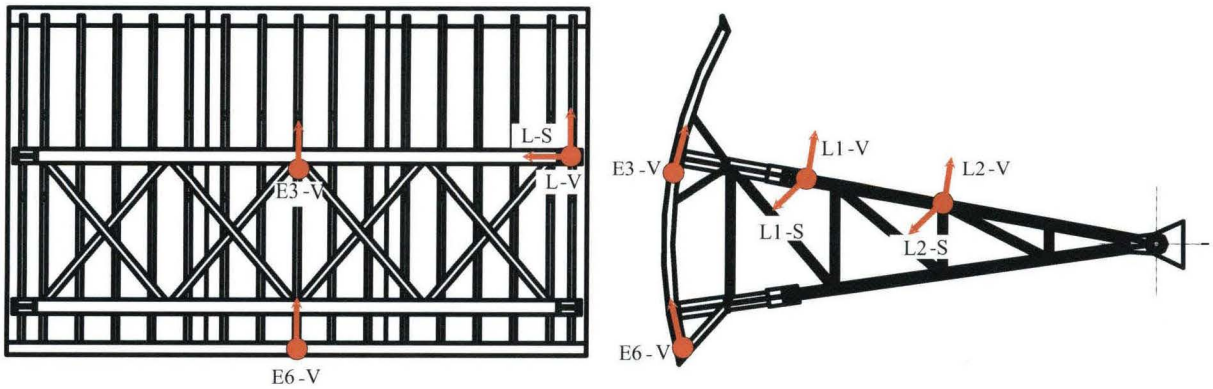

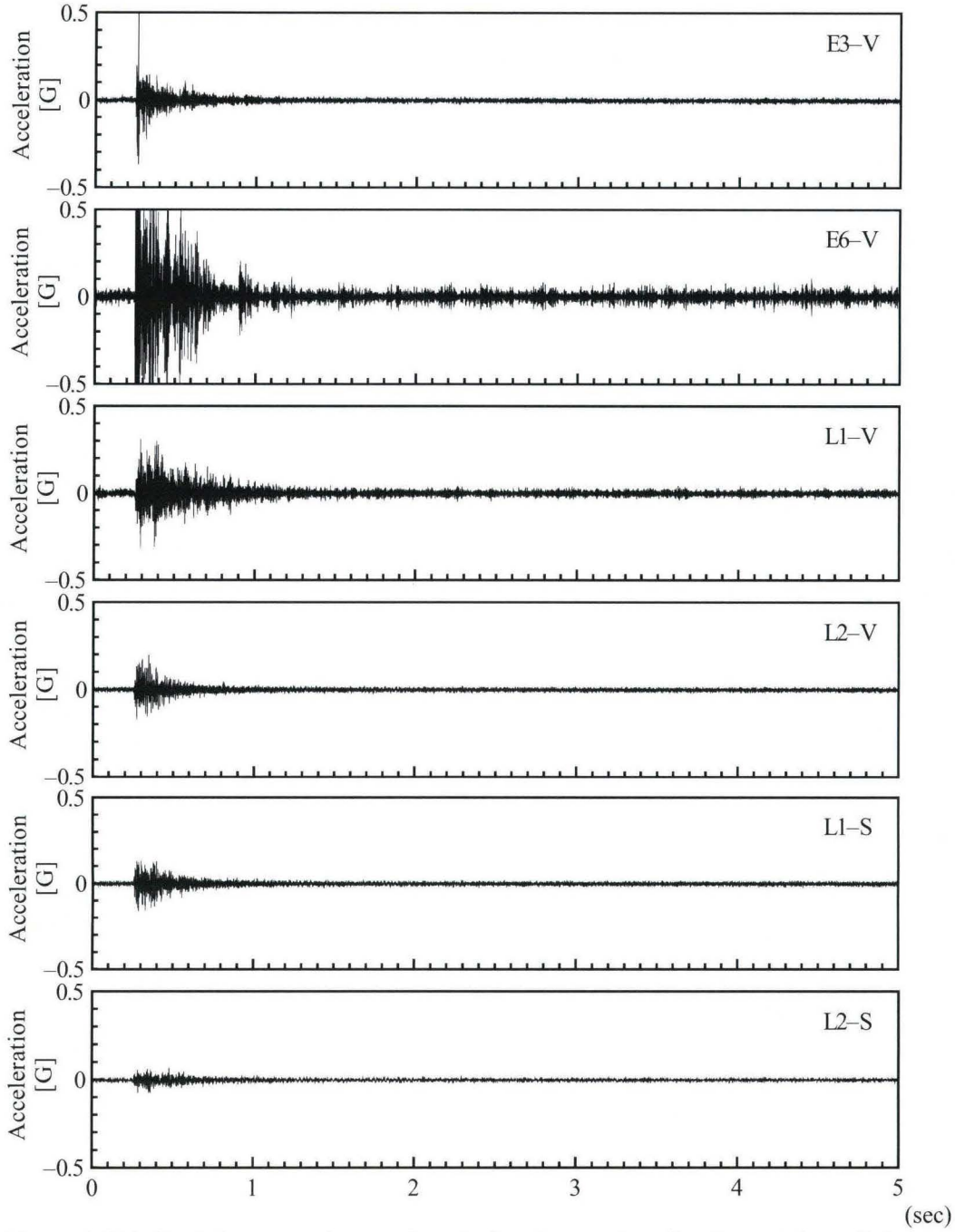

Figure 3.5(c): Real time waveforms of vertical and spanwise vibrations at the radial arm (Test No.3: steel rod breaking, d = 3 mm).

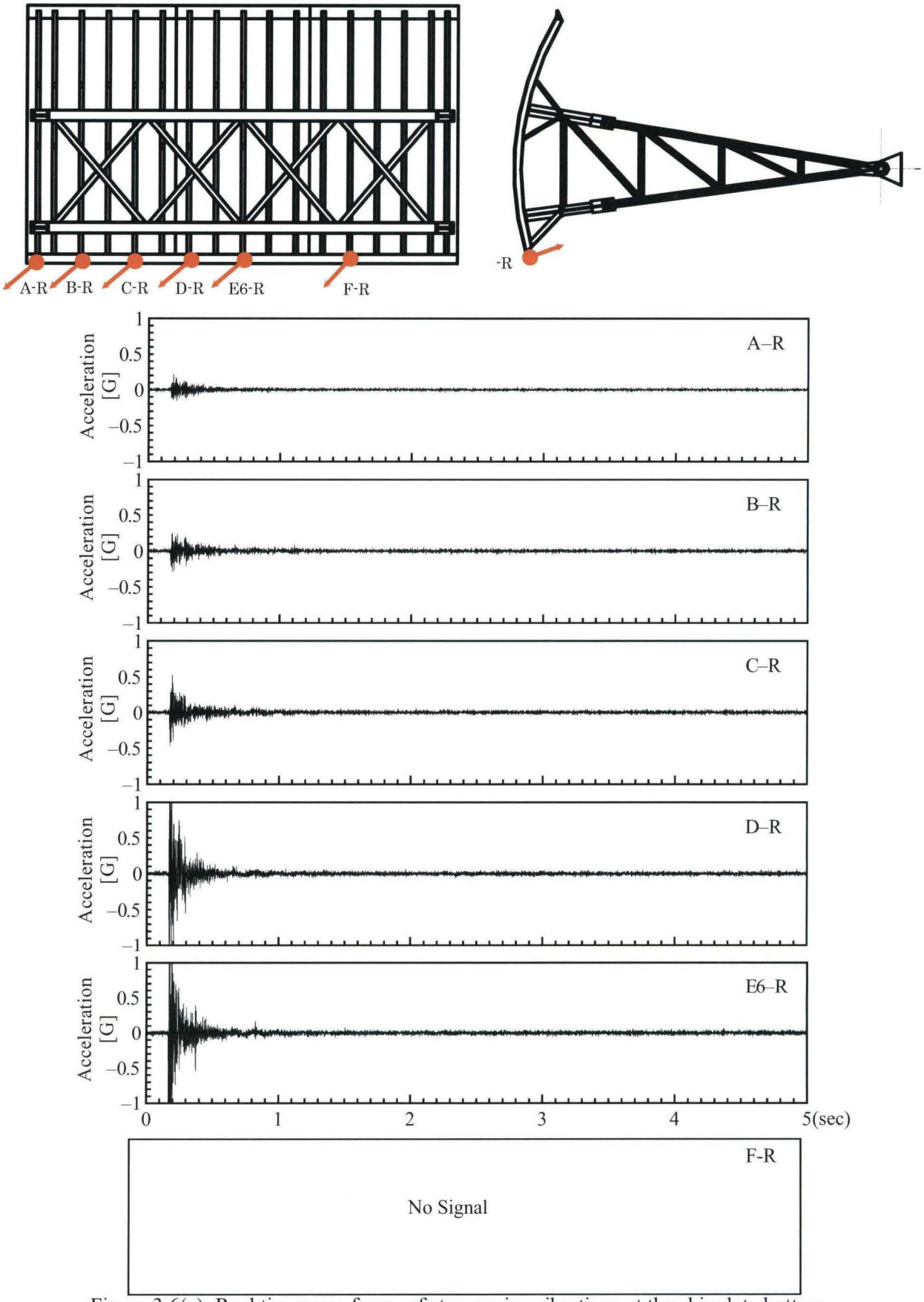

Figure 3.6(a): Real time waveforms of streamwise vibrations at the skinplate bottom (Test No.4: steel rod breaking, d = 6 mm).

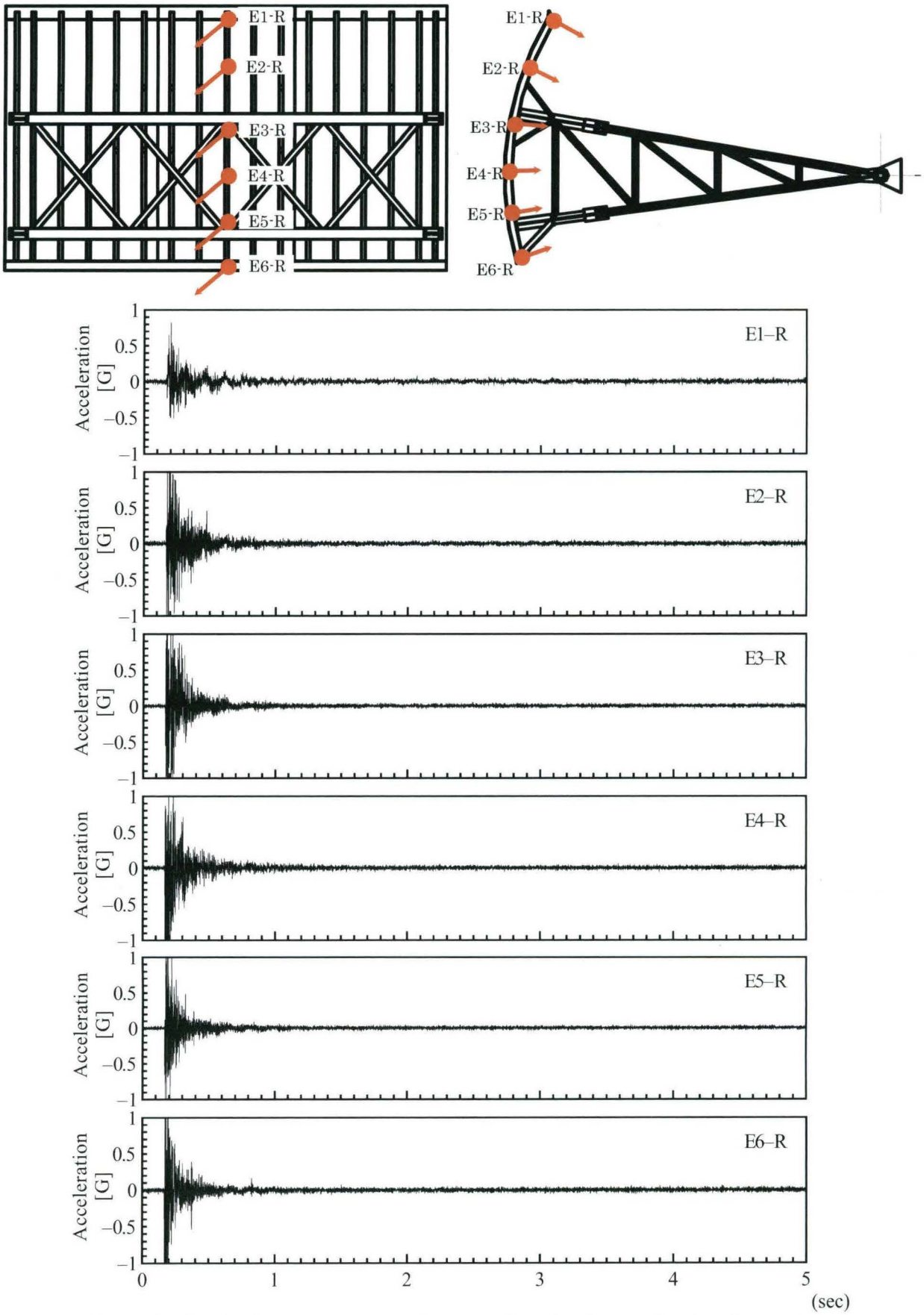

Figure 3.6(b): Real time waveforms of streamwise vibrations at the skinplate center (Test No.4: steel rod breaking, d = 6 mm).

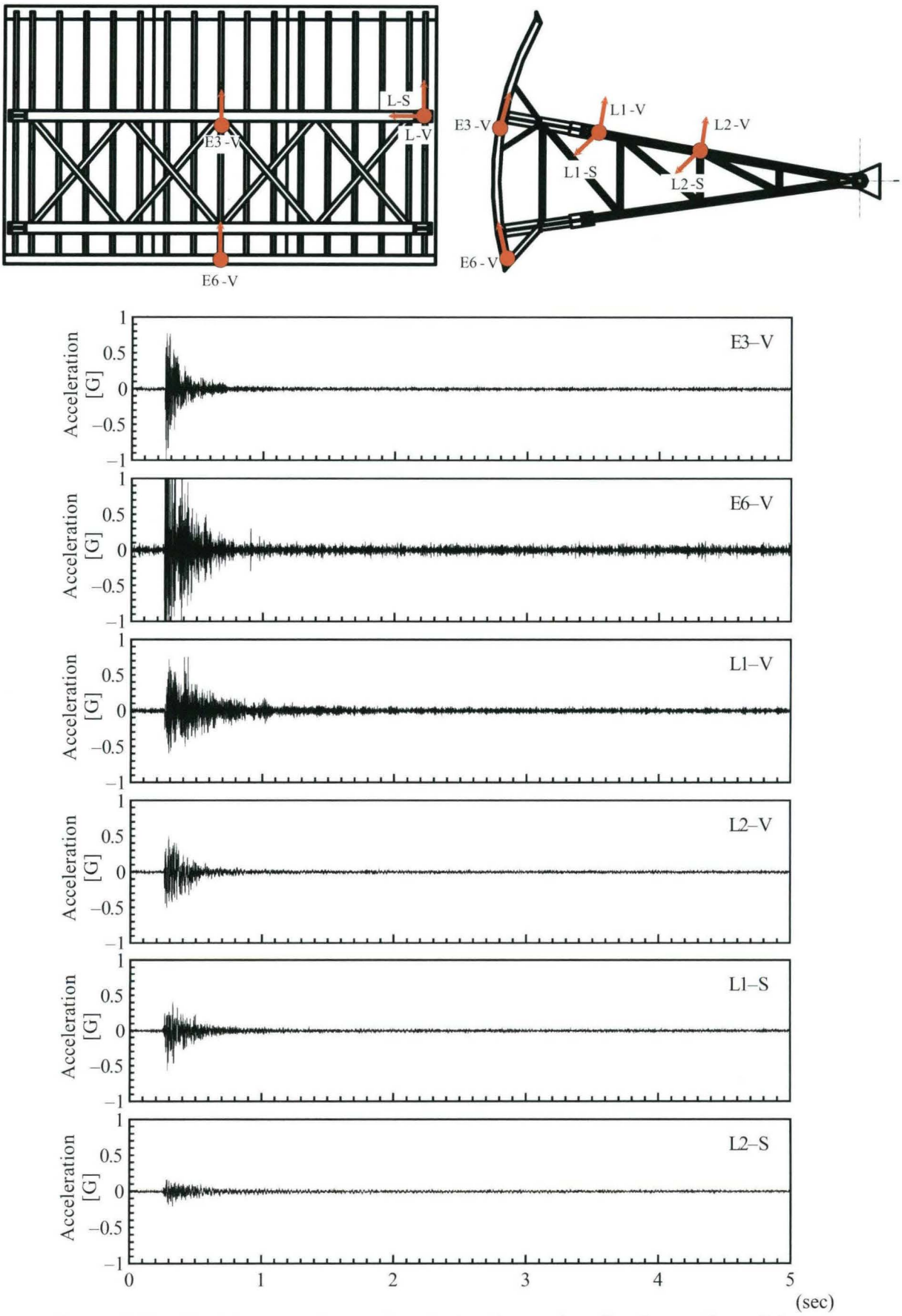

Figure 3.6(c): Real time waveforms of vertical and spanwise vibrations at the radial arm (Test No.4: steel rod breaking, d = 6 mm).

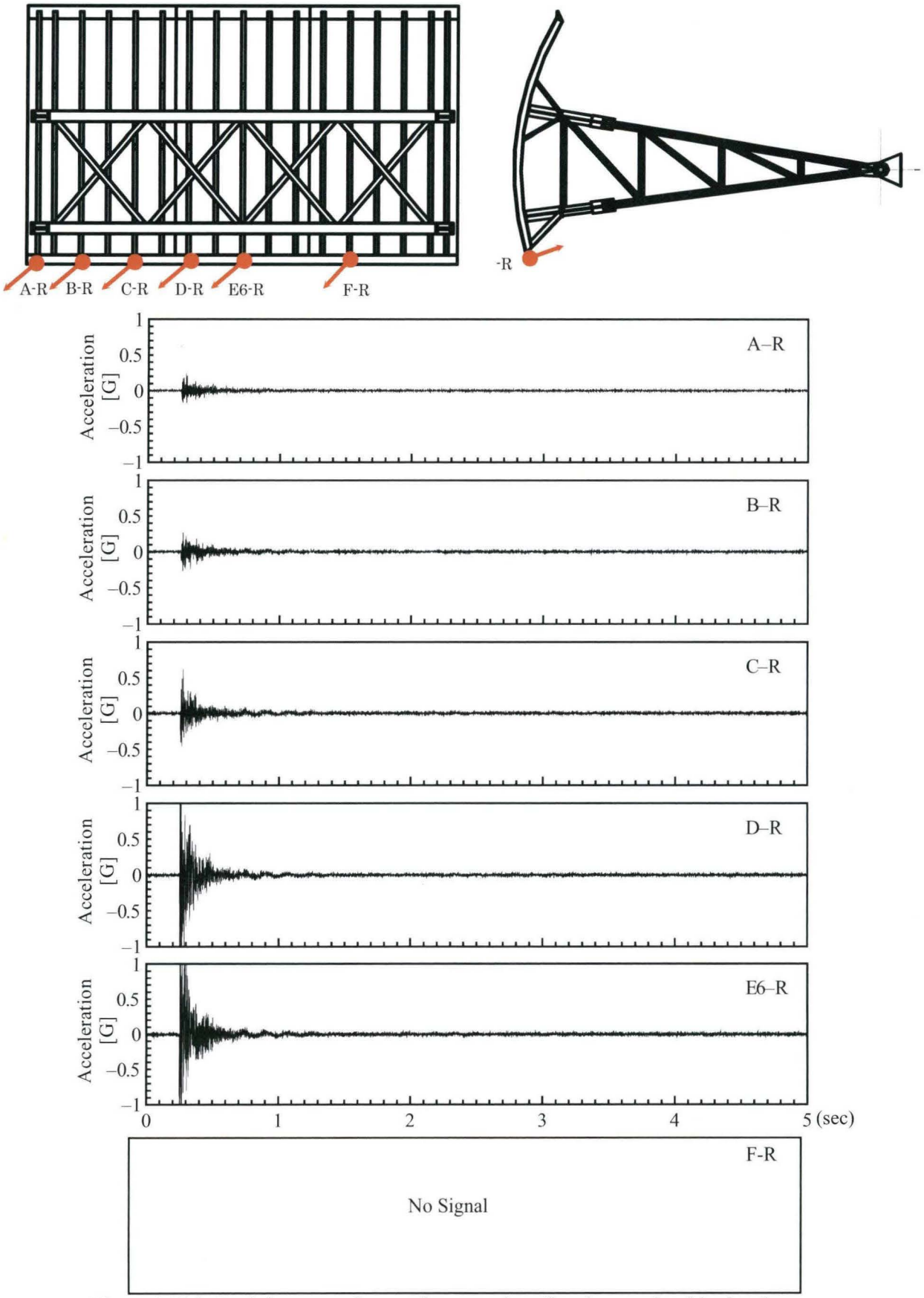

Figure 3.7(a): Real time waveforms of streamwise vibrations at the skinplate bottom (Test No.5: steel rod breaking, d = 6 mm).

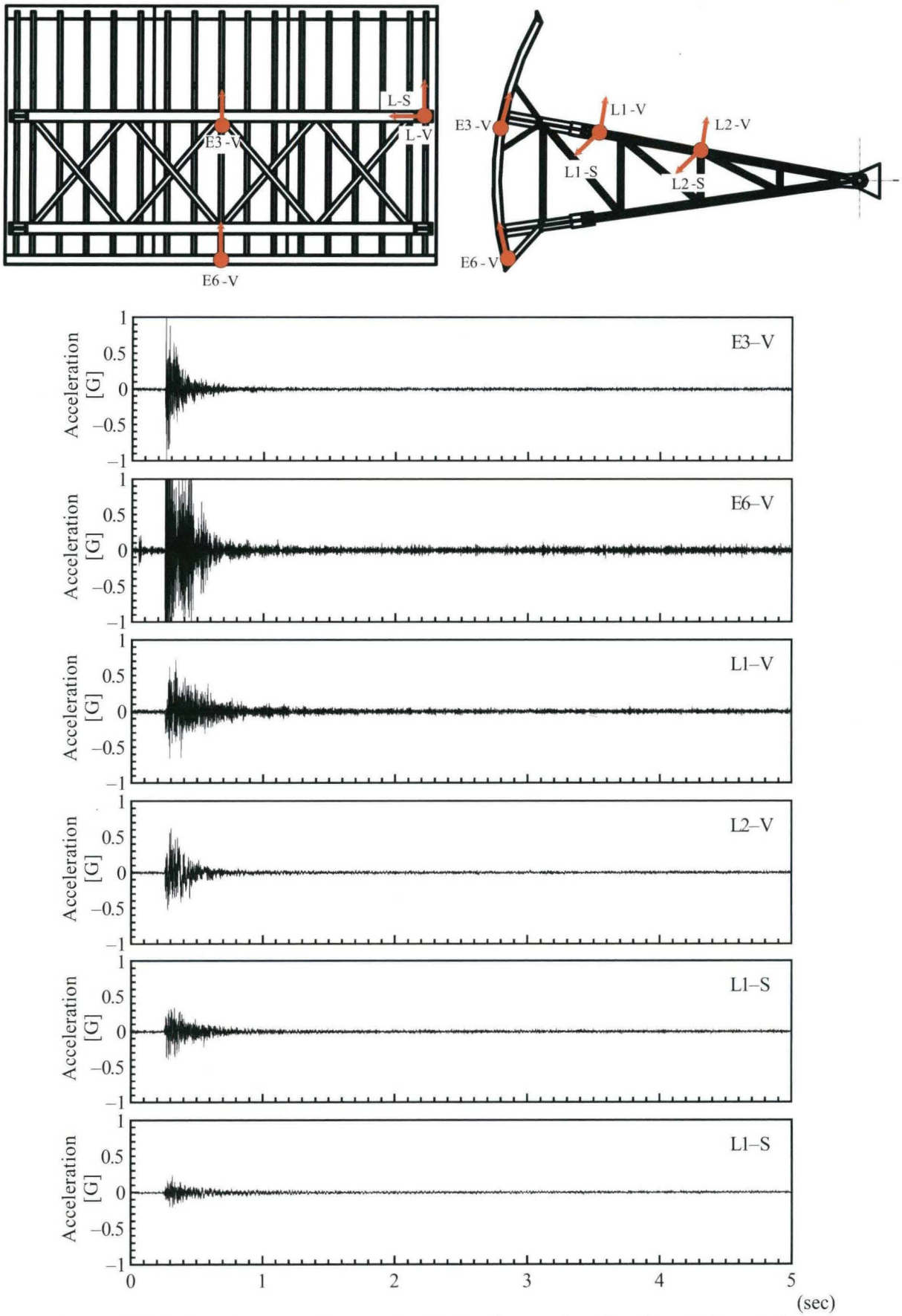

Figure 3.7(c): Real time waveforms of vertical and spanwise vibrations at the radial arm (Test No.5: steel rod breaking, d = 6 mm).

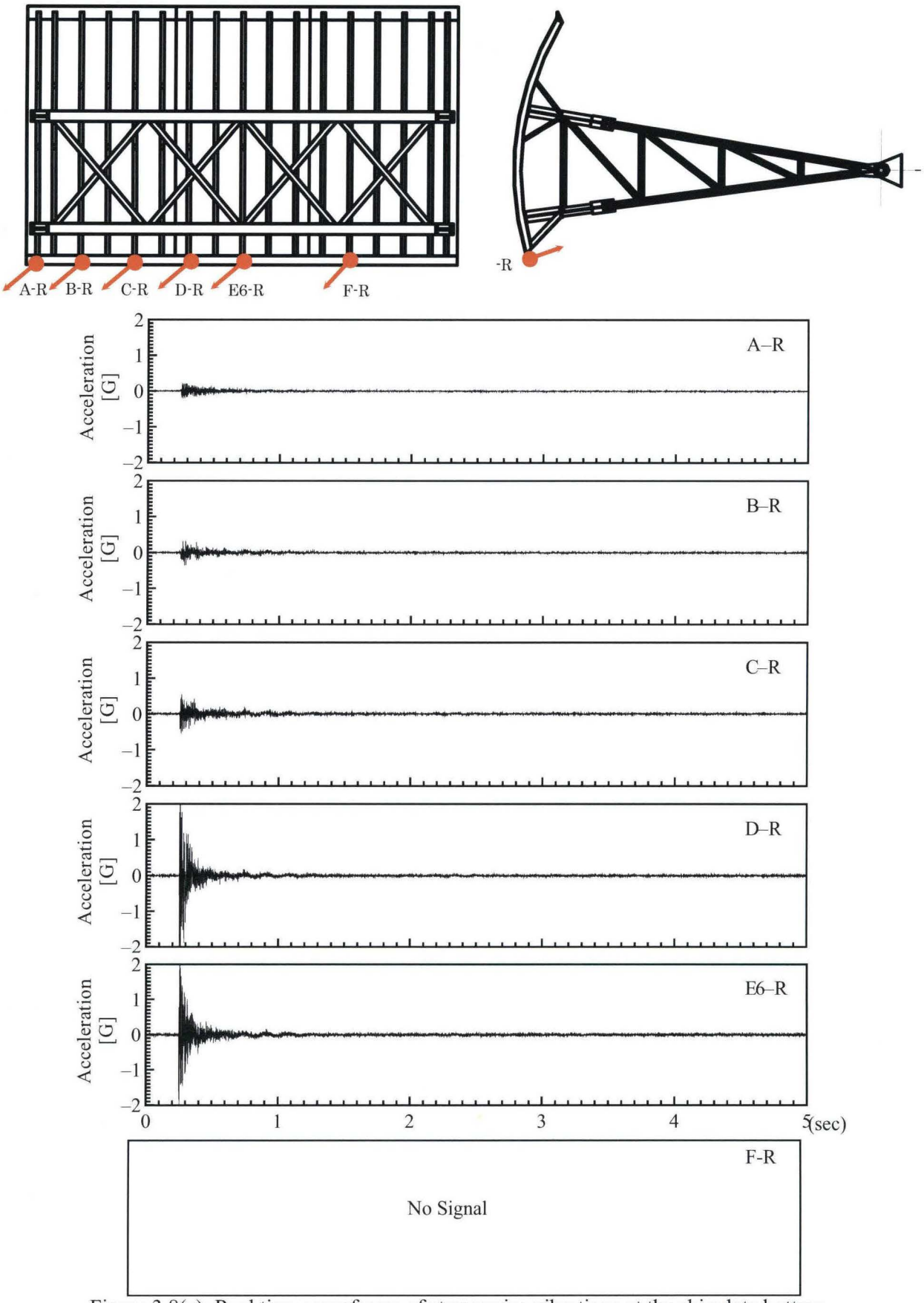

Figure 3.8(a): Real time waveforms of streamwise vibrations at the skinplate bottom (Test No.6: steel rod breaking, d = 8 mm).

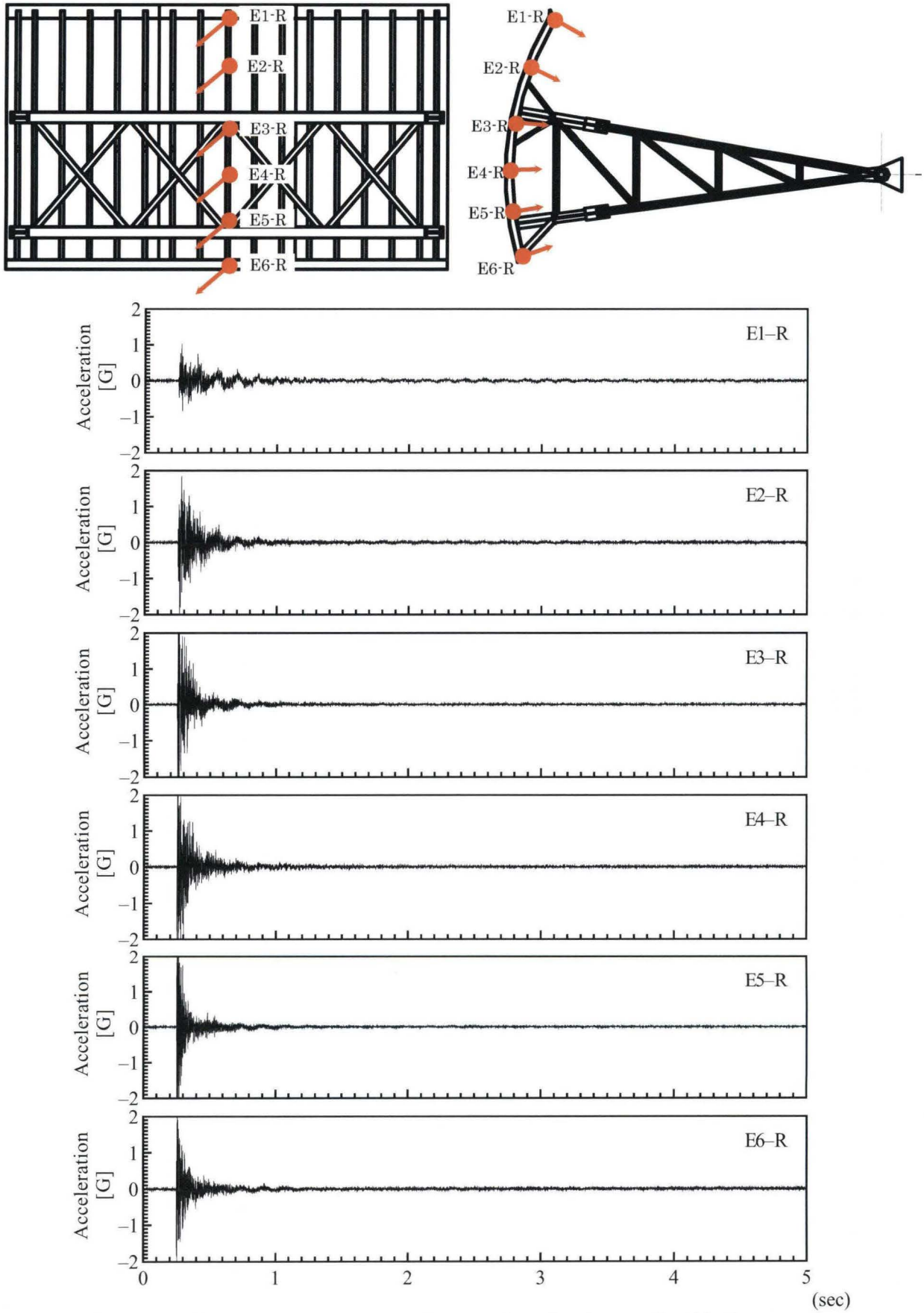

Figure 3.8(b): Real time waveforms of streamwise vibrations at the skinplate center (Test No.6: steel rod breaking, d = 8 mm).

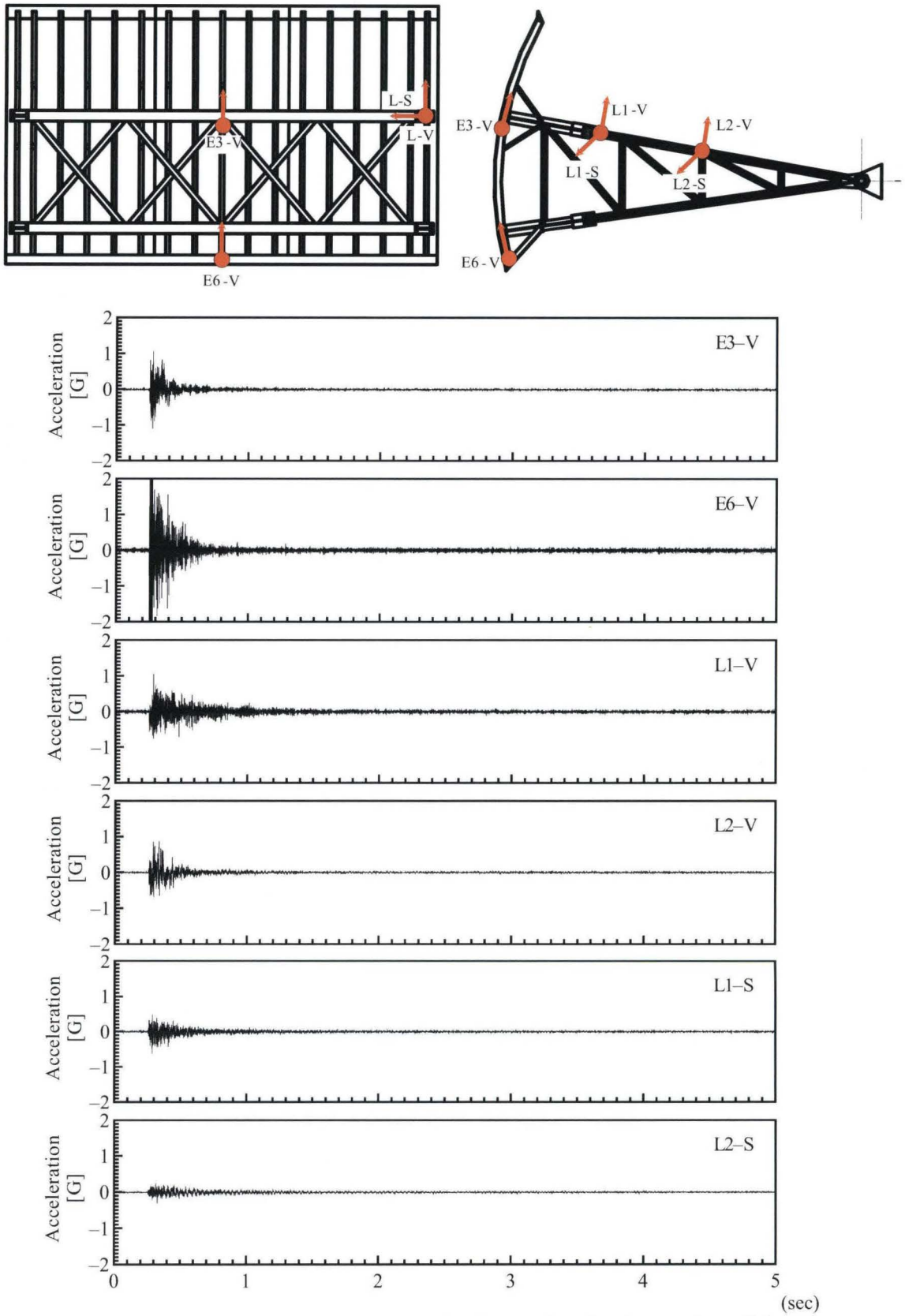

Figure 3.8(c): Real time waveforms of vertical and spanwise vibrations at the radial arm (Test No.6: steel rod breaking, d = 8 mm).

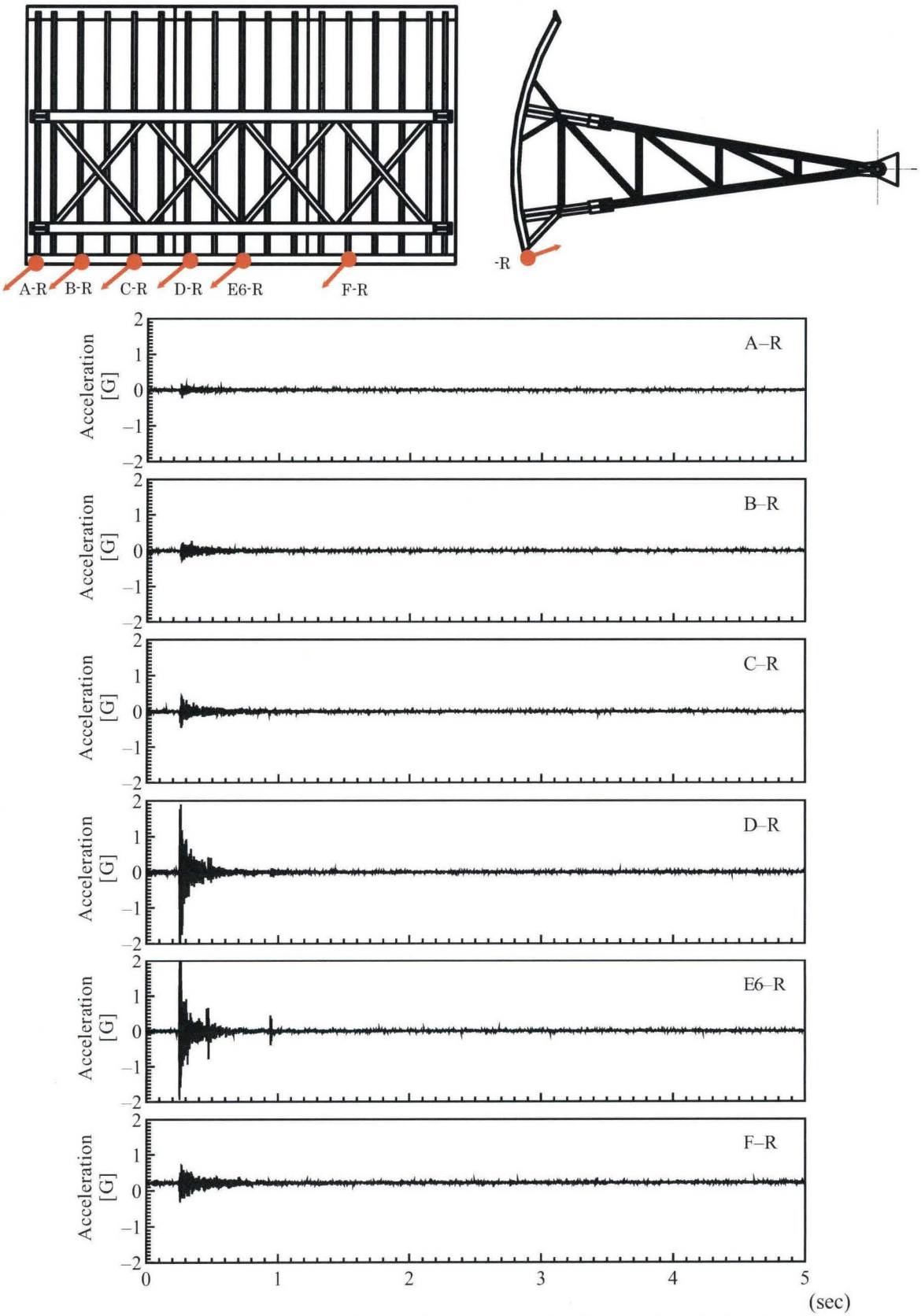

Figure 3.9(a): Real time waveforms of streamwise vibrations at the skinplate bottom (Test No.7: steel rod breaking, d = 6 mm).

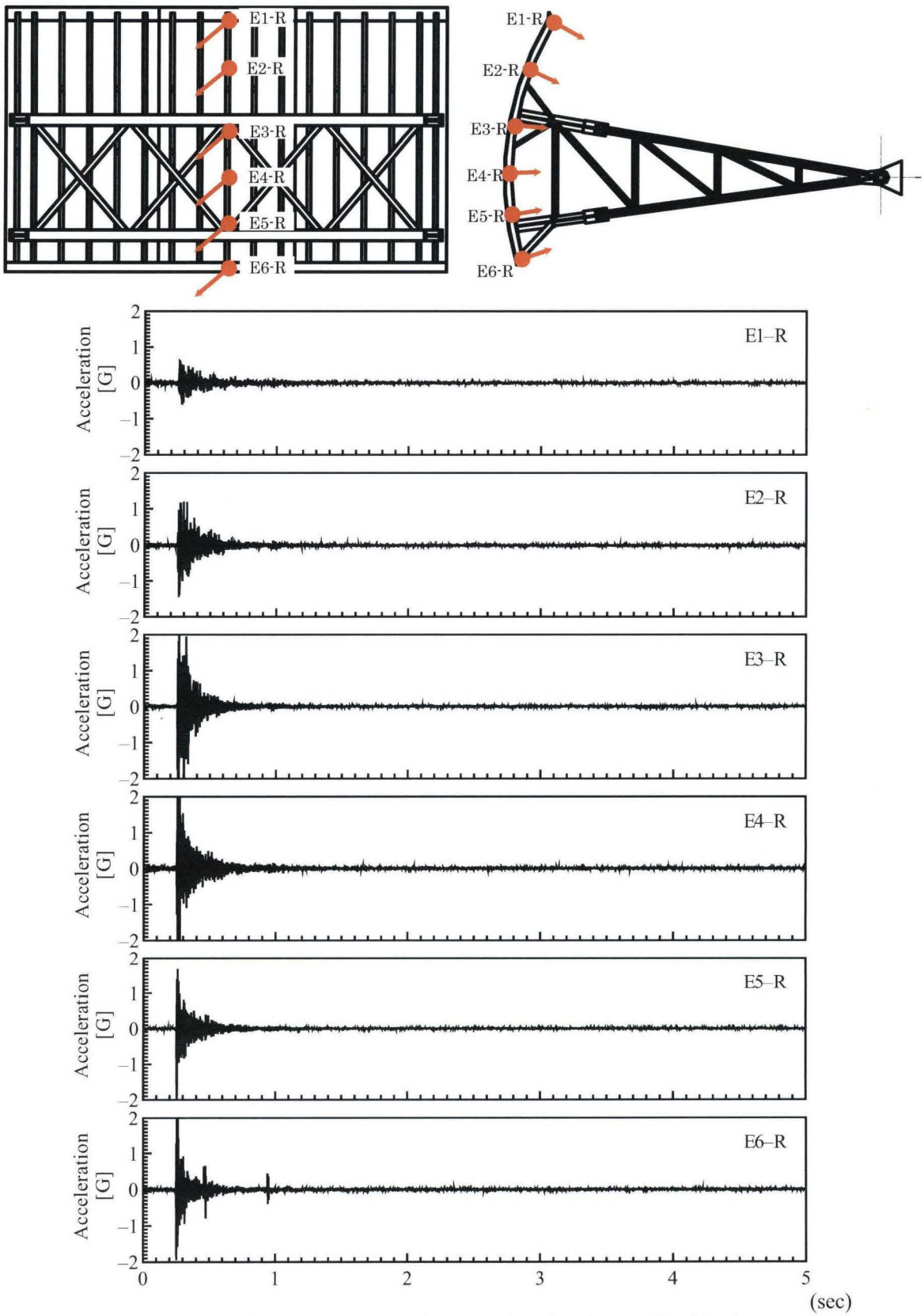

Figure 3.9(b): Real time waveforms of streamwise vibrations at the skinplate center (Test No.7: steel rod breaking, d = 6 mm).

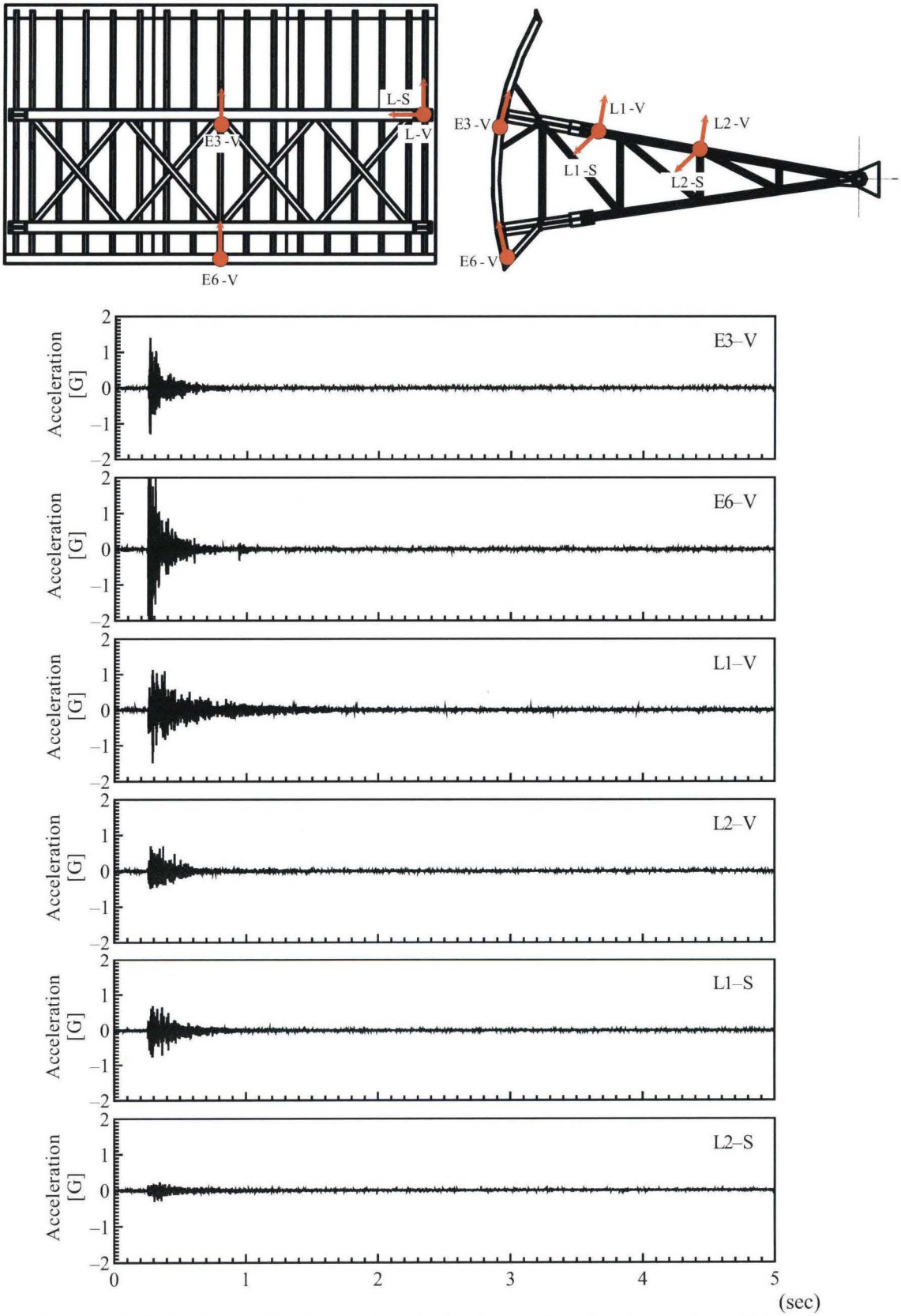

Figure 3.9(c): Real time waveforms of vertical and spanwise vibrations at the radial arm (Test No.7: steel rod breaking, d = 6 mm).

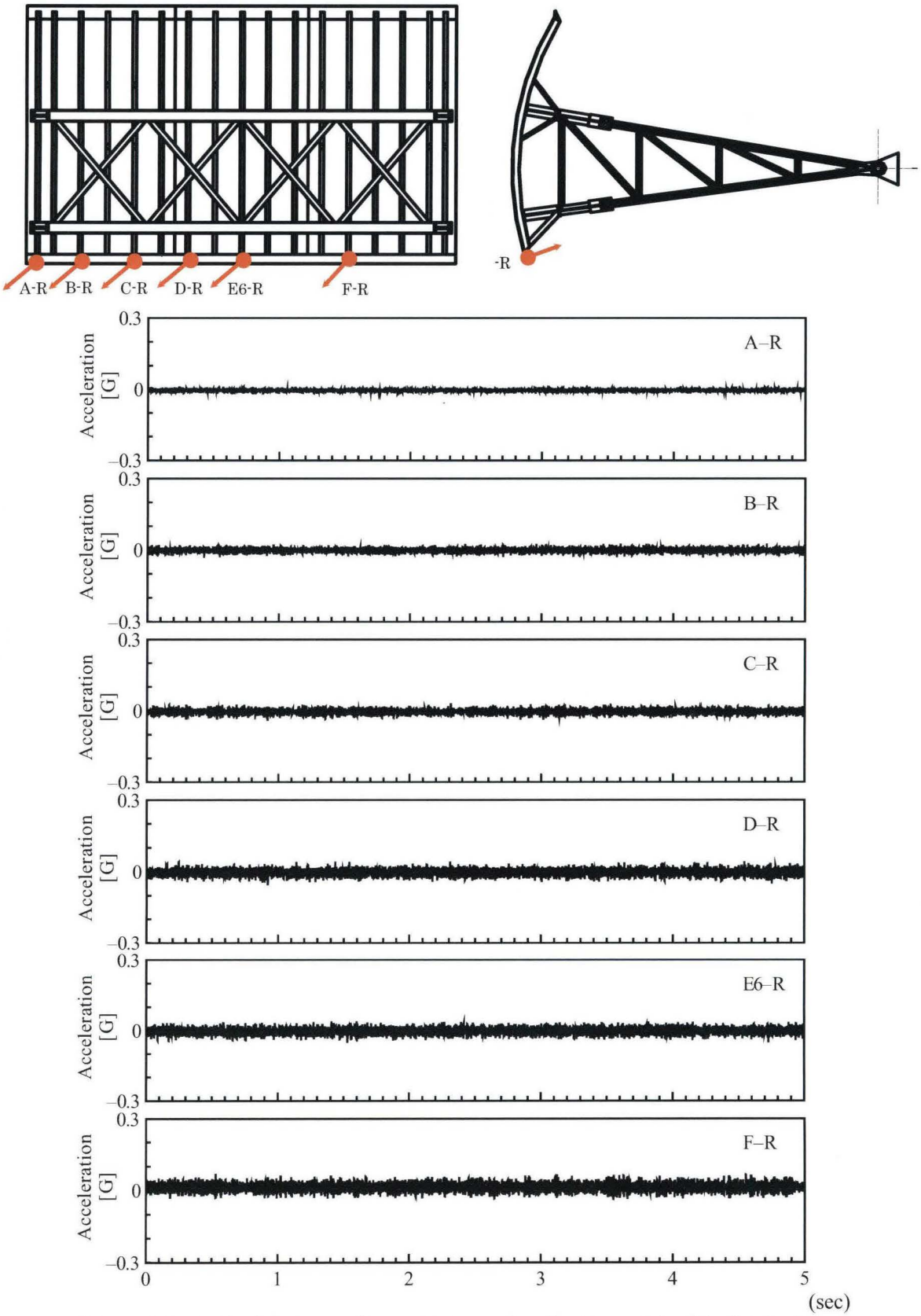

Figure 3.10(a): Real time waveforms of streamwise vibrations at the skinplate bottom (Test No.8: ambient, B = 19 mm).

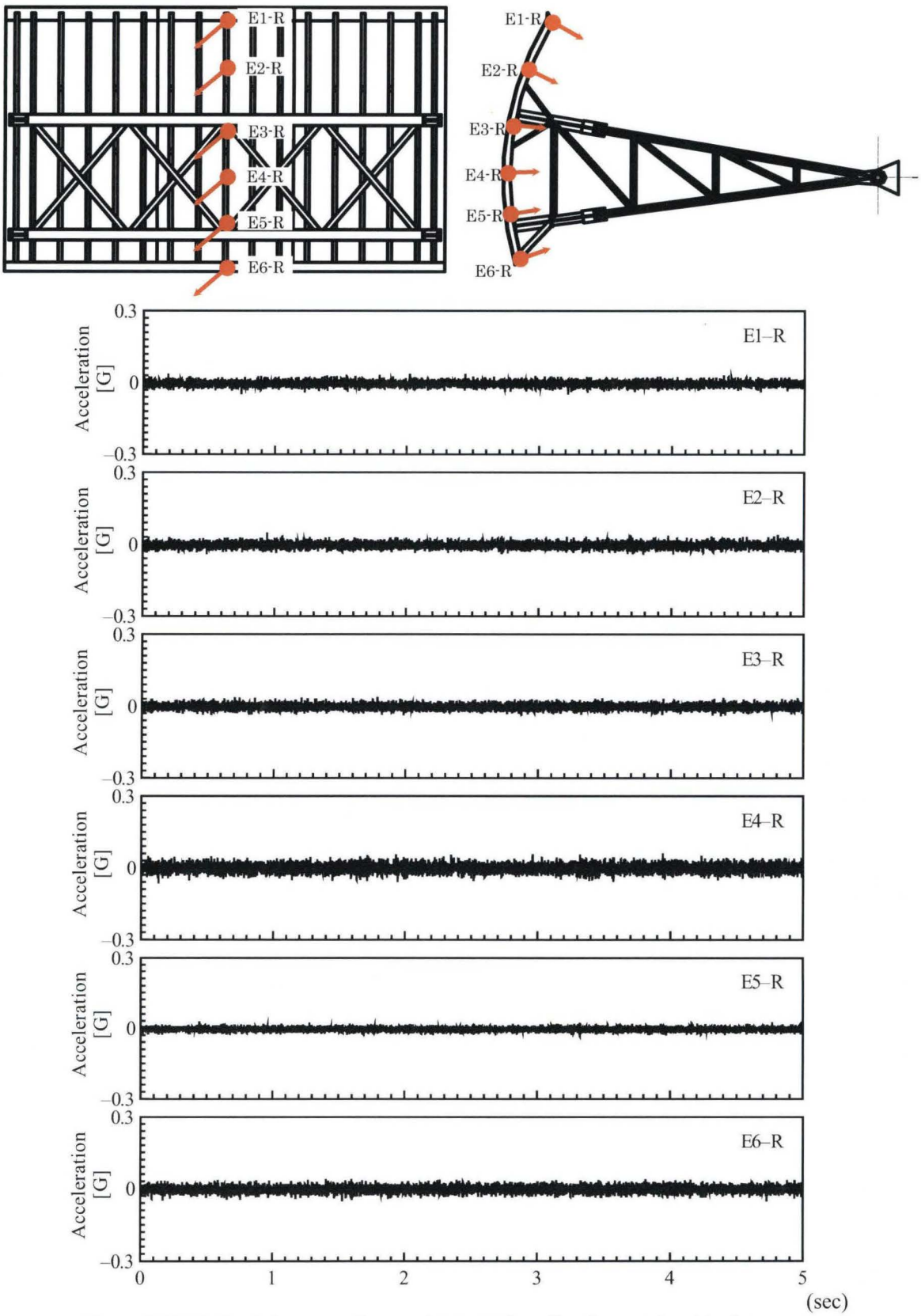

Figure 3.10(b): Real time waveforms of streamwise vibrations at the skinplate center (Test No.8: ambient B = 19 mm).

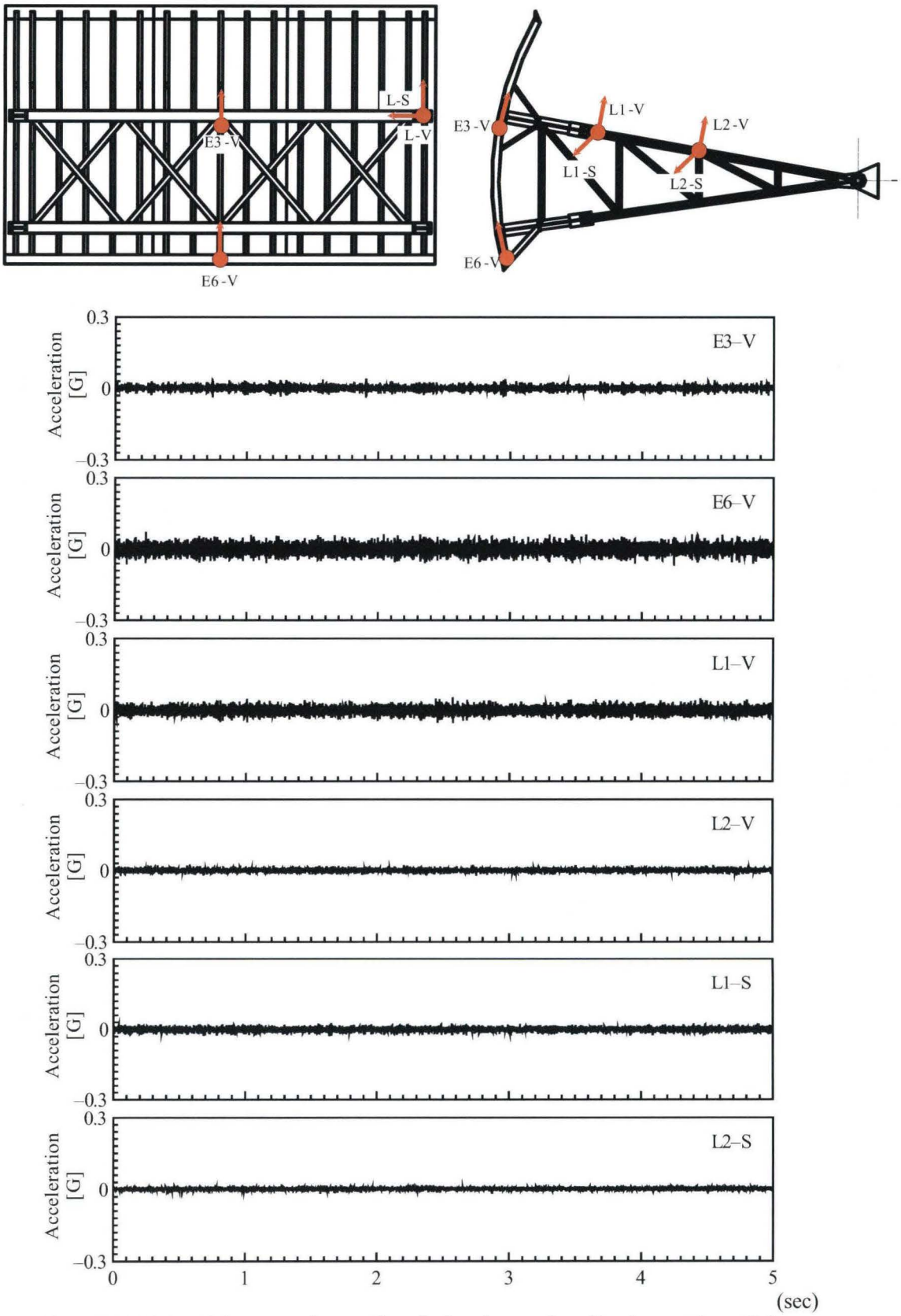

Figure 3.10(c): Real time waveforms of vertical and spanwise vibrations at the radial arm (Test No.8: ambient, B = 19 mm).

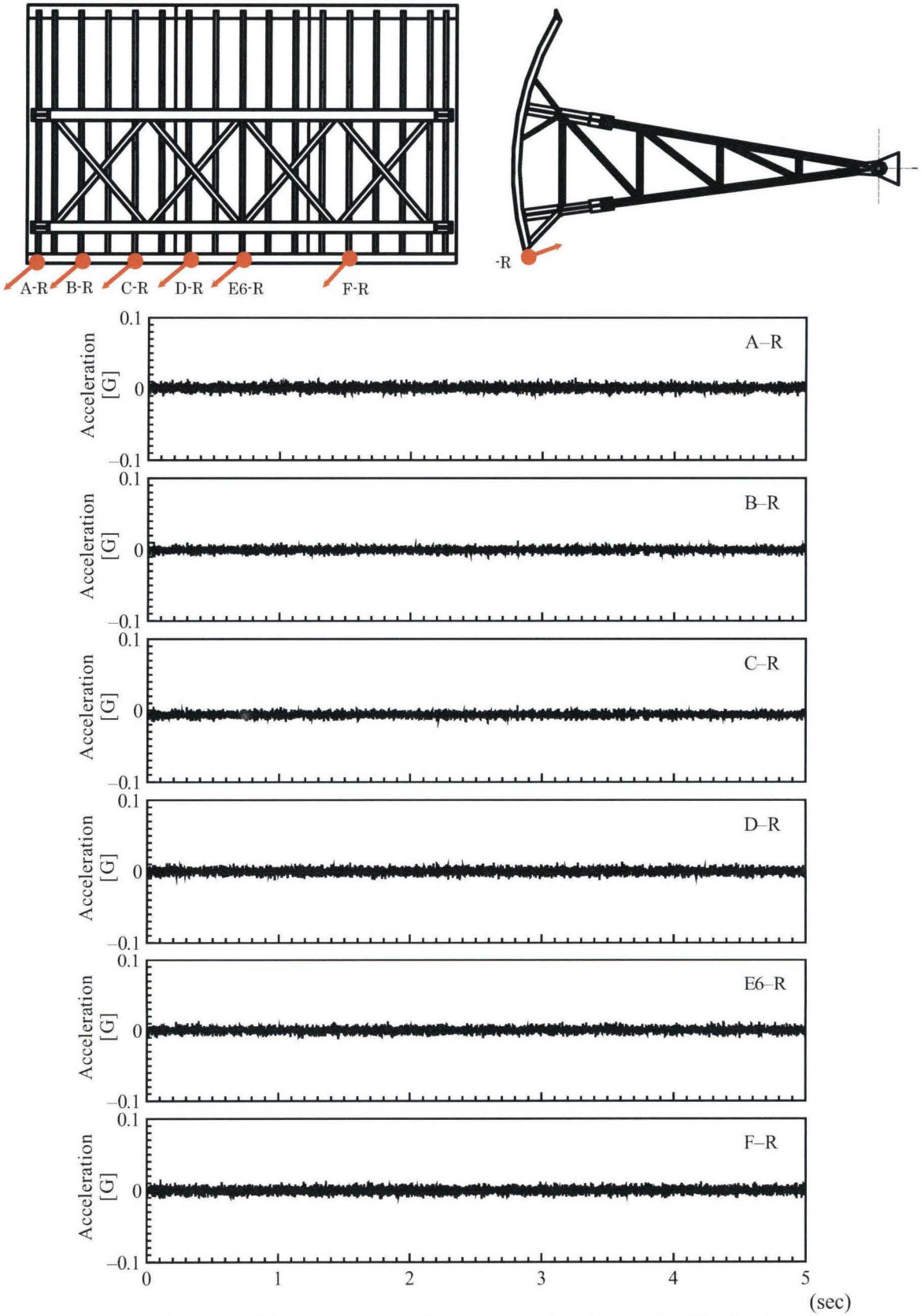

Figure 3.11(a): Real time waveforms of streamwise vibrations at the skinplate bottom (Test No.8: ambient, B = 126 mm).

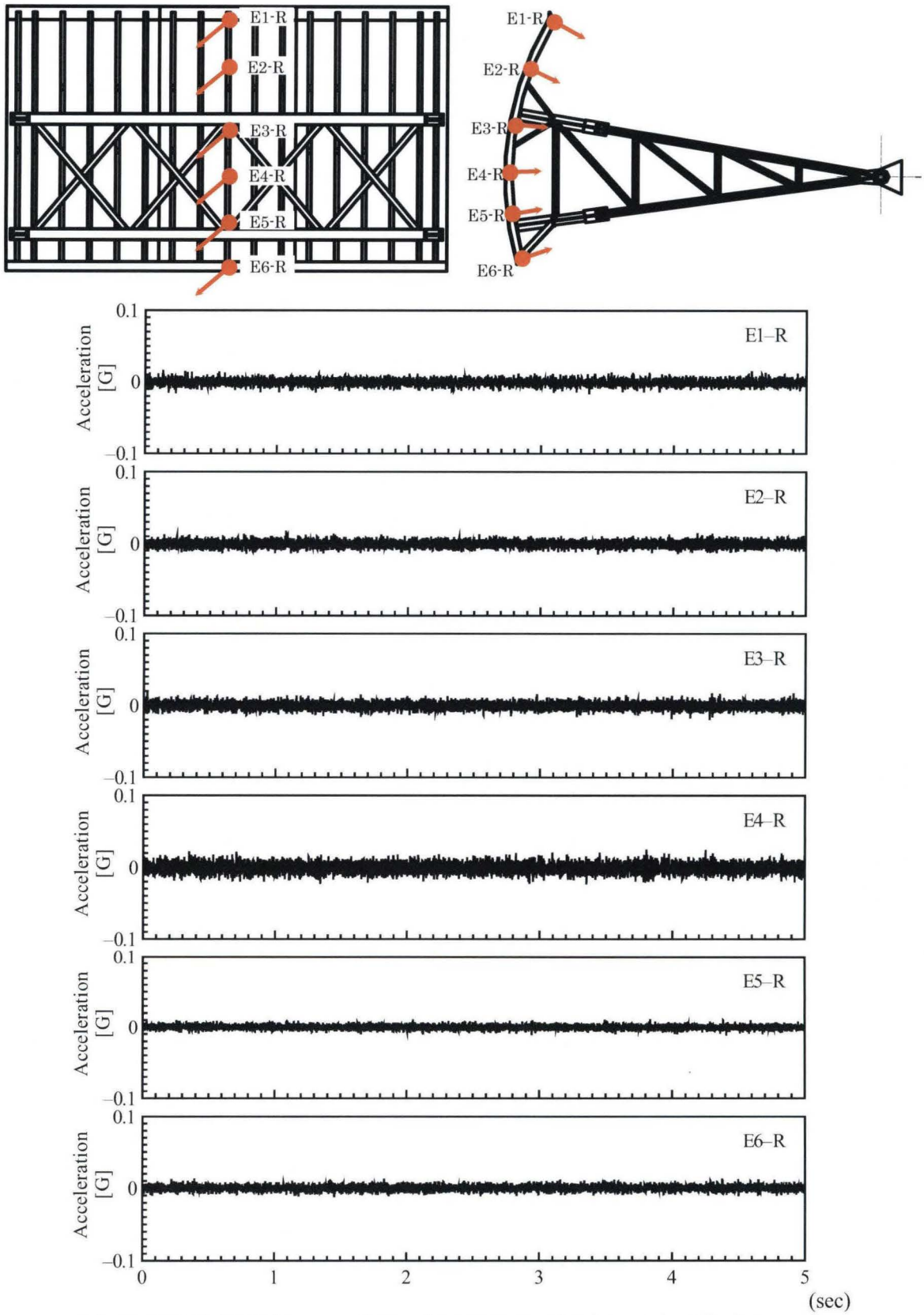

Figure 3.11(b): Real time waveforms of streamwise vibrations at the skinplate center (Test No.8: ambient, B = 126 mm).

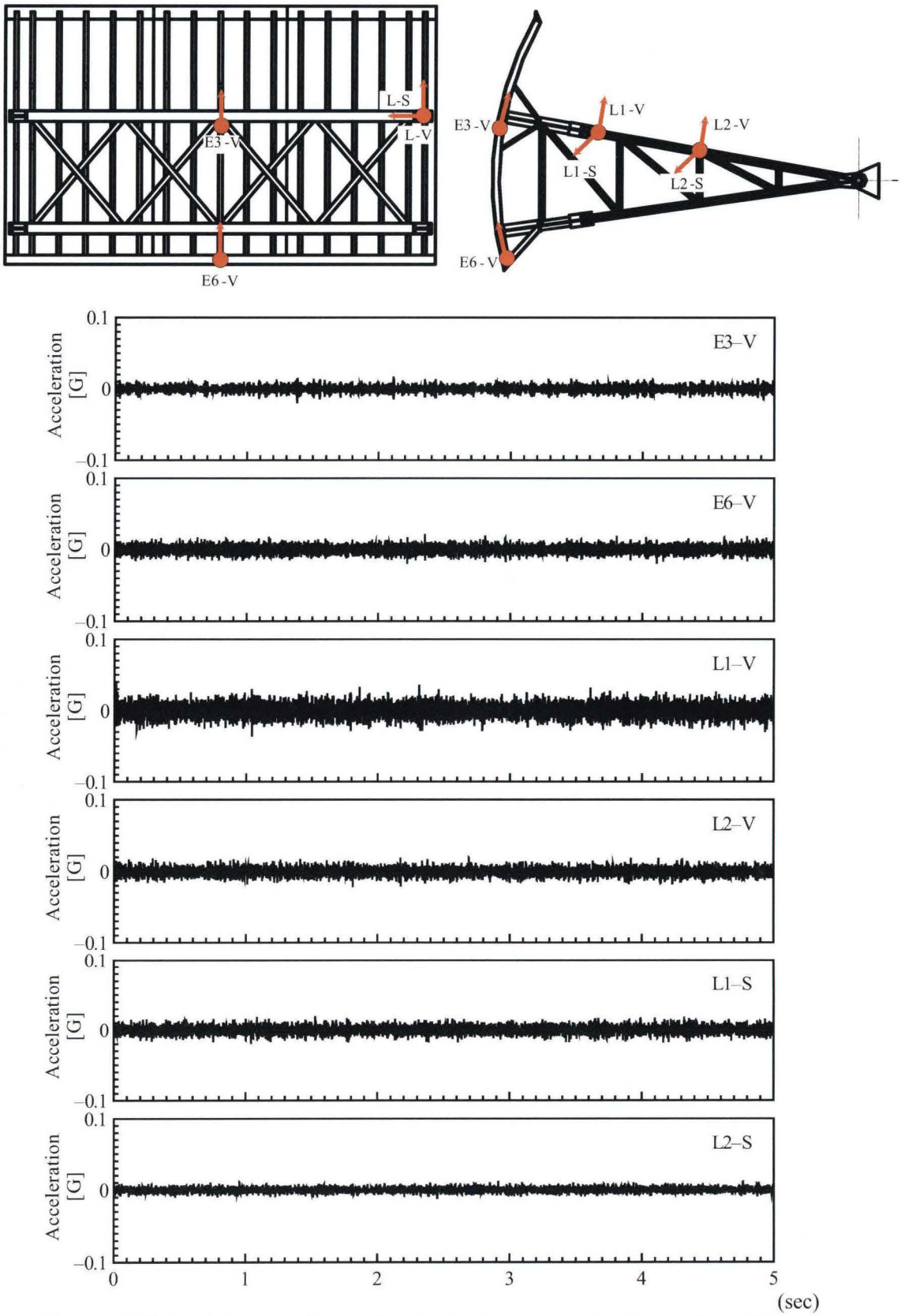

Figure 3.11(c): Real time waveforms of vertical and spanwise vibrations at the radial arm (Test No.8: ambient, B = 126 mm).

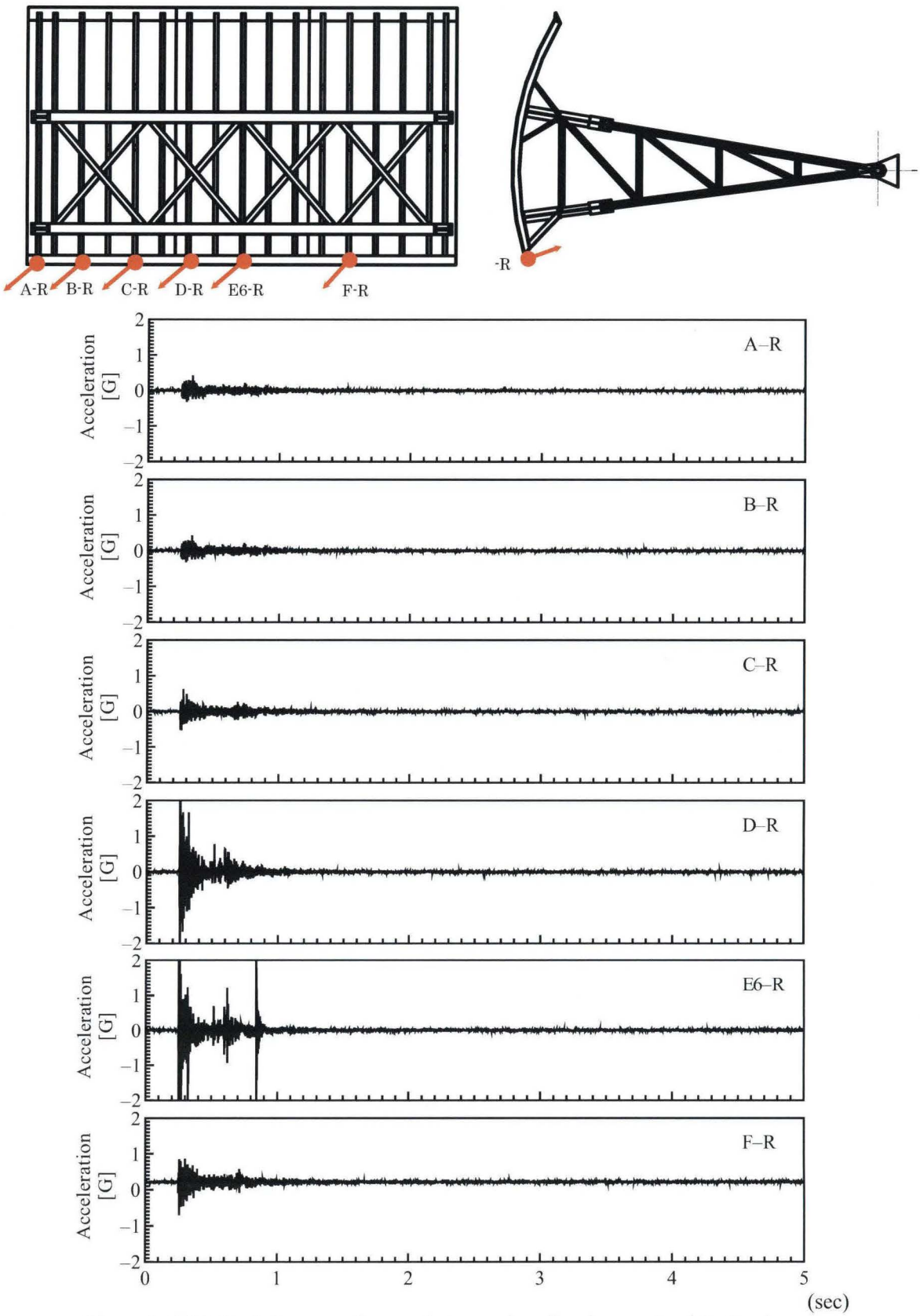

Figure 3.12(a): Real time waveforms of streamwise vibrations at the skinplate bottom (Test No.9: steel rod breaking, d = 8 mm).

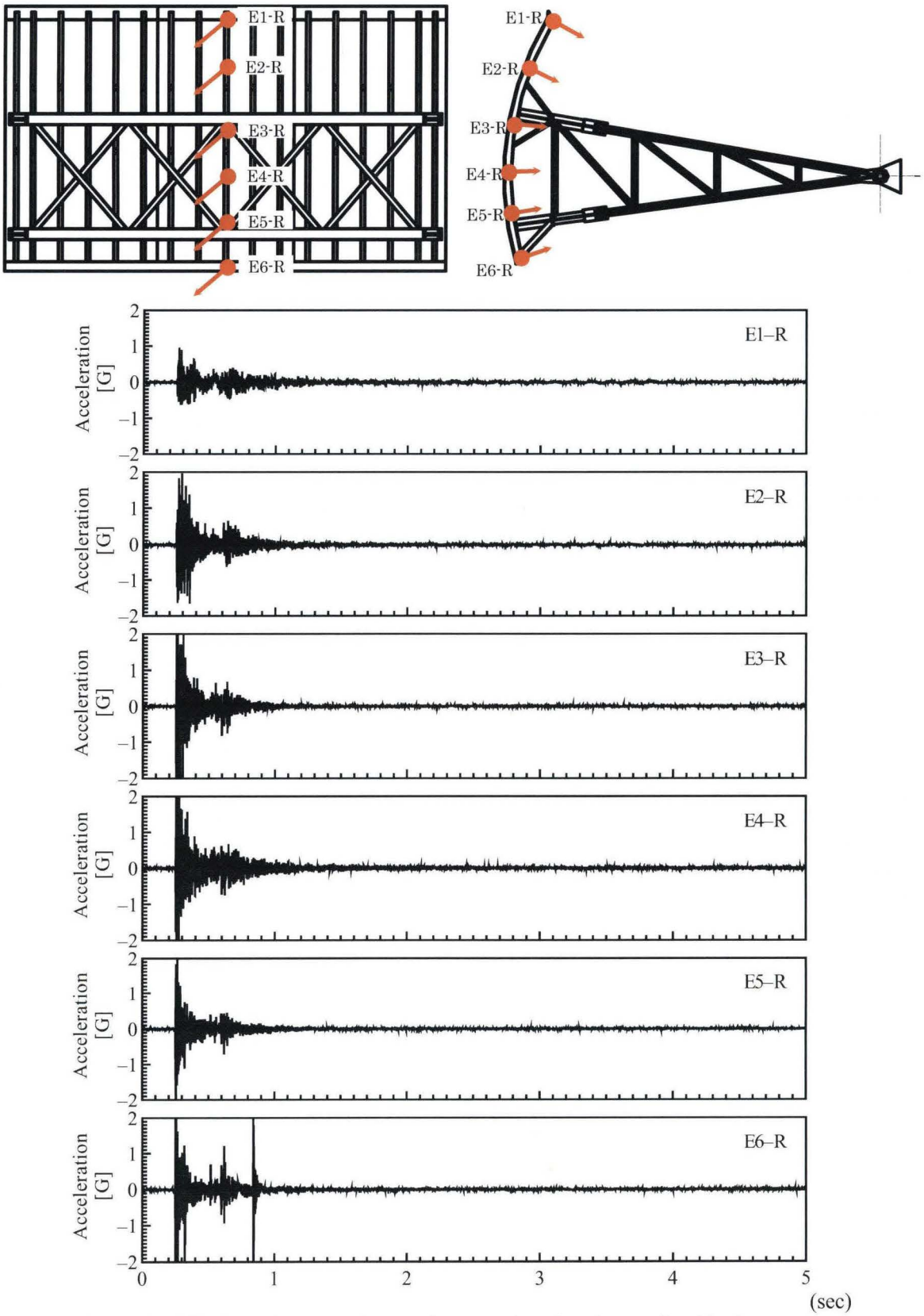

Figure 3.12(b): Real time waveforms of streamwise vibrations at the skinplate center (Test No.9: steel rod breaking, d = 8 mm).

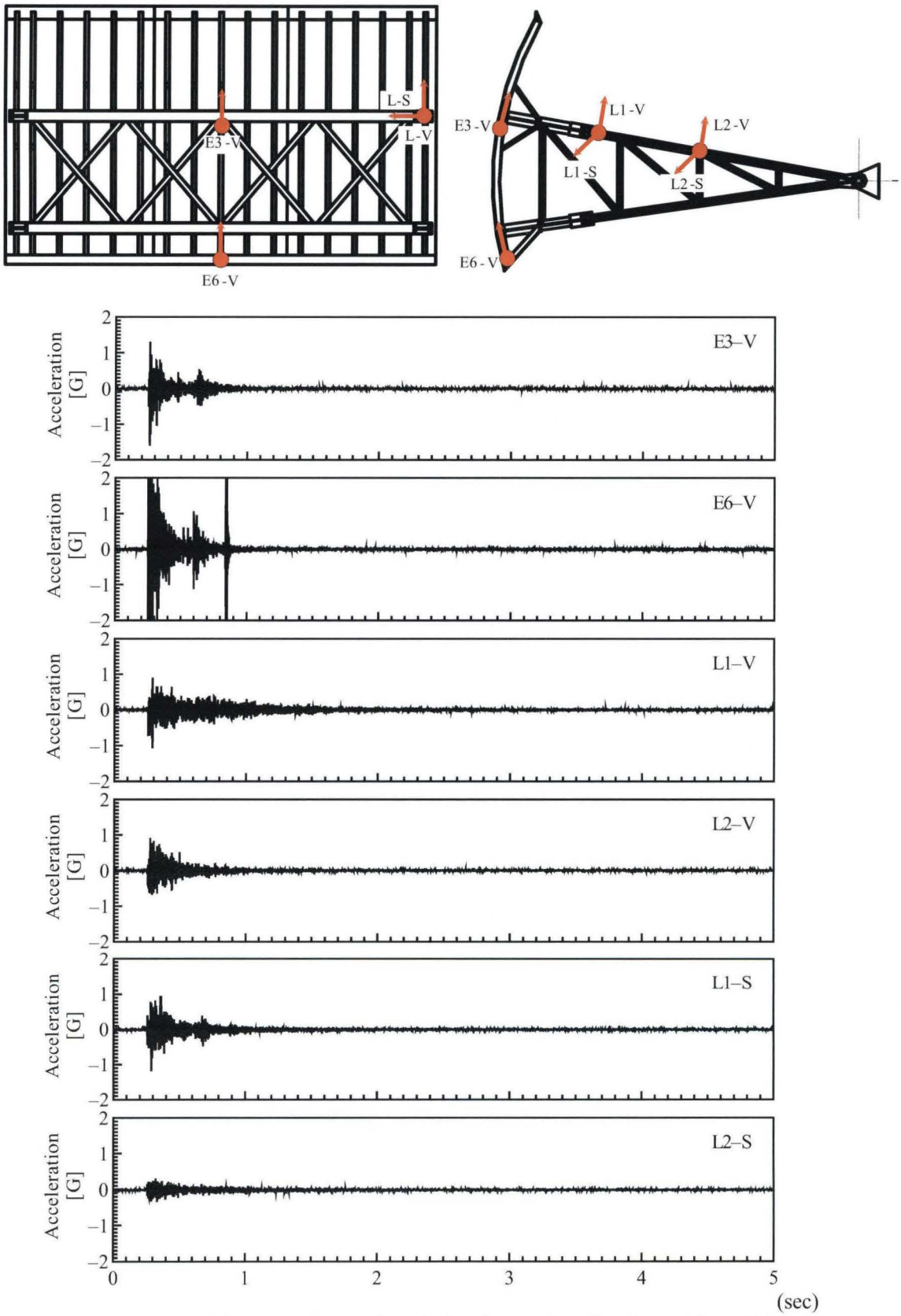

Figure 3.12(c): Real time waveforms of vertical and spanwise vibrations at the radial arm (Test No.9: steel rod breaking, d = 8 mm).

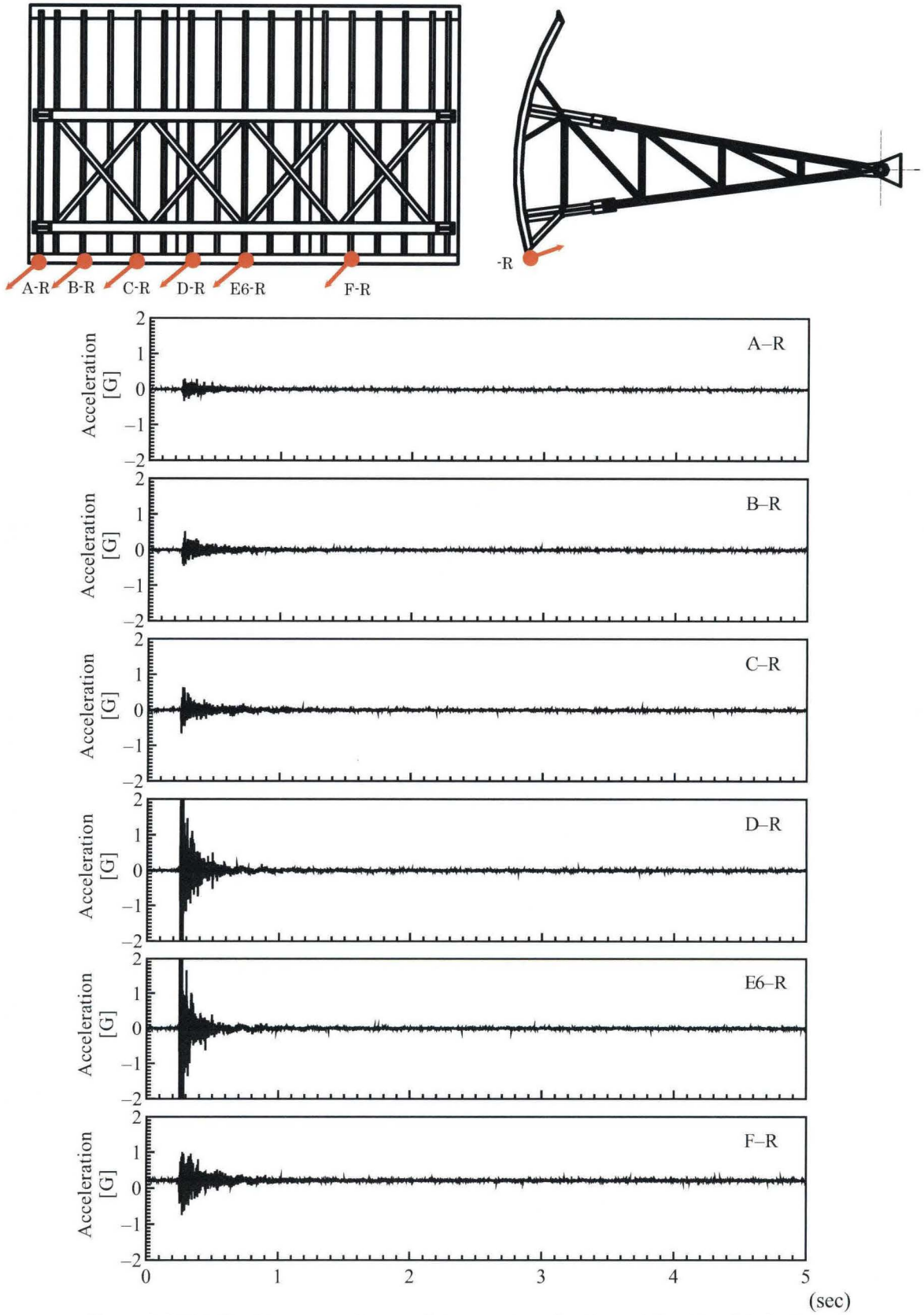

Figure 3.13(a): Real time waveforms of streamwise vibrations at the skinplate bottom (Test No.10: steel rod breaking, d = 8 mm).

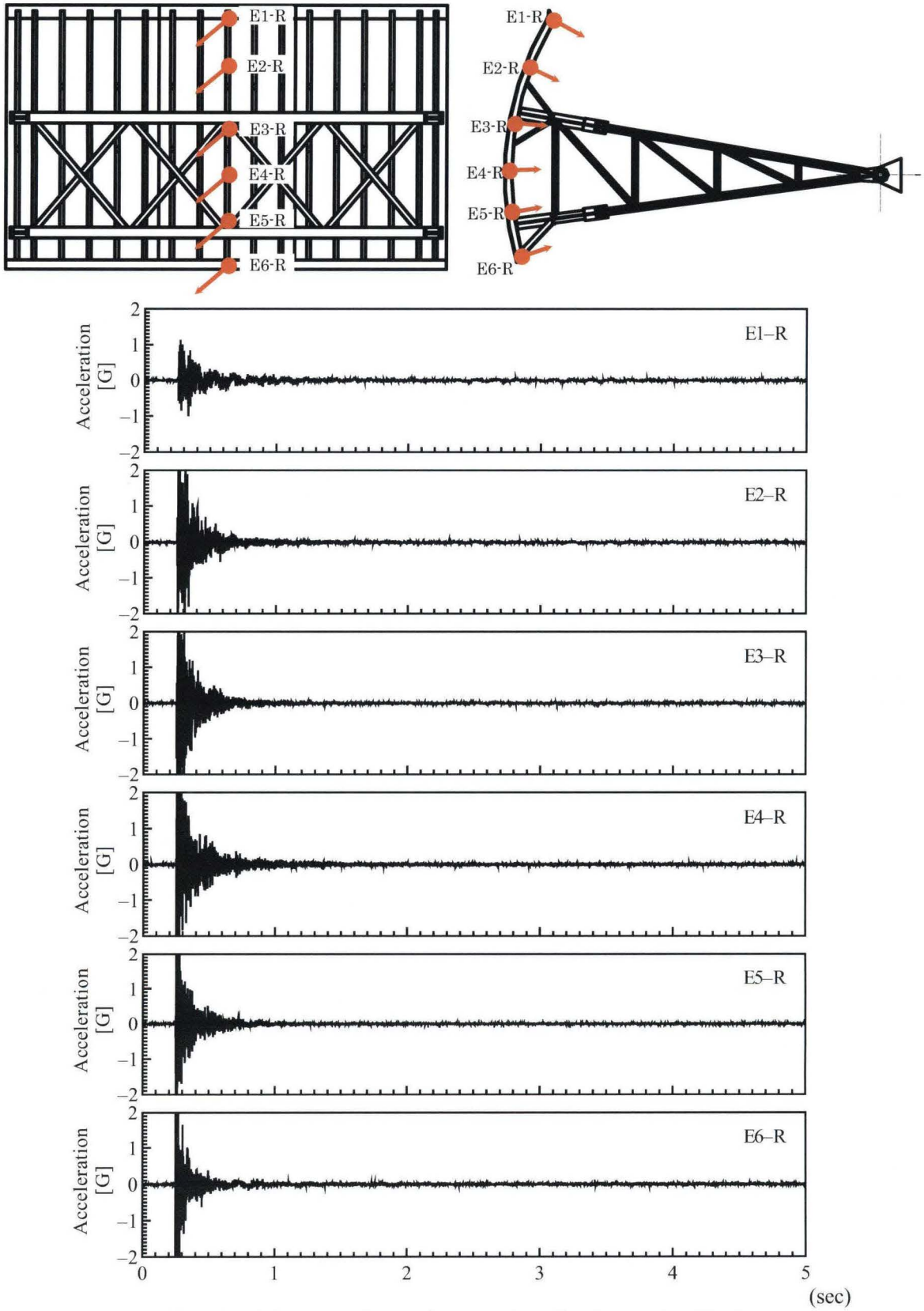

Figure 3.13(b): Real time waveforms of streamwise vibrations at the skinplate center (Test No.10: steel rod breaking, d = 8 mm).

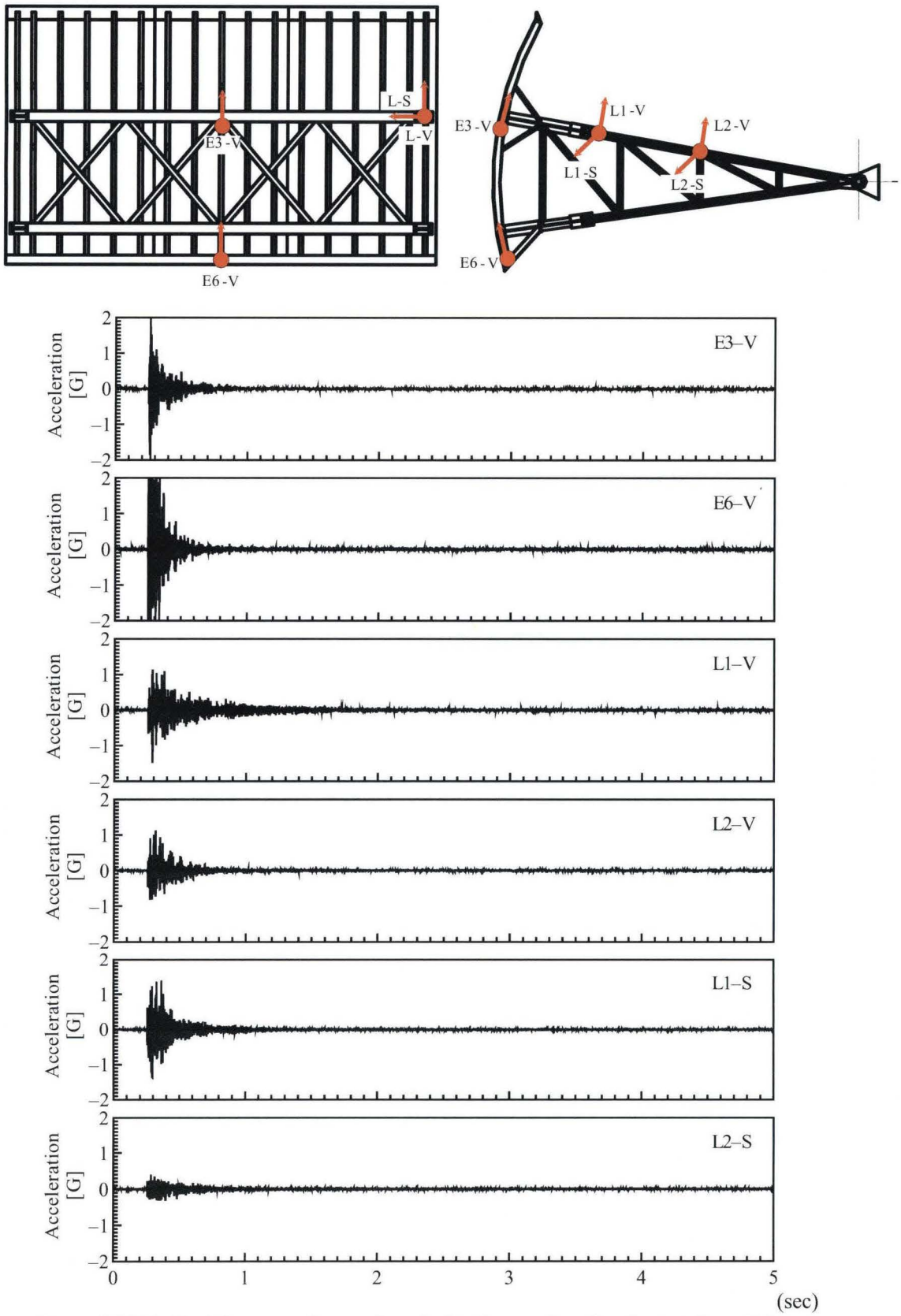

Figure 3.13(c): Real time waveforms of vertical and spanwise vibrations at the radial arm (Test No.10: steel rod breaking, d = 8 mm).

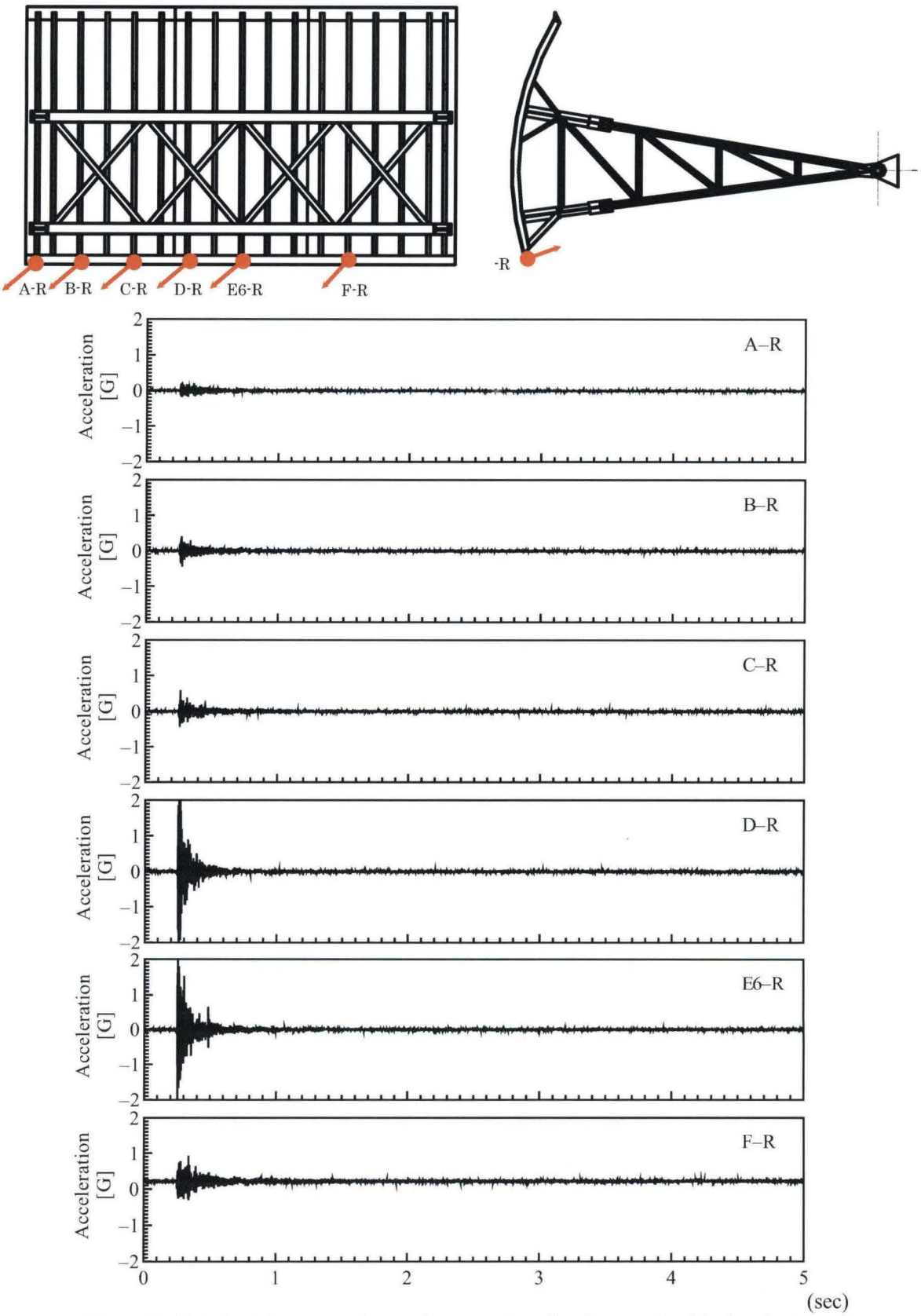

Figure 3.14(a): Real time waveforms of streamwise vibrations at the skinplate bottom (Test No.11: steel rod breaking, d = 6 mm).

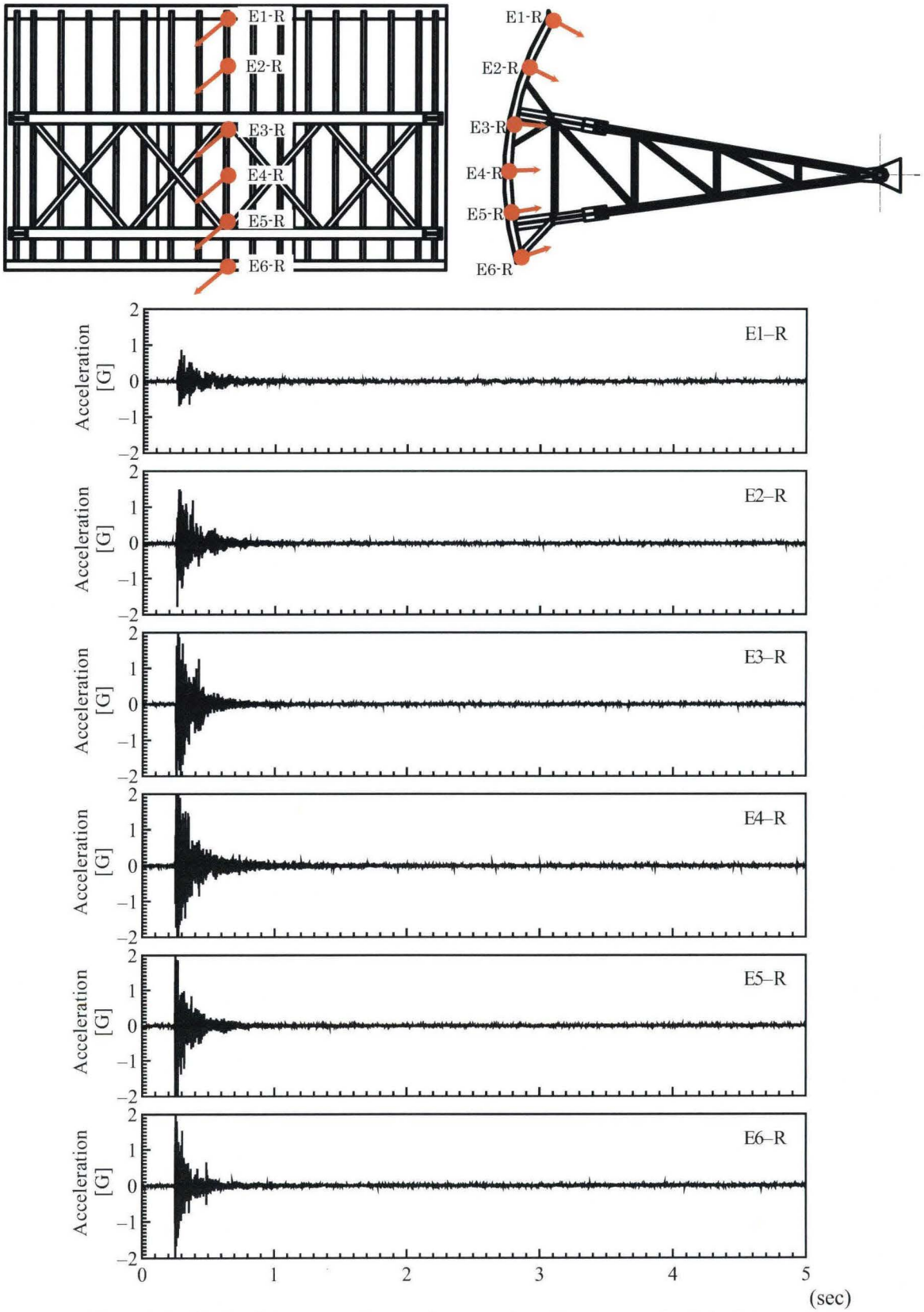

Figure 3.14(b): Real time waveforms of streamwise vibrations at the skinplate center (Test No.11: steel rod breaking, d = 6 mm).

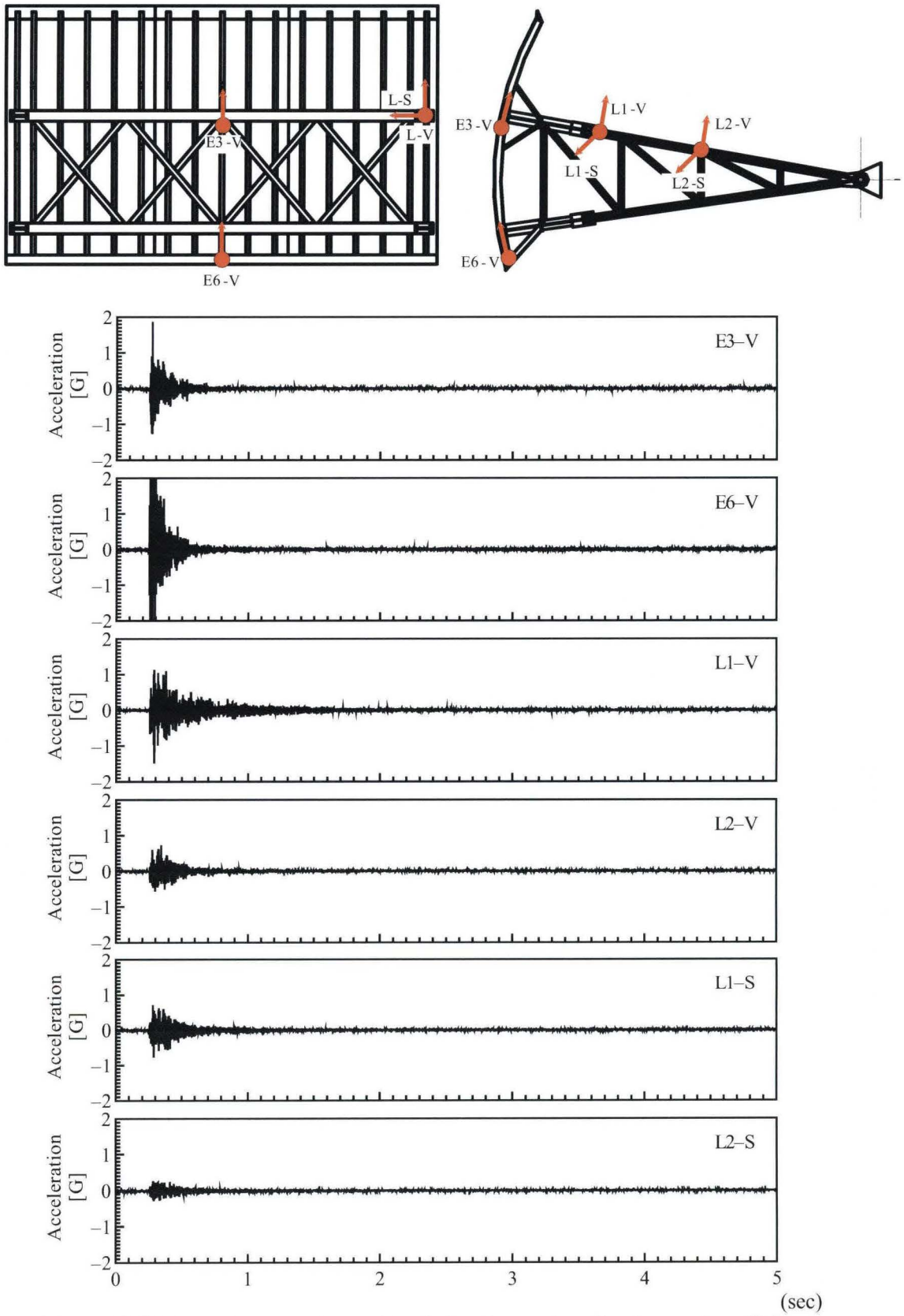

Figure 3.14(c): Real time waveforms of vertical and spanwise vibrations at the radial arm (Test No.11: steel rod breaking, d = 6 mm).

4. METHOD OF DATA ANALYSIS

4.1 Software

Measured vibration accelerations were analyzed using DADiSP/2000 WORKSHEET from Astrodesign, Inc. This software can analyze and process various data on the computer, outputting data in ASCII format. A representative analysis worksheet is shown in Figure 4.1, in which the top left figure represents a measured acceleration with a full time length of about 160 sec. The top right figure shows the same acceleration signal low-pass filtered with a cut-off frequency of 90 Hz (frequency range of the accelerometers). The middle left figure shows a portion of the signal with an expanded time-scale from about 98 to 106 sec exhibiting damped vibration. The middle right figure shows the power spectrum of the low-pass filtered signal in the frequency range from 0 to 6 kHz, the bottom. The bottom left figure is the low frequency portion of the power spectrum with an expanded frequency scale from 0 to 50 Hz. Finally the bottom right figure shows the same power spectrum for calculating the phase-lag of vibration over the same expanded frequency range of 0 to 50 Hz.

In the resulting ASCII formatted data files, only the Y-axis data values are explicitly listed. Despite this, the amount of ASCII data in an output can overwhelm the graphics software. For this reason, BASIC programs were developed to decimate the output data (selecting every *n*th data point) prior to graphing.

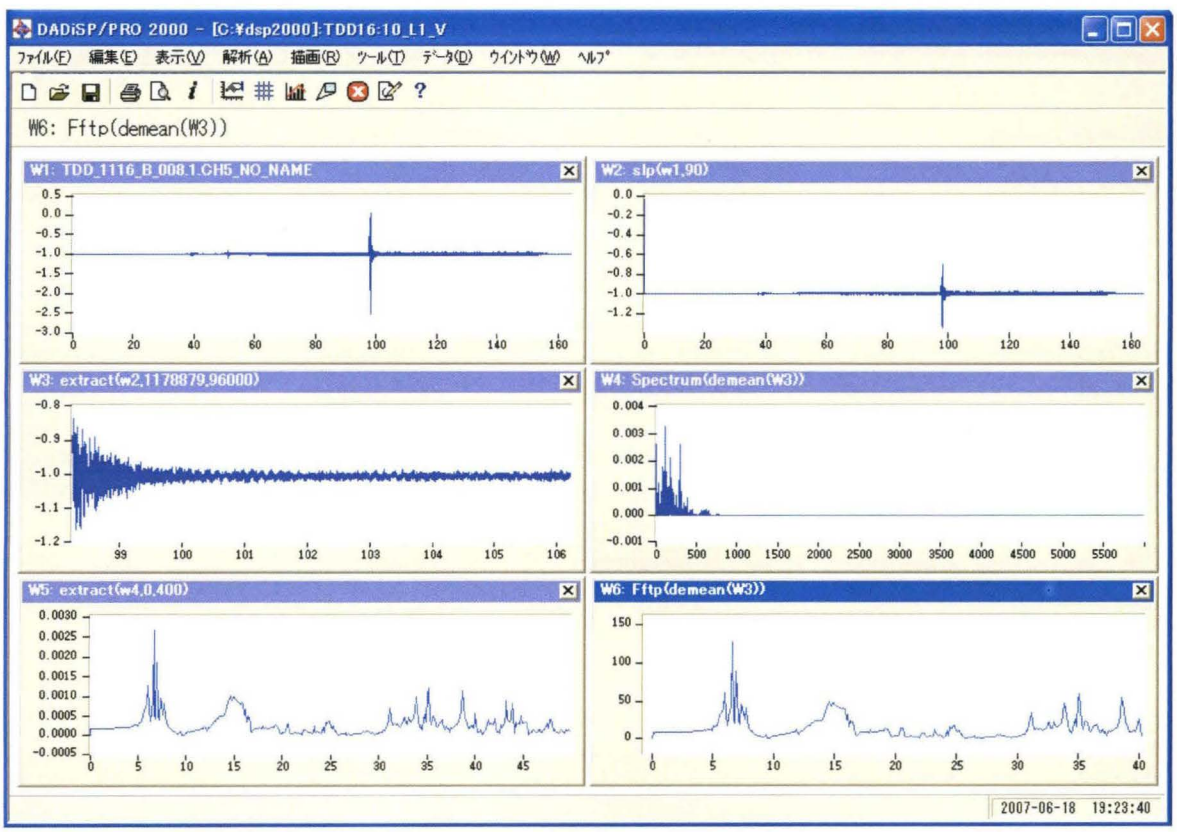

Figure 4.1: Analysis worksheet of DADiSP/2000 software.

4.2 Window Selection for Frequency Power Spectrum Analysis

The damped vibration initiated by the steel bar breaking excitation is a transient (not essentially periodic) function which includes excessively high levels of acceleration output just at the instant when the steel bar breaks. Such sudden transients can potentially lead to a significant error in the frequency-domain power spectrum analysis of the measured vibratory accelerations. To minimize the associated error, special attention must be paid to the selection of the windowing function used in analyzing the spectrum.

It is an inherent assumption when applying the Fourier transform (discrete Fourier transform) that the sampled data can be replicated infinitely to provide a periodic signal for the harmonic series expansion. In the event that the source data is not periodic or that it exhibits a discontinuity from the last data point to the replicated first data, it is necessary to multiply the source data by a function, the so-called windowing function, that forces the initial and terminal data values to go zero and eliminates the discontinuity. There are many possible choices for the windowing function, such as the Hanning window, the Hamming window.

The well-known and oft-used Hanning window employs the function $\cos^2\pi(t-T/2)/T$ $(0 \leq t \leq T)$, shown in Figure 4.2, to smooth the source data values, yielding a windowed data set that smoothly approaches zero at both the sampling-on ($t = 0$) and sampling-off ($t - T$) times. The central portion of the windowed data set closely resembles the original source data. The Hanning function takes on a value of 1.0 at $t = T/2$. Application of this Hanning window to the real time source data shown in Figure 4.3(a) results in an accurate representation of the power spectrum, shown in Figure 4.3(b). The power spectrum of the same data analyzed with no windowing function is shown in Figure 4.3(c). Clearly the un-windowed analysis produces a power spectrum that is significantly different from the more accurate windowed spectrum. The error due to the discontinuties in the replicated source data is called the leakage error. The transient nature of the acceleration signal with its excessively high levels of acceleration output just at the instant when the steel bar breaks would produce a similar leakage error.

To examine further windowing and the associated leakage error, a rectangular window was imposed on the source data of Figure 4.3(a). In the rectangular window the data are multiplied by either a one or a zero. In this application, the source data, as shown in Figure 4.4(a), from a small trigger time Δt after the instant when the steel bar breaks up to the end of the transient (here taken to be 8 sec) are multiplied by 1.0, while all remaining values in the source data are multiplied by 0. By judiciously selecting the trigger time Δt it is possible to remove the excessively high level of acceleration output at the instant when the steel bar breaks. With a trigger time of $\Delta t = 0$ sec, the resulting frequency spectrum, shown in Figure 4.4(b), becomes indistinguishable from the un-windowed spectrum, shown in Figure 4.3(c). However, with $\Delta t = 0.1$ sec, the spectrum, shown in Figure 4.4(c), drastically changes exhibiting characteristics quite similar to that of the Hanning-windowed spectrum shown in Figure 4.3(b), strongly suggesting that there is serious leakage error associated with the excessively high level of acceleration output at the instant

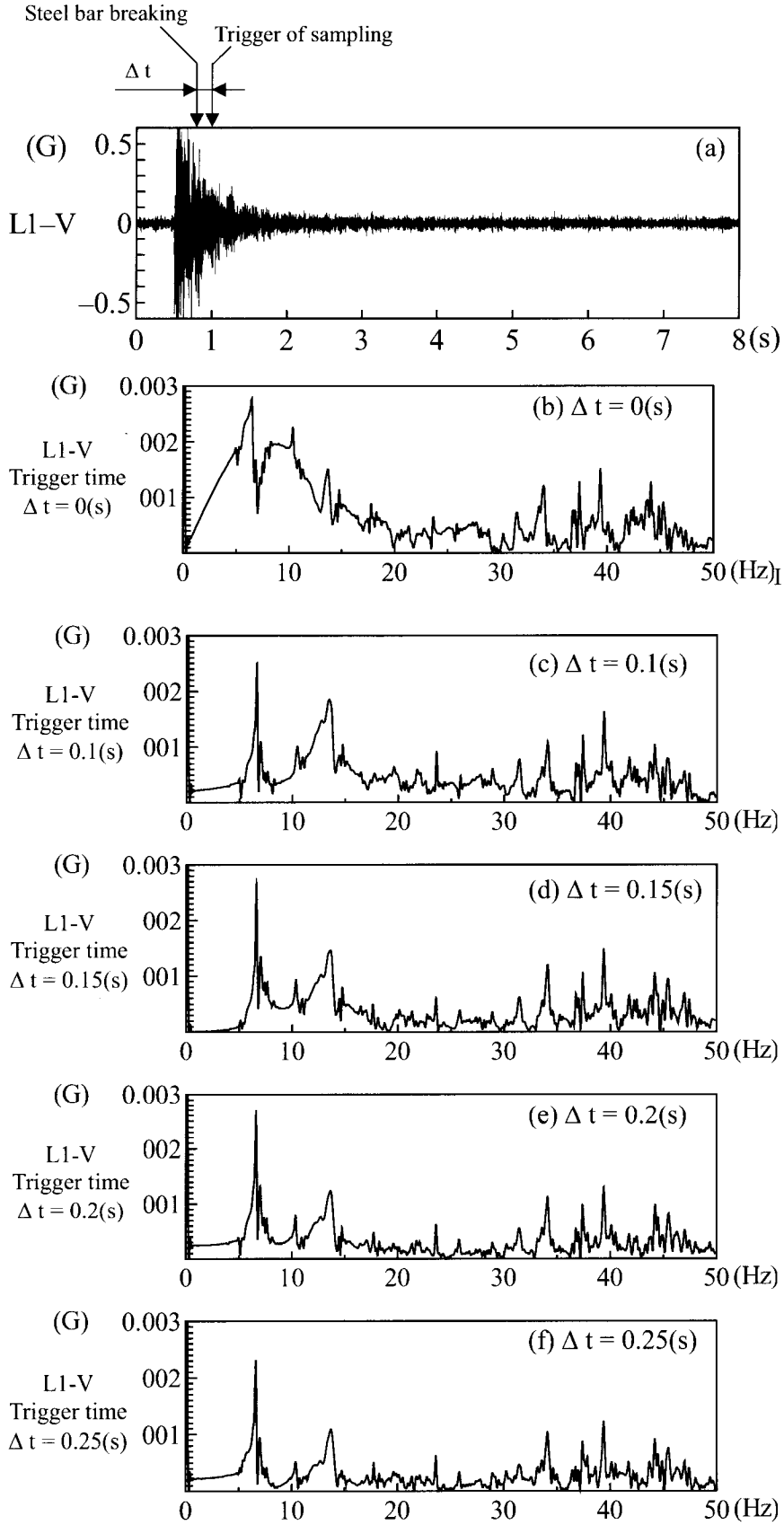

Figure 4.4: Spectrum analysis with a rectangular window.

The reader's attention is drawn to significant differences in the levels of the spectral peaks. The lowest frequency peak at about 6 Hz has a level in the Hanning-windowed spectrum that is less than one half the peak level in the rectangular-windowed spectrum. This large amplitude difference clearly results from the multiplication of source data at the beginning of the sampled signal by the smaller values of the cosine-squared function. This peak attenuation is a secondary known error associated with the use of the Hanning window which requires additional correction measures. Based on the considerations presented here, it was concluded that for the analysis of the transient acceleration signals it would be best to adopt a rectangular window with a trigger time Δt of 0.25 sec.

5. FREQUENCY POWER SPECTRUM OF VIBRATIONS

The frequency power spectra, analyzed with a rectangular window with a trigger time $\Delta t = 0.25$sec, are shown in Figures 5.1 to 5.7 for Gate #2 and in Figures 5.8 to 5.13 for Gate #3. In each of these figures, the first set of traces, labeled (a), shows the spectra of vibrations in the radial direction at various spanwise locations across the bottom of the skinplate; the next set of traces, labeled (b), shows the spectra of vibrations in the radial direction at various spanwise locations across the center of the skinplate; the third set of traces, labeled (c), shows the spectra of vibrations in the vertical and radial directions on the upper radial arm. In all spectra, the frequency resolution is 0.125 Hz.

Ambient test results are shown in Figures 5.1 and 5.2 for Gate #2 and in Figures 5.9 and 5.10 for Gate #3. In these cases, the signal to noise ratio level is very low and it is impossible to identify any stable, sharp peak the lower frequency range. In contrast, for all tests involving the breaking of the steel rod, the spectra show a very high signal-to-noise ratio, permitting the ready identification of stable, sharp spectral peaks. Spectral peaks in the low frequency range up to about 10 Hz are quite significant when considering the possibility of "movement-induced self-excitation," while peaks at frequencies above about 10 Hz are not meaningful, and can be safely disregarded.

In Test 2 with a steel rod diameter of d = 3 mm for Gate #2, many sharp peaks can be seen in Figures 5.3(a) and (b). However, it is quite difficult, if not impossible, to identify correctly the meaningful peaks in these spectra. This inability to readily identify meaningful peaks resulted directly from an inadequate impulsive excitation from the breaking steel rod which was mounted on the downstream flange of the horizontal girder (see Figures 2.14(a) and 2.23(a)).

Immediately after Test 2, the steel rod fixtures were moved to the upstream flange (see Figures 2.14(b) and 2.23(b)) to improve the effectiveness of impulsive excitation on the gate. The second test involving breaking the steel rod was Test 3 with the same steel rod diameter of d = 3 mm, the results for which are shown in Figure 5.3. Comparing the results from Test 2 with those from Test 3, one sees in Figure 5.4 (Test 3) two predominant, sharp and stable spectral peaks at the frequencies of 5.5 Hz and 6.5 Hz which are lost in the background noise in Figure 5.3. These peaks become sharper and more distinct when the steel rod diameter is increased to 6 mm and then to 8 mm, as shown in Figures 5.5 and 5.6 (Test 4 and 5 with d = 6 mm) and in Figure 5.7 (Test 6 with d = 8 mm). These peaks clearly represent intense natural vibrations of the gate.

Carefully examining the spectra in Figure 5.7 with a steel rod diameter of d = 8 mm, the following major features can be identified:

(1) Figure 5.7(a): the amplitudes of the streamwise vibration along the bottom of the skinplate for the peaks at both 5.5 Hz and 6.5 Hz peaks continuously increase as the measurement point approaches the spanwise center of the skinplate from the right hand side.

(2) Figure 5.7(b): the amplitudes of the streamwise vibration along the vertical centerline of the skinplate

show differing behavior with the vertical position of the measuring point; the amplitude of the peak at 5.5 Hz peak remains at an almost constant level, while the amplitude of peak at 6.5 Hz peak exhibits a continuous decrease initially with decreasing vertical position and then an increase as the measuring position approaches bottom of the skinplate.

(3) Figure 5.7(c): the amplitude of the peaks in the vertical vibration spectra of the skinplate (see E3-V and E6-V) again show differing behavior when moving from the skinplate centerline to the bottom of the skinplate with that of the 5.5 Hz peak showing a moderate increase while that for the 6.5 Hz peak remains approximately constant.

These major features of intense natural vibrations are common to all the tests for Gate #2, as shown in Figures 5.4 to 5.7.

Gate #3 also exhibits features basically similar to those of Gate #2, except the 5.5 Hz and 6.5 Hz peaks found for Gate #2 appear to be at slightly higher frequencies of 5.6 Hz and 6.6 Hz for Gate #3, as shown in Figures 5.8 and 5.11 to 5.13. However, between these two peaks, Gate #3 appears to have an additional peak at 6.1 Hz.

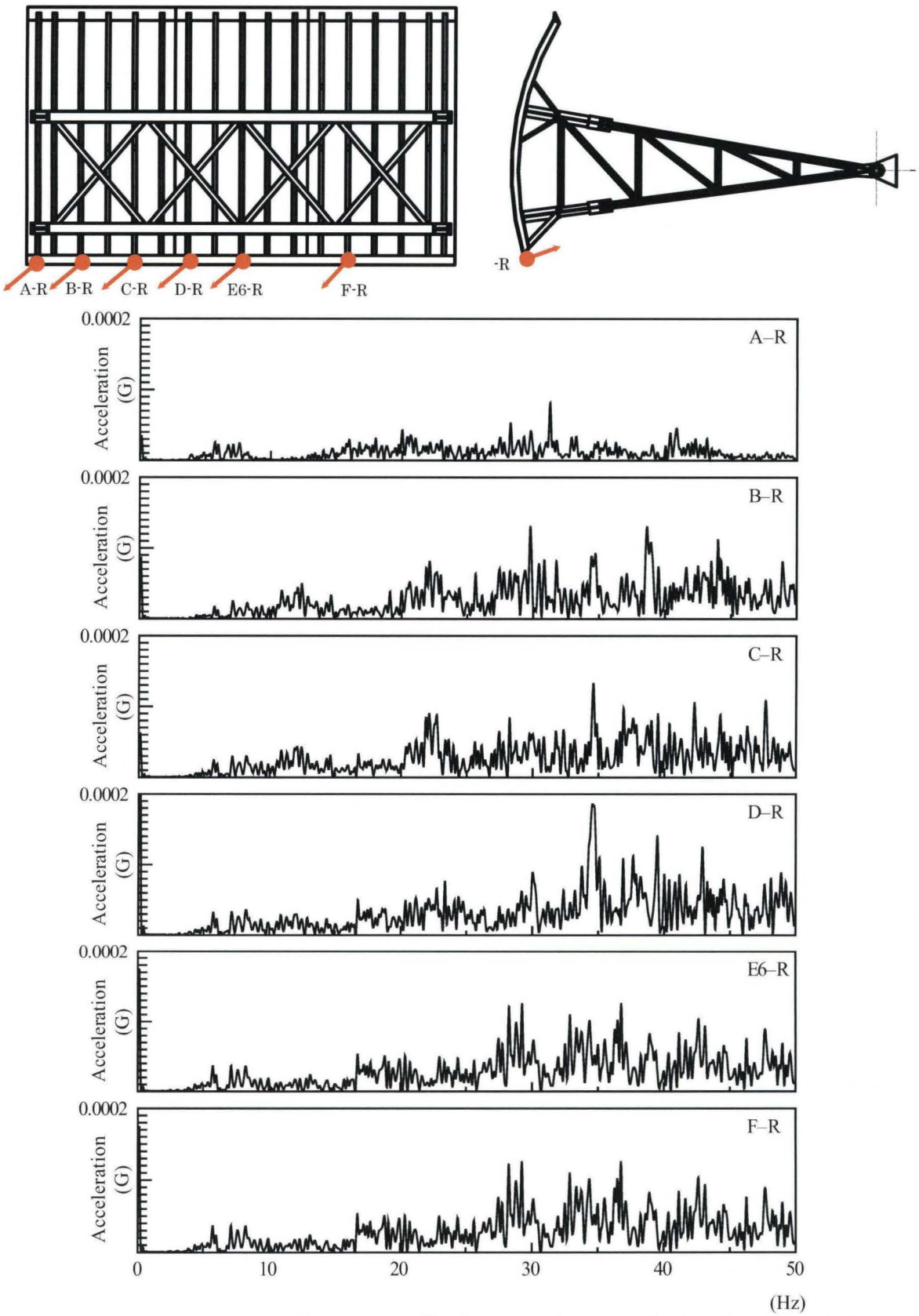

Figure 5.1(a): Frequency spectra of streamwise vibrations at various spanwise locations along the bottom of the skinplate. (Test No. 1: ambient, B = 23 mm)

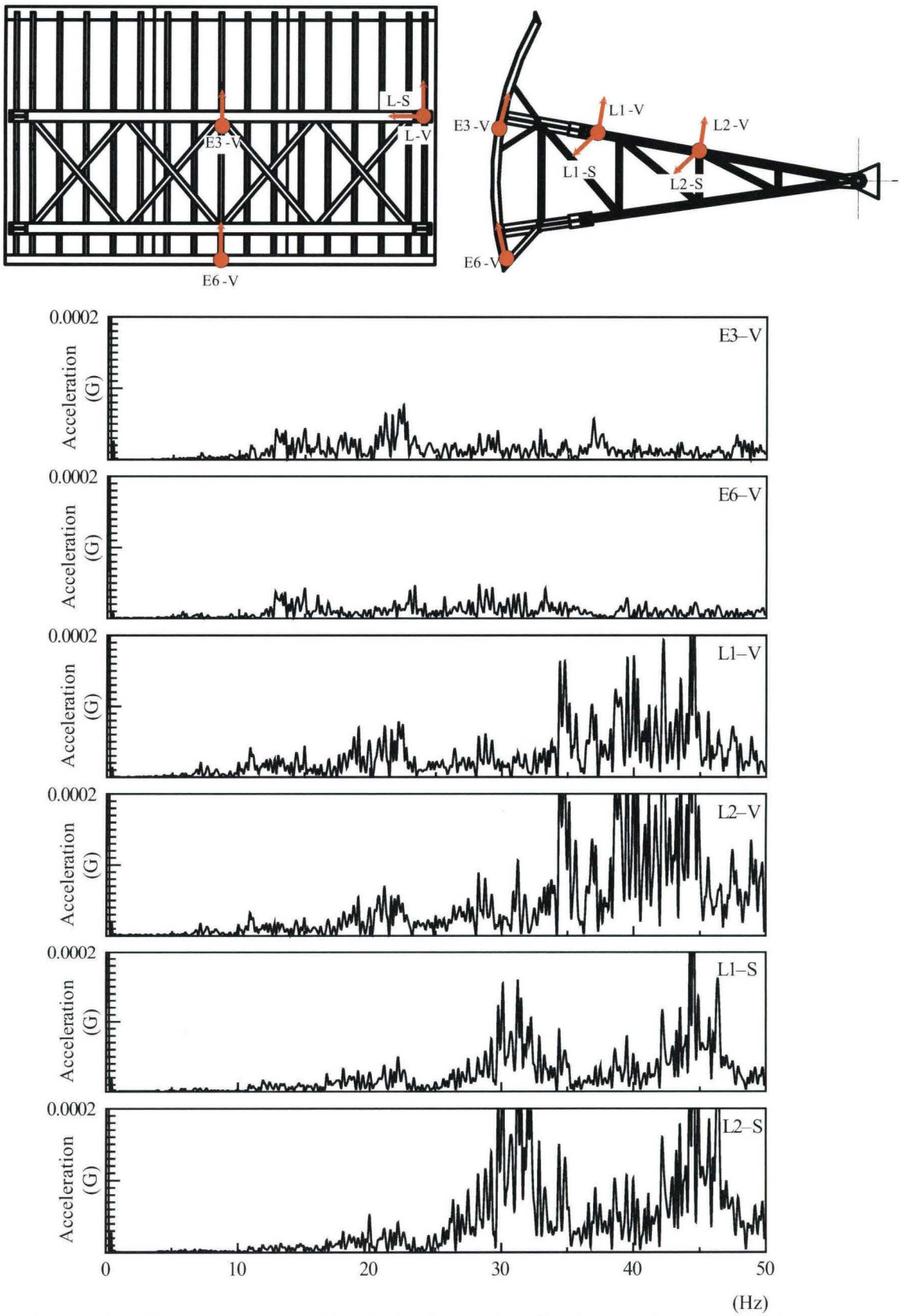

Figure 5.1(c): Frequency spectra of vertical and spanwise vibrations on the upper radial arm. (Test No. 1: ambient, B = 23 mm)

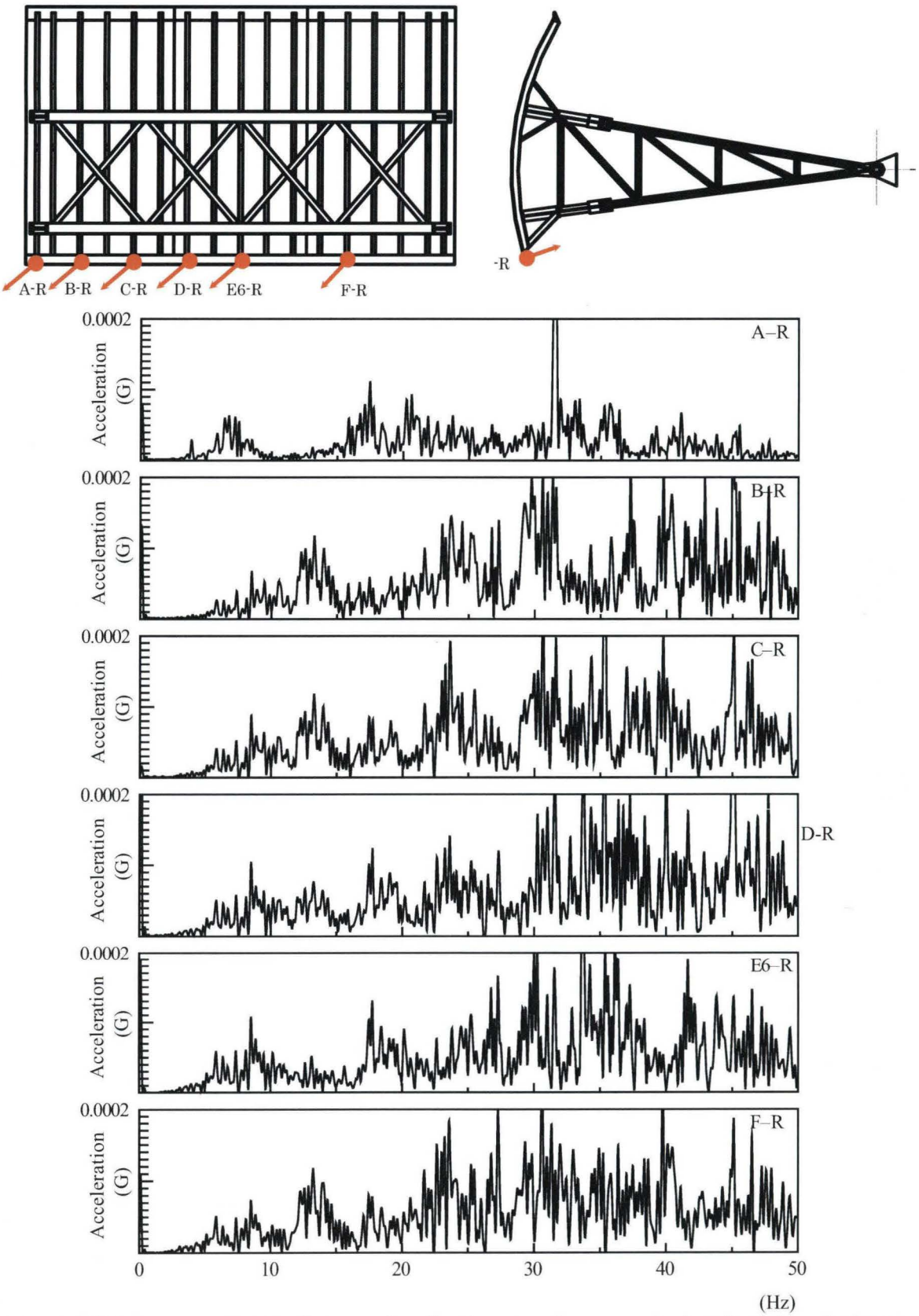

Figure 5.2(a): Frequency spectra of streamwise vibrations at various spanwise locations along the bottom of the skinplate. (Test No. 1: ambient, B = 156 mm)

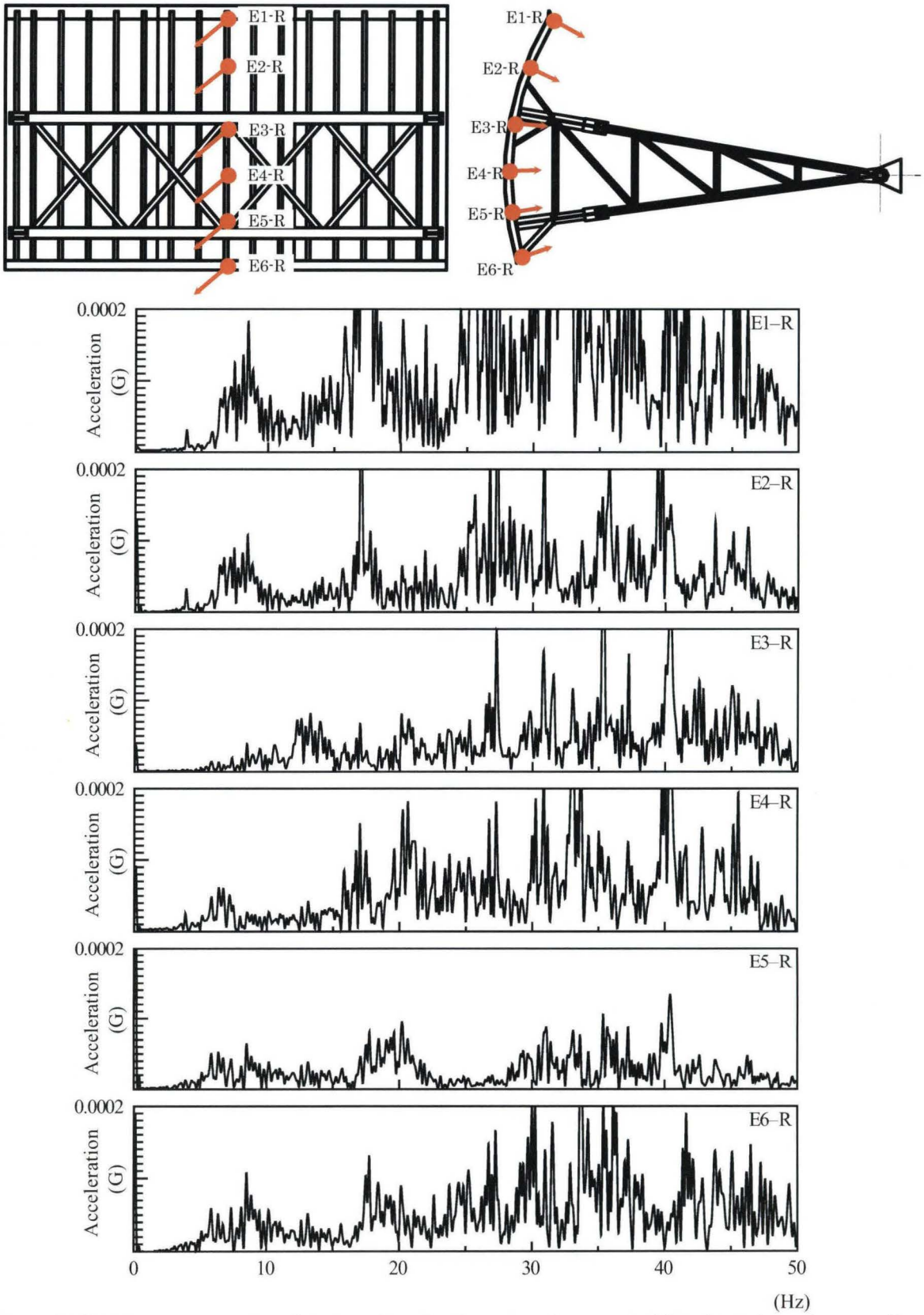

Figure 5.2(b): Frequency spectra of streamwise vibrations at various vertical locations along the centerline of the skinplate. (Test No. 1: ambient, B = 156 mm)

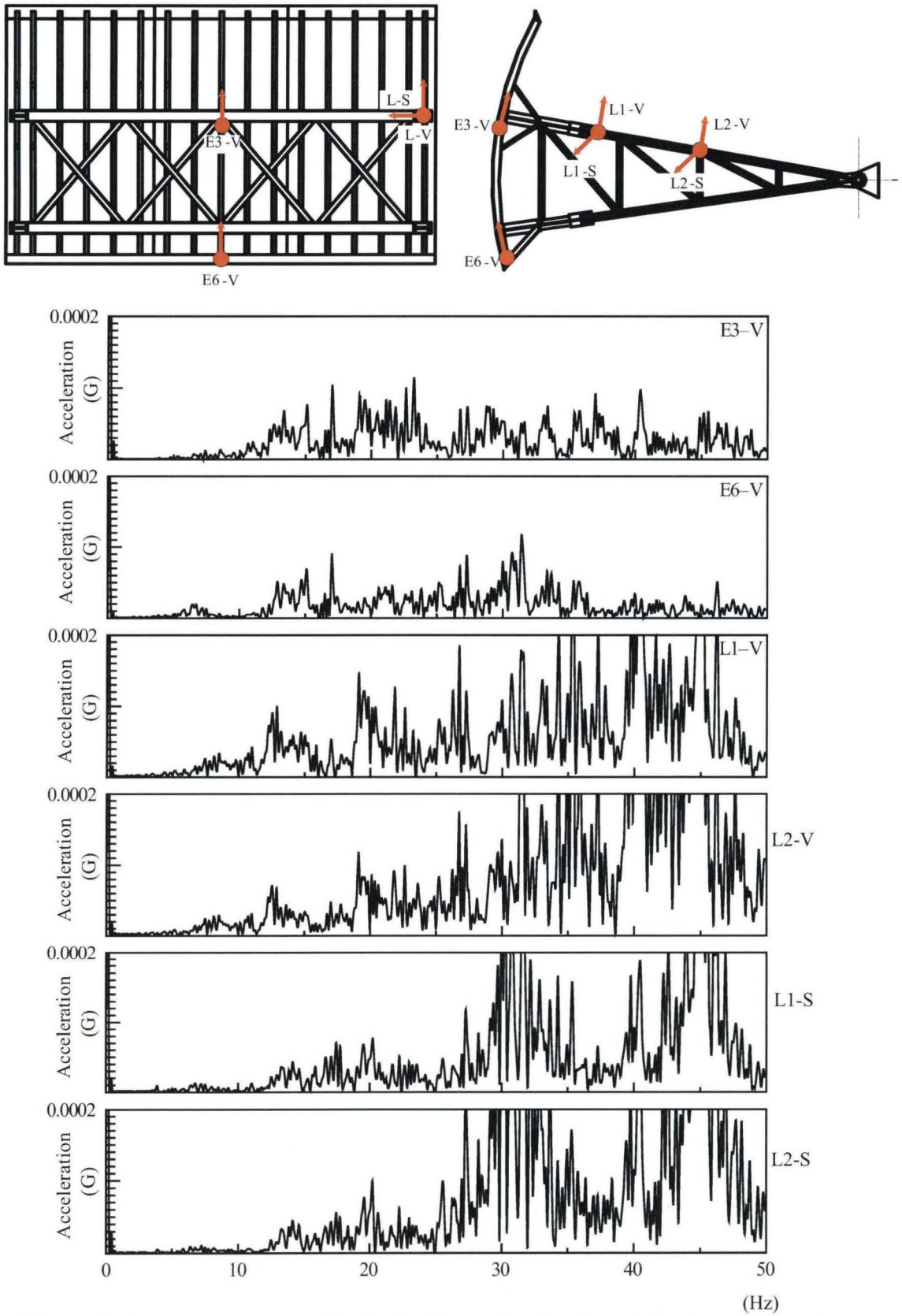

Figure 5.2(c): Frequency spectra of vertical and spanwise vibrations on the upper radial arm. (Test No. 1: ambient, B = 156 mm)

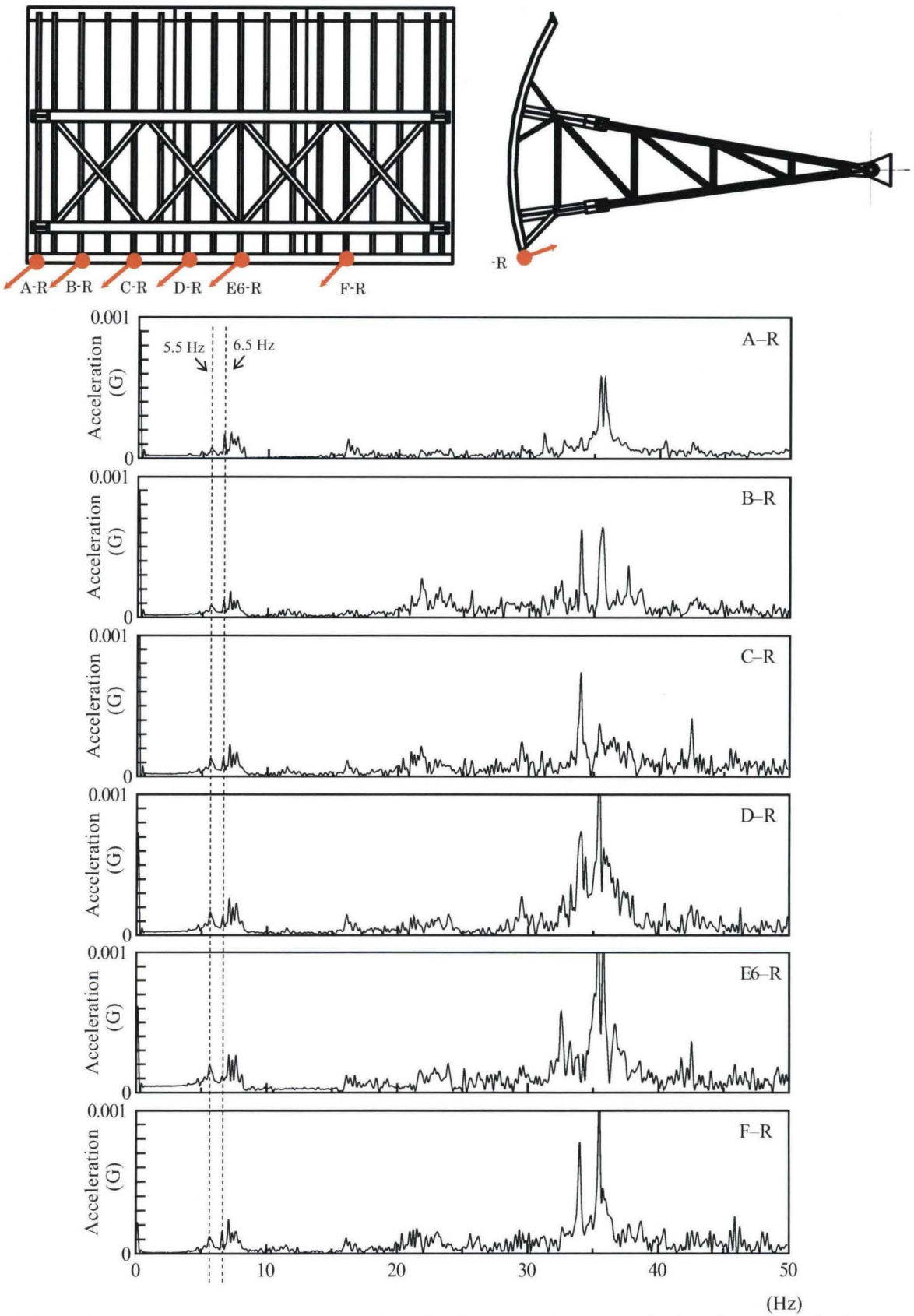

Figure 5.3(a): Frequency spectra of streamwise vibrations at various spanwise locations along the bottom of the skinplate. (Test No. 2: steel rod breaking, d = 3 mm)

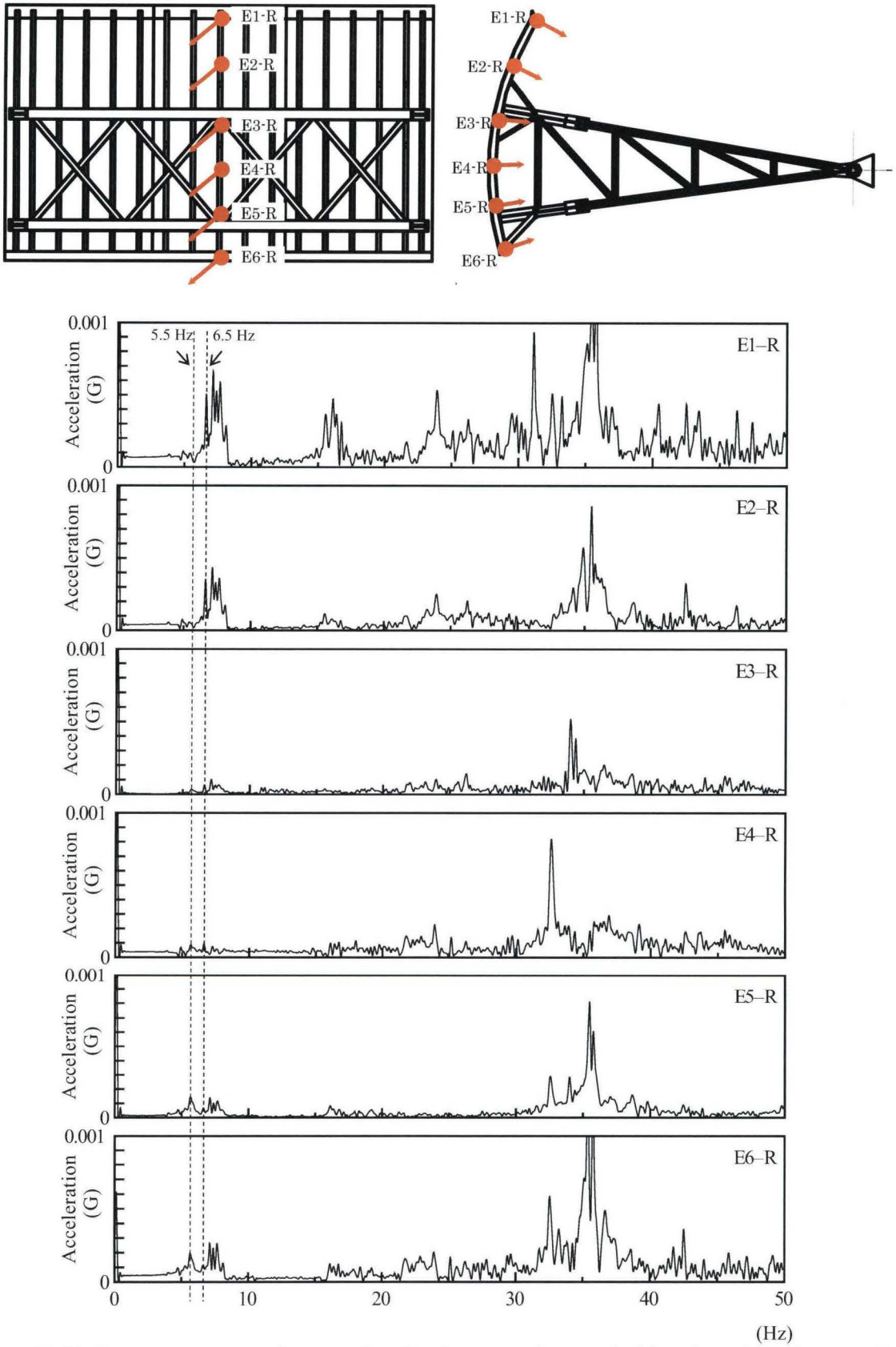

Figure 5.3(b): Frequency spectra of streamwise vibrations at various vertical locations along the centerline of the skinplate. (Test No. 2: steel rod breaking, d = 3 mm)

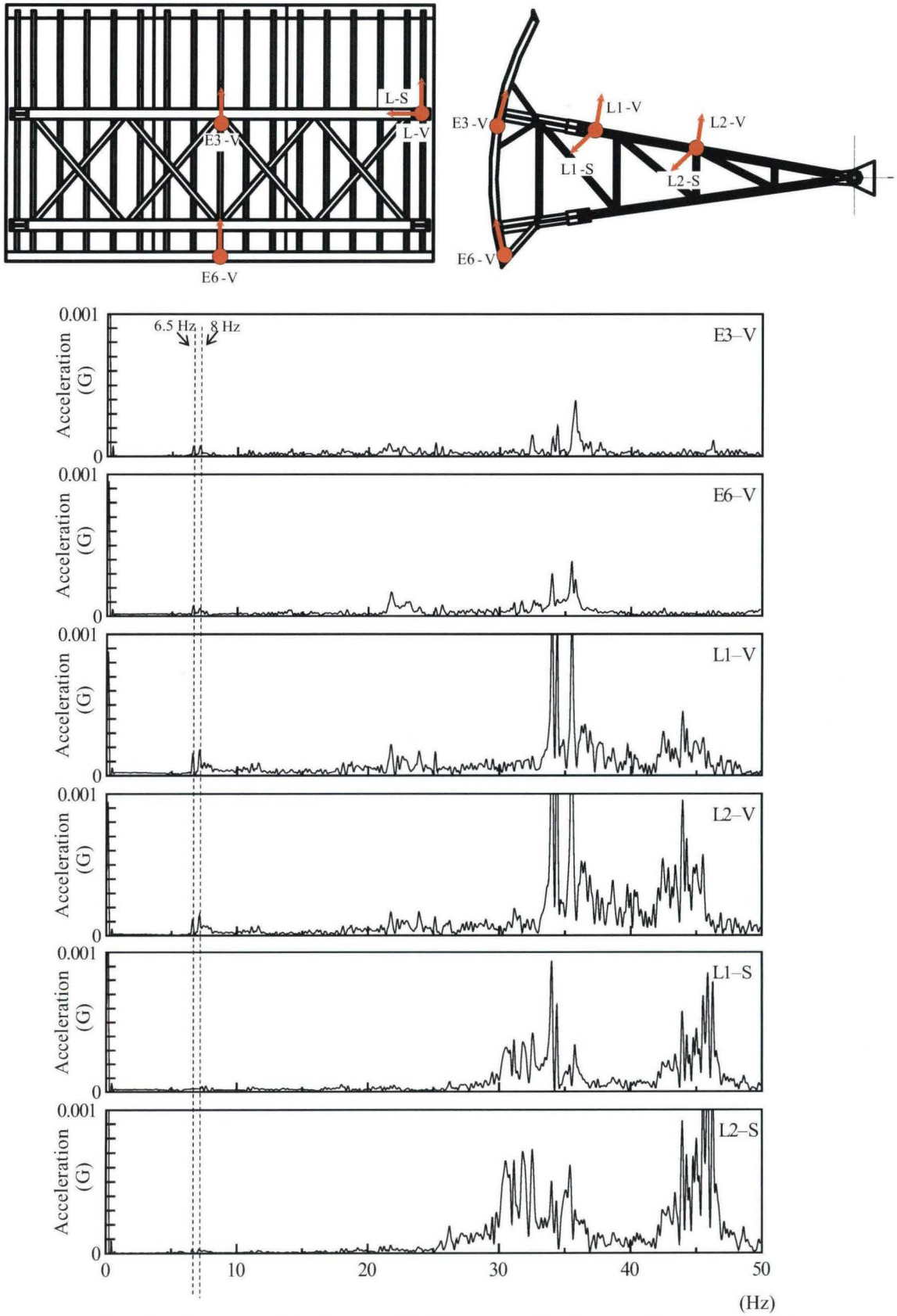

Figure 5.3(c): Frequency spectra of vertical and spanwise vibrations on the upper radial arm. (Test No. 2: steel rod breaking, d = 3 mm)

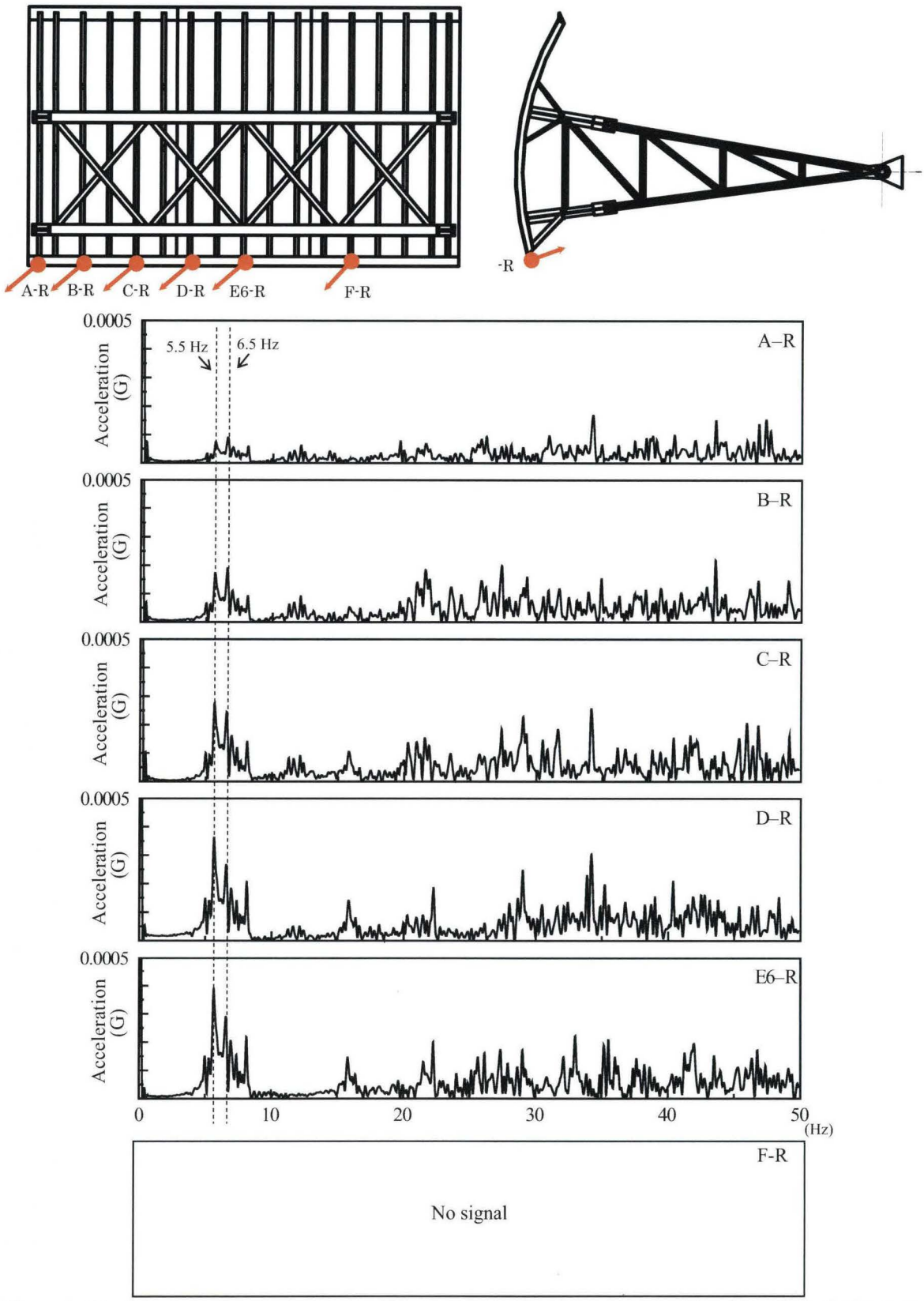

Figure 5.4(a): Frequency spectra of streamwise vibrations at various spanwise locations along the bottom of the skinplate. (Test No. 3: steel rod breaking, d = 3 mm)

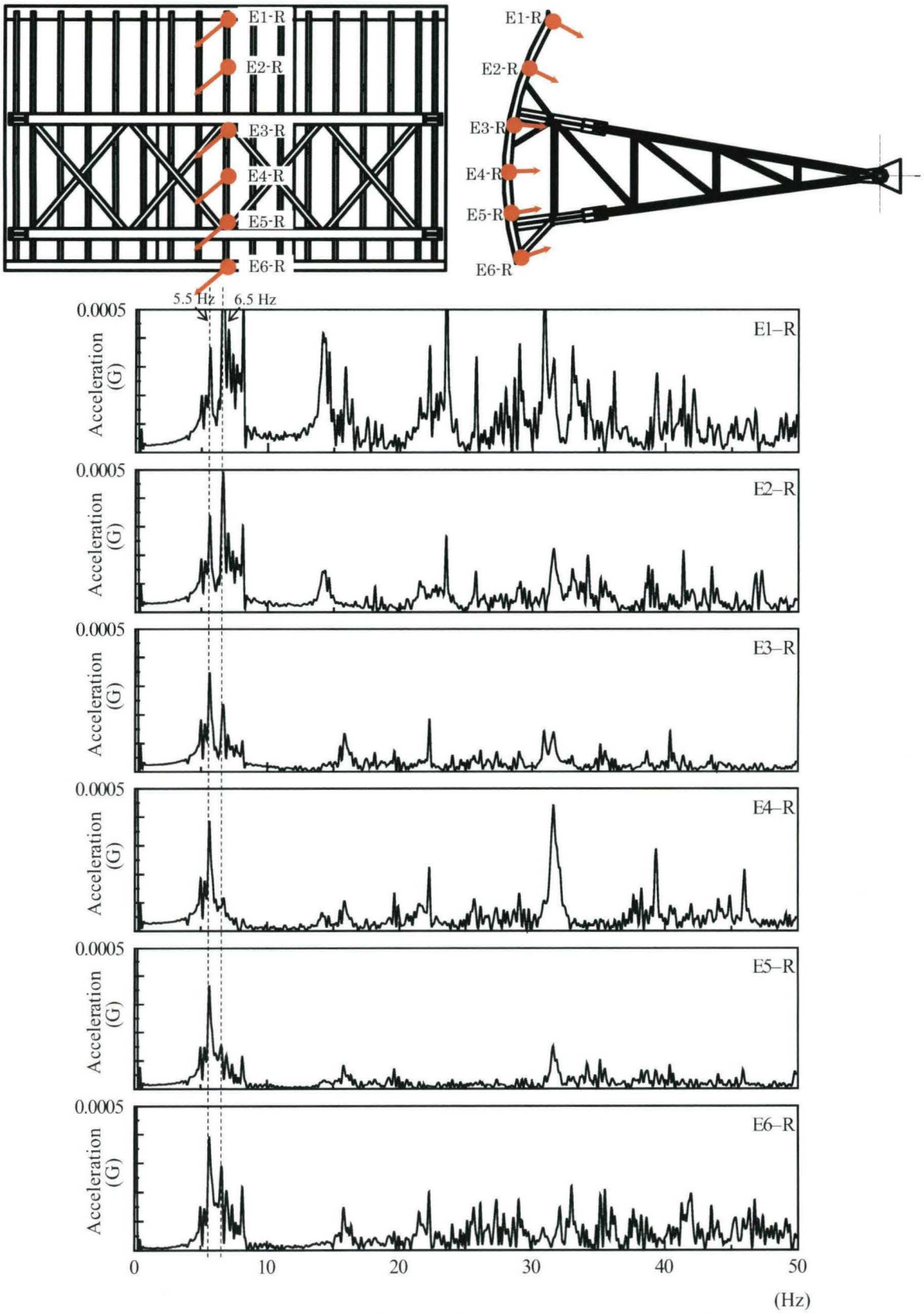

Figure 5.4(b): Frequency spectra of streamwise vibrations at various vertical locations along the centerline of the skinplate. (Test No. 3: steel rod breaking, d = 3 mm)

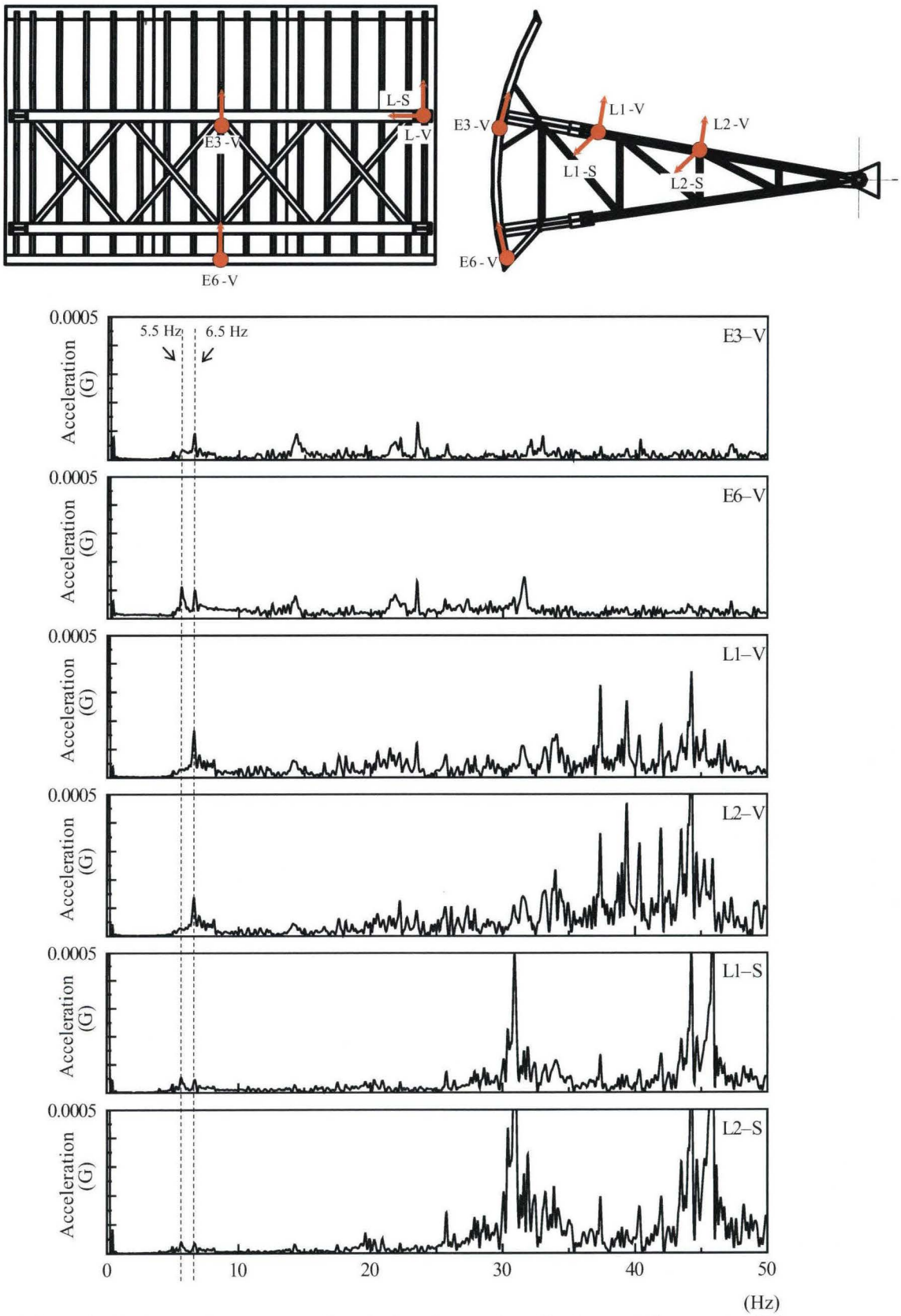

Figure 5.4(c): Frequency spectra of vertical and spanwise vibrations on the upper radial arm. (Test No. 3: steel rod breaking, d = 3 mm)

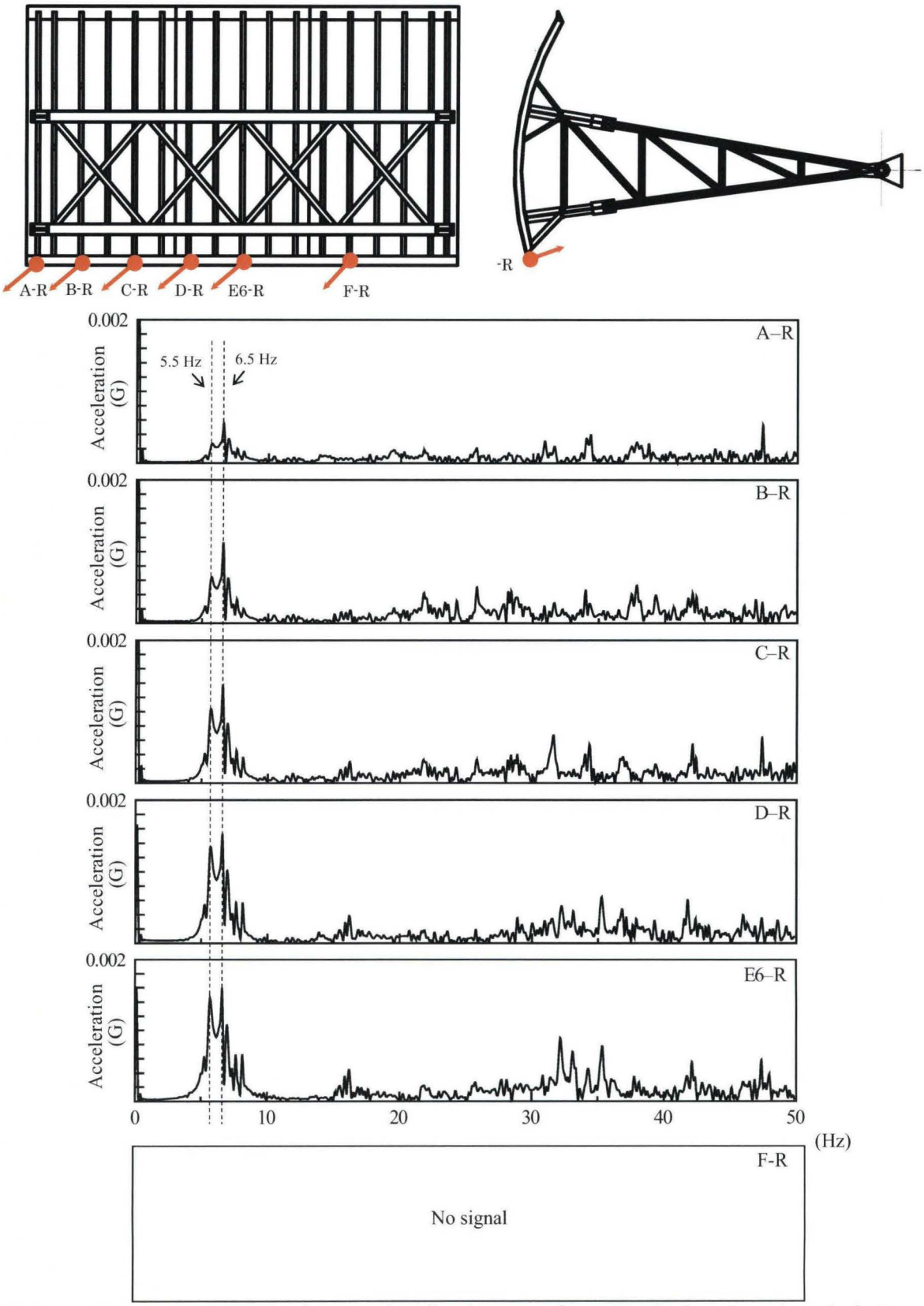

Figure 5.5(a): Frequency spectra of streamwise vibrations at various spanwise locations along the bottom of the skinplate. (Test No. 4: steel rod breaking, d = 6 mm)

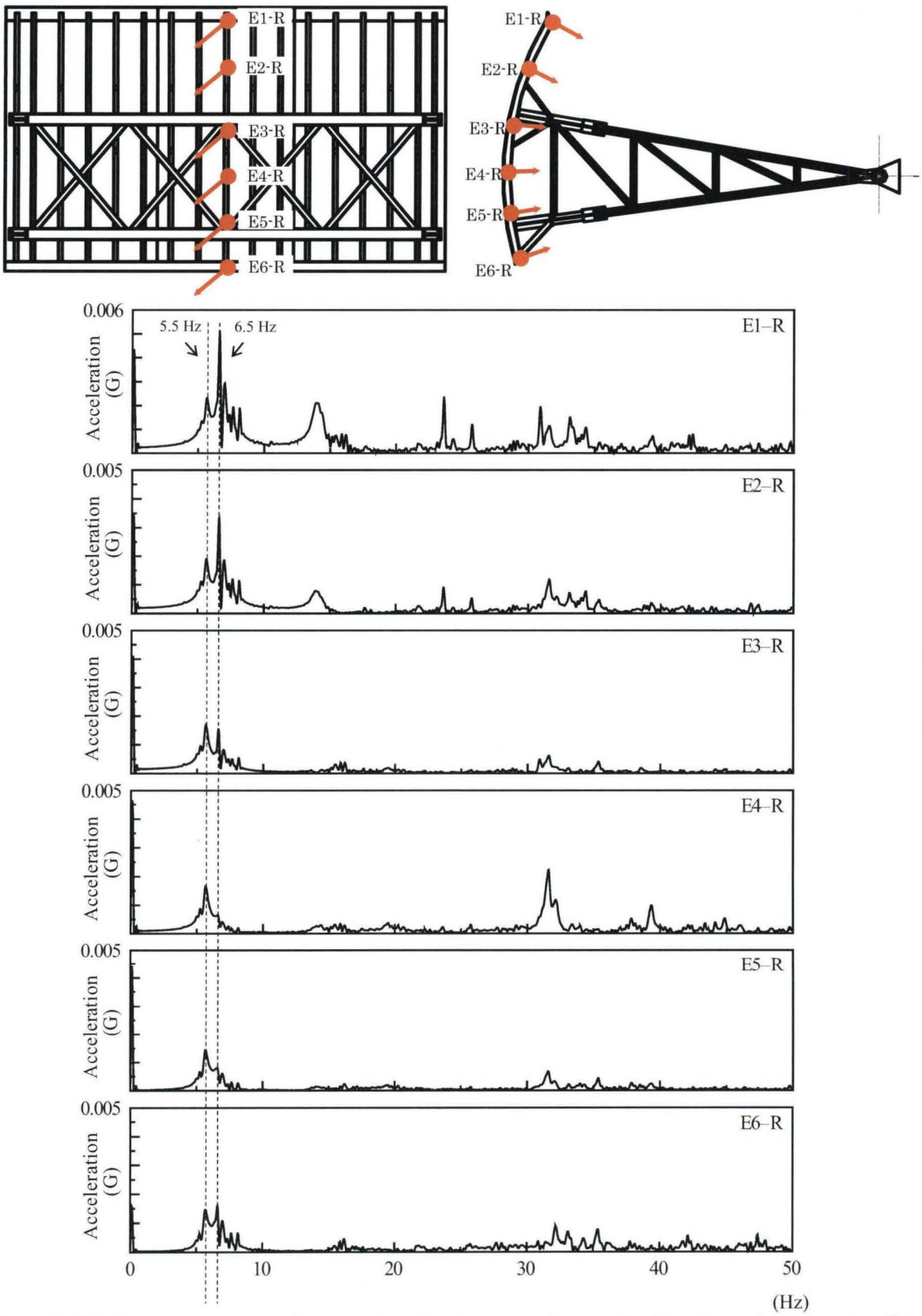

Figure 5.5(b): Frequency spectra of streamwise vibrations at various vertical locations along the centerline of the skinplate. (Test No. 4: steel rod breaking, d = 6 mm)

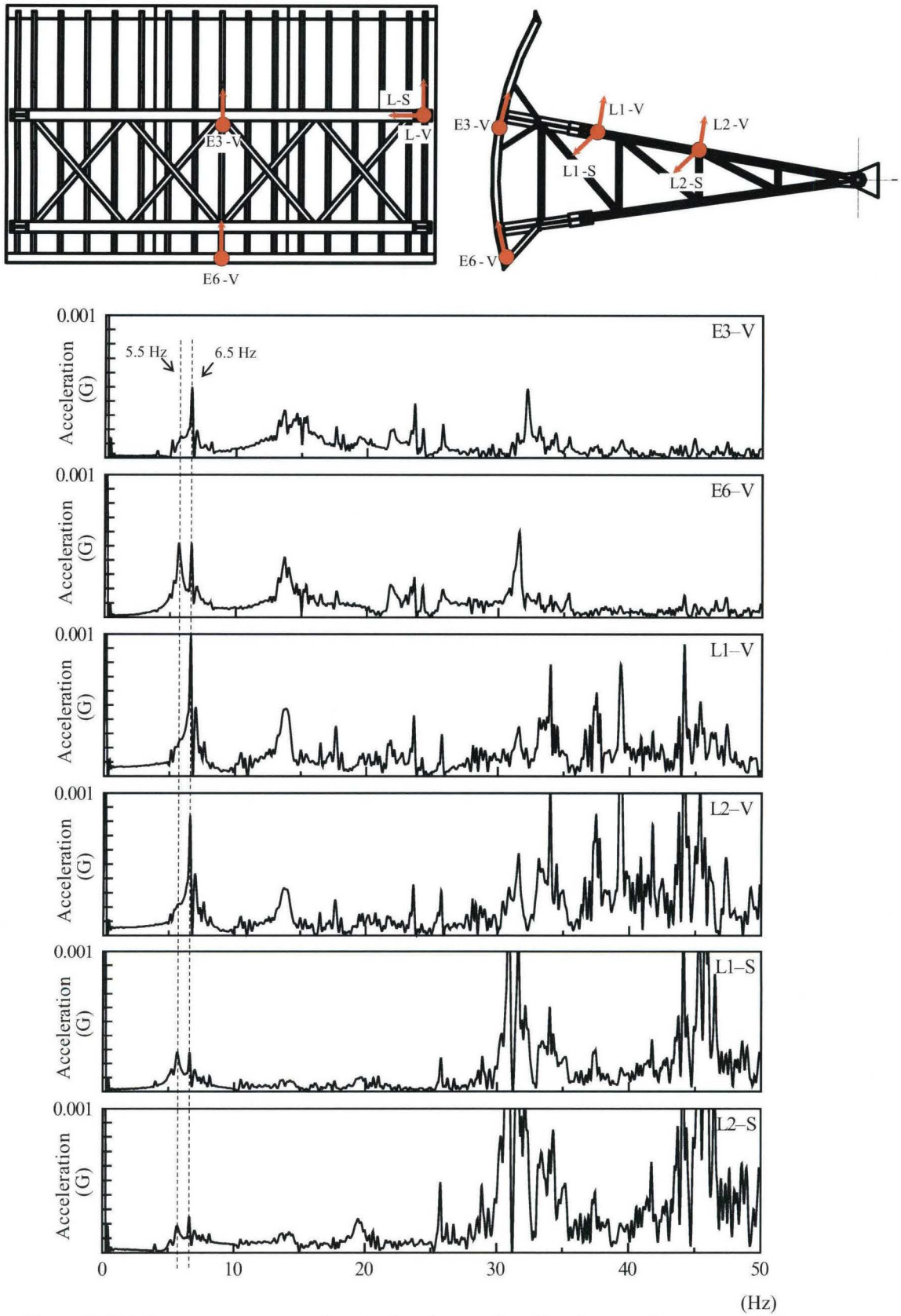

Figure 5.5(c): Frequency spectra of vertical and spanwise vibrations on the upper radial arm. (Test No. 4: steel rod breaking, d = 6 mm)

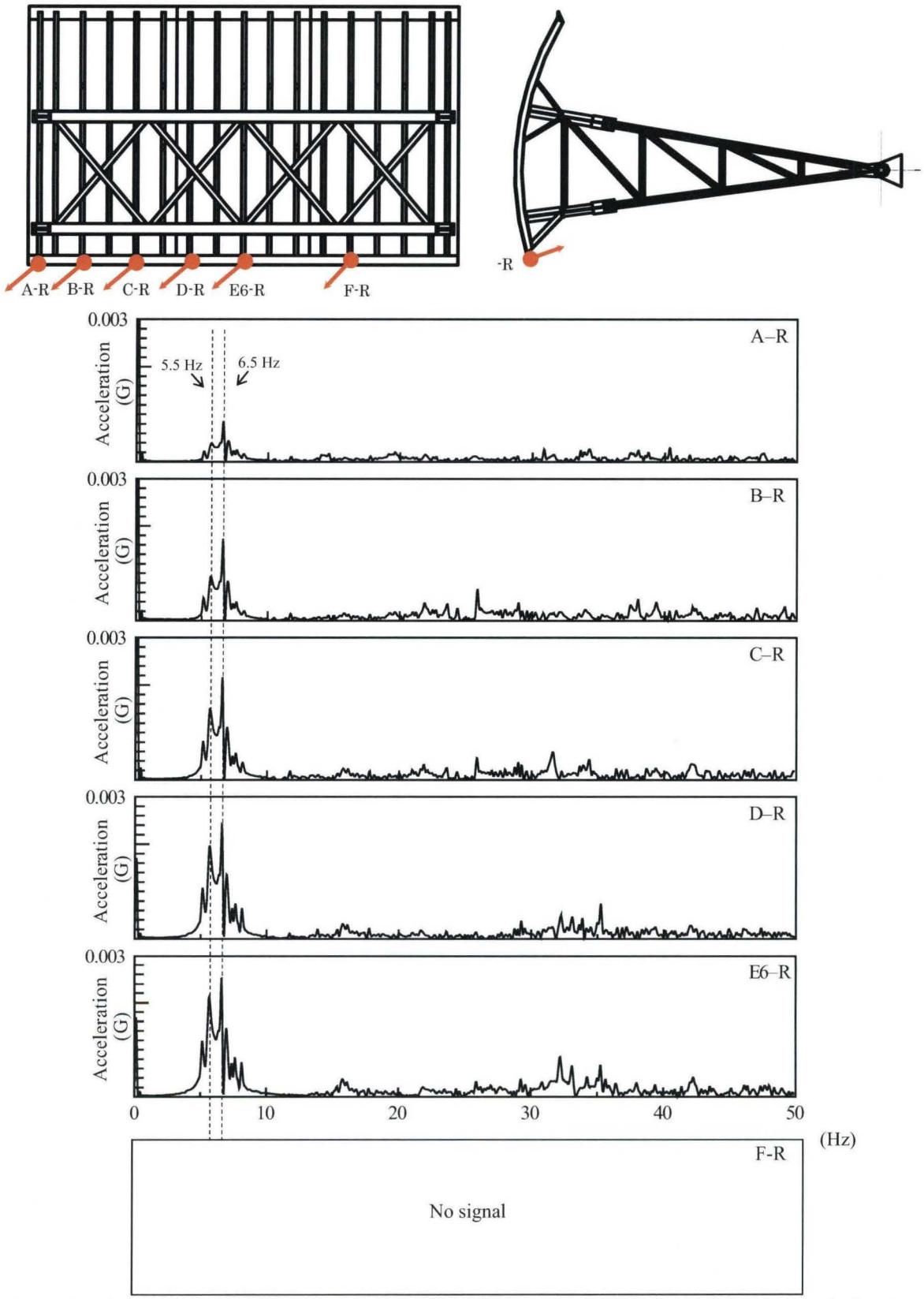

Figure 5.6(a): Frequency spectra of streamwise vibrations at various spanwise locations along the bottom of the skinplate. (Test No. 5: steel rod breaking, d = 6 mm)

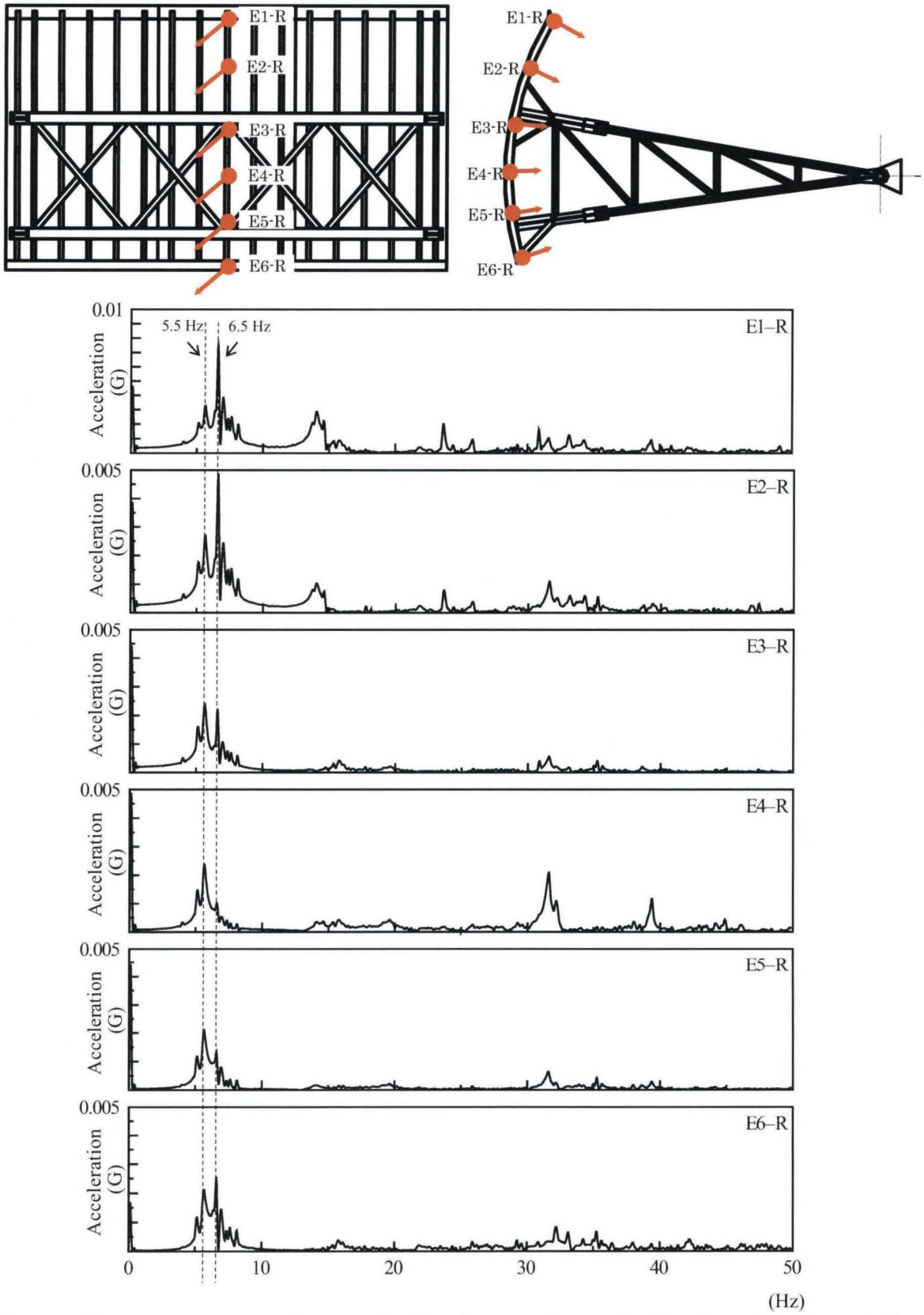

Figure 5.6(b): Frequency spectra of streamwise vibrations at various vertical locations along the centerline of the skinplate. (Test No. 5: steel rod breaking, d = 6 mm)

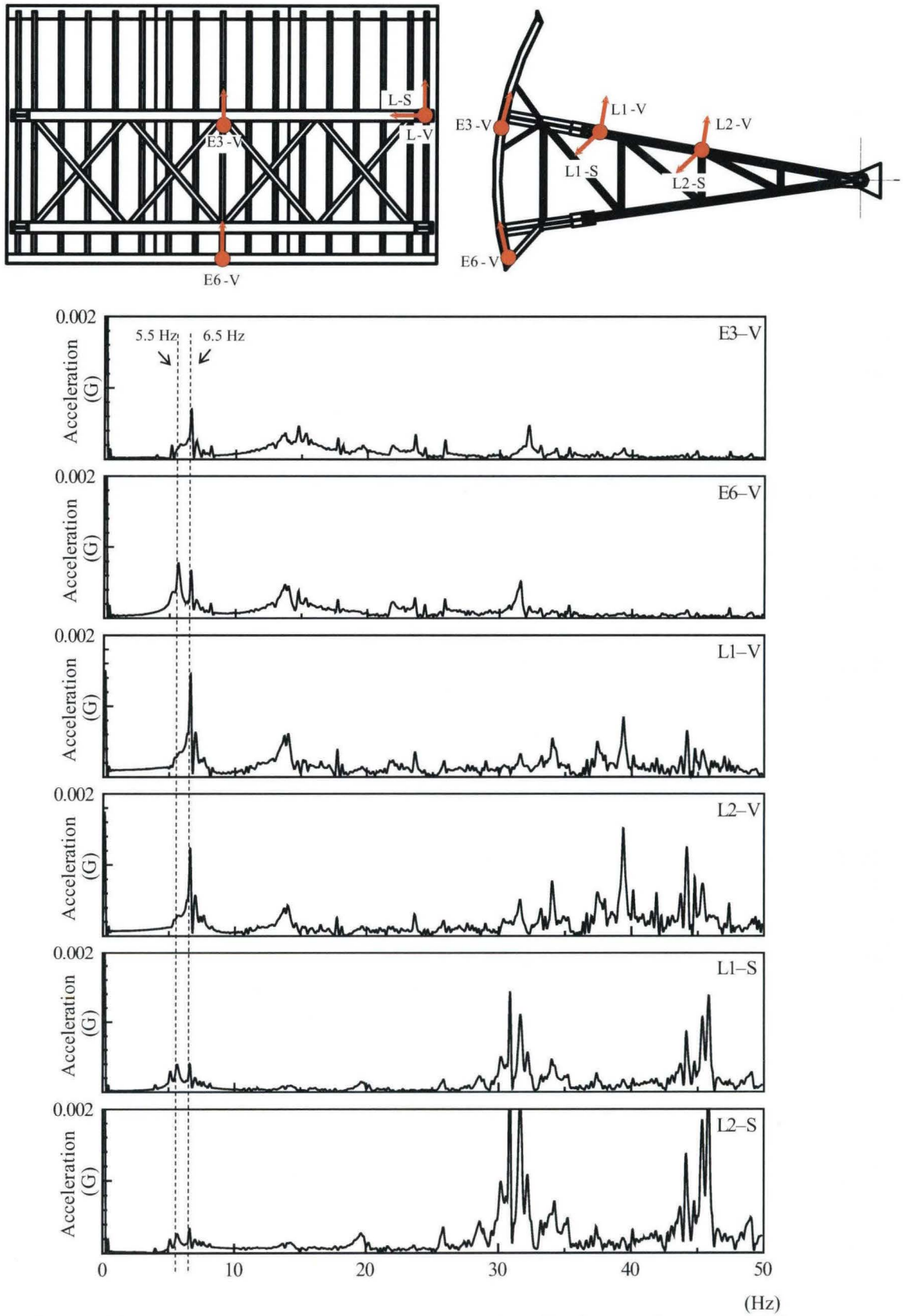

Figure 5.6(c): Frequency spectra of vertical and spanwise vibrations on the upper radial arm. (Test No. 5: steel rod breaking, d = 6 mm)

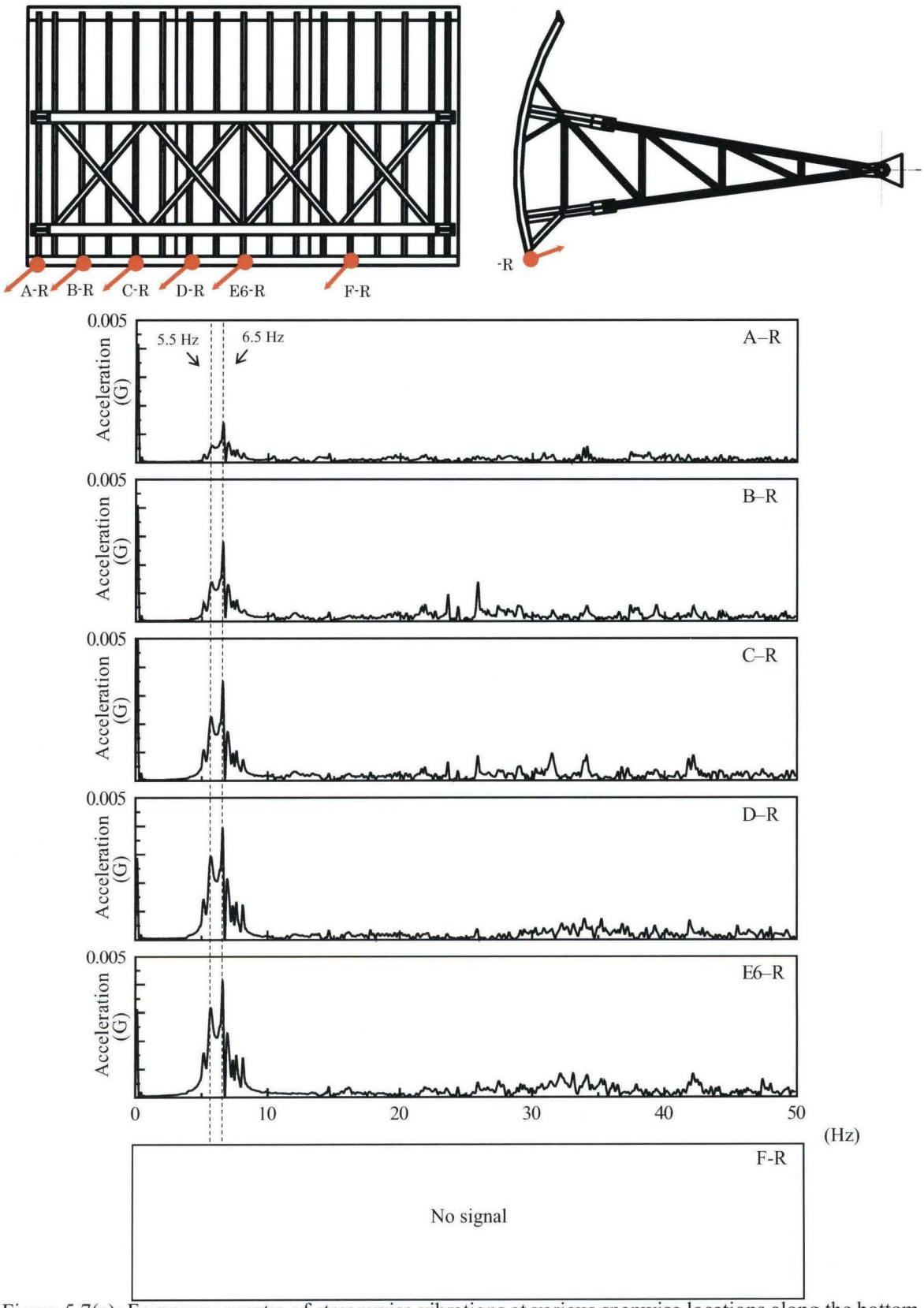

Figure 5.7(a): Frequency spectra of streamwise vibrations at various spanwise locations along the bottom of the skinplate. (Test No. 6: steel rod breaking, d = 8 mm)

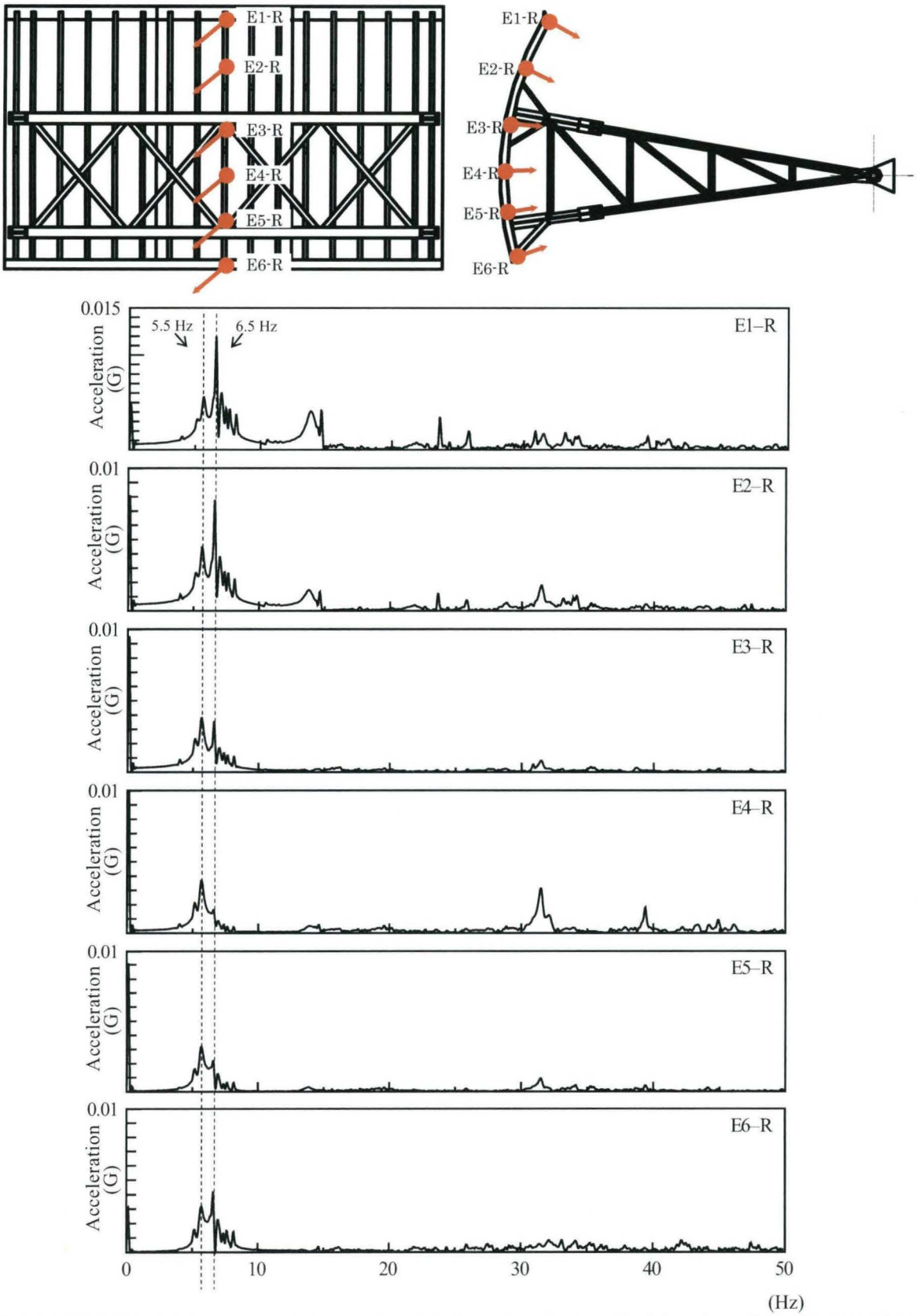

Figure 5.7(b): Frequency spectra of streamwise vibrations at various vertical locations along the centerline of the skinplate. (Test No. 6: steel rod breaking, d = 8 mm)

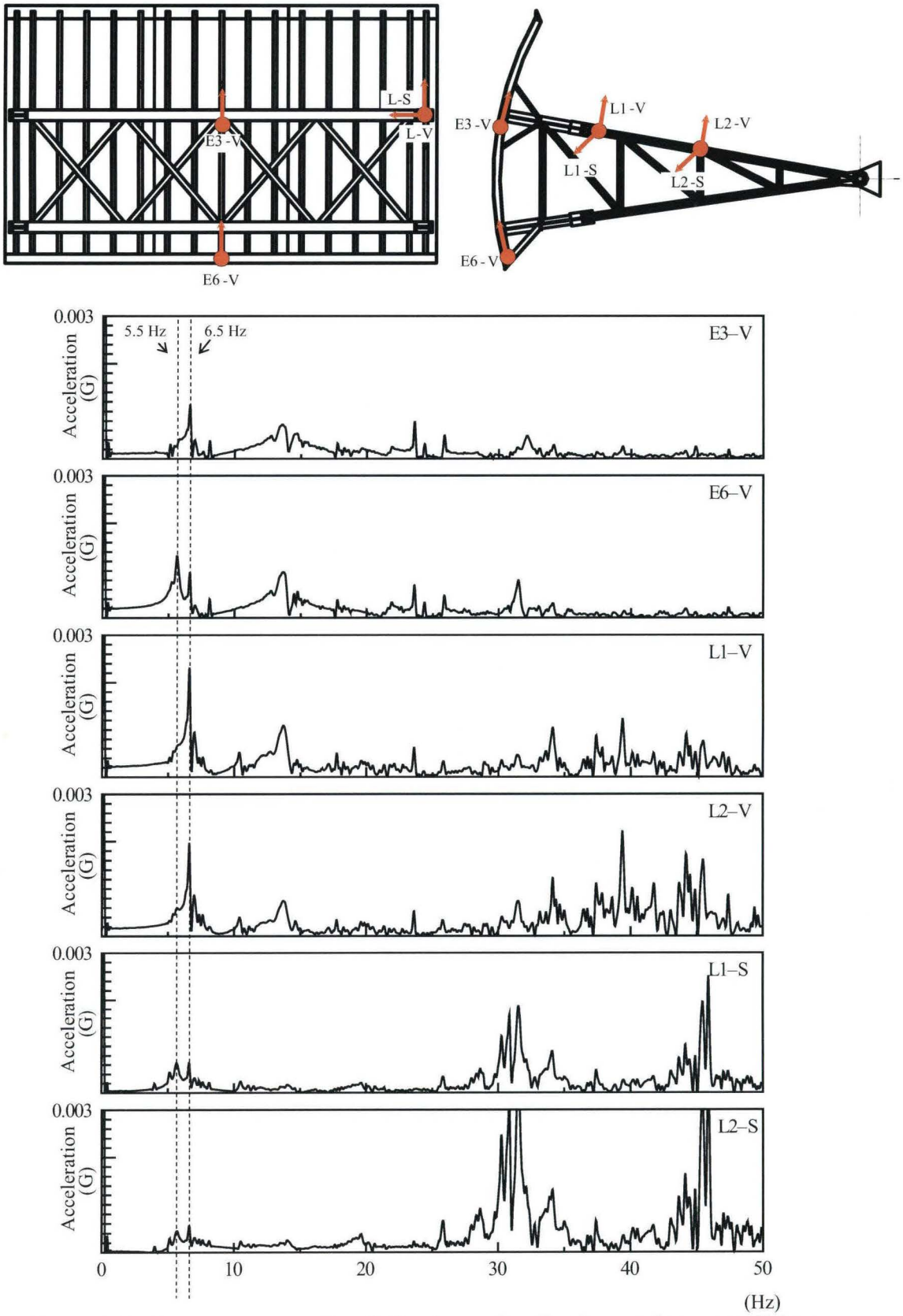

Figure 5.7(c): Frequency spectra of vertical and spanwise vibrations on the upper radial arm. (Test No. 6: steel rod breaking, d = 8 mm)

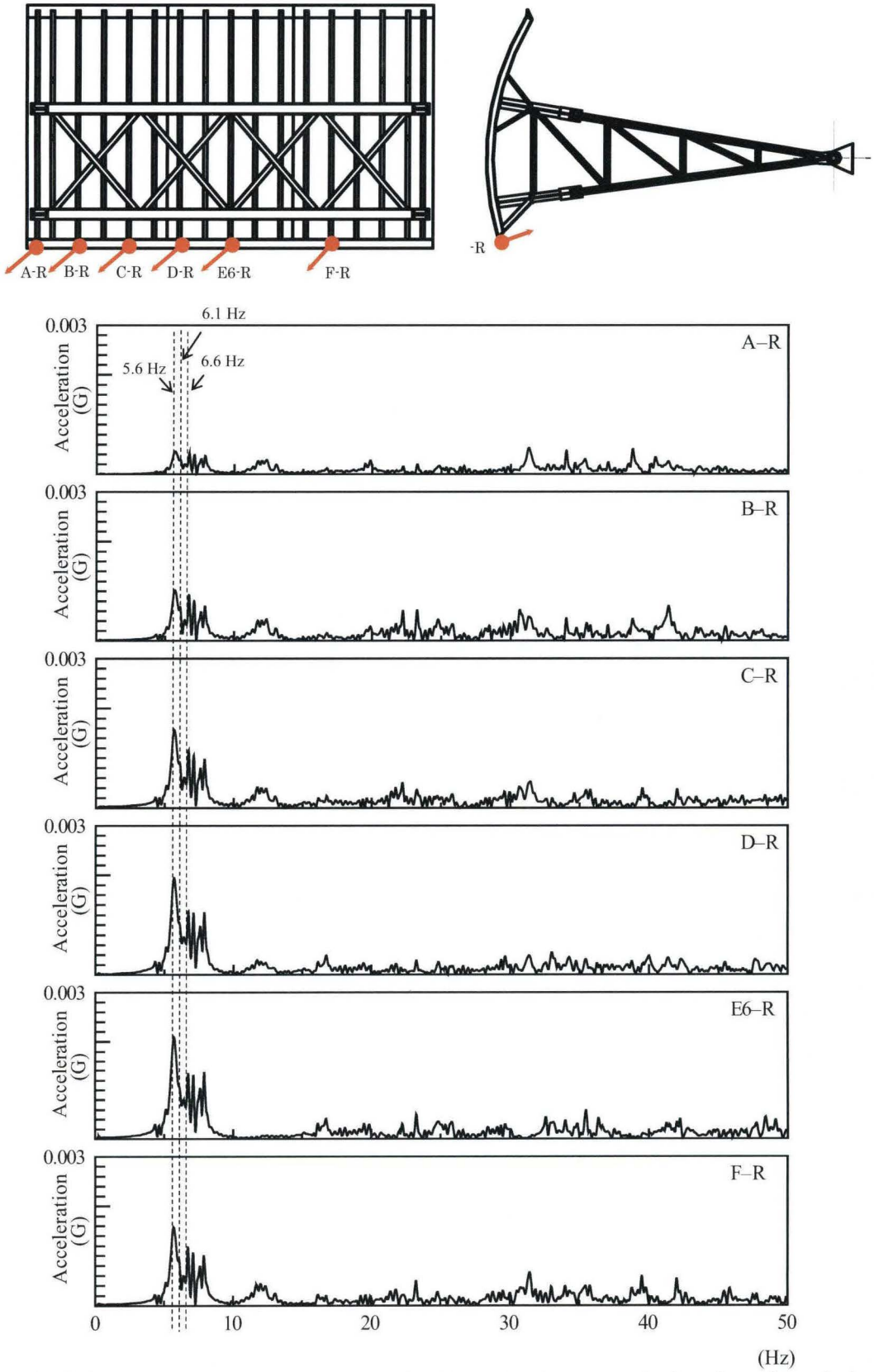

Figure 5.8(a): Frequency spectra of streamwise vibrations at various spanwise locations along the bottom of the skinplate. (Test No. 7: steel rod breaking, d = 6 mm)

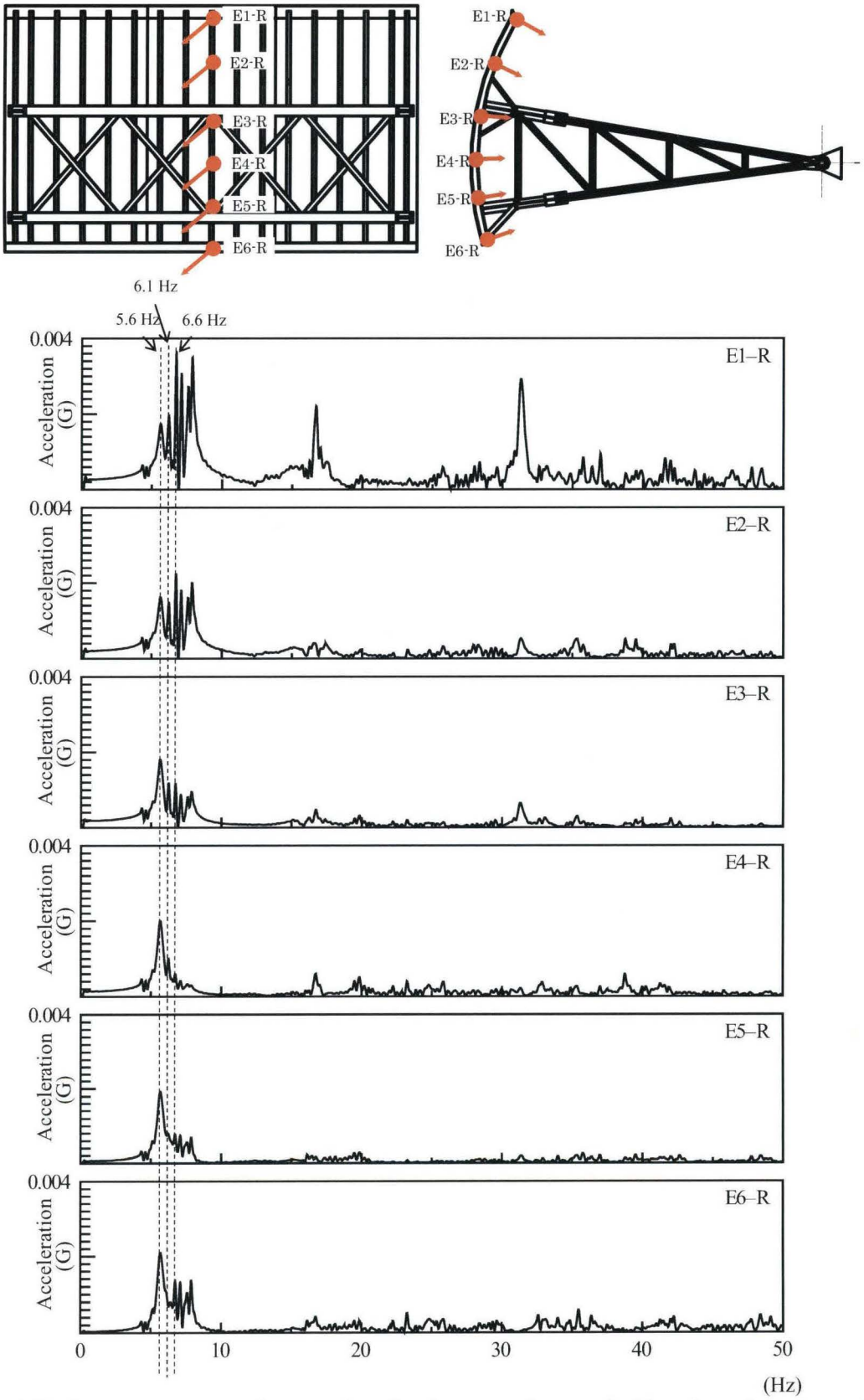

Figure 5.8(b): Frequency spectra of streamwise vibrations at various vertical locations along the centerline of the skinplate. (Test No. 7: steel rod breaking, d = 6 mm)

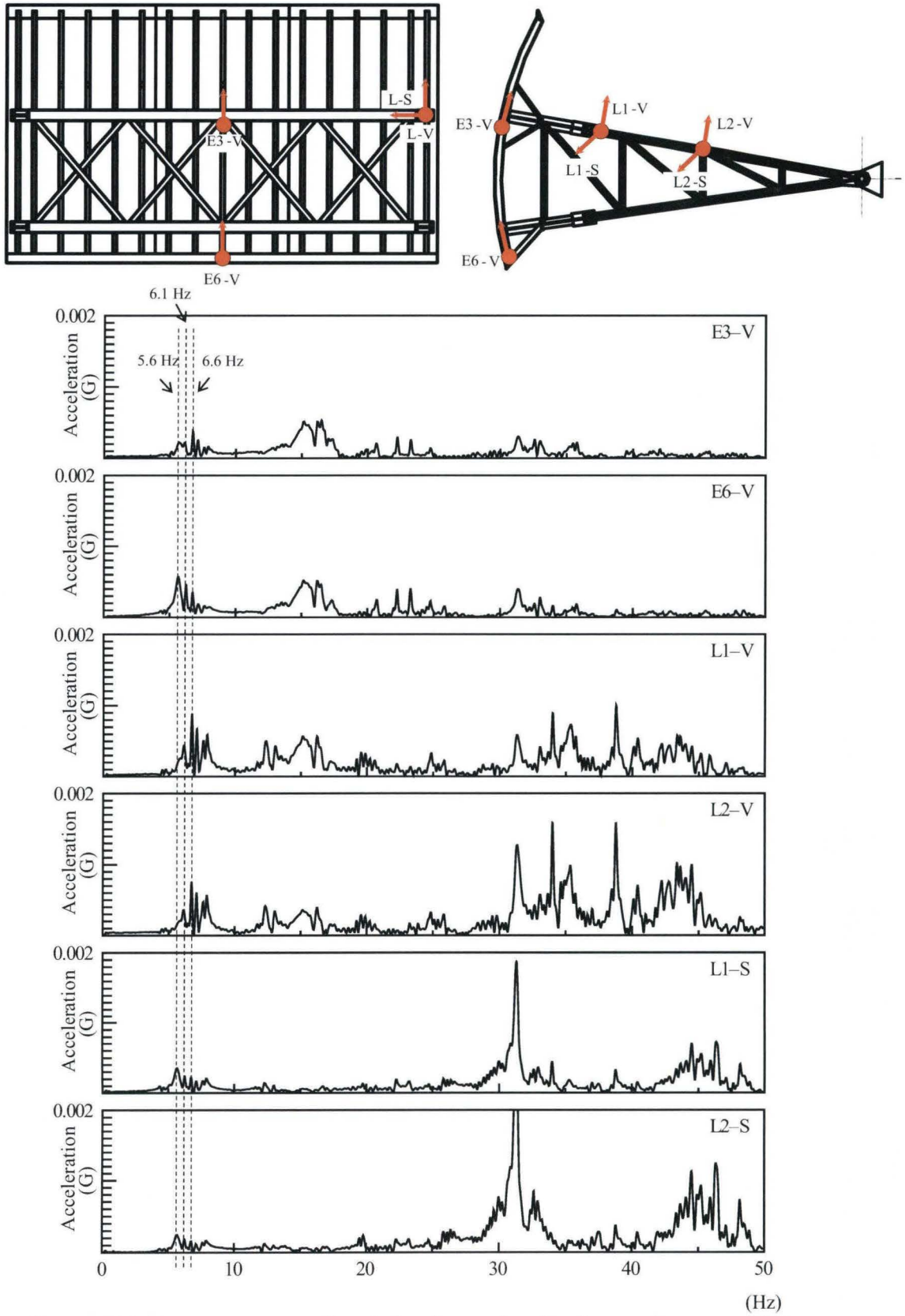

Figure 5.8(c): Frequency spectra of vertical and spanwise vibrations on the upper radial arm. (Test No. 7: steel rod breaking, d = 6 mm)

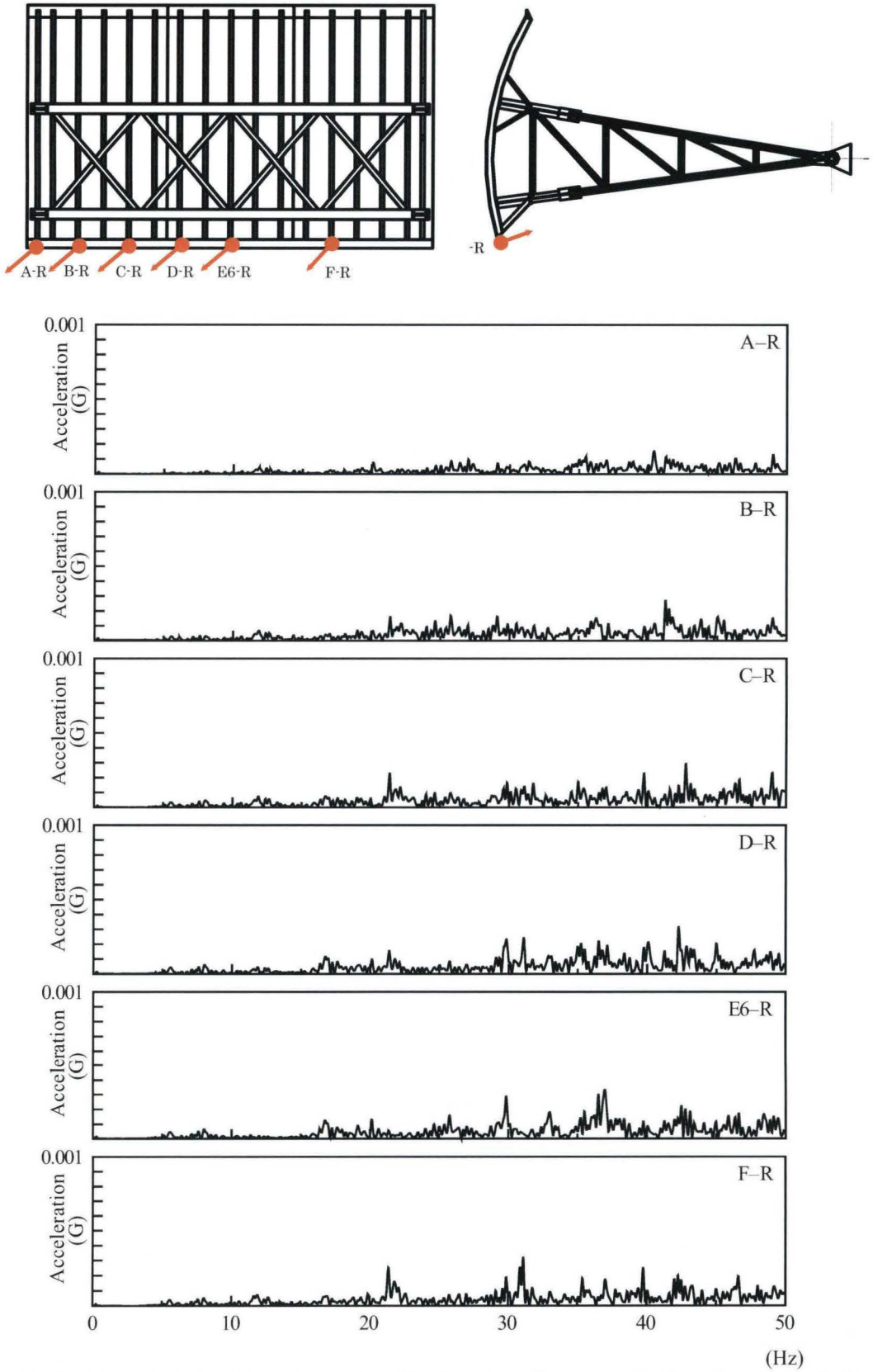

Figure 5.9(a): Frequency spectra of streamwise vibrations at various spanwise locations along the bottom of the skinplate. (Test No. 8: ambient, B = 19 mm)

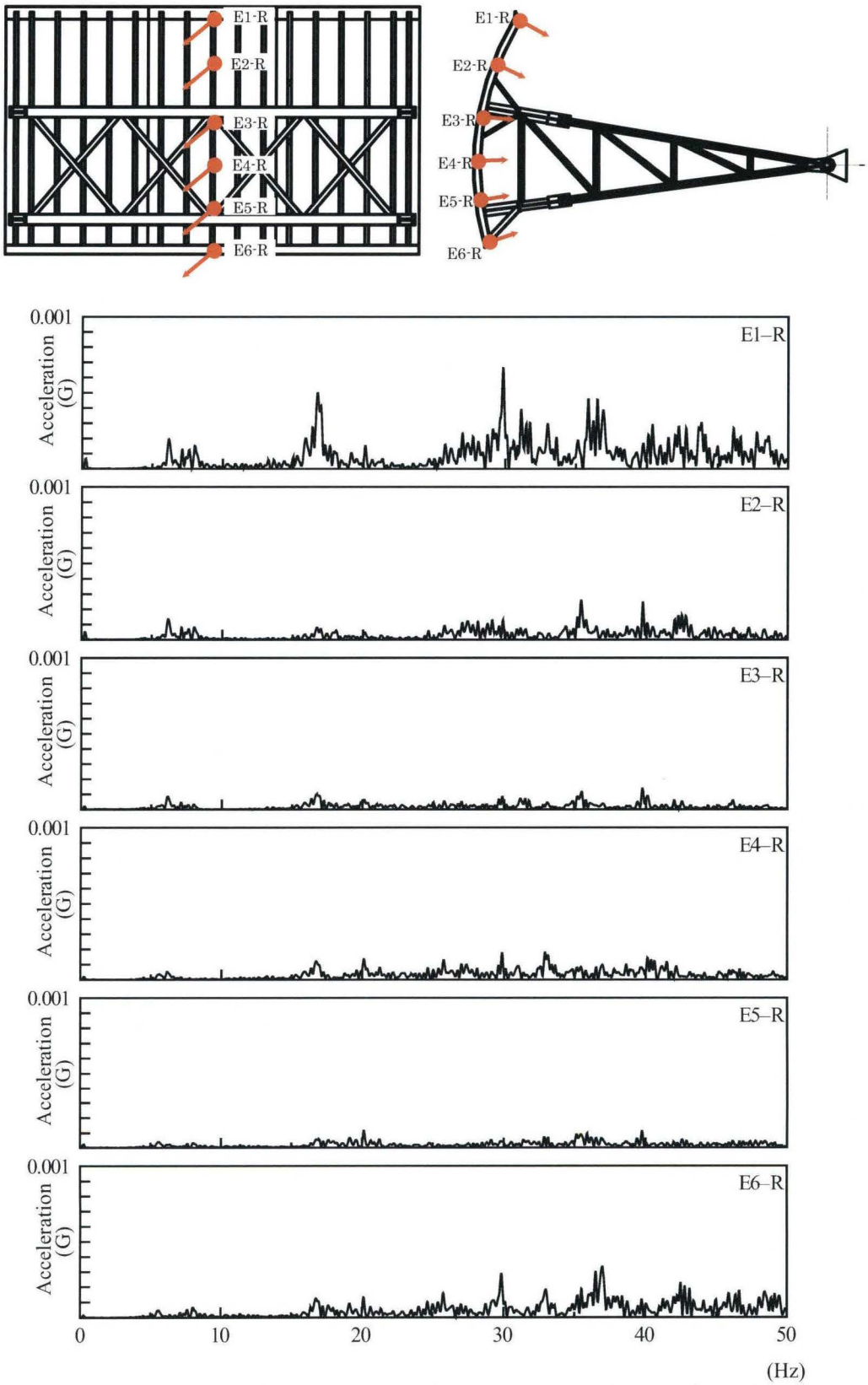

Figure 5.9(b): Frequency spectra of streamwise vibrations at various vertical locations along the centerline of the skinplate. (Test No. 8: ambient, B = 19 mm)

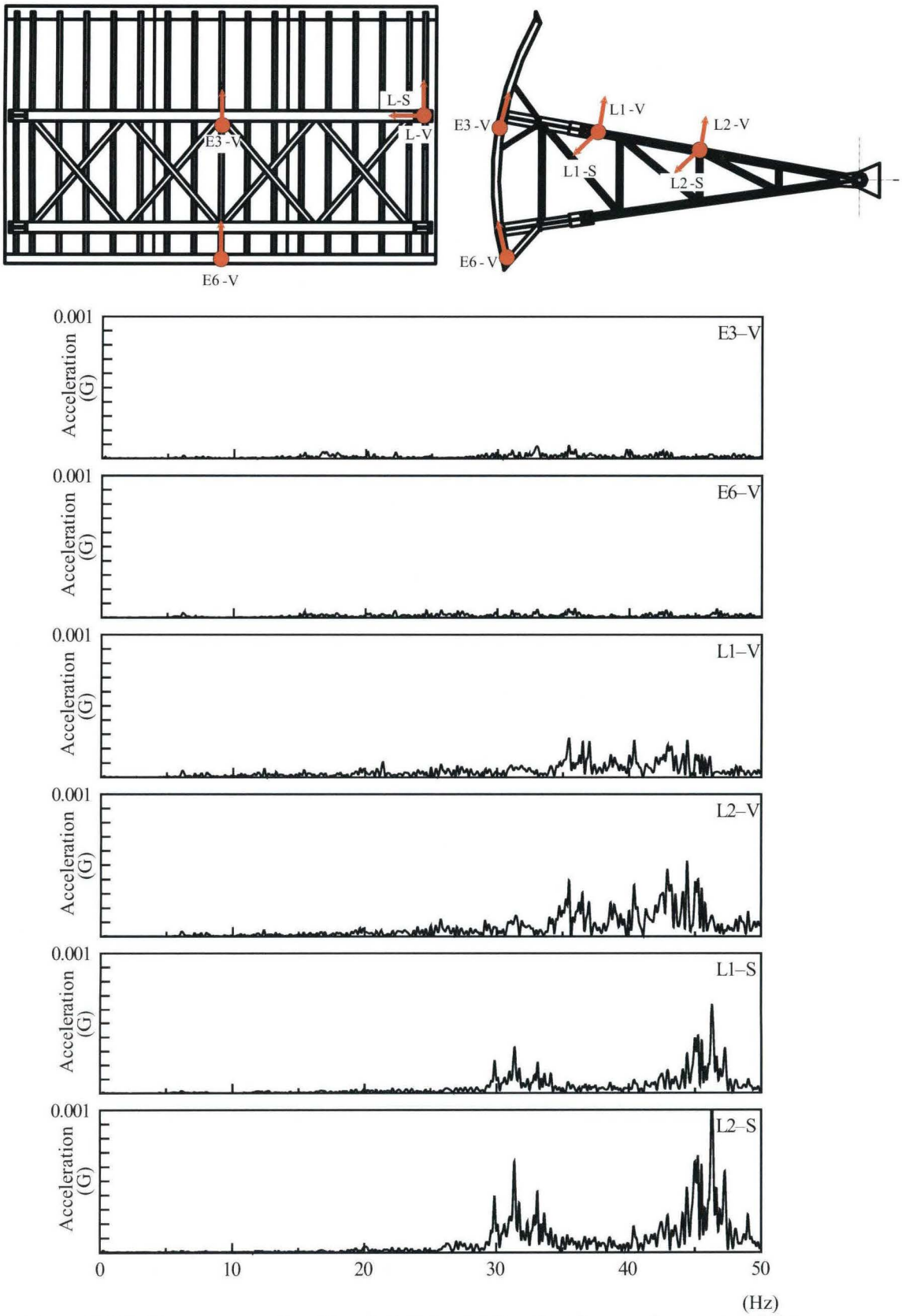

Figure 5.9(c): Frequency spectra of vertical and spanwise vibrations on the upper radial arm. (Test No. 8: ambient, B = 19 mm)

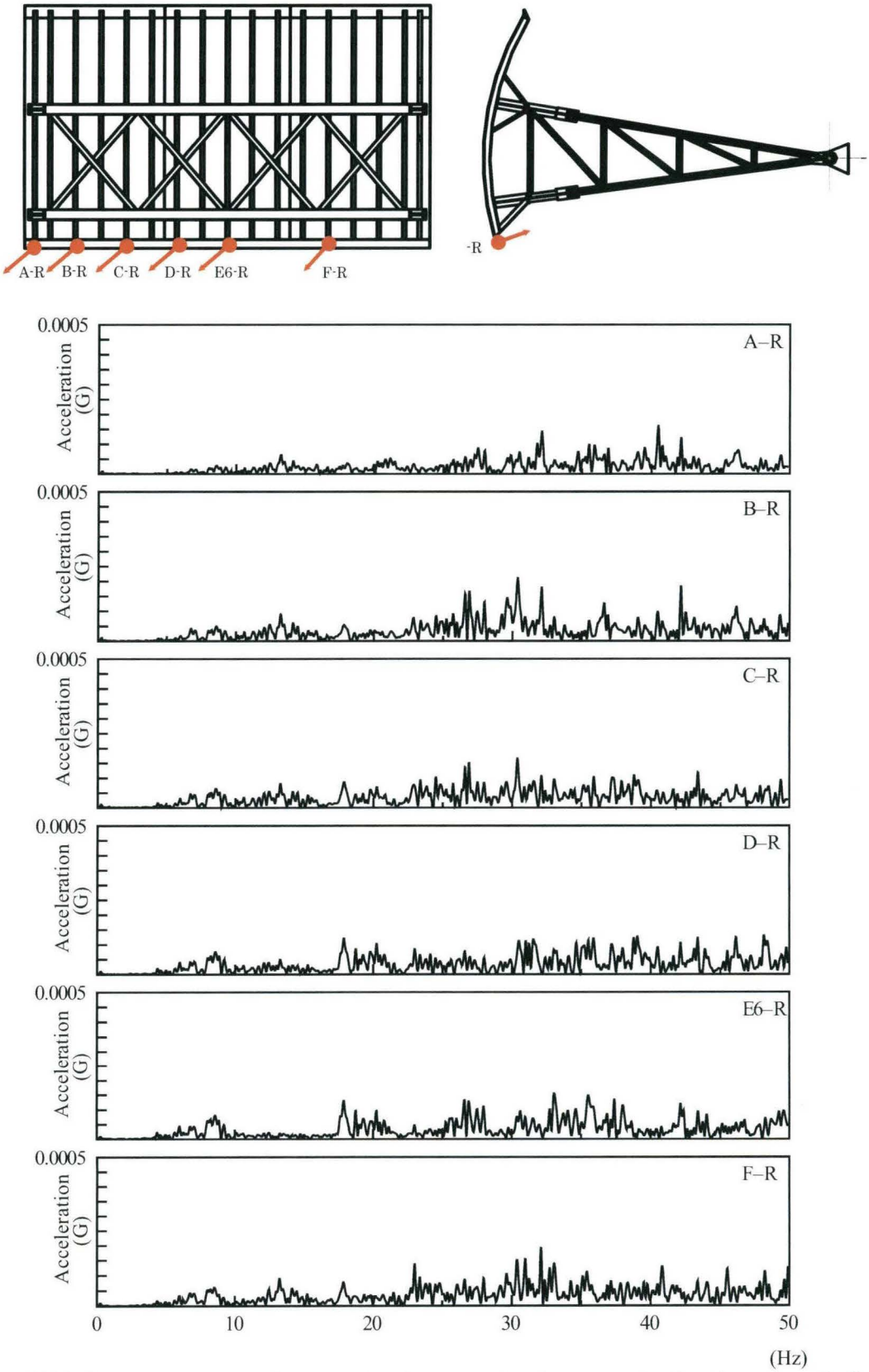

Figure 5.10(a): Frequency spectra of streamwise vibrations at various spanwise locations along the bottom of the skinplate. (Test No. 8: ambient, B = 126 mm)

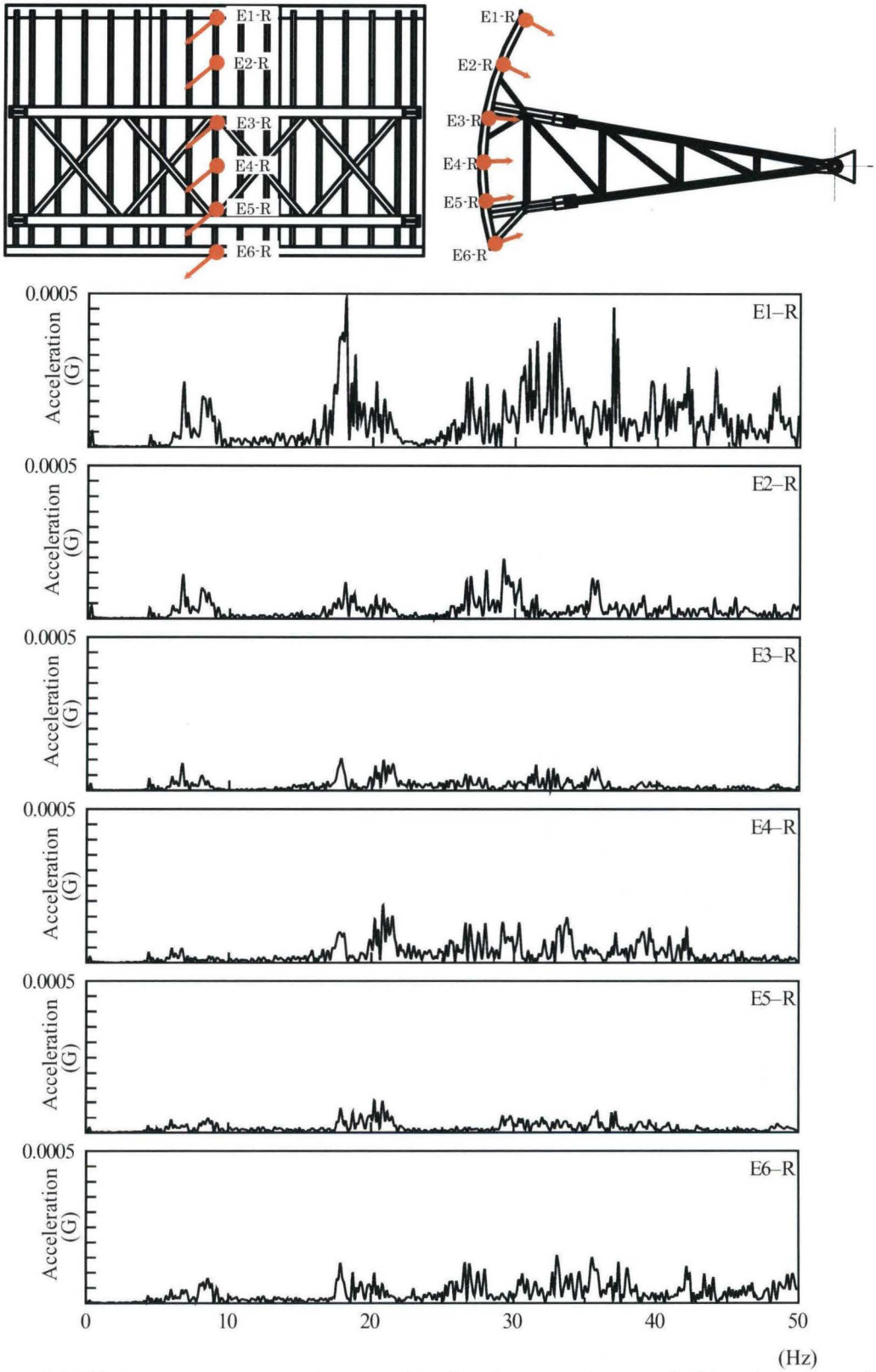

Figure 5.10(b): Frequency spectra of streamwise vibrations at various vertical locations along the centerline of the skinplate. (Test No. 8: ambient, B = 126 mm)

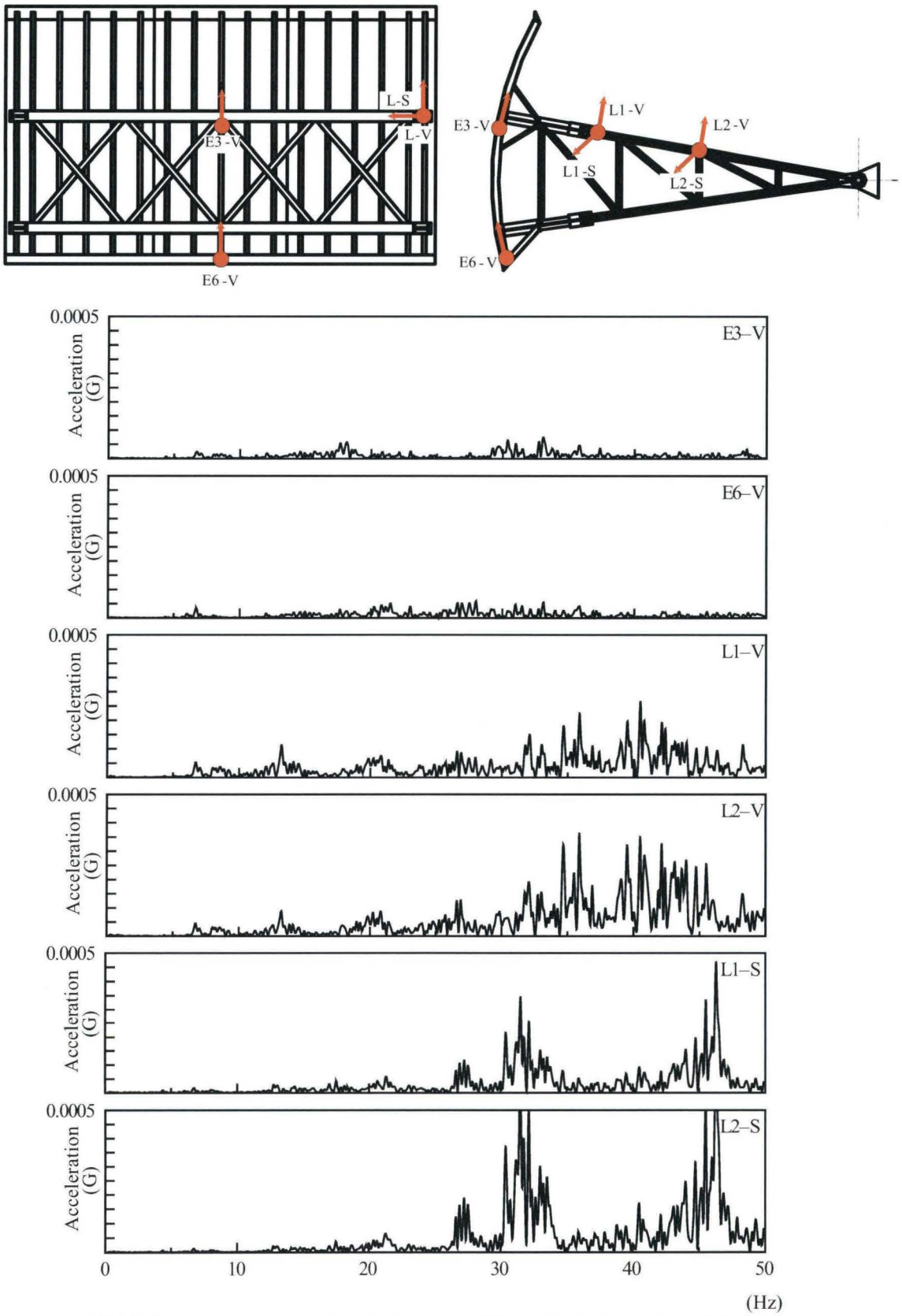

Figure 5.10(c): Frequency spectra of vertical and spanwise vibrations on the upper radial arm. (Test No. 8: ambient, B = 126 mm)

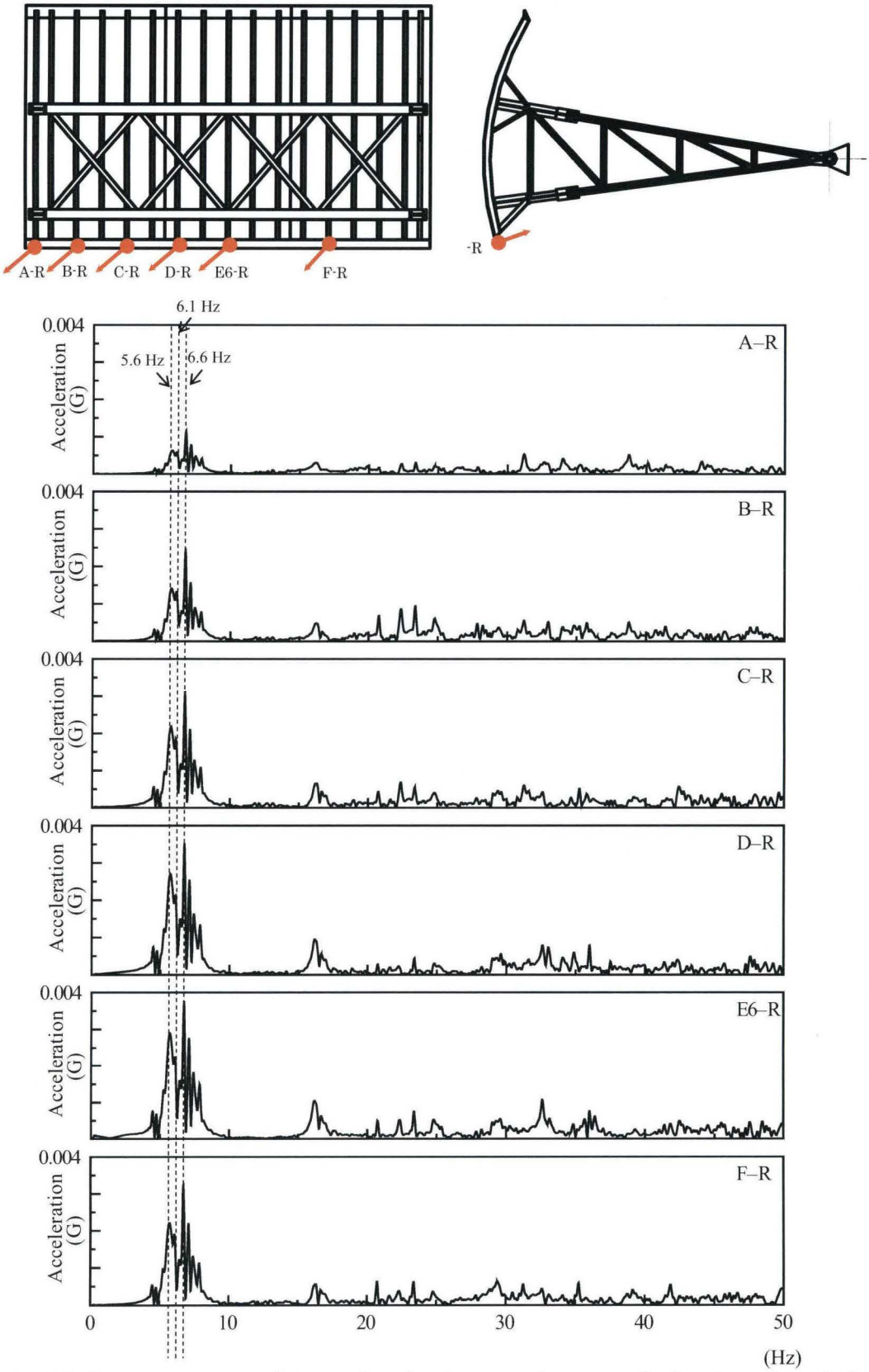

Figure 5.11(a): Frequency spectra of streamwise vibrations at various spanwise locations along the bottom of the skinplate. (Test No. 9: steel rod breaking, d = 8 mm)

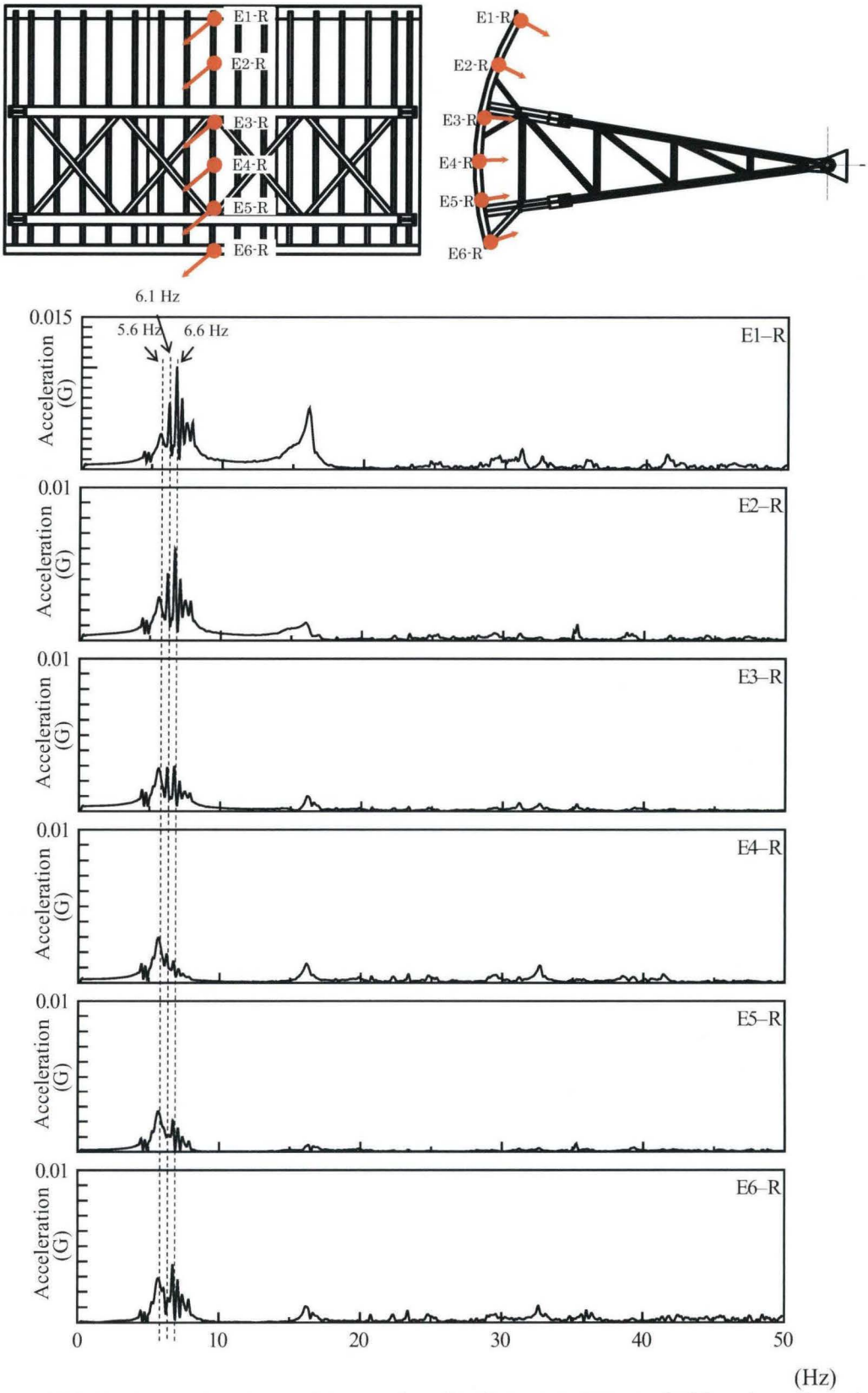

Figure 5.11(b): Frequency spectra of streamwise vibrations at various vertical locations along the centerline of the skinplate. (Test No. 9: steel rod breaking, d = 8 mm)

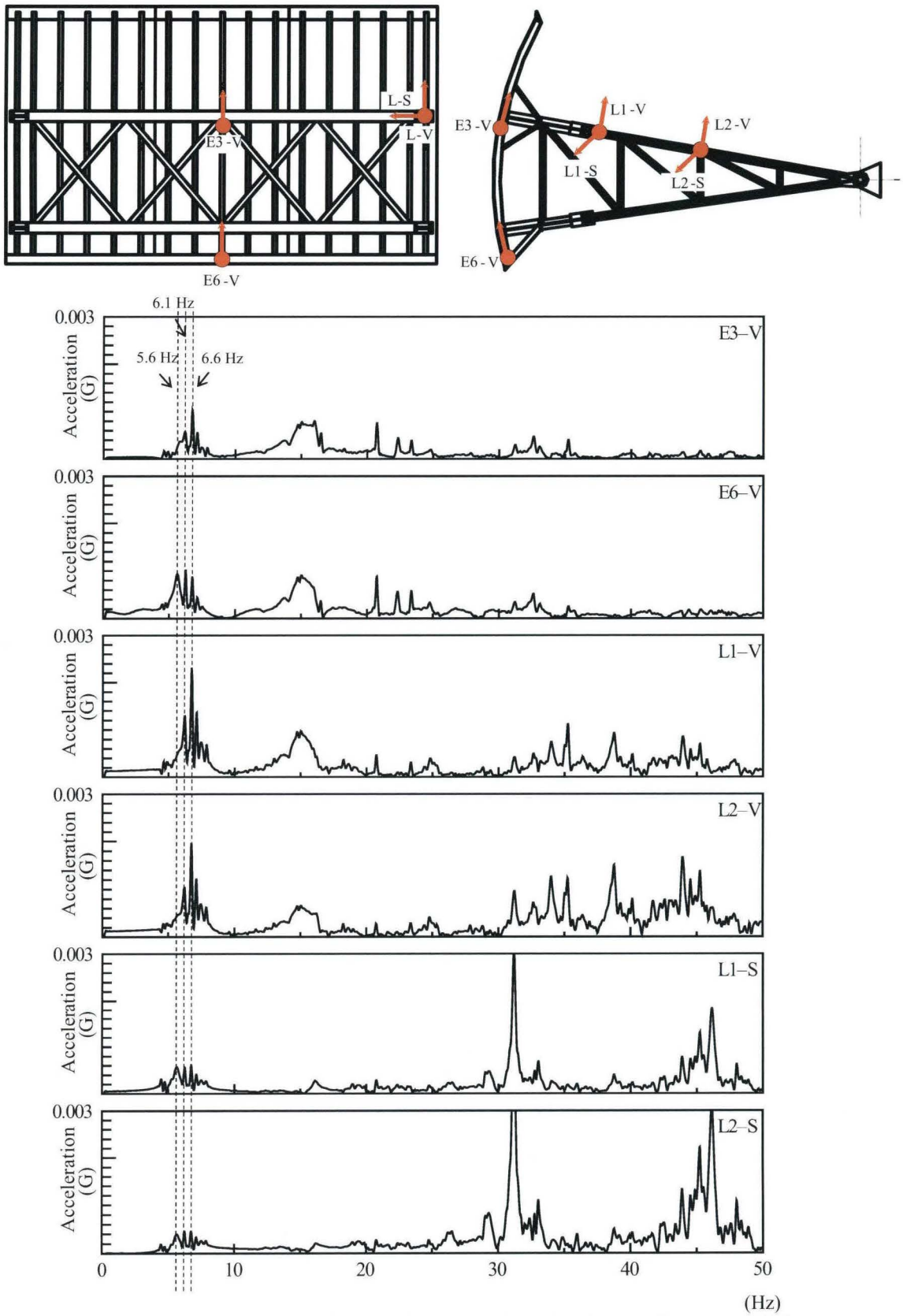

Figure 5.11(c): Frequency spectra of vertical and spanwise vibrations on the upper radial arm. (Test No. 9: steel rod breaking, d = 8 mm)

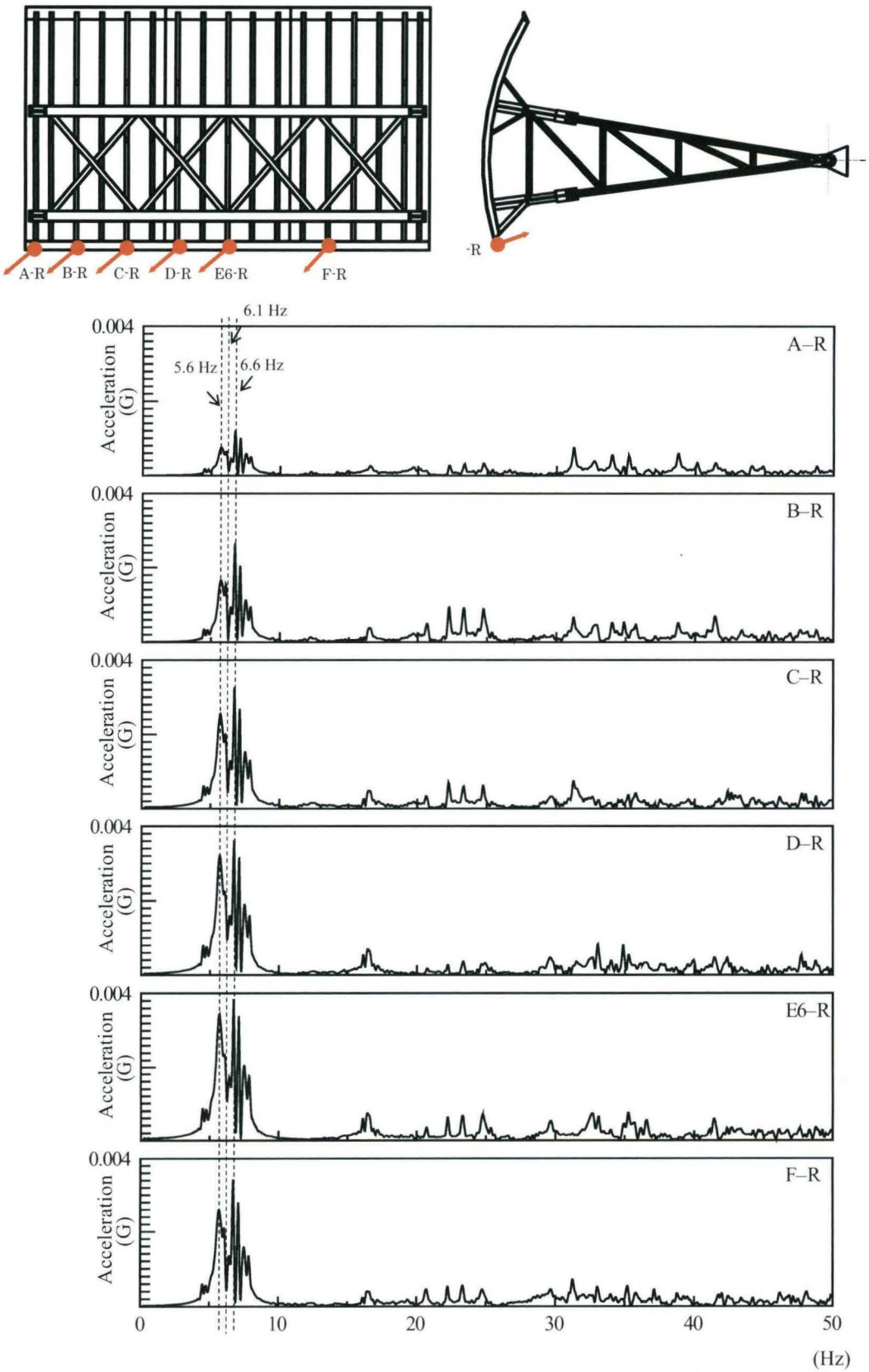

Figure 5.12(a): Frequency spectra of streamwise vibrations at various spanwise locations along the bottom of the skinplate. (Test No. 10: steel rod breaking, d = 8 mm)

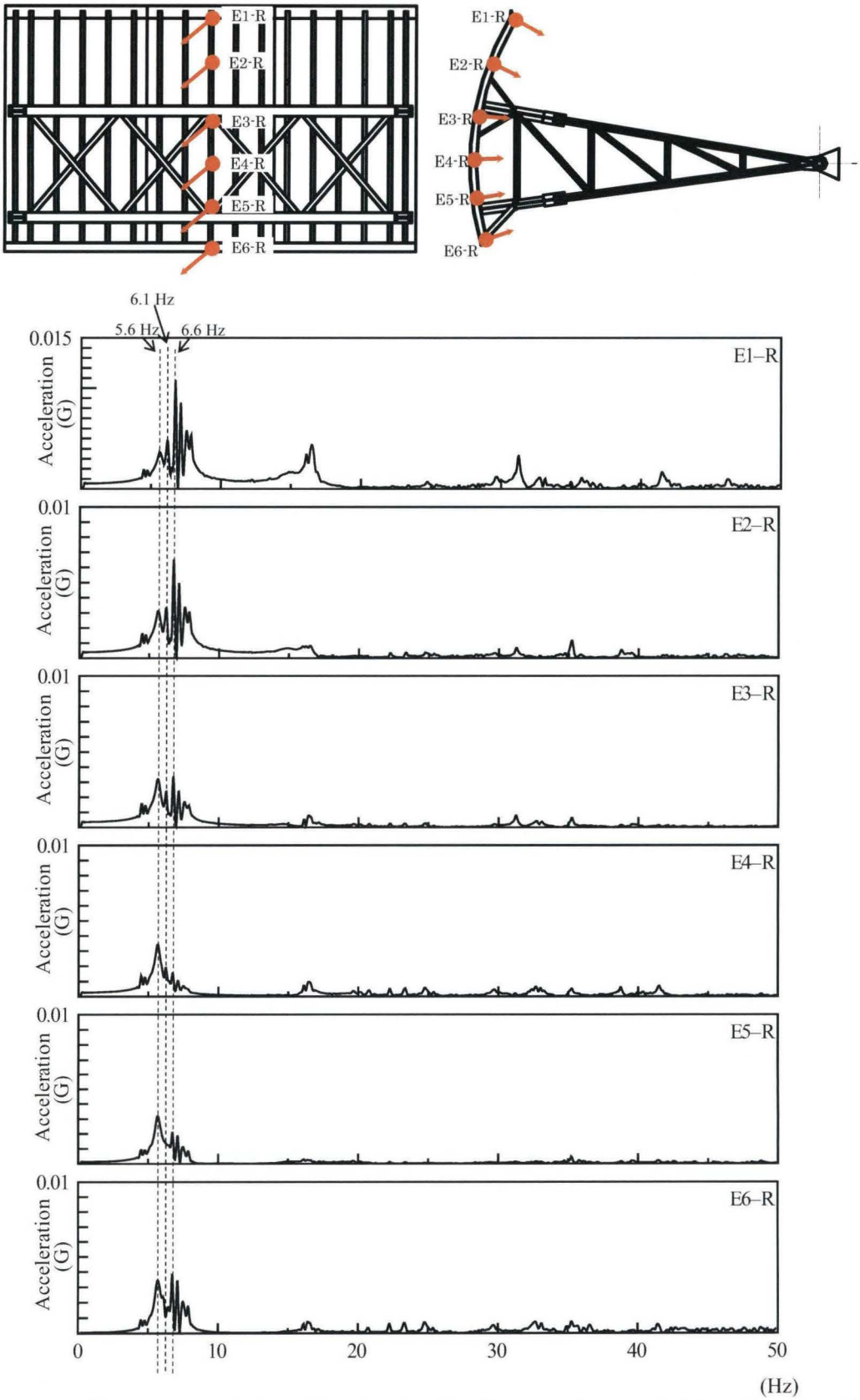

Figure 5.12(b): Frequency spectra of streamwise vibrations at various vertical locations along the centerline of the skinplate. (Test No. 10: steel rod breaking, d = 8 mm)

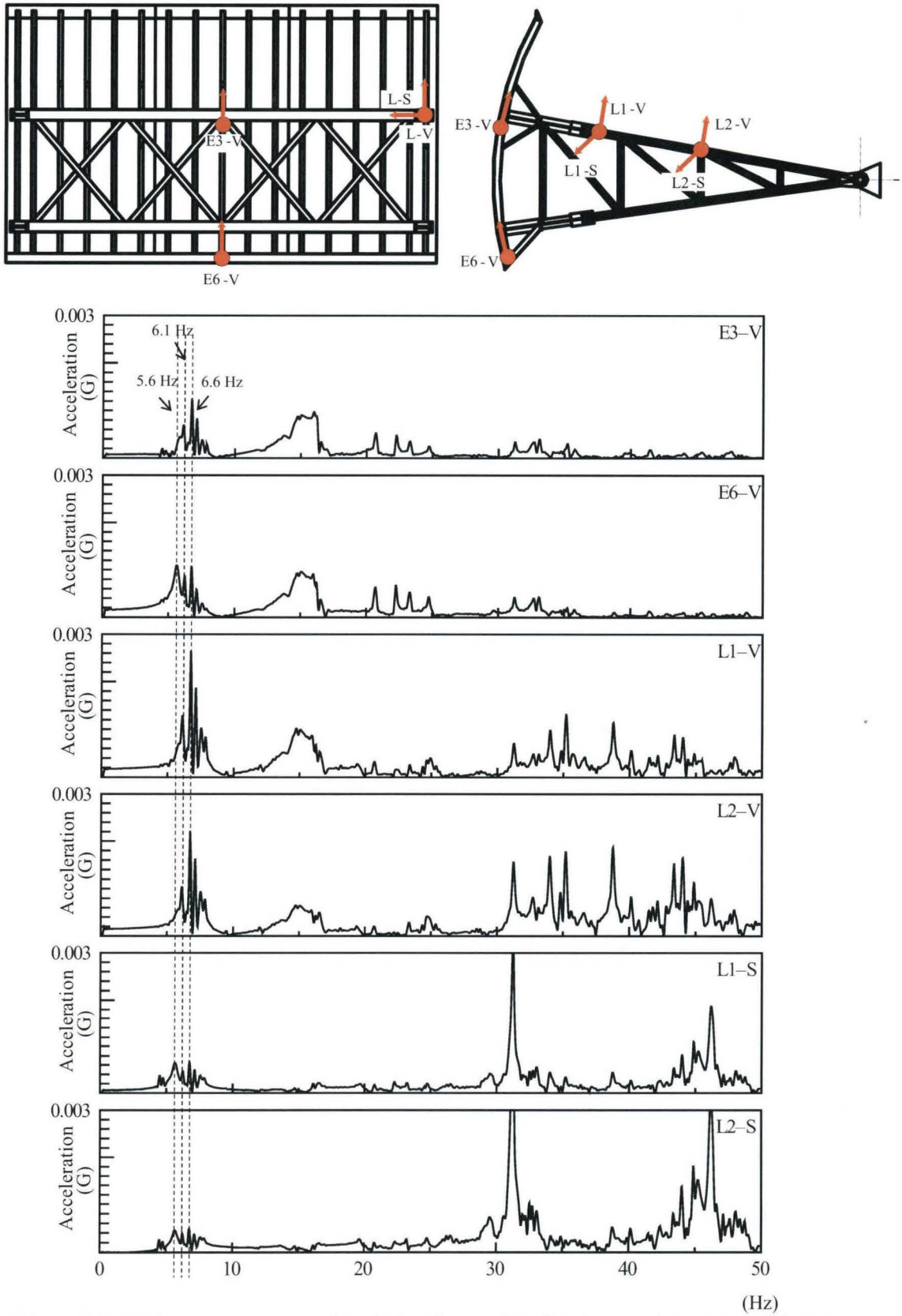

Figure 5.12(c): Frequency spectra of vertical and spanwise vibrations on the upper radial arm. (Test No. 10: steel rod breaking, d = 8 mm)

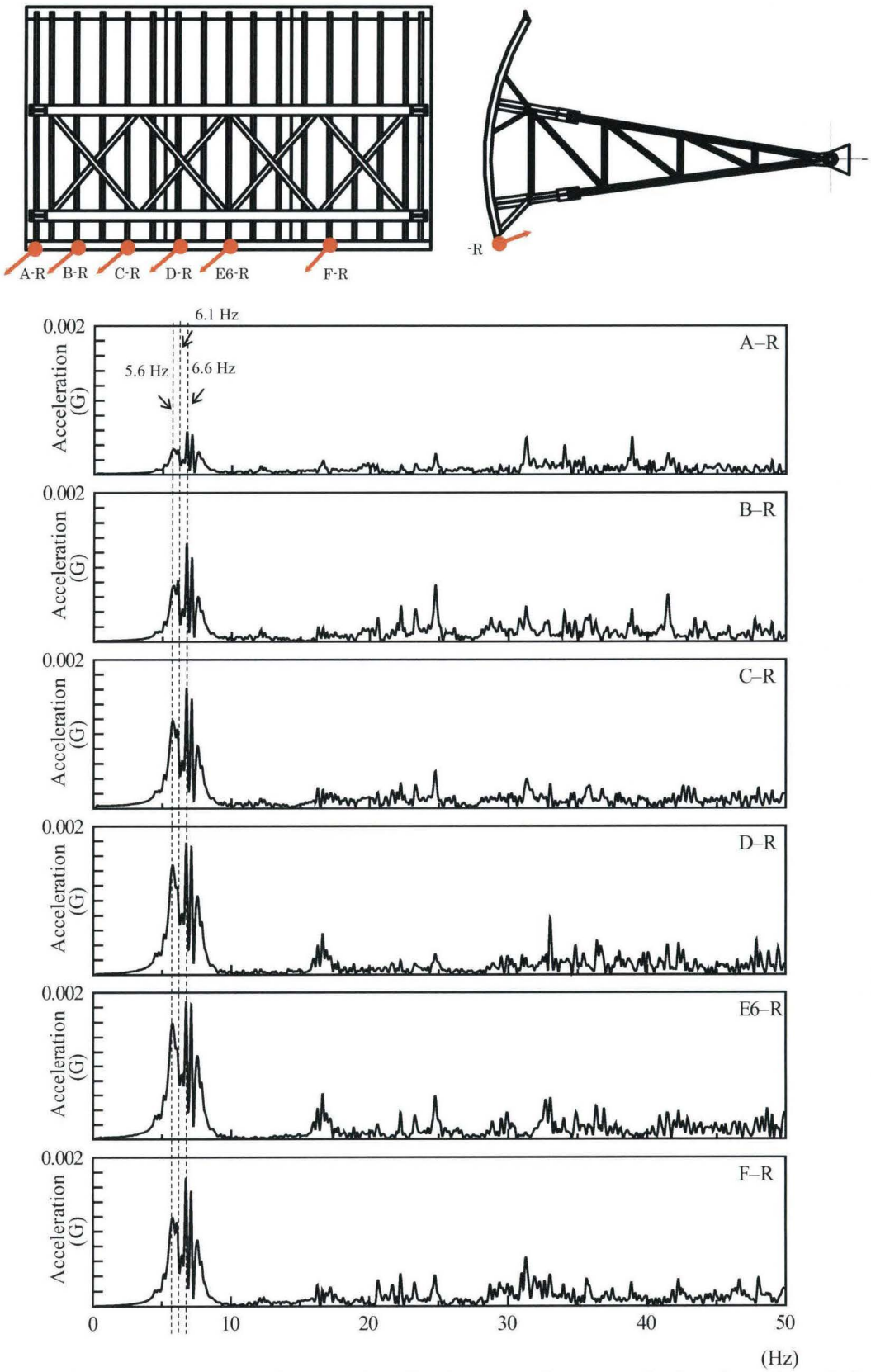

Figure 5.13(a): Frequency spectra of streamwise vibrations at various spanwise locations along the bottom of the skinplate. (Test No. 11: steel rod breaking, d = 6 mm)

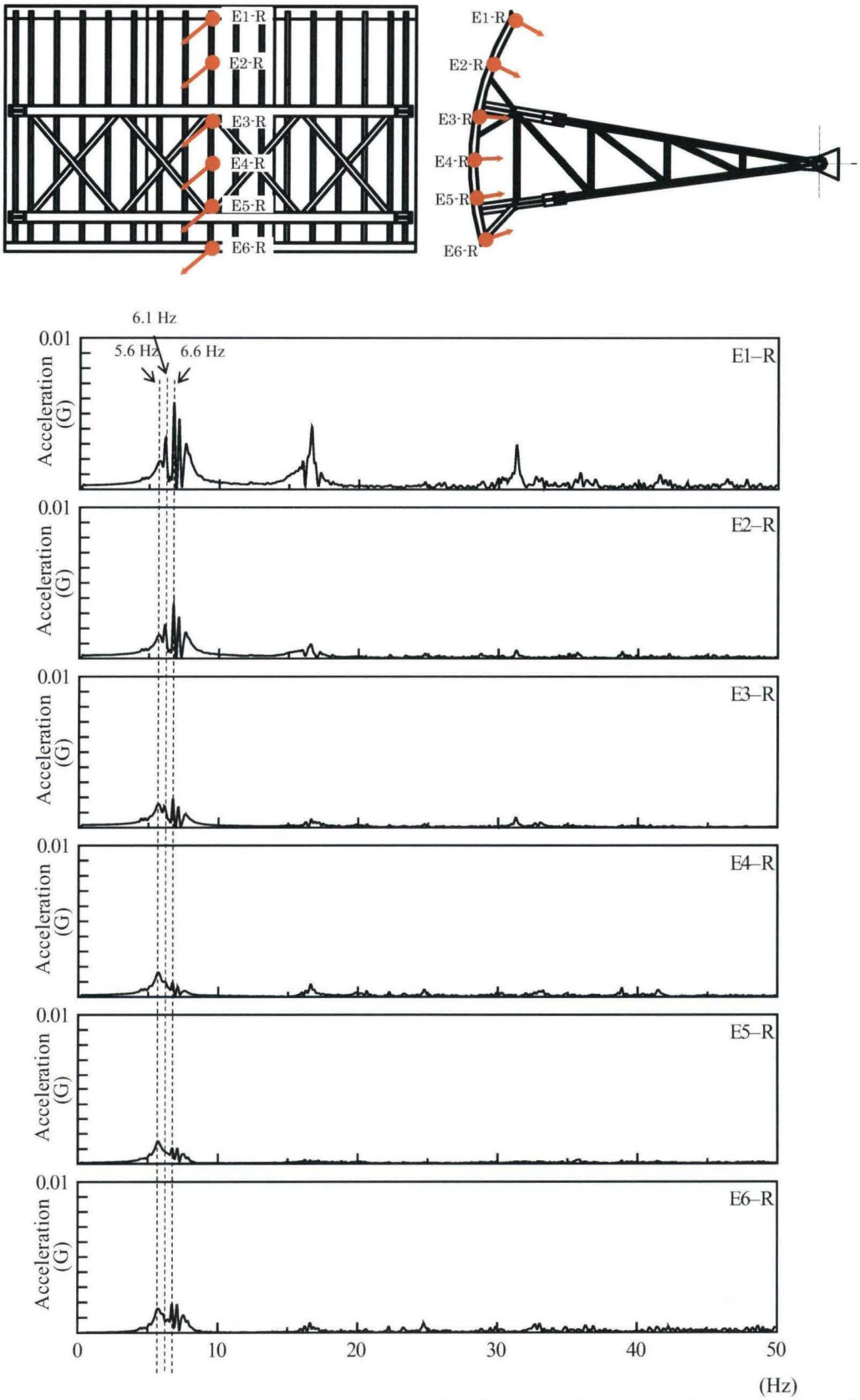

Figure 5.13(b): Frequency spectra of streamwise vibrations at various vertical locations along the centerline of the skinplate. (Test No. 11: steel rod breaking, d = 6 mm)

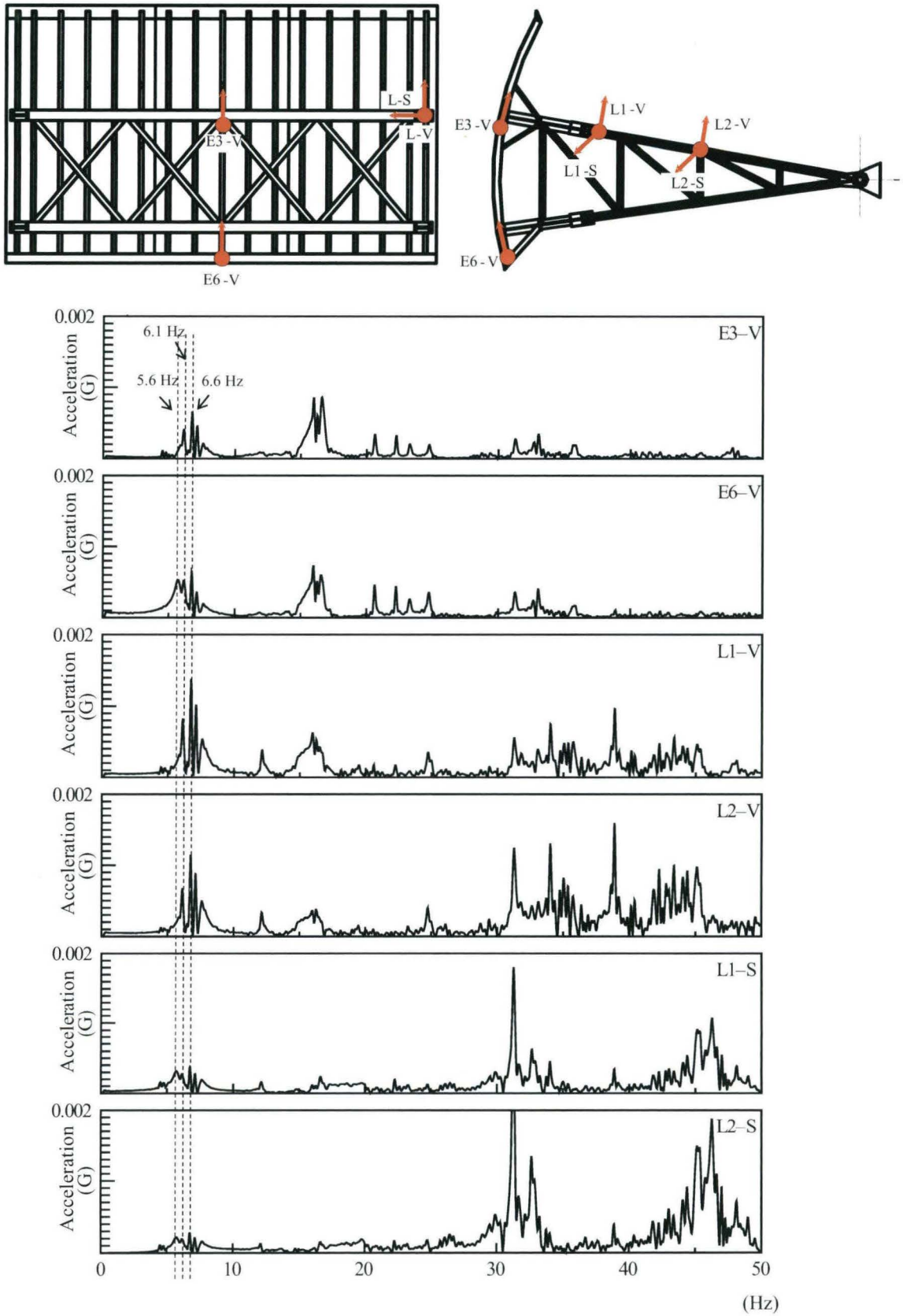

Figure 5.13(c): Frequency spectrum of vertical and spanwise vibrations on the upper radial arm (Test No. 11: steel rod breaking, d = 6 mm)

6. MEASURED IN-WATER NATURAL VIBRATIONS

6.1 Natural Vibration Frequencies

The natural vibrations of the Thermalito Diversion Dam Tainter-gates occur at relatively low frequencies indicated by the sharp peaks in the frequency power spectra, shown in Figures 5.3 to 5.8 and in 5.11 to 5.13. The values for these frequencies are listed in Table 6.1. The frequencies of vibration for Gate #2 are 5.5 Hz and 6.5 Hz, while those for Gate #3 are 5.6 Hz, 6.1 Hz and 6.6 Hz, all of which are quite significant when considering "movement-induced self-excitation."

In the following sections, consideration will be given to the determination of the corresponding mode shapes, rough illustrations of which are also shown in Table 6.1.

Table 6.1: Natural Vibration Frequencies and its mode illustrations.

Mode Name	#2 Gate	#3 Gate	Vibration Mode
M_{x1}	5.5 Hz	5.6 Hz	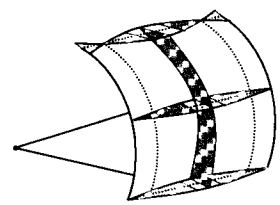
	-	6.1 Hz	Streamwise parallel vib. of skinplate.
M_z	6.5 Hz	6.6 Hz	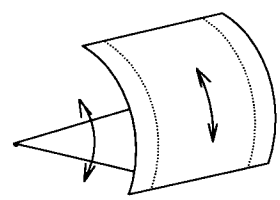 Whole gate vib. around trunnion pin
M_{x2}	6.5 Hz	6.6 Hz	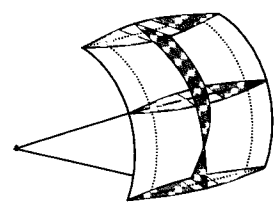 Rotational bending vib. of skinplate.

6.2 Amplitude and Phase-lag

In order to identify precisely the mode of natural vibrations, it is necessary to analyze spatial distributions of the amplitude and phase-lag of the damped vibratory response to the impulsive input provided by the breaking of the steel rod. The amplitude can be determined by dividing the spectral peak value at the frequency of interest by the square of corresponding frequency. The phase-lag results from the Fourier analysis of the response signal and is output by the DADiSP/2000 (Astrodesign) software. An example of the phase-lag plot was previously shown in the bottom right of Figure 4.1. The phase-lag represents the delay from the starting time of data sampling.

Representative calculations are presented for the data from Test 6 for Gate #2 and Test 10 for Gate #3. In both of these tests, 8 mm diameter steel rods (the largest diameter used at the Thermalito site) were employed. The results of the two sets of sample calculations are given in Tables 6.2 and 6.3, respectively. In these calculations, the displacement amplitude and the phase-lag $\Delta\phi$ are relative to those of the vibration at location E6-V (vertical vibration at the bottom center of the skinplate). The data shaded in blue are for streamwise (also denoted as radial) vibrations, while those shaded in yellow are for vertical (also denoted tangential) vibrations and the pink-shaded data are for spanwise vibrations.

Significant features of the phase-lag data for Gate #2 in Table 6.2 can be summarized as follows:

(1) For the 5.5 Hz spectral peaks, all radial vibrations have approximately the same phase difference, ranging between 0 and -40°, except at locations E1-R and E2-R.

(2) For the 5.5 Hz spectral peaks, the tangential vibrations of E6-V and E3-V have a large 97° phase difference.

(3) For the 6.5 Hz spectral peaks, the tangential vibrations of E3-V, E6-V, L1-V and L2-V all have about the same phase difference ranging between 0 and 30°.

(4) For the 6.5 Hz spectral peaks, the radial vibrations of E5-R, E6-R and A-R to D-R have about the same phase difference ranging between 210° and 240°, while the radial vibrations from E1-R to E4-R have about a -9° to 14° phase difference, approximately 180° out of phase with the other locations.

Significant features of the phase-lag data for Gate #3 in Table 6.3 can be summarized as follows:

(1) For the 5.6 Hz and 6.1 Hz spectral peaks, the phase-lag features are quite similar to those for the 5.5 Hz peaks for Gate #2.

(2) For the 6.6 Hz spectral peaks, the phase-lag features are quite similar to those for the 6.5 Hz peaks for Gate #2.

Table 6.2: Peak amplitude and phase-lag in Test 6 with d = 8 mm for Gate #2.

	5.5 Hz			
	Peak level		Phase-lag ϕ (deg)	Phase difference $\Delta\phi$ (deg)
	Acceleration (G)	Displacement (μm)		
E1-R	0.0055	43.5	-43	12
E2-R	0.0044	35.0	-47	8
E3-R	0.0038	29.8	-56	-1
E3-V	0.0003	2.2	42	97
E4-R	0.0036	28.7	-64	-10
E5-R	0.0031	24.3	-73	-18
E6-R	0.0030	23.6	-80	-25
E6-V	0.0013	10.3	-55	0
A-R	0.0005	4.0	-96	-41
B-R	0.0013	9.9	-89	-34
C-R	0.0021	16.6	-84	-29
D-R	0.0027	21.6	-82	-28
F-R				
L1-V	0.0006	4.9	-7	48
L2-V	0.0006	4.5	-16	39
L1-S	0.0006	5.0	122	177
L2-S	0.0004	3.4	117	172

	6.5 Hz			
	Peak level		Phase-lag ϕ (deg)	Phase difference $\Delta\phi$ (deg)
	Acceleration (G)	Displacement (μm)		
E1-R	0.0117	67.0	-138	14
E2-R	0.0076	43.5	-140	12
E3-R	0.0035	19.9	-153	-1
E3-V	0.0011	6.2	-122	30
E4-R	0.0016	8.9	-161	-9
E5-R	0.0020	11.6	89	241
E6-R	0.0039	22.4	68	220
E6-V	0.0009	5.4	-152	0
A-R	0.0013	7.6	59	210
B-R	0.0027	15.4	61	213
C-R	0.0033	19.1	65	217
D-R	0.0037	21.2	68	220
F-R				
L1-V	0.0022	12.8	-128	24
L2-V	0.0019	10.9	-130	22
L1-S	0.0006	3.6	26	178
L2-S	0.0006	3.1	24	176

Table 6.3 (a): Peak amplitude and phase-lag in Test 10 with d = 8 mm for Gate #3.

	5.6 Hz			
	Peak level		Phase-lag ϕ (deg)	Phase difference $\Delta\phi$ (deg)
	Acceleration (G)	Displacement (μm)		
E1-R	0.0033	26.3	-40	25
E2-R	0.0028	22.1	-52	14
E3-R	0.0029	23.0	-66	-1
E3-V	0.0004	3.3	55	120
E4-R	0.0032	25.1	-78	-12
E5-R	0.0031	24.3	-87	-22
E6-R	0.0034	26.7	-94	-29
E6-V	0.0010	7.7	-65	0
A-R	0.0007	5.9	-101	-35
B-R	0.0016	13.0	-100	-35
C-R	0.0025	19.9	-96	-31
D-R	0.0031	24.9	-95	-29
F-R	0.0026	20.3	-96	-31
L1-V	0.0006	5.0	19	84
L2-V	0.0005	4.1	9	75
L1-S	0.0006	4.7	111	176
L2-S	0.0004	3.4	105	170

	6.1 Hz			
	Peak level		Phase-lag ϕ (deg)	Phase difference $\Delta\phi$ (deg)
	Acceleration (G)	Displacement (μm)		
E1-R	0.0042	24.1	-148	4
E2-R	0.0031	18.0	-147	5
E3-R	0.0024	13.4	-145	6
E3-V	0.0002	1.4	-170	-19
E4-R	0.0019	10.8	-145	7
E5-R	0.0014	8.0	-148	4
E6-R	0.0011	6.4	-150	2
E6-V	0.0009	4.9	-152	0
A-R	0.0001	0.8	-152	0
B-R	0.0001	0.8	-127	25
C-R	0.0005	2.8	-143	9
D-R	0.0010	5.7	-149	2
F-R	0.0005	2.7	-142	10
L1-V	0.0007	3.9	-155	-3
L2-V	0.0006	3.2	-151	1
L1-S	0.0005	2.7	34	186
L2-S	0.0004	2.2	32	183

(continued)

Table 6.3 (b): Peak amplitude and phase-lag in Test 10 with d = 8 mm for Gate #3.

	6.6 Hz			
	Peak level		Phase-lag ϕ (deg)	Phase difference $\Delta\phi$ (deg)
	Acceleration (G)	Displacement (μm)		
E1-R	0.0108	61.5	-43	13
E2-R	0.0065	37.2	-46	10
E3-R	0.0033	19.0	-59	-3
E3-V	0.0012	7.1	-29	28
E4-R	0.0015	8.7	-106	-50
E5-R	0.0020	11.7	177	233
E6-R	0.0038	21.6	165	221
E6-V	0.0011	6.1	-56	0
A-R	0.0012	6.8	157	213
B-R	0.0026	14.9	158	214
C-R	0.0032	18.5	161	218
D-R	0.0036	20.4	164	221
F-R	0.0034	19.3	162	218
L1-V	0.0027	15.2	-35	22
L2-V	0.0022	12.6	-36	20
L1-S	0.0007	3.7	117	174
L2-S	0.0005	2.7	112	168

6.3 Vibration Modes

With the amplitude and phase difference data from Tables 6.2 and 6.3, mode animations of the in-water natural vibrations can be simulated using a simple BASIC program, into which the measurement locations and the (tangential and radial) directions of vibratory accelerations were input. Figure 6.1 shows the measurement locations in the computer graphics coordinates.

A simulated mode shape for the 5.5 Hz vibration of Gate #2 is shown in Figure 6.2. Specifically, Figure 6.2(a) shows the two-dimensional vibration trajectories (Lissajous figures) of measurement locations E3 and E6 at the skinplate spanwise center, where both the tangential and radial vibrations were measured. Vibration amplitudes are enlarged for clarity. When the skinplate moves in the downstream direction, the whole gate also moves downward, exhibiting known characteristics of a press-shut device which has a dangerously high likelihood of susceptibility to "movement-induced self-excitation". The press-shut angle (the inclination angle of the elliptic trajectory) relative to the horizontal line was 10.76°. Point E3 moves only in the radial direction, with no evident tangential vibration, while Point E6 translates in both the radial and tangential directions. This mode shape is derived from the frequency spectra so there is a clear correlation between spectral peaks and modal amplitudes. The mode shape provides a physical picture, explaining the small amplitude of the 5.5 Hz peak in the top figure (E3-V) of Figure 5.7(c) and the fairly large amplitude at the same frequency the second figure (E6-V).

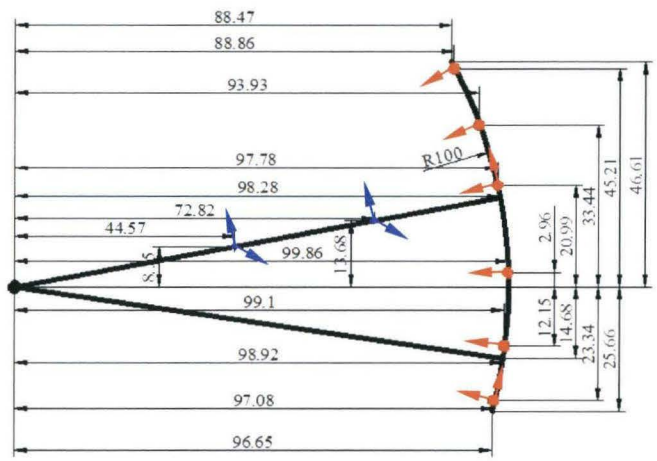

Figure 6.1: Measurement locations and directions.

Figure 6.2(b) portrays the instantaneous vibration shape of the whole skinplate at its maximum amplitude, where the radial vibrations at Points E1, E2, E4 and E5 are have been included. It is quite clear that the whole skinplate performs a streamwise "parallel vibration" in the press-shut direction.

Figure 6.2(c) represents the streamwise vibration of the skinplate bottom line, coupled with the spanwise vibration of upper radial arms. The skinplate performs a half-wavelength ideal bending vibration with nodes at both spanwise sides of the skinplate. Synchronizing with this bending vibration, the radial arms perform a spanwise bending vibration, moving outward when the skinplate moves downstream, and inward when the skinplate moves upstream. It should be noted here that the radial arms had minimal tangential (i.e., vertical) vibration amplitude at 5.5 Hz, as is shown in the Figure 6.2(b).

A simulated mode shape for the 6.5 Hz vibration of Gate #2 is shown in Figure 6.3. Figure 6.3(a) shows the vibration trajectories of Points E3 and E6. It is quite interesting to note here that the two points move exactly out of phase in the radial direction, while, at the same time, moving in-phase in the tangential direction, suggesting a streamwise rotational vibration coupled with a vertical vibration.

Figure 6.3(b) shows the vibration mode of the whole gate, which consists of the skinplate streamwise rotational vibration coupled with the whole gate vibration around the trunnion pin. These two components of the 6.5 Hz vibration are decomposed in Figures 6.3(c) and 6.3(d). Figure 6.3(c) shows only the skinplate streamwise rotational vibration, with the rotation center at a height of 2.03 m from the bottom of the skinplate. Figure 6.3(d) shows only the vertical vibration, that is, the whole gate vibration around the trunnion pin, coupled with the up and down bending vibration of the radial arms.

Finally, Figure 6.3(e) shows the streamwise half-wavelength bending vibration of the skinplate bottom line, coupled with the spanwise vibration of the radial arms, all of which is quite similar to Figure 6.2(c) for the 5.5 Hz parallel vibration mode of the skinplate.

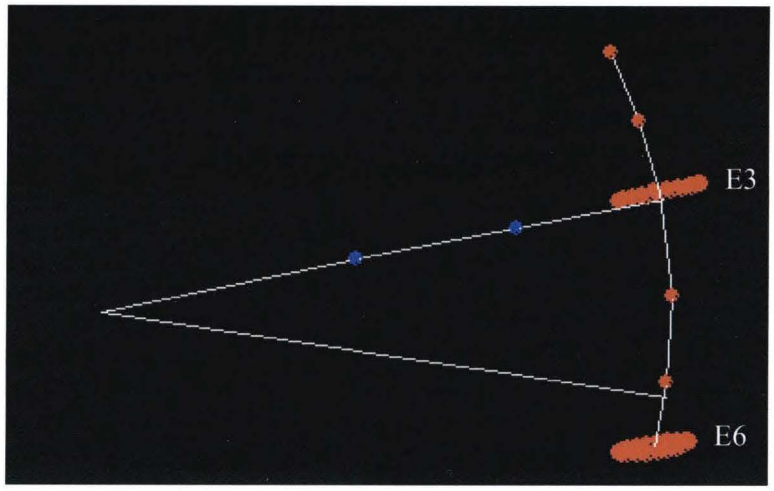

(a) Vibration trajectories of measurement locations E3 and E6 at the skinplate spanwise center.

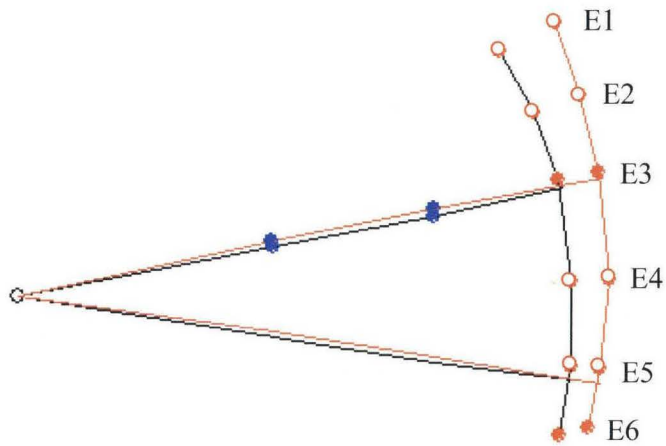

(b) Streamwise parallel vibration mode of the skinplate spanwise center.

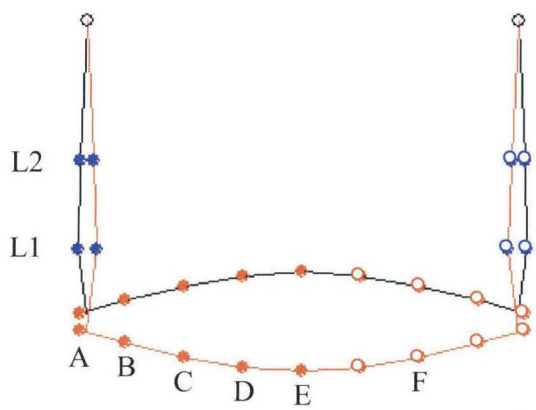

(c) Streamwise half-wavelength bending vibration mode along the skinplate bottom line, coupled with spanwise vibration of the upper radial arm.

Figure 6.2: Vibration mode at 5.5 Hz in-water natural vibration of Gate#2.

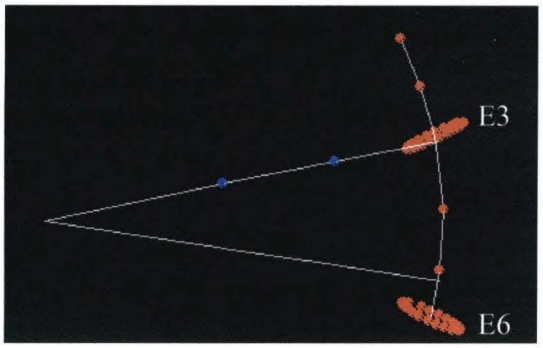

(a) Vibration trajectory.

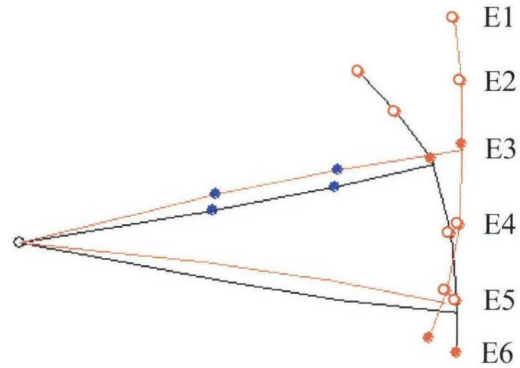

(b) Vibration mode of the skinplate.

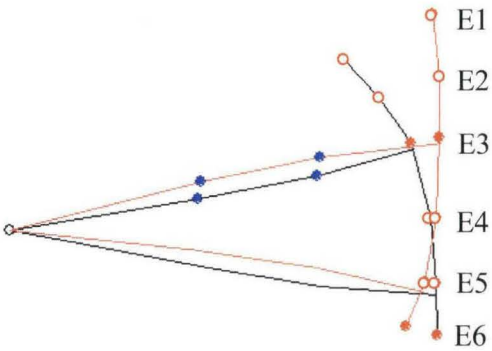

(c) Streamwise vibration mode.

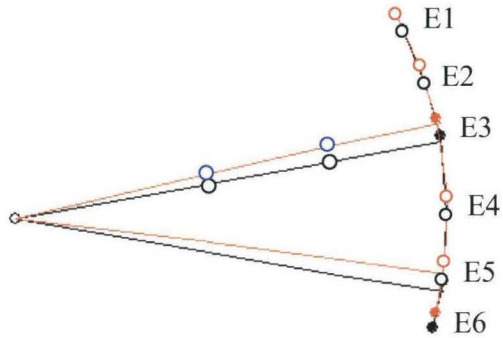

(d) Whole gate vibration mode around the trunnion pin.

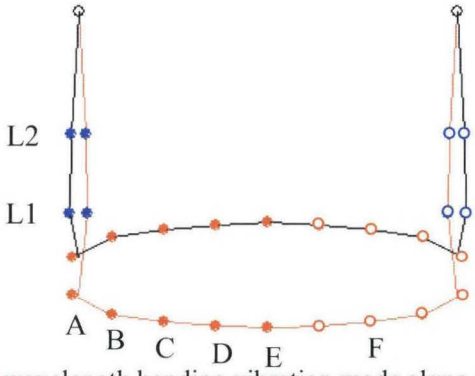

(e) Streamwise half-wavelength bending vibration mode along the skinplate bottom line, coupled with spanwise vibration of upper radial arms.

Figure 6.3: Vibration modes at 6.5 Hz in-water natural vibration of Gate #2.

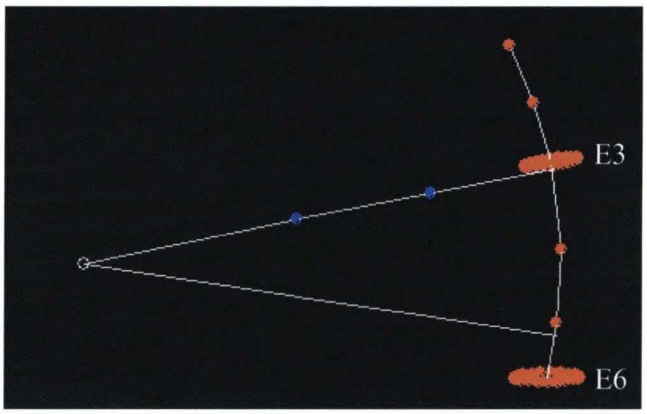

(a) Vibration trajectories of measurement locations E3 and E6 at the skinplate spanwise center.

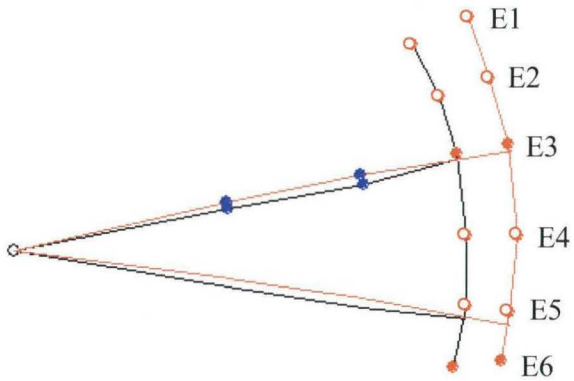

(b) Streamwise parallel vibration mode of the skinplate spanwise center.

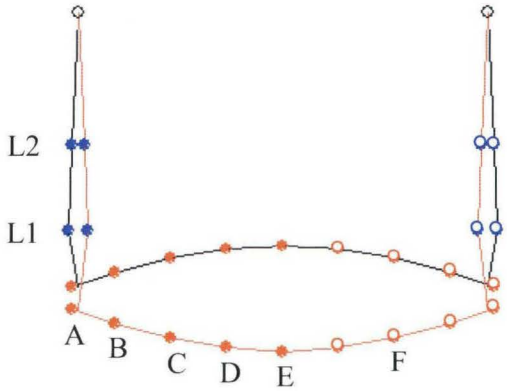

(c) Streamwise half-wavelength bending vibration mode along the skinplate bottom line, coupled with spanwise vibration of radial arm.

Figure 6.4: Vibration mode at 5.6 Hz in-water natural vibration of Gate #3.

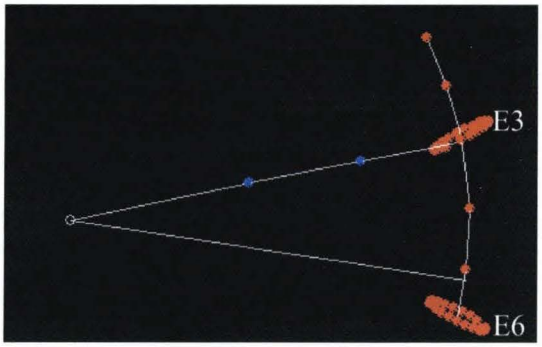

(a) Vibration trajectory.

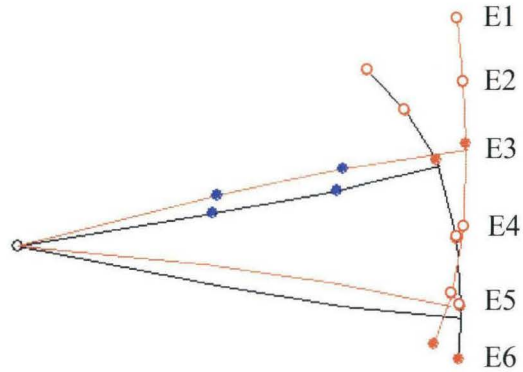

(b) Vibration mode of the skinplate.

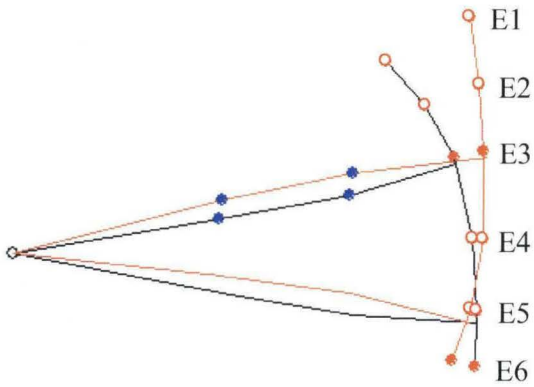

(c) Streamwise vibration mode.

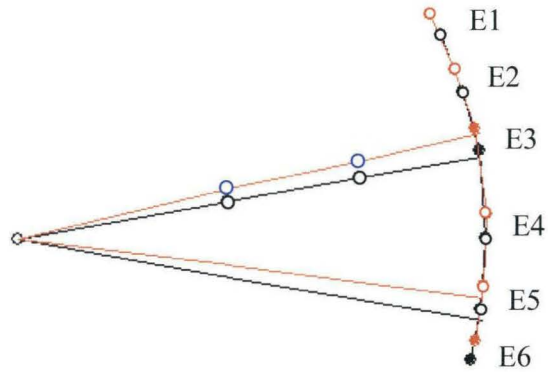

(d) Whole gate vibration mode around the trunnion pin.

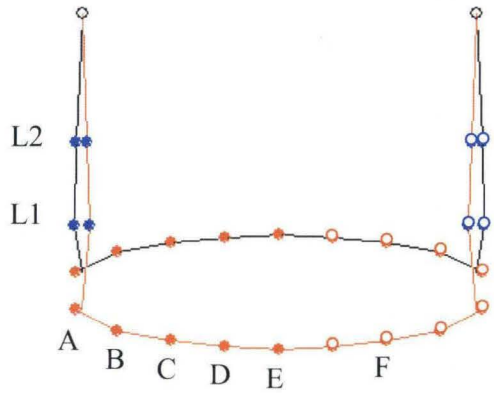

(e) Streamwise half-wavelength bending vibration mode along the skinplate bottom line, coupled with spanwise vibration of radial arm.

Figure 6.5: Vibration modes at 6.6 Hz in-water natural vibration of Gate #3.

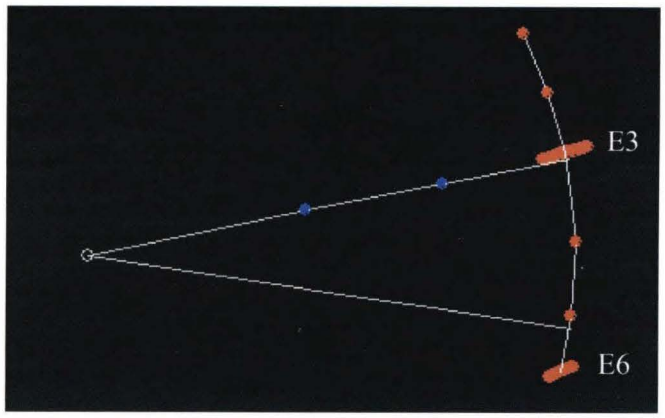

(a) still picture of the animation of vibration trajectory

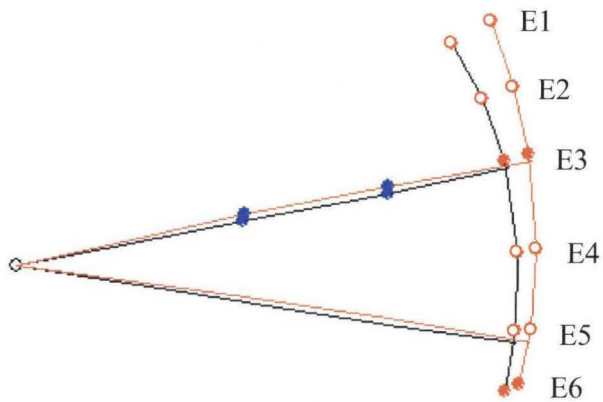

(b) side view of the in-water natural vibration mode

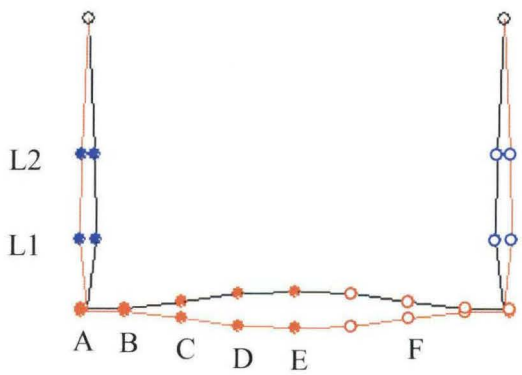

(c) Streamwise full-wavelength bending vibration mode along the skinplate bottom line, coupled with spanwise vibration of radial arm.

Figure 6.6: Vibration modes at 6.1 Hz in-water natural vibration of Gate #3.

6.4 Damping Ratio

The sharpness of the power spectral peaks correlates with the damping ratios of the natural vibrations at the same frequency. The damping ratio can be calculated by the half-power method. Resulting

damping ratio values are listed in Table 6.1 for Gate #2 and in Table 6.2 for Gate #3. For the whole gate vibration around the trunnion pin at 6.5 Hz (or 6.6 Hz) in the vertical direction, calculations were undertaken with the data from points E3-V, E6-V, L1-V and L2-V and are shaded blue. For the skinplate streamwise rotational vibration at 6.5 Hz (or 6.6 Hz) and the skinplate streamwise parallel vibration at 5.5 Hz (or 5.6 Hz), data from points E2-R, E3-R, and E4-R were used and the results are shaded yellow and pink, respectively. In Table 6.2 for Gate #3, additional calculations were made with data from points E2-R, E3-R, and E4-R for the full-wavelength skinplate streamwise parallel vibration at 6.1 Hz and are shaded green.

Table 6.1: Damping ratios of in-water natural vibrations of Gate #2.

Damping ratios for Thermalito Gate #2 Test 3(d = 3 mm)

Vibration (6.5 Hz)				Vibration (5.5 Hz)	
Vertical		Streamwise		Streamwise	
Header	Damping ratio	Header	Damping ratio	Header	Damping ratio
E3-V	0.013	E2-R	0.016	E2-R	0.016
E6-V	0.015	E3-R	0.017	E3-R	0.016
L1-V	0.014	E4-R	-	E4-R	0.017
L2-V	0.015				
Average	0.014	Average	0.017	Average	0.016

Damping ratios for Thermalito Gate #2 Test 4(d = 6 mm)

Vibration (6.5 Hz)				Vibration (5.5 Hz)	
Vertical		Streamwise		Streamwise	
Header	Damping ratio	Header	Damping ratio	Header	Damping ratio
E3-V	0.011	E2-R	0.011	E2-R	0.031
E6-V	0.011	E3-R	0.012	E3-R	0.028
L1-V	0.011	E4-R	-	E4-R	0.028
L2-V	0.011				
Average	0.011	Average	0.012	Average	0.029

Damping ratios for Thermalito Gate #2 Test 5(d = 6 mm)

Vibration (6.5 Hz)				Vibration (5.5 Hz)	
Vertical		Streamwise		Streamwise	
Header	Damping ratio	Header	Damping ratio	Header	Damping ratio
E3-V	0.011	E2-R	0.011	E2-R	0.025
E6-V	0.011	E3-R	0.011	E3-R	0.024
L1-V	0.011	E4-R	-	E4-R	0.025
L2-V	0.011				
Average	0.011	Average	0.011	Average	0.025

Damping ratios for Thermalito Gate #2 Test 6(d = 8 mm)

Vibration (6.5 Hz)				Vibration (5.5 Hz)	
Vertical		Streamwise		Streamwise	
Header	Damping ratio	Header	Damping ratio	Header	Damping ratio
E3-V	0.012	E2-R	0.012	E2-R	0.030
E6-V	0.012	E3-R	0.012	E3-R	0.029
L1-V	0.012	E4-R	-	E4-R	0.030
L2-V	0.012				
Average	0.012	Average	0.012	Average	0.030

The damping ratio for the whole gate vibration around the trunnion pin (6.5 Hz or 6.6 Hz in the vertical direction) takes on a small value between 0.009 and 0.012. In contrast, the damping ratio of the skinplate streamwise parallel vibration (5.5 Hz or 5.6 Hz) takes on a larger value between 0.025 and 0.04. The damping ratio of the full-wavelength skinplate streamwise parallel vibration (6.1 Hz for Gate #3) takes on a smaller value between 0.013 and 0.017.

Table 6.2: Damping ratios of in-water natural vibrations of Gate #3.

Damping ratios for Thermalito Gate #3 Test 7 (d = 6 mm)

Vibration (6.6 Hz)				Vibration (5.6 Hz)		Vibration (6.1 Hz)	
Vertical		Streamwise		Streamwise		Streamwise	
Header	Damping ratio	Header	Damping ratio	Header	Damping ratio	Header	Damping ratio
E3-V	0.010	E2-R	0.009	E2-R	0.032	E2-R	0.013
E6-V	0.010	E3-R	0.009	E3-R	0.032	E3-R	0.012
L1-V	0.009	E4-R	0.015	E4-R	0.033	E4-R	0.015
L2-V	0.009						
Average	0.010	Average	0.011	Average	0.032	Average	0.013

Damping ratios for Thermalito Gate #3 Test 9 (d = 8 mm)

Vibration (6.6 Hz)				Vibration (5.6 Hz)		Vibration (6.1 Hz)	
Vertical		Streamwise		Streamwise		Streamwise	
Header	Damping ratio	Header	Damping ratio	Header	Damping ratio	Header	Damping ratio
E3-V	0.010	E2-R	0.010	E2-R	0.037	E2-R	0.011
E6-V	0.011	E3-R	0.010	E3-R	0.036	E3-R	0.011
L1-V	0.010	E4-R	0.013	E4-R	0.037	E4-R	0.015
L2-V	0.010						
Average	0.010	Average	0.011	Average	0.037	Average	0.013

Damping ratios for Thermalito Gate #3 Test 10 (d = 8 mm)

Vibration (6.6 Hz)				Vibration (5.6 Hz)		Vibration (6.1 Hz)	
Vertical		Streamwise		Streamwise		Streamwise	
Header	Damping ratio	Header	Damping ratio	Header	Damping ratio	Header	Damping ratio
E3-V	0.010	E2-R	0.010	E2-R	0.042	E2-R	0.018
E6-V	0.010	E3-R	0.010	E3-R	0.037	E3-R	0.015
L1-V	0.010	E4-R	0.012	E4-R	0.037	E4-R	0.017
L2-V	0.010						
Average	0.010	Average	0.011	Average	0.039	Average	0.017

Damping ratios for Thermalito Gate #3 Test 11 (d = 6 mm)

Vibration (6.6 Hz)				Vibration (5.6 Hz)		Vibration (6.1 Hz)	
Vertical		Streamwise		Streamwise		Streamwise	
Header	Damping ratio	Header	Damping ratio	Header	Damping ratio	Header	Damping ratio
E3-V	0.009	E2-R	0.009	E2-R	-	E2-R	0.015
E6-V	0.010	E3-R	0.009	E3-R	0.042	E3-R	-
L1-V	0.009	E4-R	0.011	E4-R	0.041	E4-R	-
L2-V	0.009						
Average	0.009	Average	0.010	Average	0.042	Average	0.015

7. EXAMINATION OF STEEL ROD DIAMETER FOR VIBRATION TESTS

For use in future field vibration tests, the results from the Thermalito tests were carefully examined to determine the minimum diameter of steel rod necessary to impart sufficient energy to identify the natural vibrations of Thermalito Diversion Dam gates with a mass of 24 ton.

For this purpose, the frequency power spectra of damped vibrations in Chapter 5 were surveyed, and spectral peak values of the identified natural vibration modes were plotted against the diameter of steel rod, as shown in Figure 7.1 (at frequencies of 5.5 Hz and 6.5 Hz) for Gate #2 and in Figure 7.2 (at frequencies of 5.6 Hz, 6.1 Hz and 6.6 Hz for Gate #3). The corresponding modes shapes are also illustrated in these two figures. The data are from measurement locations E3 and E6 at the spanwise center of the skinplate. The plotted amplitude of the gate response (ordinate) represents a time-averaged amplitude in μm of damped vibrations, and is thus relatively small compared to the maximum response amplitude.

With a steel rod diameter of 8 mm, the measured time-averaged amplitude reaches its largest values of about 22 to 30μm. At these amplitudes, the spectral peaks are sufficiently sharp that the frequency, mode and damping ratio can be easily identified with high accuracy, as shown, for example, in Figures 5.6(a) to (c). With a steel rod diameter of 6 mm, the amplitude decreases to about 10 to 20μm, and the spectral peaks are still sufficiently sharp that there is no difficulty in identifying the natural vibration characteristics, as shown, for example, in Figures 5.5(a) to (c). Even with a steel rod diameter of 3mm when the amplitude decreases to less than 3μm, the spectral peaks are still sharp, as shown in Figures 5.4(a) and (b). However, in Figure 5.4(c) the accurate identification of the vibration characteristics becomes problematic for the vertical vibration spectrum.

Based on this analysis, it is concluded that a steel rod with a minimum diameter of 6 mm was necessary for the accurate vibration testing of the 24 ton Thermalito Diversion Dam gates.

In future vibration tests on different gates, the diameter of the steel rod must be carefully determined depending upon the mass of the gate, but the results for the 24 ton Thermalito gates give added input to the decision making process.

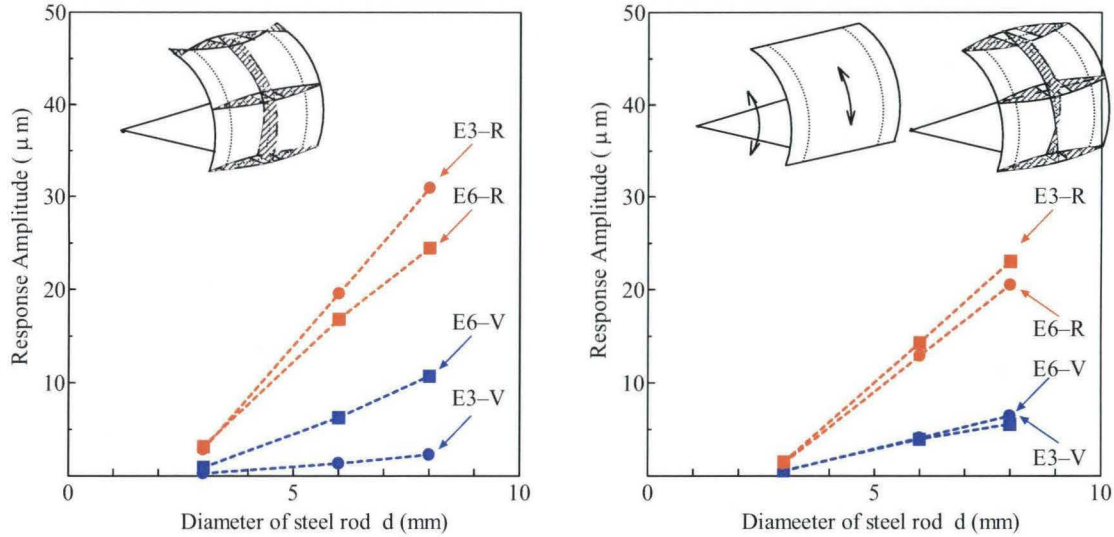

(a) 5.5 Hz vibration. (b) 6.5 Hz vibration.

Figure 7.1: Response amplitude of damped vibrations after impulsive excitation from breaking a steel rod for Gate #2.

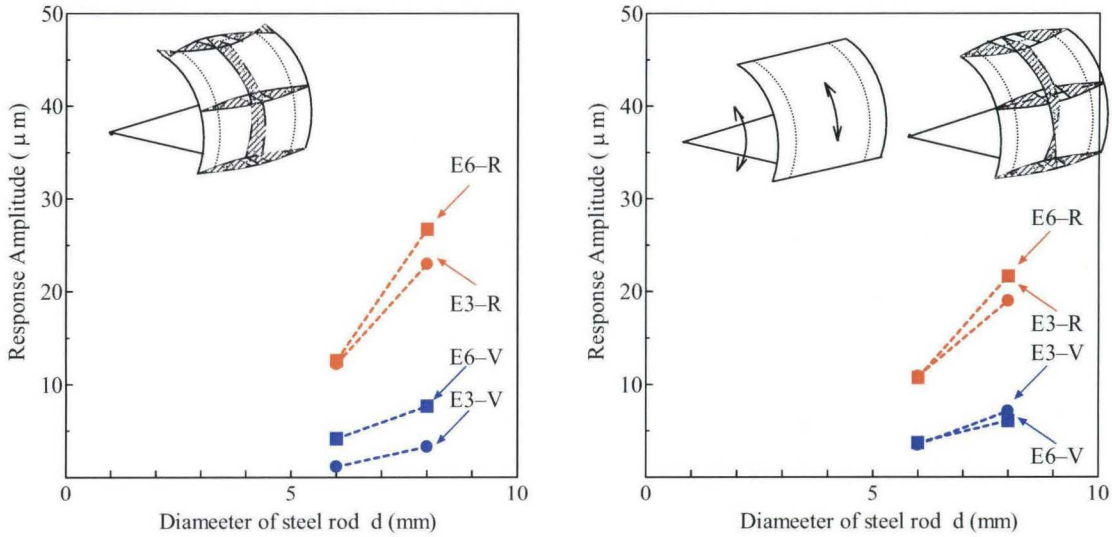

(a) 5.6 Hz vibration. (b) 6.6 Hz vibration.

Figure 7.2: Response amplitude of damped vibrations after impulsive excitation from breaking a steel rod for Gate #3.

8. FEM-SIMULATION OF IN-AIR NATURAL VIBRATIONS

8.1 FEM Model Construction

The present vibration testing was conducted for the gates immersed in water but not for the gate suspended in air. In order to examine the dynamic stability of gate applying the established theory of Anami [2000], it is necessary to know the in-air natural vibration characteristics of the gate. In the absence of experimental data, results from computer simulation using FEM modal analysis were adopted.

The structural details of the gate, taken from blueprints, were input into the computer (Dell DIMENSION 8400), with a Post-Processing Tool (FEMAP Ver.5.00), to construct a highly accurate FEM model, as shown in Figure 8.1. The FEM model included the tension-rod systems. Pre-tension loads on the tension rods are obviously unknown and could not be input into the computer. Figure 8.1(a) shows the whole model while Figures 8.1(b) to (e) provide enlarged views of the modeling of several connecting parts.

Most of the members were defined as plate elements, while the tension-rods were defined as beam elements. The four wire ropes for raising the gate were defined as 1-DOF spring elements, where the dynamic spring constant of the wire cables was required input.

In the present Tainter gates, most of structural connections are welded. Therefore, the rigidity of the joints was specified as rigid to be sufficiently high. The trunnion pin is installed in a concrete pier, and undergoes only one degree of freedom motion about its rotation axis. Therefore, the flexibilities except for rotation about its rotation axis were restrained in the trunnion pin model. The ends of the wire cables were assigned degrees of freedom in the rotational and translational directions, but the degree of freedom in the spanwise direction was restrained.

In FEM analysis, the element division is a very significant aspect in determining the accuracy of the analysis results. It is obvious that the greater the element division number, the more accurate are the results. However, the number of elements is limited by the performance of computer. Thus, it is necessary to make an effective analysis with a limited number of elements, where increased element divisions are concentrated in the significant portions in the model. In the present analysis, the fine element divisions were made for the skinplate and the radial arms, since the experimental modal analysis showed that they were significant factors determining the natural vibrations of the whole gate. The list of element division number for each component structural element is given in Table 8.1. The total element number is 19,526.

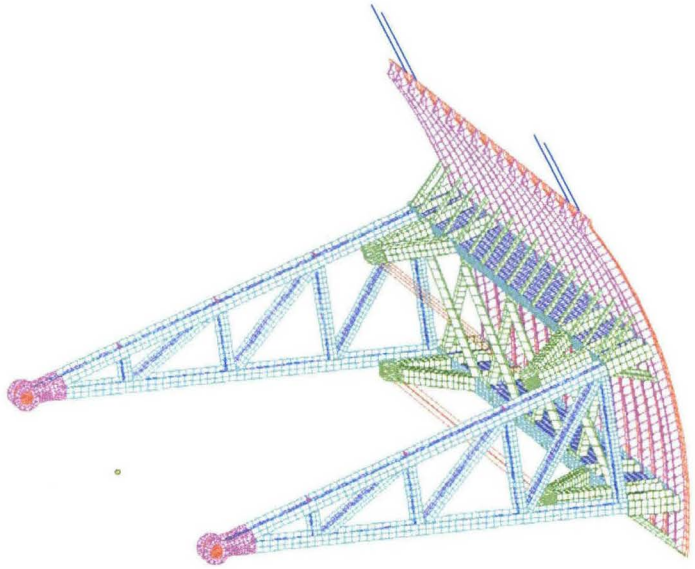

(a) 3-D view.

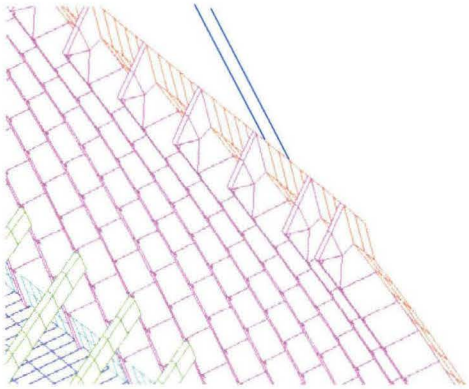

(b) Skinplate.

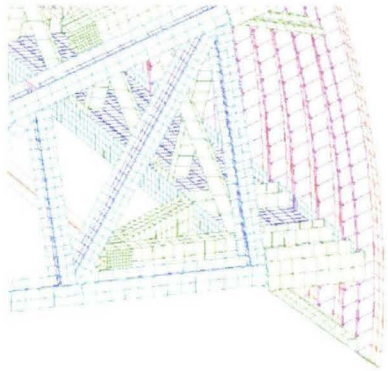

(c) Radial struts and horizontal girder.

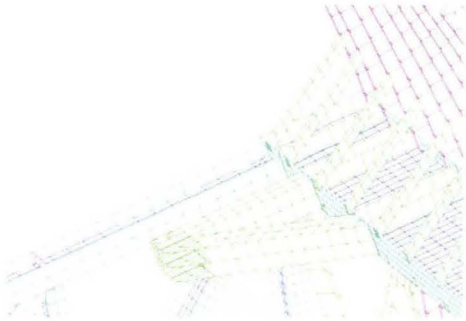

(d) Diagonal members reinforcing skinplate.

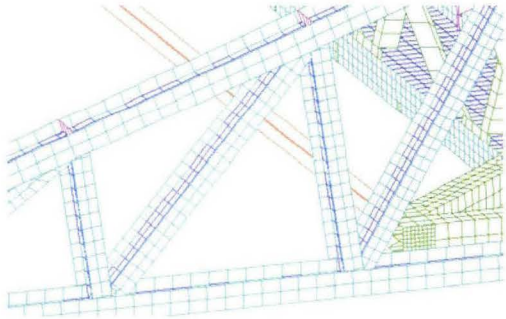

(e) Radial arm structure.

Figure 8.1: FEM model of the Thermalito Diversion Dam Tainter-gate.

Table 8.1: Number of elements for FEM model construction.

Name	Element	Name	Element
Skinplate	3920	Arm bracing	2442
Skinplate bracing	1396	Arm splicer	506
Horizontal girder	456	Trunnion pin	496
Horizontal bracing	3191	Wire rope	20
Girder bracing	3510	Others	1989
Radial arm	1600	Total	19526

8.2 Dynamic Spring Constant of Wire Cables and Equivalent Modulus of Elasticity

In general, it extremely challenging to estimate the dynamic spring constant with a high degree of accuracy, since the dynamic modulus of elasticity of the wire cables is unknown in many cases. For this reason, the dynamic spring constant of the wire cables for the Thermalito gates was selected by a trial and error method such that the FEM-simulated whole gate vibration frequency around the trunnion pin coincided with the measured frequency of 6.5 Hz in the present vibration tests for Gate #2.

As a result of this trial and error simulation, the dynamic spring constant, K_d , was assigned a value of

$$K_d = 8.078\times10^6 \text{ [N/m]} \tag{8.1}$$

for a single wire cable.

With this value of dynamic spring constant, the dynamic modulus of elasticity of Thermalito gate wire rope, M_d, can be estimated. It is of significance to note here that only the free wire rope with a length of L_f= 5.27 m plays a role in dynamic spring behavior. With this realization, the dynamic modulus of elasticity of wire rope, M_d, can be estimated as

$$M_d = \frac{K_d \cdot L_f}{A} \tag{8.2}$$

in which the wire rope area A takes a value of 321 mm^2, as previously listed in Table 2.2. For the Thermalito gate wires, the dynamic modulus of elasticity takes on a value of

$$M_d = 132 \text{ GPa}, \tag{8.3}$$

which is about 0.64 times 206 GPa, the listed modulus of elasticity for the original material of the wire cables from Table 8.2. This dynamic modification coefficient c_f of 0.64 is quite significant in the experience it provides. It is significantly larger than the static modification coefficient c_s of 0.45 for the static modulus of elasticity (see discussions in Section 2.3 in addition to Table 8.2).

After lengthy and difficult calculations using the blue prints as well as the mass lists of the Thermalito gate, the following value was found for the moment of inertia of the whole gate around the trunnion pin, I_θ:

$$I_\theta = 1.619\times10^6 \text{ [kgm}^2\text{]}. \tag{8.4}$$

With this value and using a radial arm radius of R_a = 9.144 m, the natural vibration frequency of the whole gate around the trunnion pin, Ω_n, can be calculated simply by

$$\Omega_n = \frac{1}{2\pi}\sqrt{\frac{K_c R_a^2}{I_\theta}}\,[H_z] \tag{8.5}$$

which results in 6.5 Hz, very close to the measured frequency.

Table 8.2: Characteristics of wire rope "6×19 IWRC " for the Thermalito Diversion Dam Tainter-gate.

Modulus of elasticity of material Mo	Static		Dynamic	
	Modulus of elasticity Ms	Modification coefficient Cs	Modulus of elasticity Md	Modification coefficient Cd
206 GPa	93.08 GPa	0.45	132 GPa	0.64

Table 8.3: Natural vibration frequencies and vibration modes by FEM analysis.

Mode Name	Vibration Mode Shape	In-Air Vib. Freq. by FEM Ω_a (Hz)
M_Z	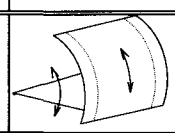	6.50
M_{X1}	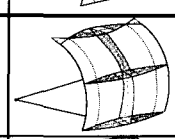	20.8
M_{X2}	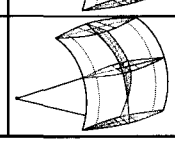	13.7

8.3 Natural Vibration Frequencies and Vibration Modes

The natural vibration frequencies and vibration modes were analyzed using FEM analysis software (MSC/N4W, NASTRAN for Windows V3 by the MacNeal-Schwendler Co.). The analyzed frequency range was 0 to 50 Hz. The vibration modes obtained by calculations are shown by animation on a computer screen. The natural vibration modes were identified as those modes for which the whole gate was carrying out orderly vibration. Major FEM-simulated natural vibration modes are illustrated in Table 8.3, with addressed vibration frequencies. The first one is the whole gate vibration mode M_z around the trunnion pin at 6.5 Hz. The second is the streamwise parallel vibration mode M_{x1} of the skinplate, at 20.8 Hz. The last one is the streamwise rotational vibration mode M_{x2} of the skinplate at 13.7 Hz.

The computer-simulated mode shapes are presented in detail in Figures 8.2 to 8.4, where in each figure the top drawing, labeled (a), is a 3-dimensional view, the center drawing, labeled (b), is a cross-sectional side view at the spanwise center of gate, and bottom drawing, labeled (c), is a top view. The red and black lines show the instantaneous vibration shapes with maximum amplitude. For clarity, the amplitudes have been amplified.

These mode shapes can be summarized as follows:

(1) The mode shape in Figure 8.2 at a frequency of 6.5 Hz represents the whole gate rigid body

rotational vibration (around the trunnion pin) mode M_z, which corresponds to the measured mode shape, shown in Figure 6.3(d) at 6.5 Hz for Gate #2 and in Figure 6.5(d) at 6.6 Hz for Gate #3. This vibration is definitely caused by the elastic support of the wire ropes which raise and lower the gate.

(2) The mode shape in Figure 8.3 at a frequency of 20.8 Hz represents the streamwise parallel vibration mode M_{x1}. In the streamwise vertical plane (see Figure 8.3(b)) at the spanwise center of gate, the skinplate is performing almost parallel vibration in the press-shut direction. The upper center portion of skinplate has a large amplitude and the whole skinplate vibrates in-phase, and is in good agreement with the measured vibration mode, shown in Figure 6.2(b) at 5.5 Hz for Gate #2 and in Figure 6.4(b) at 5.6 Hz for Gate #3. In the horizontal plane (see Figure 8.3(c)), the skinplate bottom undergoes a half wavelength vibration with nodes near each side of the skinplate, again agreeing well with the measured vibration mode, shown in Figure 6.2(c) at 5.5 Hz for Gate #2 and in Figure 6.4(c) at 5.6 Hz for Gate #3. The skinplate top undergoes a full wavelength vibration with antinodes at both sides of the skinplate, probably caused by the high bending flexibility of the long-span skinplate. Corresponding to this skinplate parallel bending vibration, the radial arm structures perform bending vibrations in both the vertical and spanwise directions, as shown in the Figures 8.3(b) and (c).

(3) The mode shape in Figure 8.4 at a frequency of 13.7 Hz represents the skinplate streamwise rotational vibration mode M_{x2}. In the streamwise vertical plane (see Figure 8.4(b)) at the spanwise center of gate, the skinplate is performing the lowest frequency bending mode vibration with the node near the lower horizontal girder, which agrees well with the measured mode shape, shown in Figure 6.3(c) at 6.5 Hz for Gate #2 and in Figure 6.5(c) at 6.6 Hz for Gate #3. The rotation center height was about 1.9 m from the skinplate bottom, which also agrees well with the measured height of 2.03 m (refer to Section 6.3). Corresponding to this skinplate parallel bending vibration, the radial arm structures perform a bending vibration in the vertical direction, as shown in the Figure 8.4(b).

It is of interest to note here the direction of the streamwise parallel vibration of the skinplate at a frequency of 20.8 Hz. In Figure 8.5 the cross-sectional view of the calculated trajectory lines for the parallel vibration of the skinplate center are presented in detail. This figure clearly shows that the whole skinplate performs a parallel vibration. The direction of skinplate streamwise vibration is of great interest. The average vibration direction of skinplate was determined by reading the direction of all auxiliary lines and then taking the arithmetic average of these directions. The average direction was determined to be about 10°, which is quite close to the measured press-shut angles of 10.76° for Gate #2 and 8.0° for Gate #3.

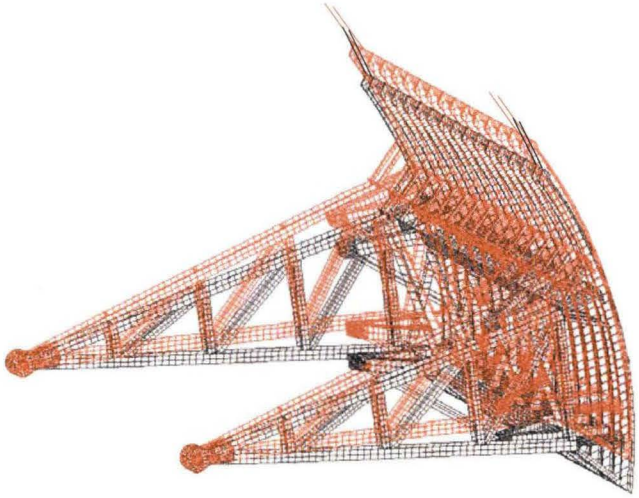

(a) 3-D view.

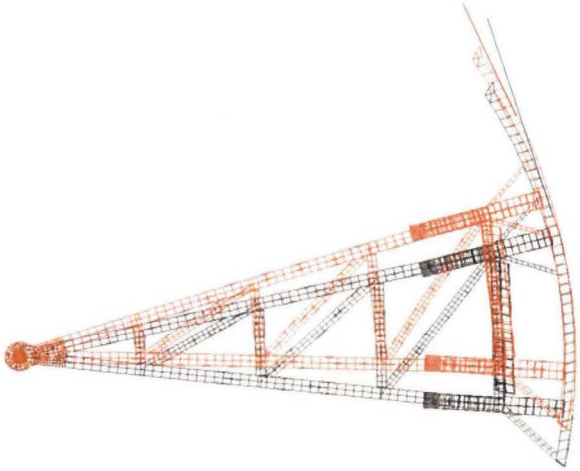

(b) Cross-sectional side view at the spanwise center of the gate.

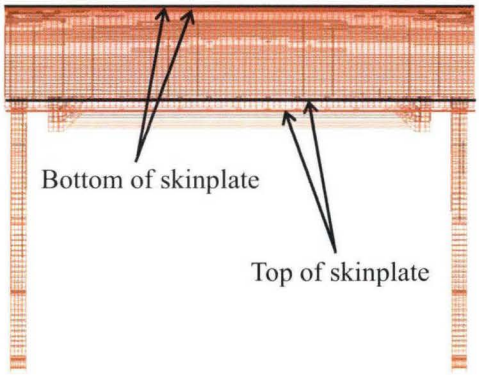

(c) Downward view.

Figure 8.2: In-air whole gate vibration (around trunnion pin) mode M_z at 6.50 Hz.

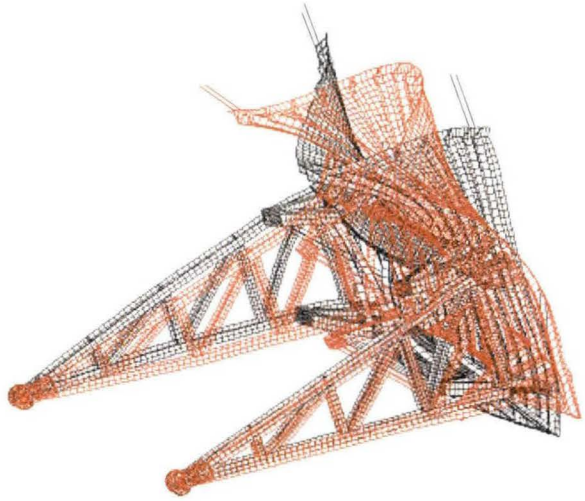

(a) 3-D view.

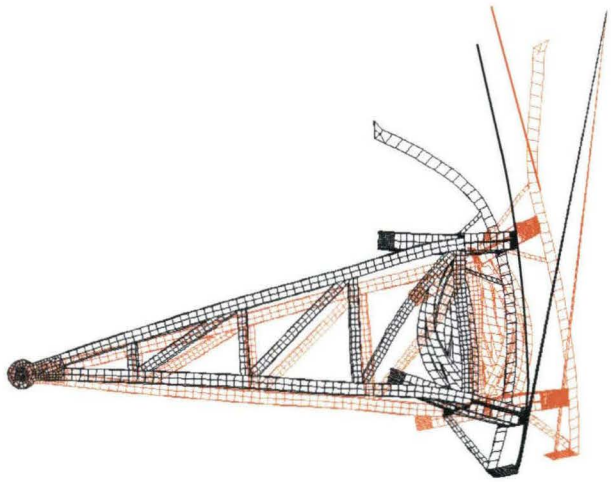

(b) Cross-sectional side view at the spanwise center of the gate.

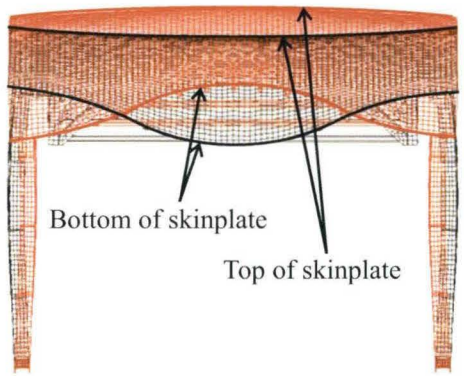

(c) Downward view.

Figure 8.3: In-air streamwise rotational vibration mode M_{x1} at 20.8 Hz.

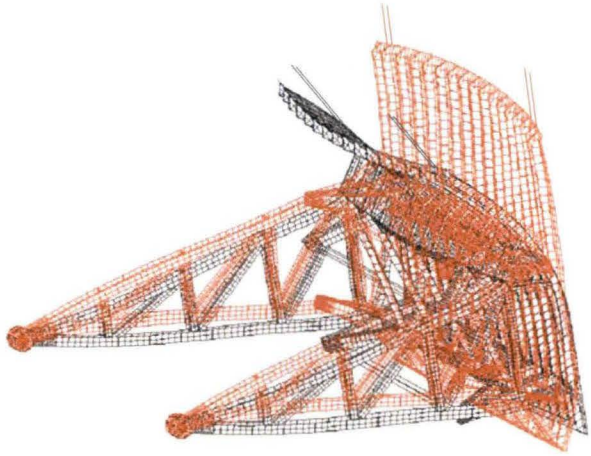

(a) 3-D view.

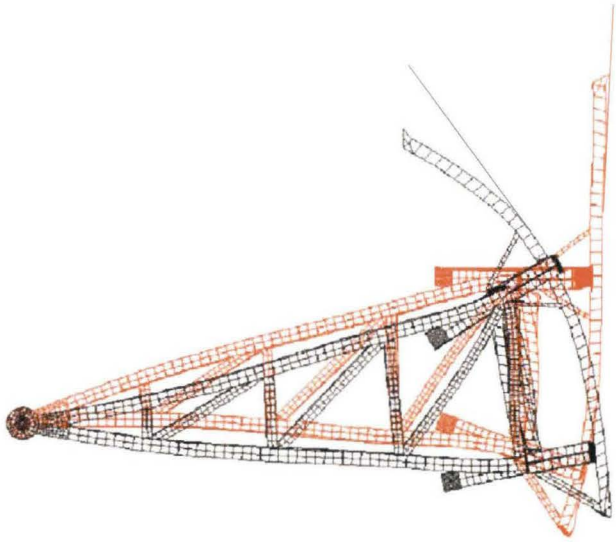

(b) Cross-sectional side view at the spanwise center of the gate.

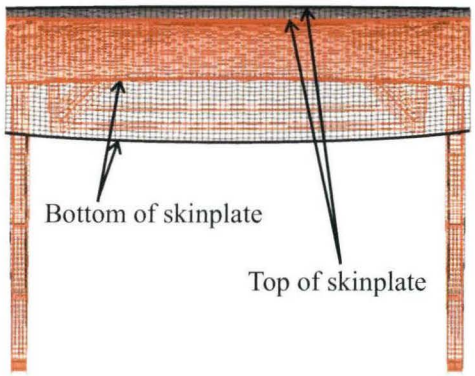

(c) Downward view.

Figure 8.4: In-air streamwise rotational vibration mode M_{x2} at 13.7 Hz.

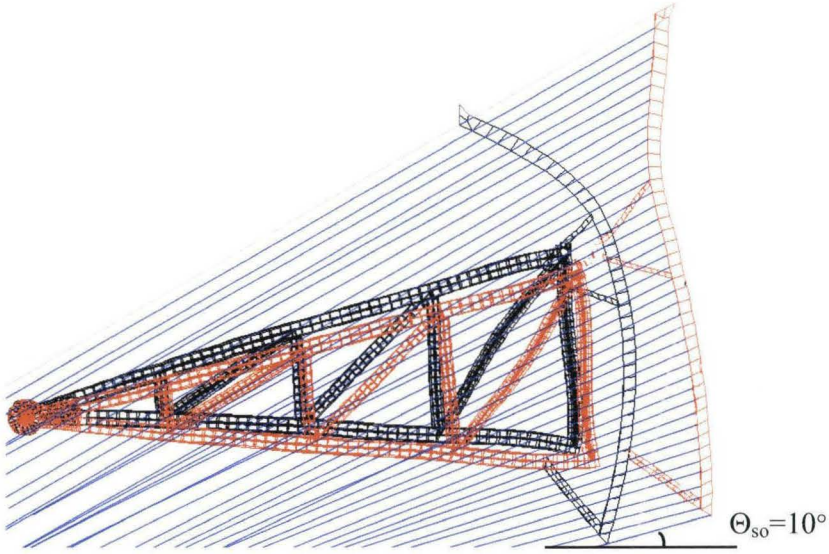

Figure 8.5: Trajectory lines of in-air streamwise parallel vibration of the skinplate at 20.8 Hz.

9. THEORETICAL EXAMINATION OF DYNAMIC STABILITY AT TESTED BACK WATER LEVEL

In the present field vibration tests, the frequency and mode shape of significant in-water natural vibrations were accurately identified by experimental modal analysis, while the corresponding in-air frequencies and mode shapes were precisely calculated using an FEM simulation. With these known values of in-water and in-air vibration characteristics, the theoretical analyses developed by Anami & Ishii [22], and Anami [3] to unveil the dynamic instability of the Folsom Dam Tainter-gates can be further validated and then, as was shown in Anami [3], be used to assess the dynamic stability of the Thermalito Diversion Dam Tainter-gates at the tested back water level.

9.1 Confirmation of Theoretical Analyses with Calculations of In-Water Natural Vibration Frequency

In the FEM analyses in Chapter 8, two significant modes of skinplate streamwise vibration in air, with the mode shapes shown in Table 9.1, were identified. One mode is a streamwise parallel vibration at 20.8 Hz, while the second mode is a streamwise rotational vibration at 13.7 Hz. The first in-air vibration mode shape, denoted as mode "M_{x1}", agrees well with the measured in-water mode shape at 5.5 Hz for Gate #2 (see Figure 6.2) and 5.6 Hz for Gate #3 (see Figure 6.4), while the second in-air vibration mode shape, denoted as mode "M_{x2}", agrees well with the measured in-water mode shape at 6.5 Hz for Gate #2 (see Figure 6.3) and 6.6 Hz for Gate #3 (see Figure 6.5). The in-water vibration frequencies are greatly reduced relative to the in-air frequencies because of the large effect of water added-mass on the skinplate.

The rotational skinplate streamwise vibration is shown in Figure 9.1, in which the vibration is represented by the angle of Ψ and the rotation center height from the skinplate bottom is represented by R_S. When R_S is far larger than the gate submergence depth of d_0, that is, when $R_S \rightarrow \infty$, the skinplate streamwise vibration reduces to the parallel vibration mode M_{x1}. The streamwise vibration of skinplate is a back and forth motion on the back water, thus inducing an excessive push-and-draw pressure, which has a correspondingly large water-added-mass effect. In the theoretical analysis of Anami [3], it was shown that the reduced water added mass $\Delta m_{x,\psi}$, which represents the hydrodynamic push-and-draw pressure p_{bs} integrated over the whole wetted area of the skinplate (y = 0 to -1.0), can be calculated by the following expression:

$$\Delta m_{x,\psi} \equiv \frac{\Delta I / R_S^2}{\rho d_0^2 W_0} = \frac{1}{F^2} \int_1^0 \left(1 - \frac{1+y}{r_s} \right) p_{bs}(0,y)\,dy \qquad (r_s \geqq 0.5) \tag{9.1a}$$

or

$$\Delta m_{\psi} \equiv \frac{\Delta I / (d_0 - R_S)^2}{\rho d_0^2 W_0} = \frac{1}{F^2} \int_1^0 \left(-1 - \frac{y}{1-r_s} \right) p_{bs}(0,y)\,dy \qquad (r_s < 0.5) \tag{9.1b}$$

The water added moment of inertia is represented by ΔI, and thus the numerator of $\Delta I/R_S^2$ or $\Delta I/(d_0-R_S)^2$ represents the equivalent water added mass. When $R_S \rightarrow \infty$, $\Delta I/R_S^2$ reduces to the water added mass ΔM and $\Delta m_{x,\psi}$ reduces to Δm_x. The denominator, $\rho d_0^2 W_0$, is the characteristic mass of water which is

Table 9.1: In-air natural vibrations and calculations of in-water vibration frequency.

Mode Name	Parallel vib. M_{x1}	Rotational vib. M_{x2}
FEM-simulated in-air vib. freq.	Ω_{ax} = 20.8 Hz	$\Omega_{a\psi}$ = 13.7 Hz
Vibration mode shape	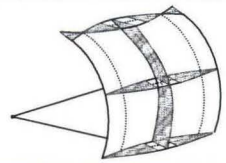	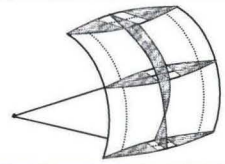
Measured in-water vib. freq.	Ω_{wx} = 5.5 Hz (for #2) 5.6 Hz (for #3)	$\Omega_{w\psi}$ = 6.5 Hz (for #2) 6.6 Hz (for #3)
Measured in-water to in-air freq. ratio	Ω_{wx}/Ω_{ax} = 0.262 (for #2) 0.269 (for #3)	$\Omega_{w\psi}/\Omega_{a\psi}$ = 0.474 (for #2) 0.482 (for #3)

Gate submergence depth d_0 and length W_0	d_0 = 6.38 m : W_0 = 12.17 m			
Rotation center height R_s	∞		2.03 m	
Reduced rotation center height r_s	∞		0.32	
Froude number F $\left(\equiv\sqrt{\frac{d_0}{g}}\times 2\pi\Omega_w\right)$	27.9 (for #2) 28.4 (for #3)		32.9 (for #2) 33.4 (for #3)	
Reduced added mass	Δm_x = 0.54		Δm_ψ = 0.04	
Basic Froude number F_0 $\left(\equiv\sqrt{\frac{d_0}{g}}\times 2\pi\Omega_a\right)$	105		69	
Representative mass of water $\rho d_0^2 W_0$	495× 10^3 kg			
Representative mass of skinplate	M_s	19.5×10^3 kg	$I_\psi/(d_0-R_s)^2$	4.7×10^3 kg
Water-to-gate mass ratio	α_x = 25.3		α_ψ = 106	
Calculated in-water to in-air freq. ratio	Ω_{wx}/Ω_{ax} = 0.262		$\Omega_{w\psi}/\Omega_{a\psi}$ = 0.434	
Calculated in-water vib. freq.	Ω_{wx} = 5.4 Hz		$\Omega_{w\psi}$ = 5.9 Hz	
Relative error of theoretical prediction	2%		9%	

contained in a rectangular parallelepiped given by the product of the square of one side d_0 and the spanwise length W_0. The reduced water added mass $\Delta m_{x,\psi}$ depends upon two parameters: the Froude number F, representing the dynamic similarity of the flow field, and the reduced rotation center height r_s. These parameters are defined as

$$F \equiv 2\pi\,\Omega_{wx,\psi}\sqrt{\frac{d_0}{g}} \qquad\qquad r_s \equiv \frac{R_s}{d_0} \tag{9.2}$$

where $\Omega_{wx,\psi}$ represent the in-water vibration frequency. A graphical representation of the functional dependence of $\Delta m_{x,\psi}$ on F and r_s is shown in Figure 9.2 For Froude numbers, F, larger than about 20, $\Delta m_{x,\psi}$ approaches a constant value depending only on the value of r_s.

As listed in Table 9.1, the Thermalito gates have F = 27.9, 28.4 and $r_s = \infty$ for the streamwise parallel vibration M_{x1}, and F = 32.9, 33.4 and r_s = 0.32 for the rotational vibration M_{x2}. With these values, the magnitude of the reduced water added mass is Δm_x = 0.54 for the parallel vibration M_{x1}, and Δm_ψ = 0.04 for the rotational vibration M_{x2}, as shown by the red and blue points, respectively, in Figure 9.2 and listed in Table 9.1.

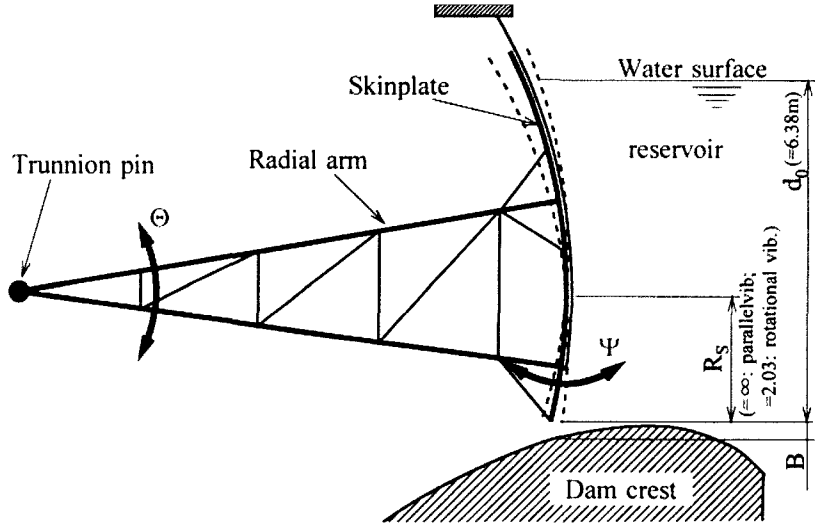

Figure 9.1: Cross-sectional view of Thermalito Diversion dam Tainter-gate.

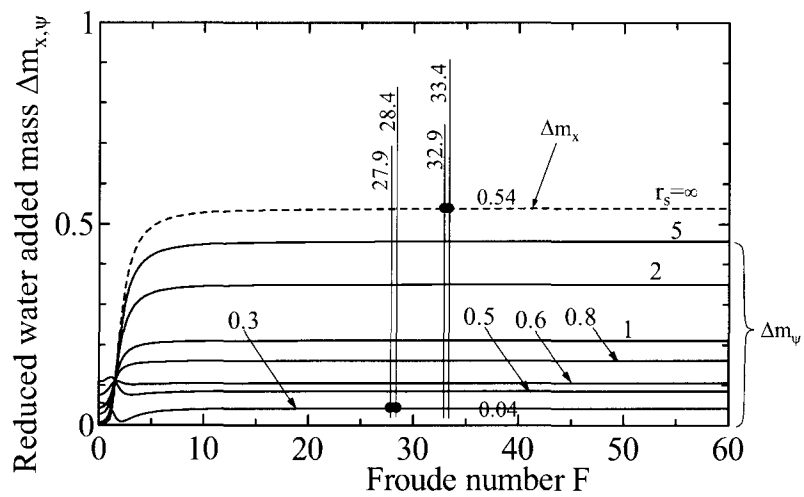

Figure 9.2: Calculated results of reduced water added mass, Δm_ψ.

With these values for the reduced water added mass, $\Delta m_{x,\psi}$, and with the in-air natural vibration frequency, $\Omega_{ax,\psi}$, the in-water natural vibration frequency, $\Omega_{wx,\psi}$, can be calculated by the following relatively simple expression:

$$\frac{\Omega_{wx,\psi}}{\Omega_{ax,\psi}} = \frac{1}{\sqrt{1+\alpha_{x,\psi}\Delta m_{x,\psi}}} \tag{9.3}$$

where $\alpha_{x,\psi}$ represents the mass ratio defined by

$$\alpha_{x,\psi} \equiv \frac{\rho d_0^2 W_0}{I_\psi / R_S^2} \quad (r_s \geq 0.5) \qquad \text{or} \qquad \alpha_\psi \equiv \frac{\rho d_0^2 W_0}{I_\psi / (d_0 - R_S)^2} \quad (r_s < 0.5) \tag{9.4}$$

The numerator is the characteristic water mass and the denominator is the moment of inertia of the skinplate around its rotation center, I_ψ, over the square of the rotation center height R_S, representing the equivalent mass of skinplate. When $R_S \rightarrow \infty$ for the parallel vibration M_{x1}, I_ψ/R_S^2 converges to the whole skinplate mass M_s. As shown in Table 9.1, the water-to-gate mass ratio is $\alpha_x = 25.3$ for the parallel vibration M_{x1}, and $\alpha_\psi = 106$ for the rotational vibration M_{x2}.

With these values mass ratio along with the corresponding values of the reduced water added mass, the in-water to in-air vibration frequency ratio becomes $\Omega_{wx}/\Omega_{ax} = 0.264$ for the parallel vibration M_{x1}, and $\Omega_{w\psi}/\Omega_{a\psi} = 0.434$ for the rotational vibration M_{x2}. Figure 9.3 portrays the theoretical dependence of the frequency ratio, $\Omega_{w\psi}/\Omega_{a\psi}$, on the mass ratio (the parameter) and on the basic Froude number (the abscissa) which is based on the in-air frequency and is defined by

$$F_0 \equiv \Omega_{ax,\psi}\sqrt{\frac{d_0}{g}} \tag{9.5}$$

For the Thermalito gates, F_0 takes on a value of 105 for the parallel vibration M_{x1} and 69 for the rotational vibration M_{x2}. The calculated frequency ratios for the parallel and rotational vibrations of the Thermalito gates are shown by the red and blue lines in Figure 9.3, respectively.

For the Thermalito gates, F_0 takes on a value of 105 for the parallel vibration M_{x1} and 69 for the rotational vibration M_{x2}. The calculated frequency ratios for the parallel and rotational vibrations of the Thermalito gates are shown by the red and blue lines, respectively. The measured values of frequency ratio ($\Omega_{wx}/\Omega_{ax} = 0.264$, 0.269 for the parallel vibration M_{x1} and $\Omega_{w\psi}/\Omega_{a\psi} = 0.474$, 0.482 for the rotational vibration M_{x2}) at their respective basic Froude numbers are plotted by the red and blue circles, respectively. Also shown for comparative purposes are the results for other full-scale gate tests (labeled Tainter gates "A", "B" and "C"). For the Thermalito gates, the corresponding dimensional values of the calculated in-water vibration frequency are $\Omega_{wx} = 5.4$ Hz for the parallel vibration M_{x1} and $\Omega_{w\psi} = 5.9$ Hz for the rotational vibration M_{x2}.

Also shown in Table 9.1 are the relative errors in the theoretical predictions. The relative errors in the theoretically predicted in-water natural vibration frequencies are less than 2 % for the parallel vibration M_{x1} and less than 9 % for the rotational vibration M_{x2}. These low levels of relative error further strengthen the confidence in the accuracy of the theoretical development.

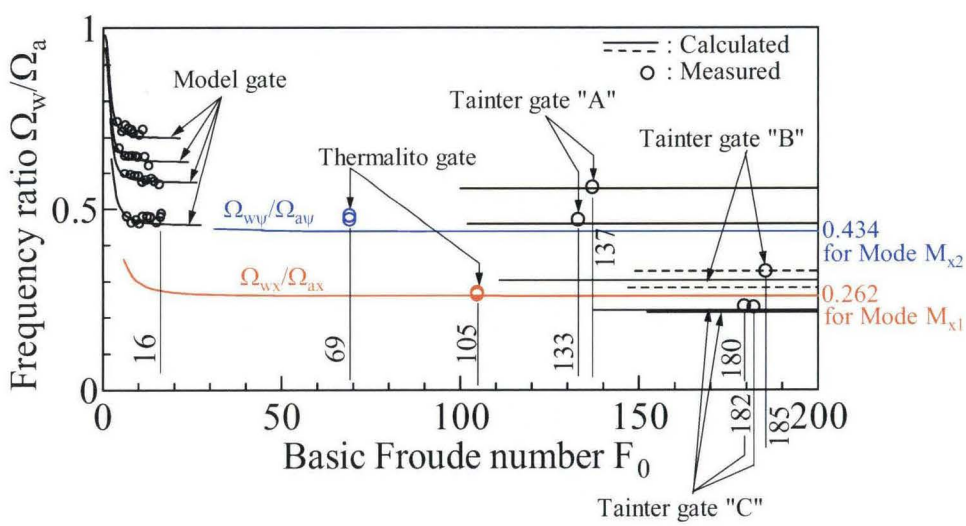

Figure 9.3: In-water to in-air vibration frequency ratio as a function of basic Froude number and mass ratio for comparison of theoretical predictions with field test results.

9.2 Self-Excitation Mechanism and Theoretical Analysis of Dynamic Stability

The Thermalito Diversion Dam Tainter-gate can potentially undergo two different coupled mode vibrations, which are:

(1) Coupling of the skinplate streamwise parallel vibration "M_{x1}" (Ω_{wx} = 5.5 Hz and 5.6 Hz) with the whole gate rigid-body rotational vibration around the trunnion pin "M_z" ($\Omega_{a\theta}$ = 6.5 Hz).

(2) Coupling of the skinplate streamwise rotational vibration "M_{x2}" ($\Omega_{w\psi}$ = 6.5 Hz) with the whole gate rigid-body rotational vibration around the trunnion pin "M_z" ($\Omega_{a\theta}$ = 6.5 Hz).

The ratio of the in-water streamwise vibration frequency $\Omega_{wx,\psi}$ to the in-air whole gate rotational vibration frequency $\Omega_{a\theta}$ takes on a value of 0.85 and 0.86 for the first possible coupled-mode vibration, and a value of 1.0 for the second coupling possibility. With these values equal to or slightly less than 1.0 (a known region of potential susceptibility), it is crucial to consider the dynamic stability of the Thermalito gates using Anami's (2000) theory.

In the following sections, the mechanisms for the coupled-mode self-excited vibration for these two cases will be presented along with the theoretical analyses of the potential dynamic stabilities.

Case (1): Coupling of the skinplate parallel vibration M_{x1} with the whole gate vibration M_z

Field test results for the streamwise parallel vibration of skinplate, shown in Figure 6.2 for Gate #2 and in Figure 6.4 for Gate #3, are reproduced in Figure 9.4, in which is also shown the trajectory line of the gravitational center "G" of whole skinplate. A special feature of this parallel vibration mode of the skinplate of Thermalito Diversion Dam Tainter-gate is that the trajectory of the skinplate center of gravity passes below the trunnion pin. The distance from this trajectory line to the trunnion pin is represented by L_G which takes on a value of 0.72 m for Gate #2 and 1.2 m for Gate #3.

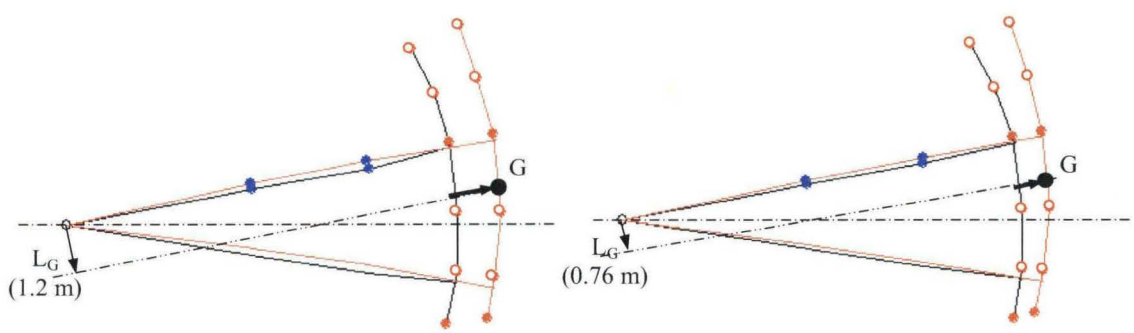

(a) Gate #2. (b) Gate #3.

Figure 9.4: Field test results of skinplate streamwise parallel vibration and the trajectory lines of the skinplate center of gravity.

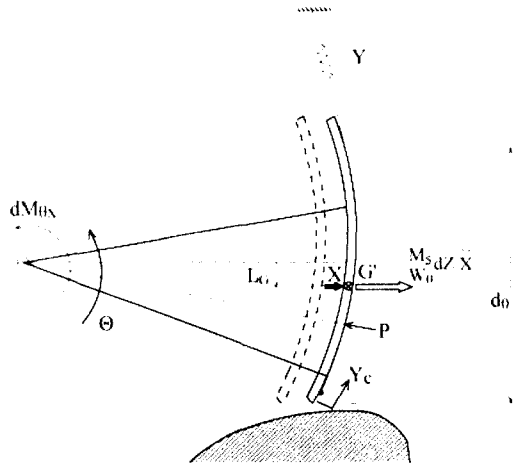

Figure 9.5: Schematic view of the translational streamwise vibration of the skinplate of the Thermalito Diversion Dam Tainter-gate, and the coupling moment around trunnion pin, due to skinplate translational vibration.

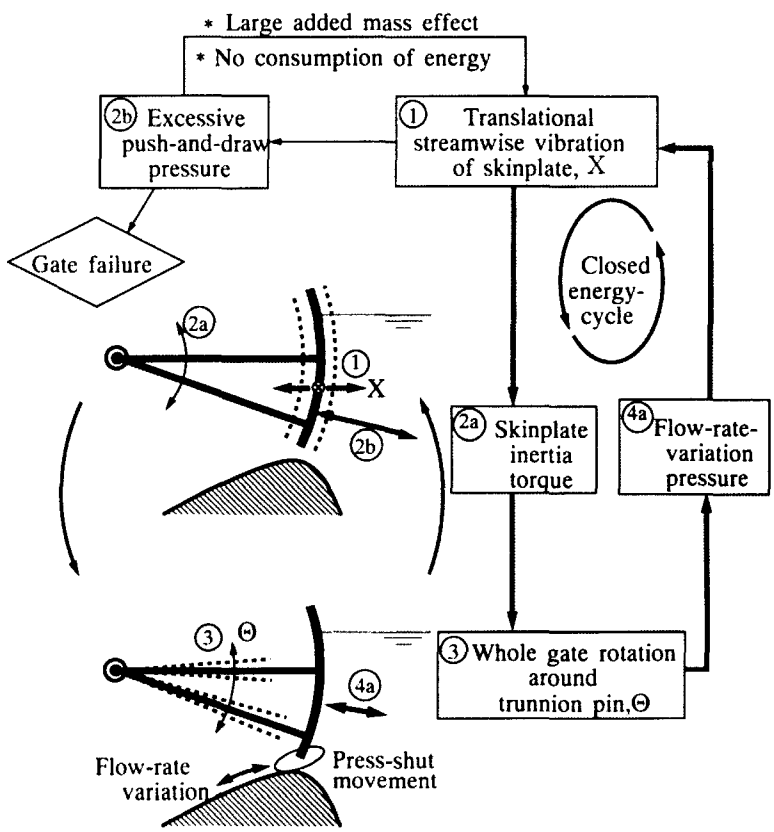

Figure 9.6: Closed energy cycle of coupled-mode self-excited vibration produced by the whole gate rigid body vibration and the skinplate streamwise parallel vibration.

Figure 9.5 is a sectional view of Thermalito Diversion Dam Tainter-gate, portraying its fundamental vibration modes. As is clear in this figure, if the whole skinplate undergoes a streamwise parallel vibration,

the inertial force induces a significant torque around the trunnion pin. This inertia torque, in turn, drives the whole gate vibration around the trunnion pin. These processes are expressed with "1" and "2a" in the closed energy cycle shown in Figure 9.6. When the whole gate undergoes vibration around the trunnion pin due to the inertial torque, the discharge opening will naturally change, thus inducing a flow-rate variation pressure. If the bottom end of the skinplate undergoes the vibration trajectory of a press-shut device, the flow-rate variation pressure supplies energy to the skinplate parallel vibration. The closed energy cycle, shown in Figure 9.6, results in the effective coupling of the skinplate parallel vibration and the whole gate vibration around the trunnion pin, producing coupled-mode self-excited vibration. The mechanism of this coupled-mode self-excited vibration is identical with that of the Folsom Dam Tainter-gate. The only difference is that the skinplate vibrates in a rotational vibration mode for the Folsom Dam Tainter-gate whereas the skinplate vibration is in a parallel streamwise mode for this case for the Thermalito Diversion Dam Tainter-gate.

The parallel skinplate vibration X shown in Figure 9.5 results in an inertia torque $dM_{\theta x}$ exciting the whole gate vibration around the trunnion pin, given by

$$dM_{\theta x} = -\frac{M_S}{W_0} dZ\, \ddot{X} \cdot L_G \,, \tag{9.6}$$

where dZ represents the small spanwise length of the skinplate. Based on the field vibration test results, a spanwise half wavelength bending vibration mode of the skinplate is assumed and can be represented by the parallel vibration X, defined by:

$$X = X_c \sin\left(\frac{Z}{W_0} + \frac{1}{2}\right)\pi \tag{9.7}$$

where X_c represents the vibration amplitude at the bottom center of the skinplate. From this expression for displacement, the inertia torque $M_{\theta x}$ can be calculated as follows:

$$\begin{aligned} M_{\theta x} &= \int_Z dM_{\theta x} = -L_G \frac{M_S}{W_0} \cdot \ddot{X}_c \int \sin\left(\frac{Z}{W_0} + \frac{1}{2}\right)\pi dZ \\ &= -\frac{2}{\pi} \cdot L_G \cdot M_s \cdot \ddot{X}_c \end{aligned} \tag{9.8}$$

The equation of motion for the whole gate vibration around the trunnion pin can then be given as

$$\ddot{Y}_c + 2\Omega_{a\theta}\zeta_{a\theta}\dot{Y}_c + \Omega_{a\theta}^2 Y_c + \frac{2}{\pi} \cdot \frac{R_a}{L_G} \cdot \frac{L_G^{\,2} M_s}{I_\theta} \ddot{X}_c = 0 \tag{9.9}$$

On the other hand, the equation of motion for the skinplate being acted upon by the hydraulic pressure, P, can be written as follows:

$$\left(M_s \ddot{X}_c + C_x \dot{X}_c + K_x X_c\right) \frac{1}{W_0} \int_{-W_0/2}^{W_0/2} \sin\left(\frac{Z}{W_0} + \frac{1}{2}\right)\pi\, dZ + \int_Z \int_Y P\, dY dZ = 0 \tag{9.10}$$

where Y represents the vertical upward vibration of skinplate and dY is the corresponding infinitesimal increment. Thus, PdYdZ represents the horizontal component of hydrodynamic force acting on the differential area dYdZ. Equation (9.10) can be re-arranged as follows:

$$\ddot{X}_c + 2\zeta_{ax}\Omega_{ax}\dot{X}_c + \Omega_{ax}{}^2 X_c + \frac{\pi}{2}\frac{1}{M_s}\int_Z\int_Y P\,dY\,dZ = 0 \tag{9.11}$$

Now, in order to normalize the two equations of motion, Equations (9.9) and (9.11), the following dimensionless variables are introduced:

$$x_c \equiv \frac{X_c}{X_{co}} \quad , \quad y_c \equiv \frac{Y_c}{Y_{co}} \quad , \quad t \equiv \Omega_{a\theta}T \quad , \quad y \equiv \frac{Y}{d_0} \tag{9.12}$$

In terms of these non-dimensional variables, the equations of motion can be reduced ultimately to the following forms:

$$y_c'' + 2\zeta_{a\theta}y_c' + y_c + \frac{2}{\pi}\frac{\alpha_I}{l_G \cdot \alpha_{co}}x_c'' = 0 \tag{9.13}$$

$$\begin{aligned}(1+\delta_p\alpha_m\Delta m_x + \frac{2}{\pi}\sqrt{2}c_f k\alpha_m\Delta m_\theta)x_c'' \\ + 2\gamma_{x\theta}\left(\zeta_{ax} + \zeta_{fx} - \frac{\frac{2}{\pi}\sqrt{2}c_f k\alpha_m\Delta c_\theta}{2\gamma_{x\theta}F_{a\theta}}\right)x_c' + \gamma_{x\theta}^2 x_c \\ = \sqrt{2}c_f\alpha_{co}\left(\frac{\alpha_m\Delta c_\theta}{F_{a\theta}}y_c' - \alpha_m\Delta m_\theta y_c''\right)\end{aligned} \tag{9.14}$$

where, l_G is the reduced eccentricity of the center of gravity from the trunnion pin, α_I is the moment-of-inertia ratio, α_{co} is the vibration amplitude ratio, each of which can be defined, respectively, along with other useful parameters as

$$\begin{aligned} l_G \equiv \frac{L_G}{R_a} \quad , \quad \alpha_I \equiv \frac{L_G{}^2 M_s}{I_\theta} \quad , \quad \alpha_{co} \equiv \frac{Y_{co}}{X_{co}} \\ \gamma_{x\theta} \equiv \frac{\Omega_{ax}}{\Omega_{a\theta}} \quad , \quad \alpha_m \equiv \frac{\rho d_0{}^2 W_0}{M_s} \quad , \quad F_{a\theta} \equiv \Omega_{a\theta}\sqrt{\frac{d_0}{g}} \end{aligned} \tag{9.15}$$

The dimensionless factors Δm_x, Δm_θ, Δc_x and Δc_θ all represent effects of the hydrodynamic force. The first two parameters, Δm_x and Δm_θ, are the reduced added masses, while Δc_x and Δc_θ are the fluid excitation ratio and the fluid damping ratio, respectively. As the Froude number F increases, Δm_θ and Δc_x rapidly decrease to zero, while Δm_x and Δc_θ increase rapidly and approach asymptotic constant values of 0.54 and 1.25, respectively.

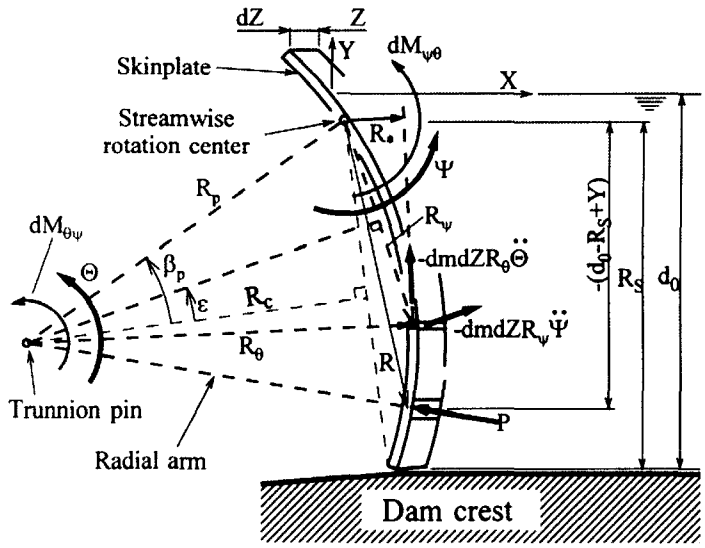

Figure 9.7: Schematic view of the streamwise rotational vibration of the Thermalito Diversion Dam Tainter-gate, and the coupling moment around trunnion pin, due to the skinplate rotational vibration.

The dynamic stability criterion diagram of the gate can be determined from the simultaneous solution of Equations (9.13) and (9.14), which must be undertaken numerically in a computer-simulation to obtain their approximate solutions.

Case (2): Coupling of the skinplate rotational vibration M_{x2} with the whole gate vibration M_z

When the skinplate undergoes streamwise rotational vibration, the inertial force induces a significant torque around the trunnion pin, as schematically shown in Figure 9.7. This inertia torque, in turn, drives the whole gate vibration around the trunnion pin. These processes are expressed with "1" and "2a" in the closed energy cycle shown in Figure 9.8. When the whole gate undergoes vibration around the trunnion pin due to the inertial torque, the discharge opening will naturally change, thus inducing a flow-rate variation pressure. If the bottom end of the skinplate has the vibration trajectory of a press-shut device, the flow-rate variation pressure supplies energy to the skinplate parallel vibration. The closed energy cycle, shown in Figure 9.8, results in the effective coupling of the skinplate streamwise rotational vibration and the whole gate vibration around the trunnion pin, producing the coupled-mode self-excited vibration.

The skinplate rotational vibration Ψ_Z results in an inertia torque $dM_{\theta\psi}$ exciting the whole gate vibration around the trunnion pin, given by

$$dM_{\theta x} = -\frac{I_\psi}{2W_0}\ddot{\Psi}_Z dZ \qquad (9.16)$$

where dZ represents an infinitesimal spanwise length of the skinplate. Based on the field vibration test results, a spanwise half wavelength bending vibration mode of the skinplate is assumed and can be represented by the parallel vibration X, defined by:

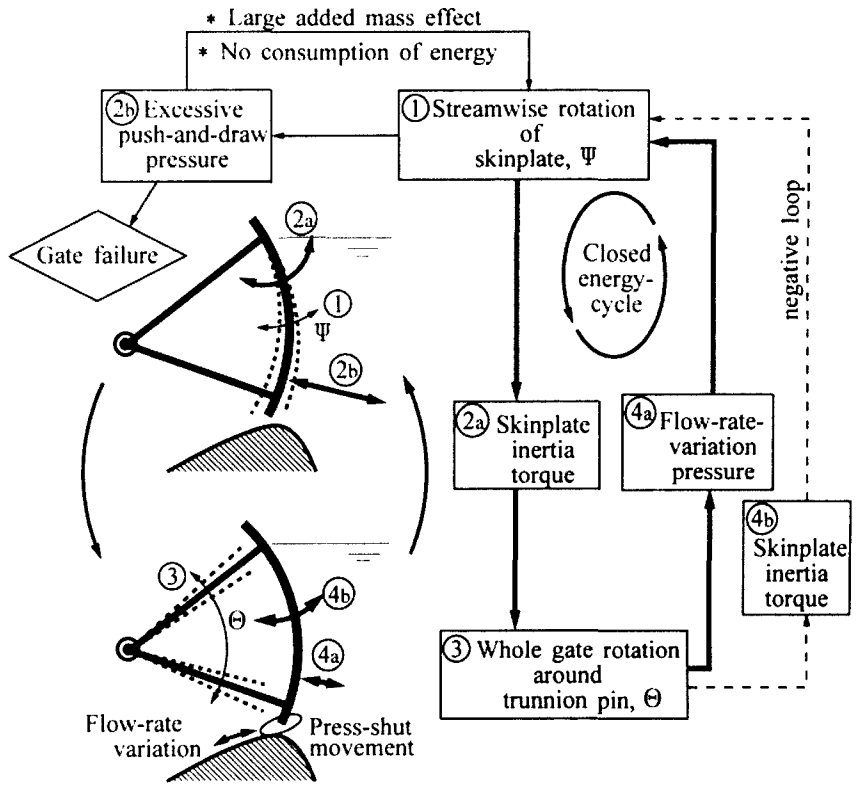

Figure 9.8: Closed energy cycle of coupled-mode self-excited vibration produced by the whole gate rigid body vibration and the skinplate streamwise rotational vibration.

$$\Psi_Z = \Psi \sin\left(\frac{Z}{W_0} + \frac{1}{2}\right)\pi \tag{9.17}$$

where Ψ represents the streamwise rotation angle of the skinplate at its spanwise center. From this expression for displacement, the inertia torque $M_{\theta\psi}$ can be calculated as follows:

$$M_{\theta\psi} = \int_Z dM_{\theta\psi} = -\frac{I_\psi}{2W_0}\ddot{\Psi}\int_{-W_0/2}^{W_0/2}\sin\left(\frac{Z}{W_0}+\frac{1}{2}\right)\pi\, dZ$$

$$= -\frac{I_\psi}{2W_0}\ddot{\Psi}\frac{2W_0}{\pi} = -\frac{1}{\pi}I_\psi\ddot{\Psi} \tag{9.18}$$

The equation of motion for the whole gate vibration around the trunnion pin can then be given as

$$\ddot{\Theta} + 2\Omega_{a\theta}\zeta_{a\theta}\dot{\Theta} + \Omega_{a\theta}^2\Theta + \frac{1}{\pi}\frac{I_\psi}{I_\theta}\ddot{\Psi} = 0 \tag{9.19}$$

On the other hand, the equation of motion of the skinplate streamwise rotational vibration can be derived and results in the following expression:

$$\int_Z\left(\ddot{\Psi}_Z + 2\zeta_{a\psi}\Omega_{a\psi}\dot{\Psi}_Z + \Omega_{a\psi}^2\Psi_Z\right)dZ - \frac{W_0}{I_\psi}\int_Z dM_{\psi\theta} + \frac{W_0}{I_\psi}\int_Z\int_R PR\, dR\cdot dZ = 0 \tag{9.20}$$

When the skinplate vibrates in the spanwise half-wavelength bending mode with a node of each side of the skinplate, the vibration-induced hydrodynamic pressure is naturally influenced by the half-wavelength

bending vibration. Therefore, the integration with respect to Z can be carried out except for the last erm on the left hand side (hydrodynamic pressure term) resulting in the following expression:

$$\ddot{\Psi} + 2\Omega_{a\psi}\zeta_{a\psi}\dot{\Psi} + \Omega_{a\psi}^{2}\Psi + \frac{\pi}{2}\frac{I_{\psi\theta}}{I_{\psi}}\ddot{\Theta} + \frac{\pi}{2I_{\psi}}\int_{-W_0/2}^{W_0/2} dZ \int_R PR\,dR = 0 \qquad (9.21)$$

Here, in order to normalize the equations of motion, Equations (9.19) and (9.21), the following dimensionless variables are introduced:

$$\psi \equiv \frac{\Psi}{\Psi_0} \quad , \quad \theta \equiv \frac{\Theta}{\Theta_0} \quad , \quad t \equiv \Omega_{a\theta}T \quad , \quad y \equiv \frac{Y}{d_0} \qquad (9.22)$$

With this non-dimensionalization, the equations of motion can be reduced ultimately to the following form:

$$\theta'' + 2\zeta_{a\theta}\theta' + \theta + \frac{1}{\pi}\frac{\alpha_I}{\alpha_*}\psi'' = 0 \qquad (9.23)$$

$$\left(1 + \delta_p\alpha_\psi\Delta m_\psi + \frac{2}{\pi}\sqrt{2}\,c_f k\alpha_\psi\Delta m_\theta\right)\psi''$$

$$+ 2\gamma_{\psi\theta}\left(\zeta_{a\psi} + \zeta_{f\psi} - \frac{1}{\pi}\sqrt{2}\,c_f k\frac{\alpha_\psi\Delta c_\theta}{\gamma_{\psi\theta}F_{a\theta}}\right)\psi' + \gamma_{\psi\theta}^{2}\psi$$

$$= \alpha_*\left\{-\left(\frac{\pi}{2}\alpha_{I\psi} + \sqrt{2}\,c_f\frac{\alpha_\psi\Delta m_\theta}{r_{sa}}\right)\theta'' + \sqrt{2}\,c_f\frac{\alpha_\psi\Delta c_\theta}{r_{sa}F_{a\theta}}\theta'\right\} \qquad (9.24)$$

where, l_G is the reduced eccentricity of the center of gravity from the trunnion pin, α_I is the moment-of-inertia ratio, α_* is the vibration amplitude ratio, each of which can be defined, respectively, along with other useful parameters as

$$\alpha_I \equiv \frac{I_\psi}{I_\theta} \quad , \quad \alpha_* \equiv \frac{\Theta_0}{\Psi_0}, \quad \gamma_{\psi\theta} \equiv \frac{\Omega_{a\psi}}{\Omega_{a\theta}} \quad , \quad \alpha_\psi \equiv \frac{\rho d_0^{2}W_0}{I_\psi / R_S^{2}} \quad , \quad F_{a\theta} \equiv \Omega_{a\theta}\sqrt{\frac{d_0}{g}} \qquad (9.25)$$

The dimensionless factors Δm_ψ, Δm_θ, Δc_ψ and Δc_θ all represent the effects of the hydrodynamic force. The first two parameters, Δm_ψ and Δm_θ , are the reduced added mass, while Δc_ψ and Δc_θ are the fluid excitation ratio and the fluid damping ratio, respectively. As the Froude number F increases, Δm_θ and Δc_ψ rapidly decrease to zero, while Δm_ψ and Δc_θ increase rapidly and approach asymptotic constant values depending on the rotation center height.

The dynamic stability criterion diagram of the gate can be determined from the simultaneous solution of Equations (9.23) and (9.24), which must be undertaken numerically in a computer-simulation to obtain their approximate solutions

9.3 Dynamic Stability of Gate #2

Major specifications of the Thermalito Diversion Tainter-gate are listed in Table 9.2, in which reservoir flow conditions, sizes, mass, moments of inertia, in-air natural vibration frequencies, streamwise rotation center height, vibration angle, dam crest angle, eccentricity of trajectory line of the center of

gravity from trunnion pin, and press-open angle. The last these factors, the press-open angle Θ_{s0} is a key factor in the determination of the dynamic stability. This press-open angle can be determined by subtracting the vibration angle of depression, Θ_{vib}, from the inclination angle of the dam crest sill just under the skinplate, Θ_{crest}. The press-open angle takes on a value of 7.74° (for Gate #2) and 10.5° (for Gate #3) for the parallel vibration mode M_{x1} and 31.5° for the rotational vibration mode M_{x2}. Increasing the press-open angle, decreases the dynamic instability in terms of both its instability level and its frequency region.

The required non-dimensional factors necessary for the calculation of the hydrodynamic pressures induced by gate vibrations are presented in Table 9.3. Water depth ratio β^* representing a reduced gate submergence depth takes a value of 1.0, since the over-hang length of dam crest in front of the skinplate is larger than the half of the gate submergence depth, as seen in Figure 2.3. Instantaneous flow rate coefficient c_f takes a value of 0.7, while pressure correction coefficient δ_p takes on a value of 1.1, which was determined by careful experimentation with model gates (see references [9], [16]).

The in-air natural vibration frequencies, calculated by FEM analysis, and in-water vibration frequencies and damping ratios, determined in the present field tests, are all listed in Table 9.4 for each natural vibration mode. A key factor in determining the dynamic stability of the Thermalito gates is the in-water frequency ratio γ_{nw}, defined by

$$\gamma_{nw} \equiv \frac{\Omega_{nwx,\psi}}{\Omega_{a\theta}} \quad , \tag{9.26}$$

where $\Omega_{nwx,\psi}$ is the in-water natural vibration frequency of the streamwise vibration and $\Omega_{a\theta}$ is natural vibration frequency of the whole gate vibration around the trunnion pin. This frequency ratio takes a value of 0.85 and 0.86 for the parallel vibration mode M_{x1} and 1.0 for the rotational vibration mode M_{x2}, as explained at the beginning of the preceding Section 9.1. The in-air damping ratios in Table 9.4 are assigned the same values as the in-water ones, for non-conservative estimate, predicting stability when there is really instability.

With all the data in Table 9.2 to 9.4, the dynamic stability analysis can now be performed both for the coupling of Mode M_{X1} with Mode M_Z, and of Mode M_{X2} with Mode M_Z.

Table 9.2: Major specifications of the Thermalito Diversion Dam Tainter-gate.

gate submergence depth d_0	6.38 m	
gate opening B	about 0.1 m	
spanwise length W_0	12.166 m	
radial arm length R_a	9.144 m	
moment of inertia of whole gate around trunnion pin I_θ	1.62×10^6 kgm^2	
mass of skinplate M_s	19.5×10^3 kg	
moment of inertia of skinplate I_ψ	–	88.1×10^3 kgm^2
in-air natural vibration frequency	Ω_{nax} = 20.8 Hz	$\Omega_{na\psi}$ = 13.7 Hz
in-air skinplate vibration mode	M_{X1} (parallel)	M_{X2} (rotational)
rotation center height R_S	∞	about 2.0 m
vibration angle of depression Θ_{vib}	10.76° for #2 8.0° for #3	-13°
inclination angle of dam crest sill Θ_{crest}	18.5°	
eccentricity of gravity trajectory L_G	1.2 m for #2 0.76 m for #3	—
press-open angle $\Theta_{s0}(=\Theta_{crest}-\Theta_{vib})$	7.74° for #2 10.5° for #3	31.5°

Table 9.3: Non-dimensional factors for calculations of hydro-dynamic pressures.

skinplate vibration mode	M_{X1} (parallel)	M_{X2} (rotational)
basic Froude number F_0	105	69
depth ratio β^*	1.0	
water-to-gate mass ratio α_ψ	25.3	106
instantaneous flow rate coefficient c_f	0.7	
pressure correction coeddicient δ_p	1.1	

Table 9.4: In-air and in-water vibration frequencies and damping ratios for each natural vibration mode.

Mode Name	Viberation Mode Shape	In-water (measured)			Caluclated in-air freqency Ω_a (Hz)	Over-estimated in-air damping ratio ζ_a	In-water frequency ratio γ_{nw} $\left(\equiv\frac{\Omega_{nw,x}}{\Omega_{n\theta}}\right)$
		Freqency Ω_w (Hz)	Damping ratio ζ_w	Height of rotation center R_S (m)			
M_z	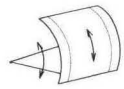	$\Omega_{nw\theta}$ 6.5 (for #2) 6.6 (for #3)	$\zeta_{w\theta}$ 0.012	-	$\Omega_{a\theta}$ 6.5	$\zeta_{a\theta}$ 0.012	-
M_{x1}	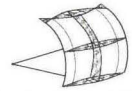	Ω_{nwx} 5.5 (for #2) 5.6 (for #3)	ζ_{wx} 0.030	∞	Ω_{ax} 20.9	ζ_{ax} 0.030	0.85 (#2, #3)
M_{x2}	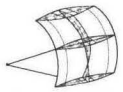	$\Omega_{nw\psi}$ 6.5 (for #2) 6.6 (for #3)	$\zeta_{w\psi}$ 0.012	2.0	$\Omega_{a\psi}$ 14.9	$\zeta_{a\psi}$ 0.012	1.0

Case (1): Coupling of the skinplate parallel vibration M_{X1} with the whole gate vibration M_Z

The dynamic stability criterion diagram of Thermalito Gate #2, calculated for the coupling of the skinplate parallel vibration mode M_{X1} and the whole gate vibration mode M_Z, is shown in Figure 9.9, in which the ordinate is the critical damping ratio ζ_c required for entire dynamic stability, while the abscissa

is the in-water natural vibration frequency ratio γ_{nw}, defined by Equation (9.26). The region under the curve is the region of instability, while the region above the curve is the region of stability. It is of significance to note the very intense dynamic instability that appears in the region where the frequency ratio is just slightly smaller than 1.0.

As listed in Table 9.4, the measured value of Ω_{nwx} is 5.5 Hz and $\Omega_{a\theta}$ is 6.5 Hz, yielding an in-water natural vibration frequency ratio of γ_{nw} = 0.846. In addition, the in-air damping ratio is over-estimated to be ζ_{ax} = 0.030 for the skinplate streamwise parallel vibration. These values can then be plotted as the filled circle on the stability diagram in Figure 9.9. The location of the data point for Gate #2 undergoing coupled vibration of the parallel streamwsie vibration mode with the whole gate rotation mode indicates a narrow escape from the unstable region.

Based on this analysis, one may conclude that the Thermalito Diversion Dam Gate #2 barely maintained its dynamic stability for the coupling of Modes M_{XI} and M_Z at the tested condition with a gate submergence depth of d_0 = 6.38 m.

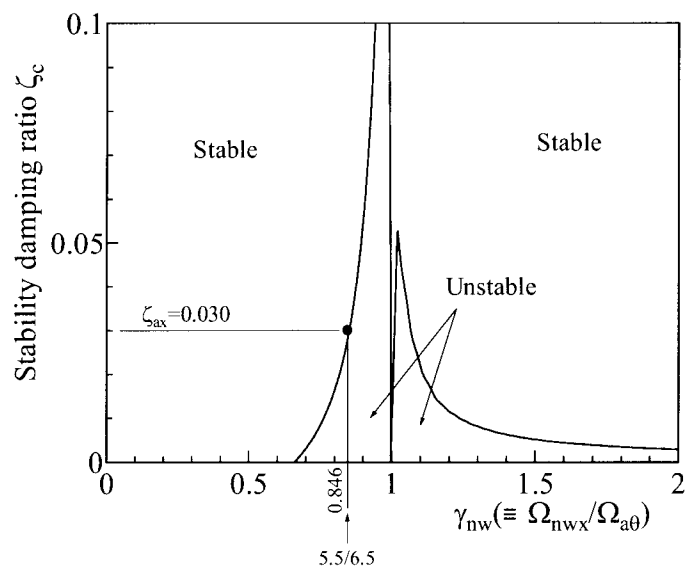

Figure 9.9: Dynamic stability criterion diagram for the coupling of Modes M_{XI} and M_Z for Gate #2 at the tested condition with d_0 = 6.38 m.

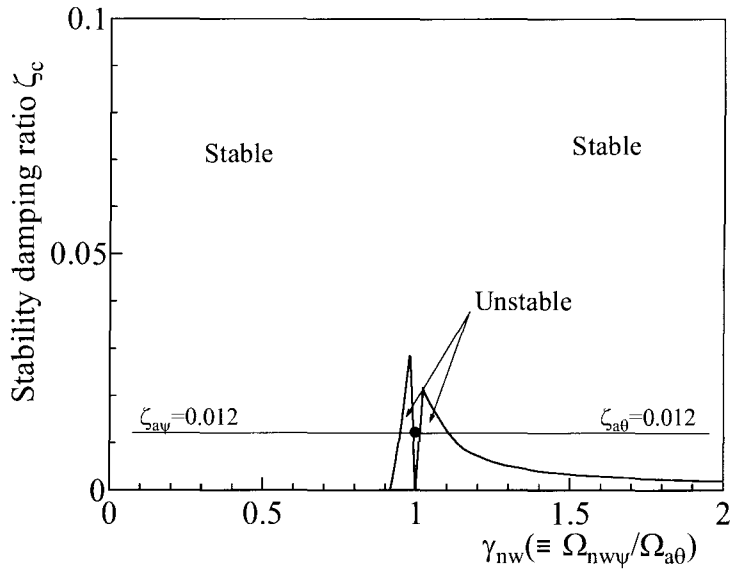

Figure 9.10: Dynamic stability criterion diagram for the coupling of Modes M_{X2} and M_Z For both Gates #2 and #3 at the tested condition with d_0 = 6.38 m.

Case (2): Coupling of the skinplate rotational vibration M_{x2} with the whole gate vibration M_z

Similar calculations were made for the coupling of Modes M_{X2} and M_Z, thus resulting in the dynamic stability criterion shown in Figure 9.10, where the dynamic instability level is far smaller than for the previous coupling shown in Figure 9.9. As listed in Table 9.4, the measured value of $\Omega_{nw\psi}$ is 6.6 Hz and $\Omega_{a\theta}$ is also 6.6 Hz, resulting in a natural vibration frequency ratio γ_{nw} of exactly 1.0. In addition, the in air damping ratio is over-estimated to be 0.012 for both the skinplate streamwise rotational vibration and whole gate vibration. These values can then be plotted as the filled circle on the stability diagram in Figure 9.10. The location of the data point again indicates a narrow escape from the unstable region.

Based on this analysis, one may conclude that the Thermalito Diversion Dam Gate #2 barely maintained its dynamic stability for the coupling of Modes M_{X2} and M_Z at the tested condition with a gate submergence depth of d_0 = 6.38 m.

9.4 Dynamic Stability of Gate #3

The present field tests for Gate #3 identified Modes M_Z, M_{X1} and M_{X2}, as shown in Table 9.4, all of which exhibit modes shapes and in-water vibration frequencies that are very similar with those of Gate #2. The only substantial difference is in the press-open angle Θ_{so} for the parallel vibration mode M_{X1}, which takes on a value of 10.5°, somewhat larger than that for Gate #2. Because of this difference in press-open angle, the dynamic stability criterion curve for Gate #3 for the coupling of Modes M_{X1} and M_Z differs from that for Gate #2 shown previously in Figure 9.9. However, the dynamic stability curve for the coupling of Modes M_{X2} and M_Z for Gate #3 is just the same as that for Gate #2, as shown in Figure 9.10.

Since the press-open angle Θ_{so} for Gate #3 is larger than that for Gate #2, the dynamic stability

criterion curve is more compressed yielding a narrower frequency region of dynamic instability, as shown in Figure 9.11. However, it should be carefully noted that there is still a region of very intense dynamic instability for the reduced frequency range just less than 1.0.

The measured value of Ω_{nwx} is 5.6 Hz and $\Omega_{a\theta}$ is 6.6 Hz, yielding an in-water natural vibration frequency ratio of $\gamma_{nw} = 0.85$. Using an in-air damping ratio $\zeta_{ax} = 0.030$, the filled circle, representing the measured state of stability, can be plotted on the dynamic stability curve in Figure 9.11. Again this data point lies just within the region of stability.

Based on this analysis, one may conclude that the Thermalito Diversion Dam Gate #3 also barely maintained its dynamic stability for the coupling of Modes M_{X2} and M_Z at the tested condition with a gate submergence depth of $d_0 = 6.38$ m.

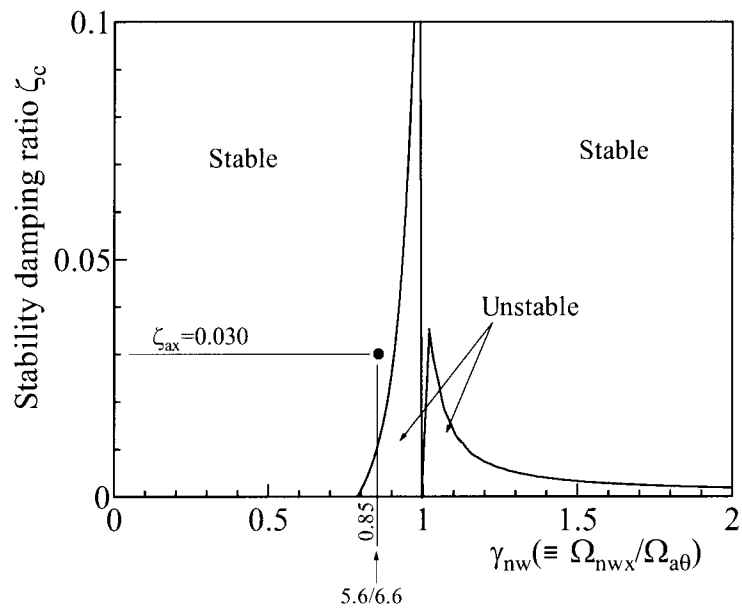

Figure 9.11: Dynamic stability criterion diagram for the coupling of the Mode M_{X1} and M_Z for Gate #3 at the tested condition with $d_0 = 6.38$ m.

10. THEORETICAL EXAMINATION OF DYNAMIC STABILITY AT OTHER SUBMERGENCE LEVELS

It is of great importance to understand the behavior of the dynamic stability curves in Figures 9.9 and 9.11 with variation in the submergence level. In the following it will be shown that for the Thermalito gates decreasing the submergence from the tested level of d_0 = 6.38 m moves the condition point to the right along the abscissa of the dynamic stability curve, *i.e.*, just into the region of intense dynamic instability. The reasoning for this statement is that as the submergence level decreases, the effect of water added mass on the skinplate streamwise vibrations decreases, yielding an increase in the in-water natural vibration frequency Ω_{nwx} and a correspondingly higher frequency ratio, $\gamma_{nw,}$, moving the condition point to the right along the abscissa of Figures 9.9 and 9.11. Just the opposite trend occurs with increasing submergence. Clearly, it is desirable to determine precisely the gate stability under these different submergence conditions. In the present chapter, stability analyses will be presented for various upstream submergence levels, to provide an overall picture of the stability of the tested Thermalito gates.

10.1 Dynamic Stability of Gate #2

Case (1): Coupling of the skinplate parallel vibration M_{x1} with the whole gate vibration M_z

Obviously, the gate submergence depth d_0 decreases with decreasing upstream water level producing a corresponding decrease in the water-to-gate mass ratio α_x. In fact according to Equation (9.4), with a constant value of skinplate mass in the denominator, the decrease in the water-to-gate mass ratio is proportional to d_0^2, as is shown by the blue line in Figure 10.1. In contrast, the reduced water added mass Δm_x, defined by Equation (9.1a), remains constant with changing submergence depths, as shown by the dashed line in Figure 9.2 and by the blue line in Figure 10.2. As a result, the frequency ratio Ω_{wx}/Ω_{ax}, calculated using Equation (9.3), significantly increases with decreasing d_0, as shown in Figure 10.3 where the frequency ratio is on the right vertical axis and the submergence depth is on the abscissa. The inherent frequency ratio γ_{nw}, a key factor in the stability calculation defined by Equation (9.26), can be rewritten as

$$\gamma_{nw}(\equiv \frac{\Omega_{nwx,\psi}}{\Omega_{a\theta}}) = \frac{\Omega_{nwx,\psi}}{\Omega_{ax,\psi}} \frac{\Omega_{ax,\psi}}{\Omega_{a\theta}} \quad , \qquad (10.1)$$

The first quotient on the right hand side of Equation (10.1) is the value plotted on the right vertical axis in Figure 10.3. The second quotient on the right-hand side of Equation (10.1) is just the ratio of in-air frequencies and takes on the fixed value of 3.23 (with Ω_{ax} = 20.99 Hz and $\Omega_{a\theta}$ = 6.5 Hz) for the Thermalito gates (see Table 9.4). Thus, the inherent frequency ratio γ_{nw} is just a scaled version of the frequency ratio and is also represented by the plotted line in Figure 10.3 using the left vertical scale.

In consideration of Figure 10.3, it is clear that the inherent frequency ratio γ_{nw} increases rapidly with decreasing gate submergence d_0. The value of $\gamma_{nw} = 0.846$ at the tested gate submergence of $d_0 = 6.38$ m increases to $\gamma_{nw} = 1.0$ at a gate submergence of $d_0 = 5.3$ m with rather serious consequences.

With these variations in the reduced added mass and the inherent frequency ratio, calculation of the dynamic stability curve, similar to those in Chapter 9, can be undertaken for a variety of upstream water levels. In addition to the previously explained decrease in water-to-gate mass ratio (α_x decreases proportionally with d_0^2), decreasing the submergence depth d_0 also decreases the wetted area of the skinplate, there by decreasing the amount of energy that can be supplied to the skinplate vibration. As a result, the level of the dynamic instability decreases, but relatively slowly, with decreasing upstream water depth, as shown in Figure 10.4, where five dynamic stability curves are shown for gate submergences ranging from 6.38 m (as tested) to 4.5 m. It should be noted here that, for all values of d_0, a very intense region of dynamic instability appears over a limited frequency range when the frequency ratio is slightly smaller than 1.0.

In the dynamic stability diagrams in Figures 10.4(a) to 10.4(c), data points are plotted at each inherent frequency ratio γ_{nw} (calculated for each gate submergence d_0 in Figure 10.3) for the presumed condition of the Thermalito Gate #2, assuming the in-air damping ratio $\zeta_{ax} = 0.03$ for synchronized streamwise parallel vibration remains constant. The gate condition point for $d_0 = 6.38$ m (as tested) in Figure 10.4(a), just barely in the stable region, moves into the center of the unstable region when $d_0 = 5.8$ m, as shown in Figure 10.4(b), and then moves to the right-side of the unstable region when $d_0 = 5.4$ m, as shown in Figure 10.4(c). With a further decrease in d_0, the gate condition point moves into the center of right-side unstable region when $d_0 = 5.0$ m, as shown in the Figure 10.4(d). For this right side region of instability, the vibration can be considered forced vibration of the rigid-body rotation mode about the trunnion pin (see Anami, 2000). Therefore, the assumed value for the in-air damping ratio of $\zeta_{a\theta} = 0.012$ for the synchronized whole gate rotational vibration around trunnion pin was used in plotting the gate condition point. With a further reduction in the gate submergence, to a value of $d_0 = 4.50$ m, the gate condition point moves to the right-side of this second unstable region, as shown in Figure 10.4(e). For submergence levels less than 4.5 m the gate condition point is in the stable region.

Based on this analysis, it is concluded that the coupled-mode dynamic instability involving the coupling of Modes M_{X1} and M_Z can appear over a range of gate submergence depths where $4.5 \text{ m} < d_0 < 6.38$ m. The dynamic instability level over this range of submergence depths can be quantified as the value of the excitation ratio. The excitation ratio, ξ, is the difference between the stability damping ratio ζ_c, shown in Figure 10.4, and the appropriate value of in-air damping ratio ζ_a for the gate condition points plotted in the same figure. That is, $\xi = (\zeta_c - \zeta_{ax})$ for $\gamma_{nw} < 1.0$ and $\xi = (\zeta_c - \zeta_{a\theta})$ for $\gamma_{nw} > 1.0$. Figure 10.5 shows the excitation ratio as a function of the gate submergence depth. The most intense dynamic instability appears at $d_0 = 5.5$ m with an excitation ratio significantly in excess of 0.1.

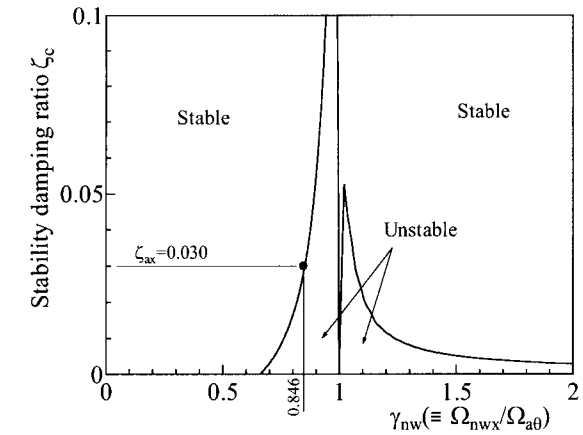

(a) d_0 = 6.38 m

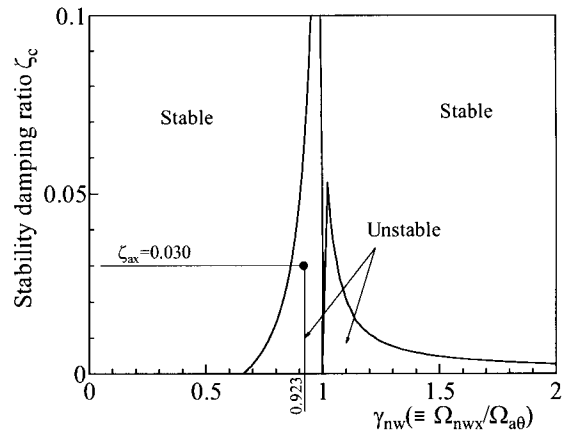

(b) d_0 = 5.8 m

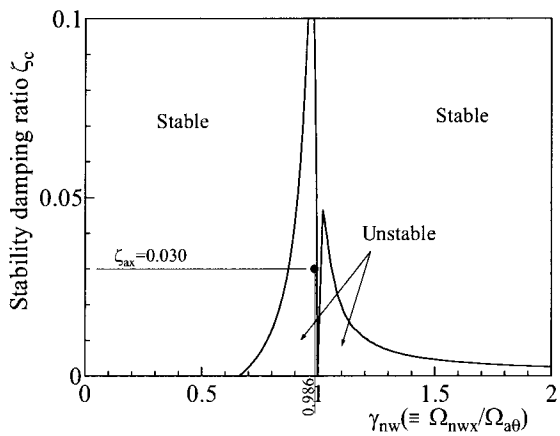

(c) d_0 = 5.4 m

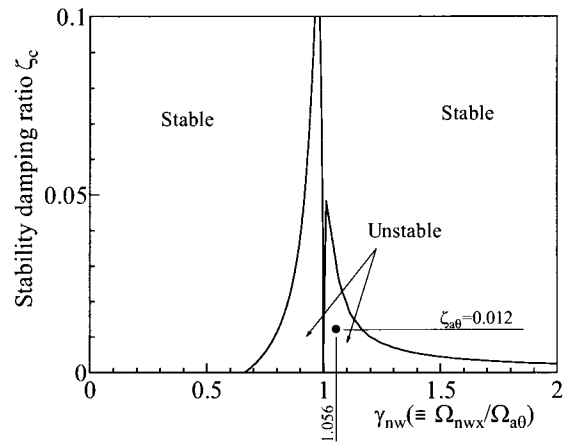

(d) d_0 = 5.0 m

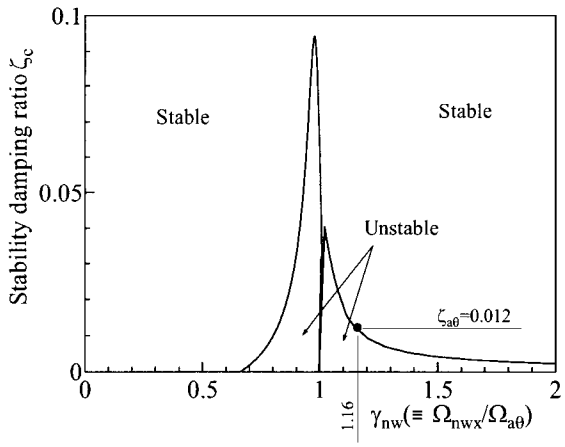

(e) d_0 = 4.5 m

Figure 10.4: Dynamic instability of the coupled-mode vibration of Modes M_{x1} and M_z of the Thermalito Diversion Dam Gate #2 at various submergence levels.

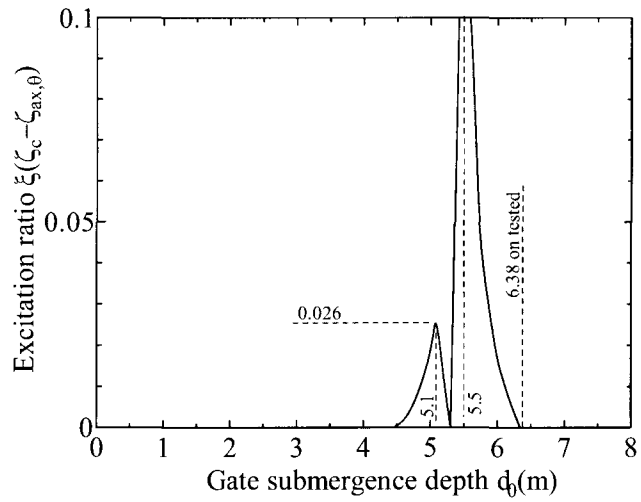

Figure 10.5: Dynamic instability level of the coupled-mode vibration of Modes M_{x1} and M_z of the Thermalito Diversion Dam Gate #2

Case (2): Coupling of the skinplate rotational vibration M_{x2} with the whole gate vibration M_z

Similar calculations can be made for the coupling of Modes M_{x2} and M_z. The water-to-gate mass ratio α_ψ, defined by Equation (9.4), is shown by the red line in Figure 10.1, while the reduced water added mass Δm_x, defined by Equations (9.1a and 9.1b), is shown by the red line in Figure 10.2. As a result, the frequency ratio Ω_{wx}/Ω_{ax} and the inherent frequency ratio γ_{nw} both change with d_0, as shown in Figure 10.6, where γ_{nw} increases the values greater than 1.0 with decreasing d_0 and decreases to values less than 1.0 with increasing d_0.

The dynamic stability diagrams are shown in Figure 10.7, for values of submergence depth ranging from 6.55 m to 6.05 m. The gate condition points are also plotted using an in-air damping ratio $\zeta_{a\psi,\theta}$ = 0.012.

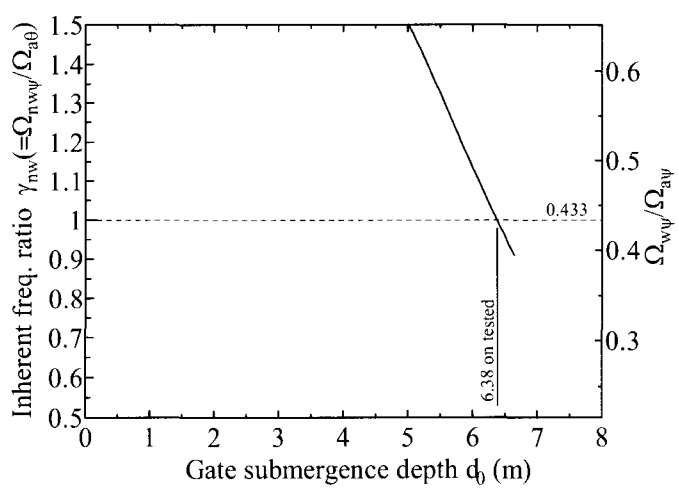

Figure 10.6: Frequency ratio γ_{nw} and in-water to in-air vibration frequency ratio $\Omega_{w\psi}/\Omega_{a\psi}$ of skinplate streamwise rotational vibration.

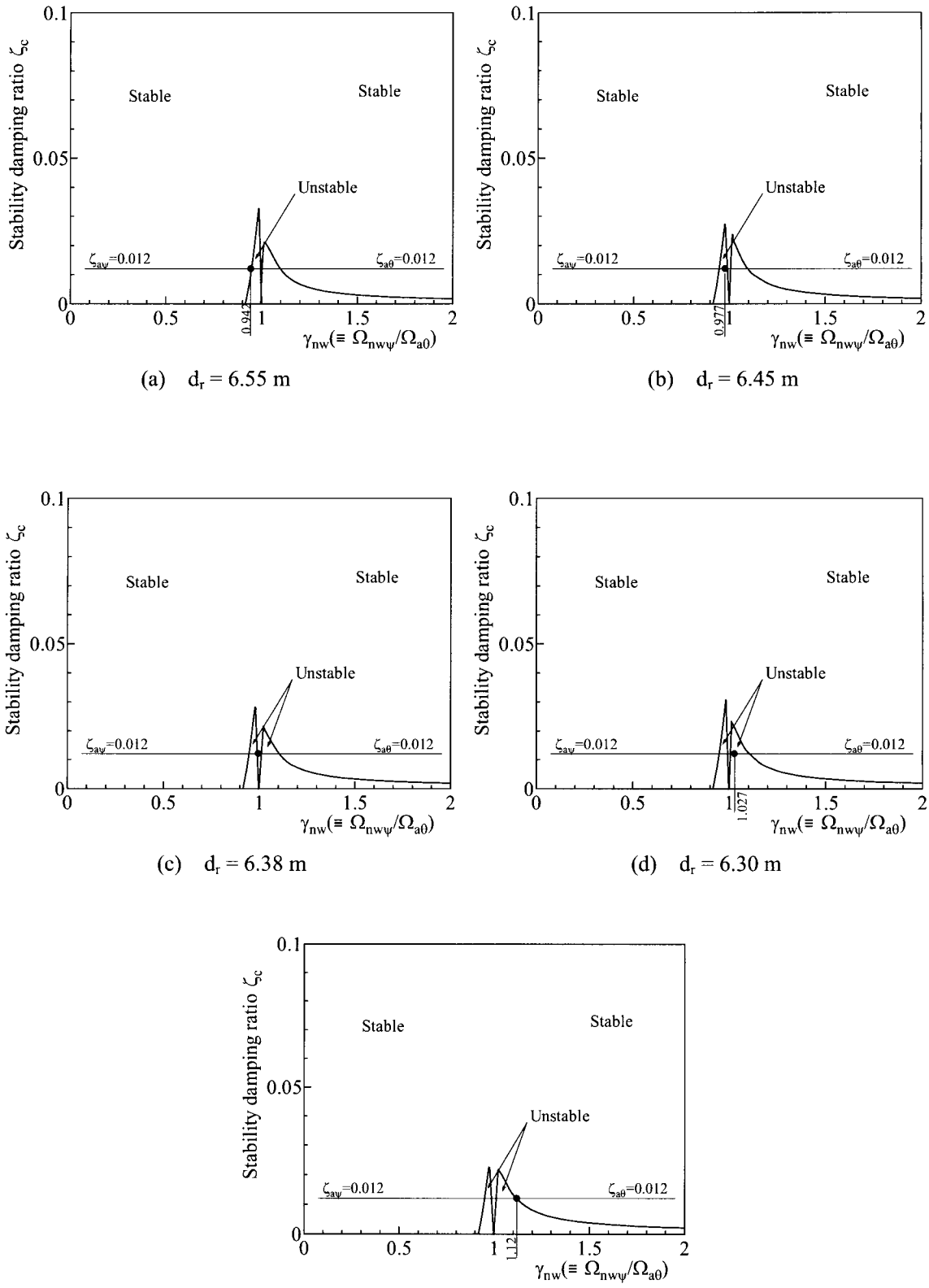

(a) d_r = 6.55 m

(b) d_r = 6.45 m

(c) d_r = 6.38 m

(d) d_r = 6.30 m

(e) d_r = 6.05 m

Figure 10.7: Dynamic instability of the coupled-mode vibration of Modes M_{x2} and M_z of the Thermalito Diversion Dam Gate #2 at various submergence levels.

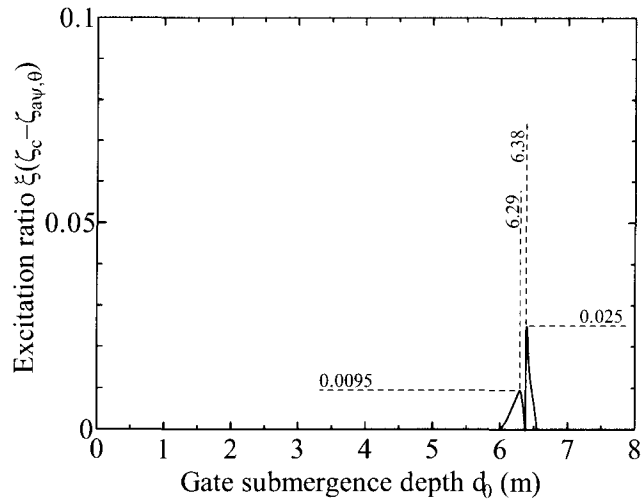

Figure 10.8: Dynamic instability level of the coupled-mode vibration of Modes M_{x2} and M_z of the Thermalito Diversion Dam Gate #2.

On the basis of this analysis, it is concluded that the coupled-mode dynamic instability involving the coupling of Modes M_{X2} and M_Z can appear over the gate submergence range 6.05 m < d_0< 6.55 m. The dynamic instability level represented by the excitation ratio, where $\xi = (\zeta_c - \zeta_{a\psi})$ for $\gamma_{nw} < 1.0$ and by $\xi = (\zeta_c - \zeta_{a\theta})$ for $\gamma_{nw} > 1.0$, is shown in Figure 10.8. The dynamic instability appears for 6.05 m< d_0<6.55 m, but at a level that is far smaller than that found for the coupling of Modes M_{X1} and M_Z, previously shown in Figure 10.5

10.2 Dynamic Stability of Gate #3

Similar calculations can be carried out for Gate #3, with the predominant difference being the value of the press-open angle Θ_{so} for the parallel vibration mode M_{X1}, which takes a value of 10.5° for Gate #3, compared with the value of 7.74° for Gate #2. The value of this pres-open angle changes the dynamic stability curve for the coupling of Modes M_{X1} and M_Z , but does not affect the coupling of Modes M_{X2} and M_Z.

Case (1): Coupling of the skinplate parallel vibration M_{x1} with the whole gate vibration M_z

The dynamic stability criterion diagrams and gate condition points are plotted in Figure 10.9, in which an in-air damping ratio of $\zeta_{ax} = 0.030$ was used for $\gamma_{nw} < 1.0$ and $\zeta_{a\theta} = 0.012$ for $\gamma_{nw} > 1.0$. The dynamic instability of the coupled-mode vibration of Modes M_{X1} and M_Z can appear over the range of gate submergence depths 6.0 m < d_0< 4.65 m. The dynamic instability level, represented by the excitation ratio $\xi = (\zeta_c - \zeta_{ax})$ for $\gamma_{nw} < 1.0$ and by $\xi = (\zeta_c - \zeta_{a\theta})$ for $\gamma_{nw} > 1.0$, is shown in Figure 10.10, and is seen to be relatively smaller than the corresponding level for Gate #2, as shown previously in Figure 10.5. However, the intense dynamic instability still appears at d_0 = 5.5 m, with an excitation ratio of about 0.1, which is still cause for concern.

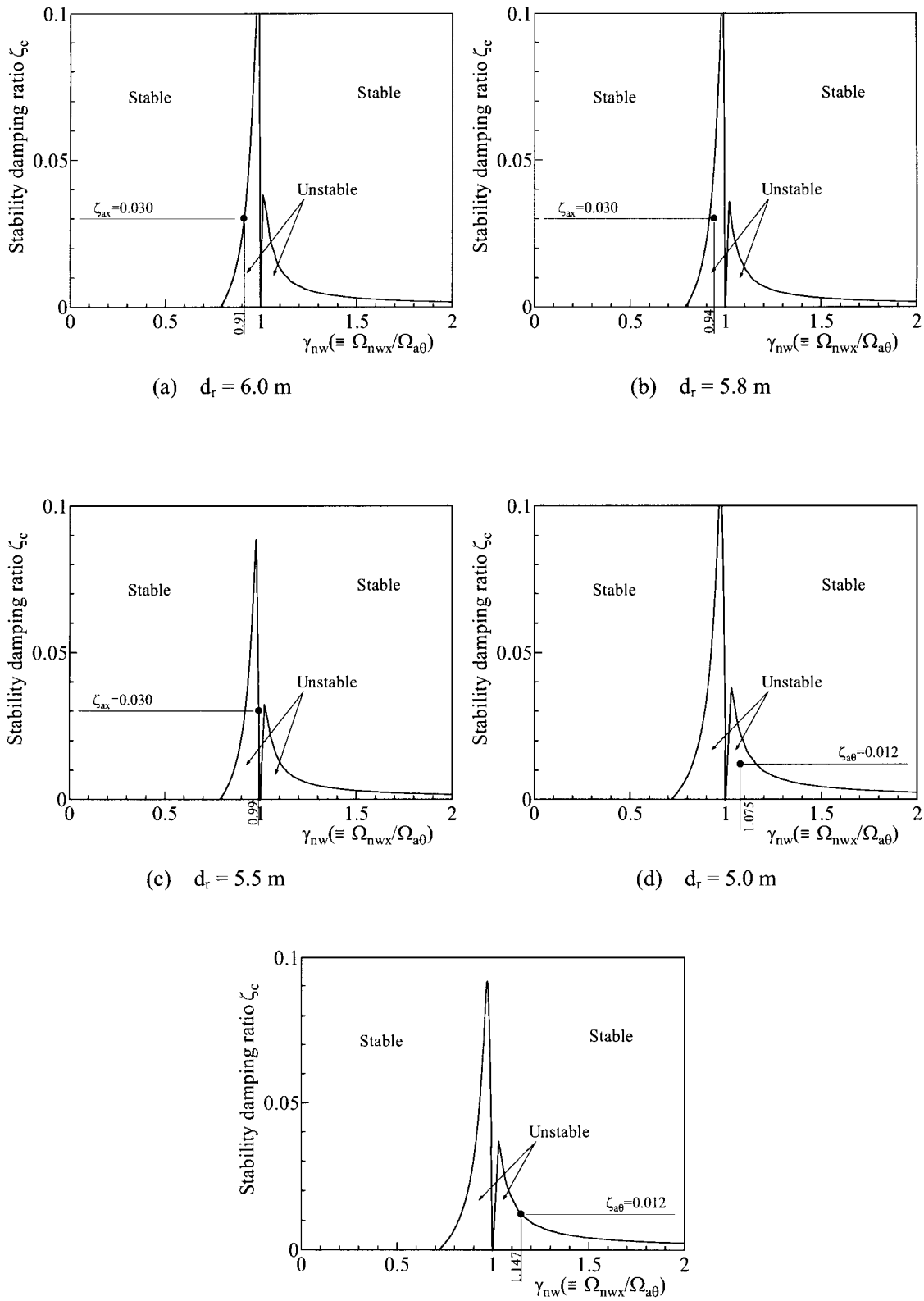

Figure 10.9: Dynamic instability of the coupled-mode vibration of Modes M_{x1} and M_z for the Thermalito Diversion Dam Gate #3 at various submergence levels.

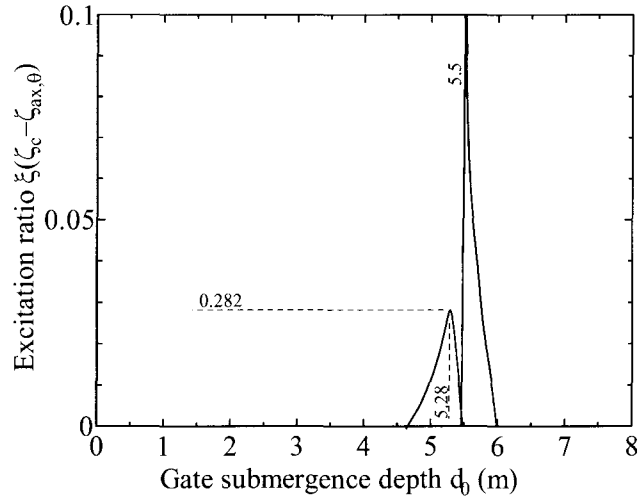

Figure 10.10: Dynamic instability level of the coupled-mode vibration of Modes M_{x1} and M_z of the Thermalito Diversion Dam Gate #3.

11. TRIGGER LEVEL OF VIBRATION NEEDED TO INITIATE SELF-EXCITED VIBRATIONS

As presented in Chapter 10, the Thermalito Diversion Dam Tainter gate possesses potential intense coupled-mode dynamic instabilities for certain upstream submergence levels. In the dynamic stability diagrams, shown in Figures 10.4, 10.7 and 10.9, special attention should be paid to the value of the in-air damping ratio for whole gate vibration around trunnion pin, $\zeta_{a\theta}$, which was assumed to take on a value of 0.012. This value was identified in the present field tests in which a very small amplitude damped vibration was trigged. Therefore, this in-air damping ratio does not include the Coulomb damping effects, but rather mainly results from the internal damping of wire cables and gate structures. In Tainter gates, the watertight rubber seals on both sides of the skinplate are pressed by the hydrostatic pressure against the seal plates embedded in the concrete piers, producing a large Coulomb friction force. At the same time, the large hydraulic force on the skinplate presses the trunnion pins against the bushings, producing an additional Coulomb friction force.

The damping effects due to these frictional forces can potentially cancel the intense dynamic instability, shown in Figures 10.4, 10.7 and 10.9. To quantify the effects of Coulomb damping, it will be represented as an equivalent viscous damping ratio ζ_e (see Timoshenko, et al. (1974)) given by

$$\zeta_e = \frac{2}{\pi} \cdot \frac{A_0}{A} \quad , \tag{11.1}$$

where A_0 represents the static displacement of the hoisting chains/cables, due to the frictional force, and A is the vibration amplitude of the skinplate in the whole gate rotary mode around the trunnion pin. Therefore, as the vibration amplitude A decreases, the equivalent viscous damping ratio ζ_e increases resulting in a corresponding increase in the resultant damping ratio for the whole gate vibration around the trunnion pin, as given by $(\zeta_{a\theta} + \zeta_e)$. Increasing the resultant damping ratio lowers the dynamic stability damping ratio (the damping the gate must possess to remain stable) in the frequency region of $\gamma_{nw} < 1.0$, as shown by the red arrow in Figure 11.1(a). When $(\zeta_{a\theta} + \zeta_e)$ takes on a critical value of $\zeta_{ca\theta} = 0.078$, the dynamic stability curve intersects the line of plotted data with $\zeta_{ax} = 0.030$ for the Thermalito gate. At this critical value of resultant damping, the gate is neutrally stable, vibrations will neither grow nor attenuate. Under routine conditions with no vibration (*i.e.*, $A = 0$), the equivalent viscous damping ratio ζ_e becomes infinite and hence the gate condition point is in the stable region, thus resulting in apparent complete dynamic stability for the gate. This apparent stability is denoted as "friction-maintained dynamic stability."

However, this friction-maintained dynamic stability is actually a meta-stable state, a dangerous state that can suddenly become unstable. With a sudden triggering event (such as a sudden release from "bound-up" rusty condition at the trunnion pin (see Final Report for Folsom Gate Failure, 2005), a rusted gate chain, or an earthquake/landslide-induced tsunami) that produces a sufficiently large displacement, the damping effect due to the Coulomb friction drastically decreases in inverse proportion to the vibration amplitude. Thus, the essential dynamic instability may occur any time such a triggering event occurs, as

shown by the red arrow in Figure 11.1(b). It is absolutely essential to establish the amplitude of the initial displacement trigger that reduces the damping below the required stability level and leads to instability.

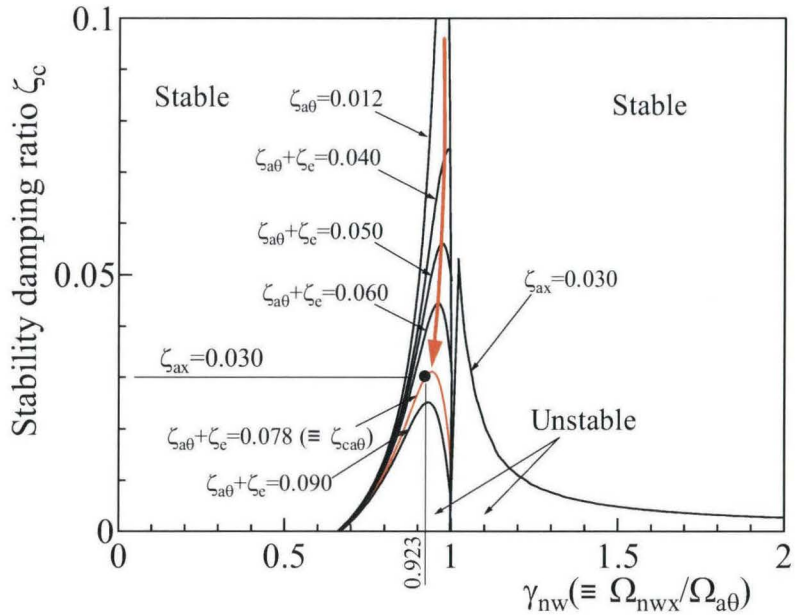

(a) With increasing Coulomb damping, ie. with decreasing vibration amplitude.

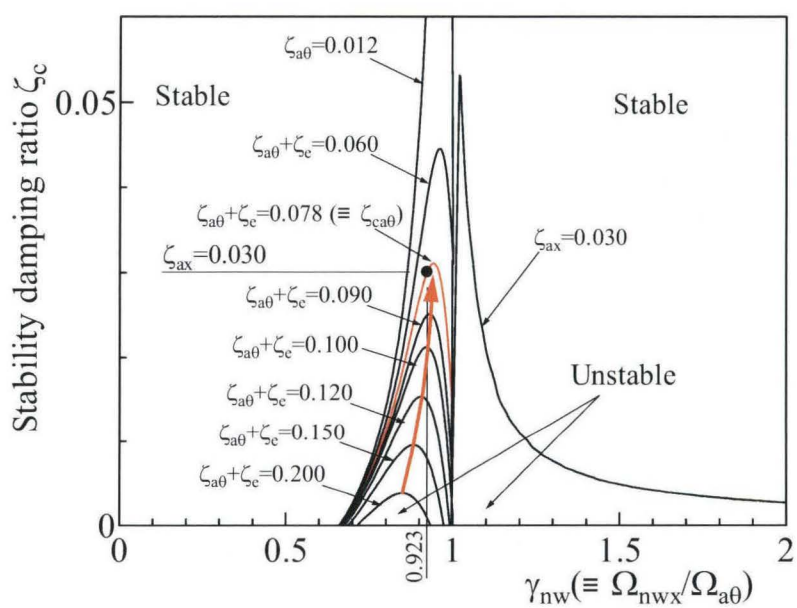

(b) With decreasing Coulomb damping, ie. with increasing vibration amplitude.

Figure 11.1: Stability damping ratio ζ_c (for $\gamma_{nw} < 1.0$) depending upon Coulomb damping ζ_e, for the coupling of Mode M_Z and M_{X1} of Gate #2 at a critical damping ratio of 0.078, with the conditions of $d_r = 5.8$ m and B = 0.01 m.

The data point plotted in the region of $\gamma_{nw} < 1.0$ in Figure 11.1 lies in the unstable region when the damping is less than the critical values, that is when

$$\zeta_{a\theta} + \zeta_e < \zeta_{ca\theta} \tag{11.2}$$

where the streamwise length from the fulcrum to the contact point on the side plate is 54 mm. Assuming the friction force acting on the side J-seal and on the trunnion pin, the extensional displacement A_0 (= F_r/K) of the wire ropes can be calculated.

Trial and error calculations of dynamic instability were made for various values of $\zeta_{ca\theta}$ (= 0.012 + ζ_e), in order to ascertain the equivalent damping ratio ζ_e. After that, the initial displacement A was calculated with a trunnion frictional coefficient μ_t of 0.15 (a common value for a new trunnion) and a frictional coefficient μ_s of the rubber side J-seals of 0.5.

The calculated equivalent damping ratio ζ_e and threshold value of the initial displacement trigger A for the coupling of Modes M_Z and M_{X1} of Gate #2 are shown in Figure 11.4 and Figure 11.5, respectively. The abscissa is the gate submergence depth d_0 (= d_r - B). For completely stable operation of the gate, the initial displacement trigger A must never exceed 2.3 mm with d_0 = 5.7 m. With such a small triggering threshold amplitude, careful consideration of the coupling of Modes M_Z and M_{X1} and the resulting self-excited vibrations must be included in the operation of the gate.

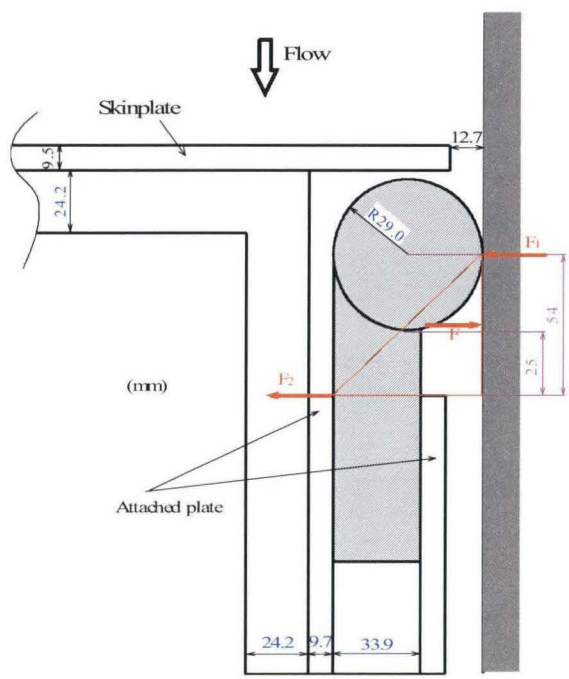

Figure 11.3: Schematic view of the rubber J-seal on each side of the skinplate.

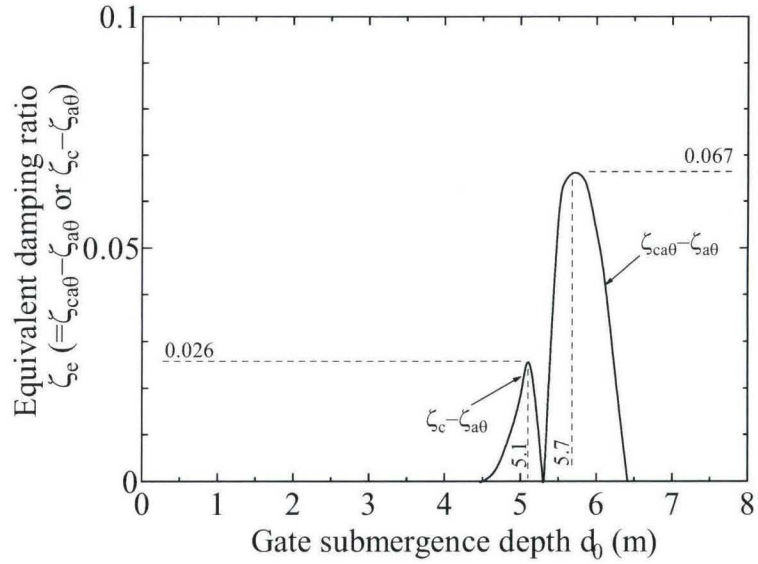

Figure 11.4: Equivalent damping ratio to initiate self-excited vibrations for the coupling of Modes M_Z and M_{X1} for Gate #2.

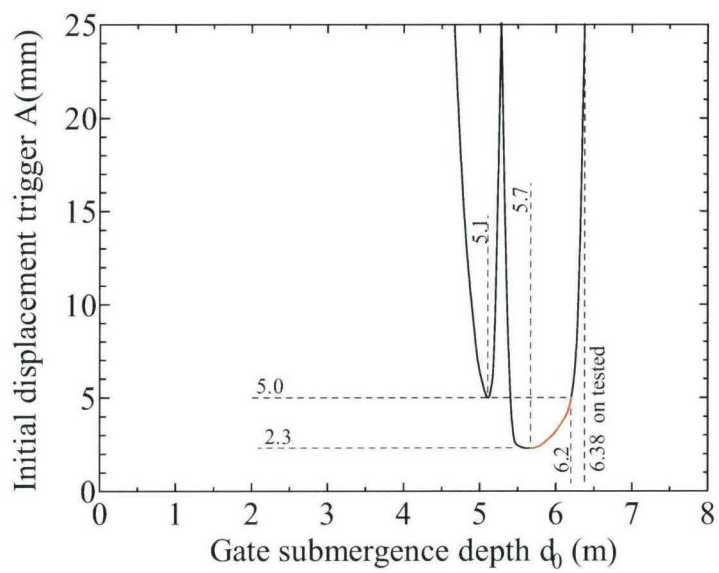

Figure 11.5: Initial displacement trigger to initiate self-excited vibrations for the coupling of Modes M_Z and M_{X1} for Gate #2.

Similar calculations were made for the coupling of Modes M_Z and M_{X2} for Gate #2. The calculated equivalent damping ratio ζ_e and threshold value of the initial displacement trigger *A* are shown in Figure 11.6 and Figure 11.7, respectively. The abscissa is gate submergence depth d_0 (= d_r - B). The minimum initial trigger amplitude to overcome the Coulomb friction damping is a comparatively large value of 19 mm at d_0 = 6.44 m, suggesting the coupling of these two modes is less likely than the coupling of Modes M_Z and M_{X1}.

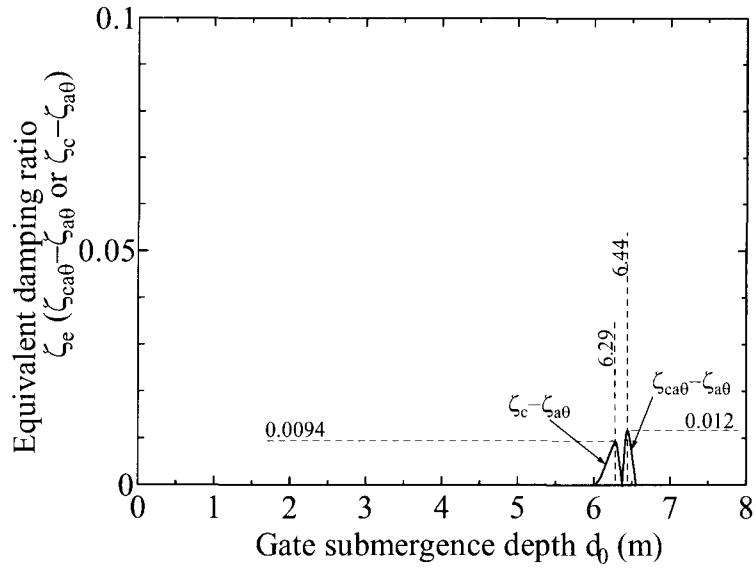

Figure 11.6: Equivalent damping ratio to initiate self-excited vibrations, for the coupling of Modes M_Z and M_{X2} of Gate #2.

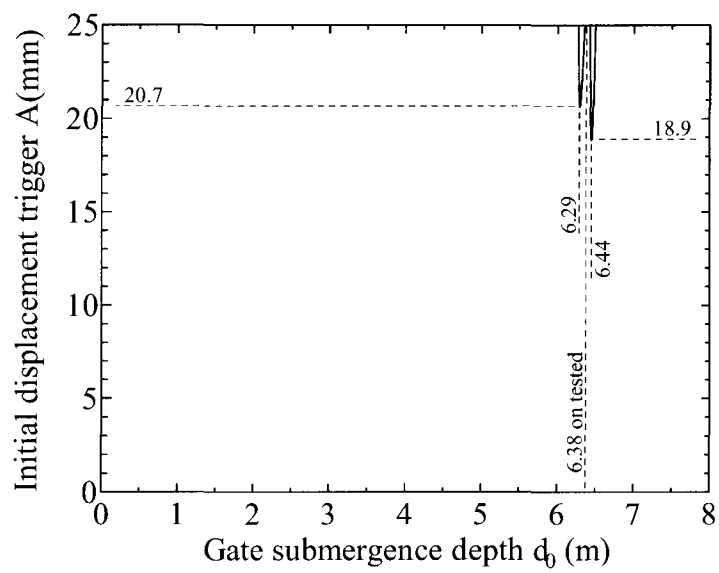

Figure 11.7: Initial displacement trigger to initiate self-excited vibrations, for the coupling of Modes M_Z and M_{X2} of Gate #2.

Similar calculations were made for the coupling of Modes M_Z and M_{X1} of Gate #3. The calculated equivalent damping ratio ζ_e and threshold value of the initial displacement trigger A is shown in Figure 11.8 and Figure 11.9. The abscissa is the gate submergence depth d_0 (= d_r - B). The minimum initial trigger needed to overcome the Coulomb friction damping is about 4.5 mm at d_0 = 5.6 m. Again, this small triggering amplitude requires careful consideration for the coupling of the skinplate streamwise parallel vibration and the whole gate vibration for Gate #3 also.

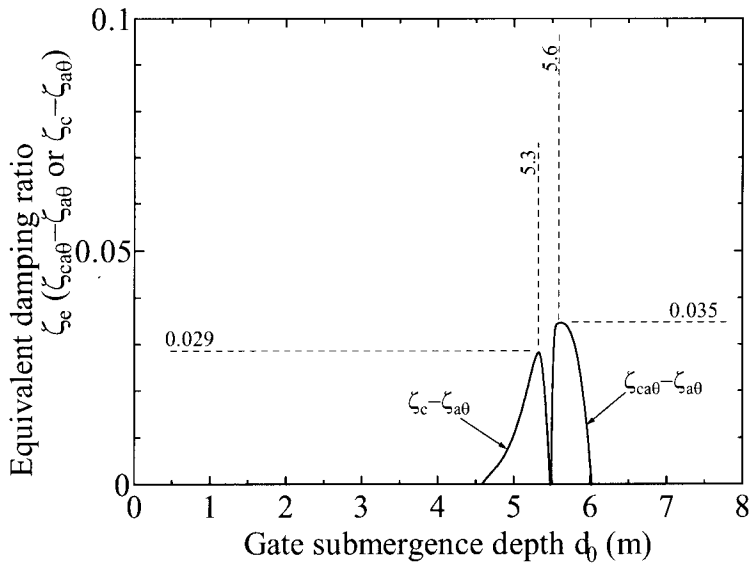

Figure 11.8: Equivalent damping ratio to initiate self-excited vibrations, for the coupling of Modes M_Z and M_{X1} of Gate #3.

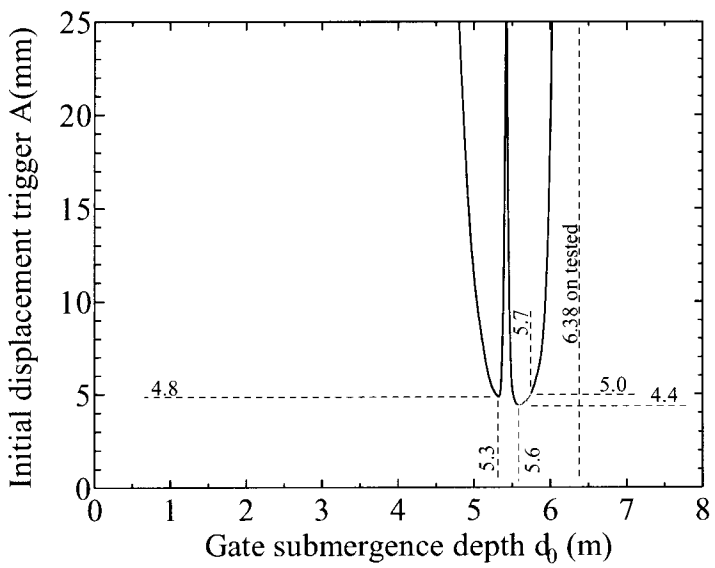

Figure 11.9: Initial displacement trigger to initiate self-excited vibrations for the coupling of Modes M_Z and M_{X1} for Gate #3.

12. STRUCTURAL STRENGTH OF GATES UNDERGOING SELF-EXCITED VIBRATION

Of ultimate importance is the response of the Thermalito gates once coupled-mode self-excited vibration is initiated. Will the vibrations lead to gate failure or not? If a gate does fail, at what vibration amplitude will incipient failure of the gate occur?

In order to answer these questions, an FEM analysis was undertaken to calculate the static structural deformation of gate with an upstream submergence of d_0 = 5.7 m, the condition at which the Thermalito gates were found to be most dynamically unstable. The deformation of the gate in this most unstable state will be useful in understanding what vibration amplitude is needed to initiate the incipient failure of the gate. As was previously shown in Figure 11.5, the gate with this upstream submergence requires only a very small the small threshold displacement trigger to initiate the self-excited vibration. Subsequently, after the FEM analysis, the stress concentration on the gate structure was carefully analyzed to identify possible gate failure due to excessive hydrodynamic loading. With this critical hydrodynamic load identified, the vibration amplitude producing this load is determined and then incorporated into our theoretical analysis. Third, the tensile loads on the strut brace are analyzed to examine the failure of welded joints on the main radial struts. Finally, a linear buckling analysis of the Thermalito gate was performed to identify the safety factor against buckling of the gate structure, in addition to its buckling mode. With these known buckling characteristics, the vibration amplitude needed to initiate the incipient buckling failure of the gate was identified and, again, incorporated into our theoretical analysis.

12.1 Static Structural Deformation

With the highly accurate FEM model shown in Figure 8.1, the structural deformation of Thermalito gate was calculated for d_0 = 5.7 m, and is shown by the color contour plot in Figure 12.1. The skinplate undergoes a half wavelength bending deformation in the spanwise direction, with nodes on each side. Along the spanwise centerline of the skinplate the gate deflection increases continually from the top to the bottom of the gate, with the maximum deflection at the bottom of the gate. The radial arm structures undergo a bending deformation, deflecting toward the outside of the gate span.

The spanwise center deflection of the skinplate is shown in Figure 12.2 for the upstream submergence d_0 = 6.38 m from the present field test. The deflection reaches its maximum value of 15 mm at the skinplate bottom and decreases gradually to about 4 mm at the water surface level at 6.30 m above the bottom of the skinplate.

The parameter in Figure 12.2 is the reduced hydrodynamic load on the skinplate, which is defined as the ratio of the resultant hydrodynamic load (given by the sum of the hydrostatic load plus the push-and-draw hydrodynamic load) to the hydrostatic load, where the maximum push-and-draw hydrodynamic load was assumed to act statically on the skinplate. When the resultant hydrodynamic load reaches 3 times the hydrostatic load, the maximum deflection also increases 3 times its hydrostatic value to 45 mm.

For the original Thermalito gate before reinforcement, the deflection with just the hydrostatic load would have been 22 mm, or 47% larger than that for the reinforced gate, and would have reached 82 mm with a reduced hydrodynamic load of 3.0, or about 82% larger than that for the reinforced gate

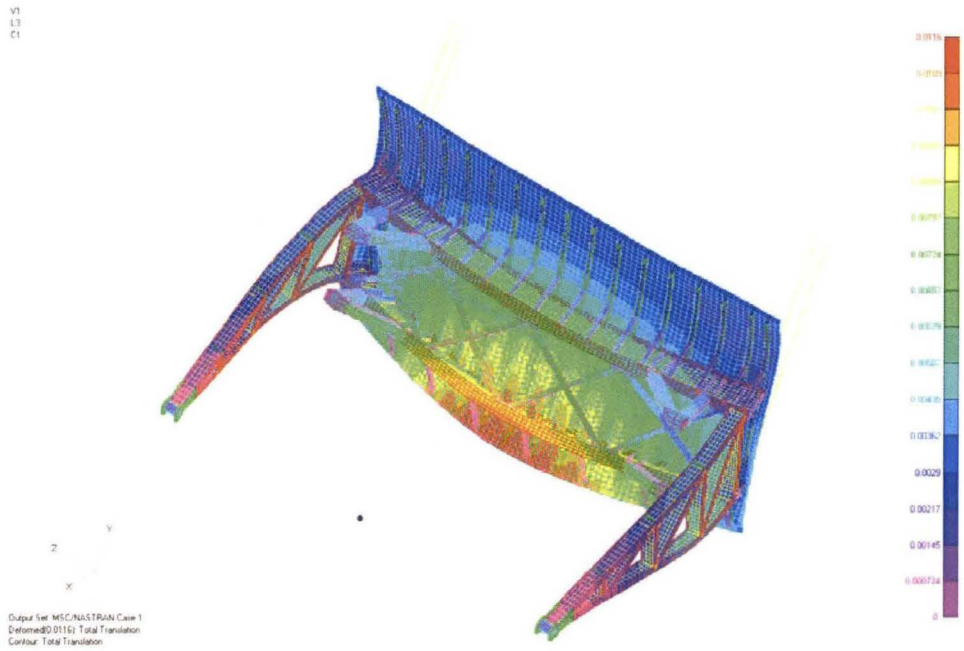

Figure 12.1: Color contours of static structural deformation of the Thermalito gate with d_0 = 5.7 m

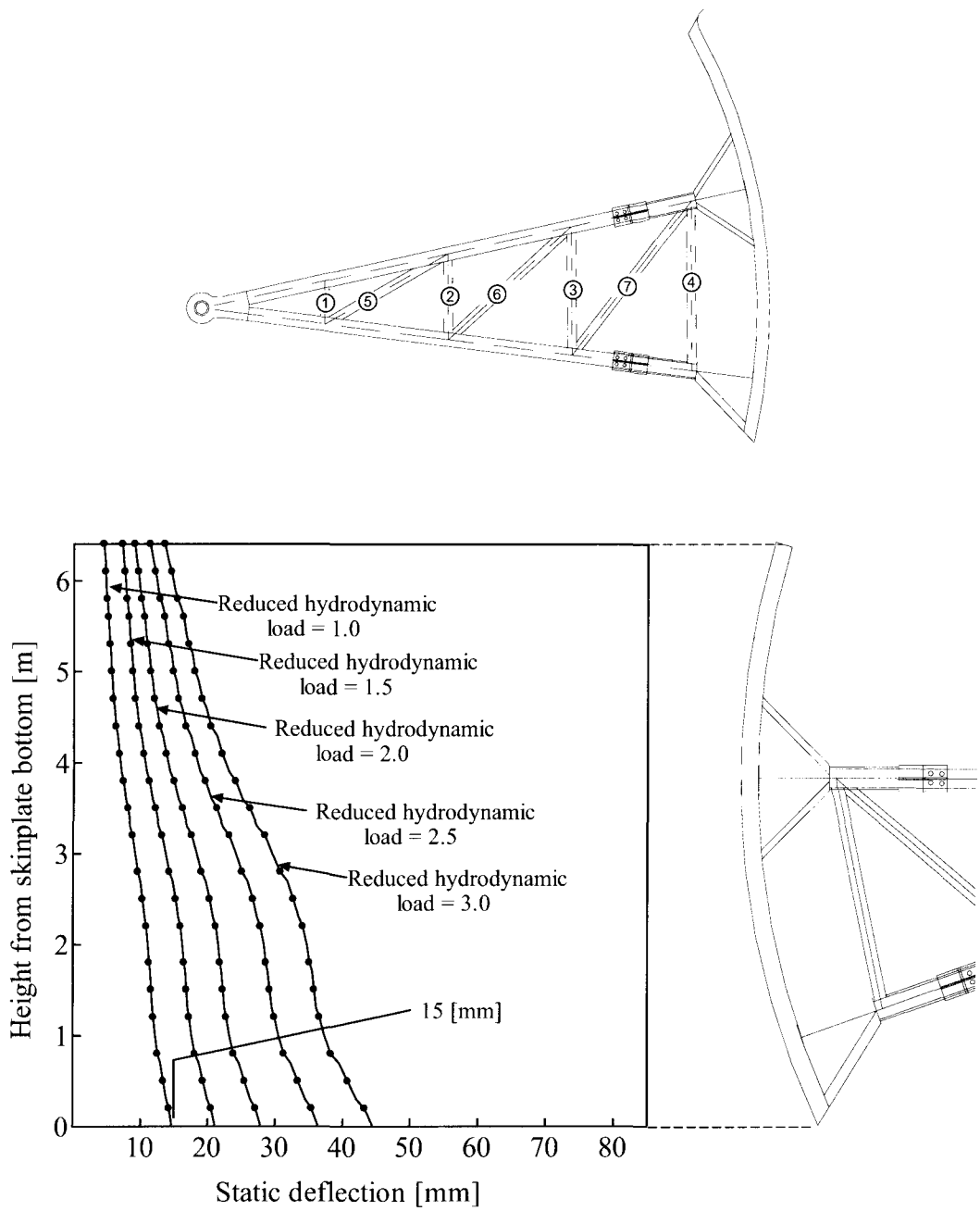

Figure 12.2: Bending deflection of the skinplate along its spanwise center with d_0 = 6.38 m from the present field test of the Thermalito gate

12.2 Failure due to Stress Concentration

With the same FEM model shown in Figure 8.1, the stress at all element cells was calculated for d_0 = 5.7 m, as shown by the color contour plot in Figure 12.3. A very large stress concentration appears at the rigid 1 inch (25.4 mm) thick stiffener plate holding the lower tension rods, in the region marked with an *A* in Figure 12.3. An enlarged view of region *A* is given in Figure 12.3 (b), in which the stress reaches 184 MPa (about 46% of its failure stress, yielding a safety factor of about 2.17). The second largest stress value appears region *B* in the same rigid stiffener plate where the upper tension rods are secured. Figure

12.3(c) shows the enlarged view of this region where the stress is 100 MPa. In both the spanwise center flange of the lower horizontal girder and in the T-shaped stiffener along the skinplate the stress rose to 57.8 MPa. These two locations are both within region C and are shown in the enlarged view in Figure 12.3(d).

In order to carefully examine the gate failure due to stress concentration at the rigid stiffener plate securing the lower tension rods, the reduced hydrodynamic load on the skinplate was increased to 2.0 and then subsequently to 3.0 to simulate the stress concentration due to the resultant hydrodynamic load. Figures 12.4 and 12.5, show the stress levels for the reduced hydrodynamic loads of 2.0 and 3.0, respectively. The maximum stress in the rigid stiffener plate holding the lower tension rods increases to 371 MPa for a reduced hydrodynamic load of 2.0 and to 550 MPa for a rduced hydrodynamic load of 3.0, which far exceeds the breaking stress of 400 MPa. In Figure 12.6, the stress concentration data are plotted over the reduced hydrodynamic load, in which the ordinate represents the reduced stress, defined by the ratio of the stress to the breaking stress of 400 MPa. The data in Figure 12.6 suggest that the rigid stiffener plate holding the lower tension rods would break at a reduced hydrodynamic load of 2.16.

The theoretical analysis can be used to predict the streamwise vibration amplitude at the bottom spanwise center of the skinplate that would produce a reduced hydrodynamic load of 2.16. The results for the streamwise vibration Modes M_x with a Froude number F of 29.2 for Gate #2 (d_0 = 5.7 m; Ω_{mwx} = 6.11 Hz) are shown in Figure 12.7. Using the plotted solid line for F = 29.2, one may find that the reduced hydrodynamic load of 2.16 corresponds to a reduced vibration amplitude X_0/d_0 of 1.82×10^{-3}, or in dimensional terms, a streamwise vibration amplitude of X_0 = 10.4 mm for the assumed d_0 of 5.7 m.

As a result, one may conclude that the lower stiffener plate holding the tension rods will start to fail, when the streamwise vibration at the bottom spanwise center of the skinplate reaches a relatively small amplitude of only 10.4 mm.

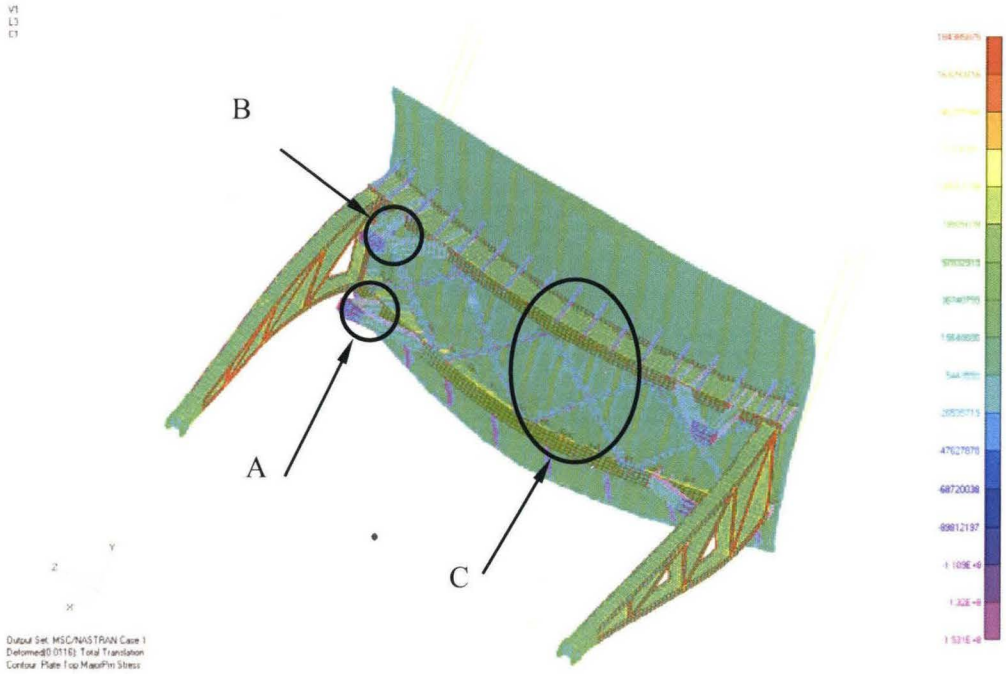

(a) 3-D view

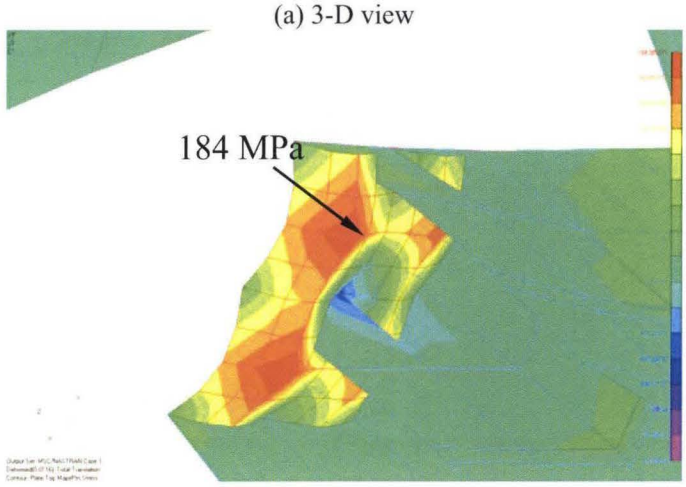

(b) Enlarged A

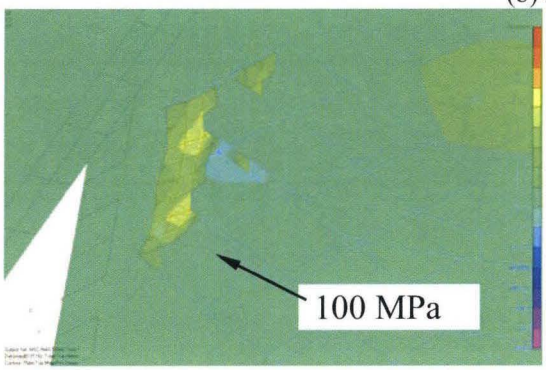

(c) Enlarged B

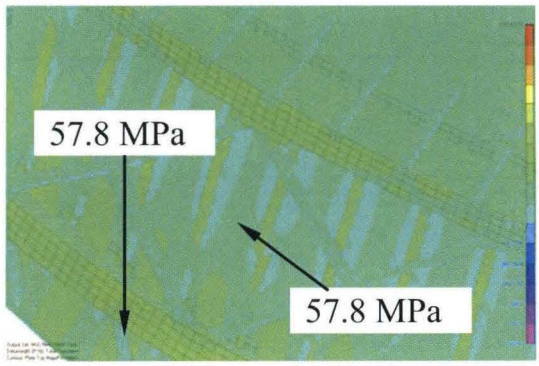

(d) Enlarged C

Figure 12.3: Color contours of stress in the Thermalito gate for $d_0 = 5.7$ m

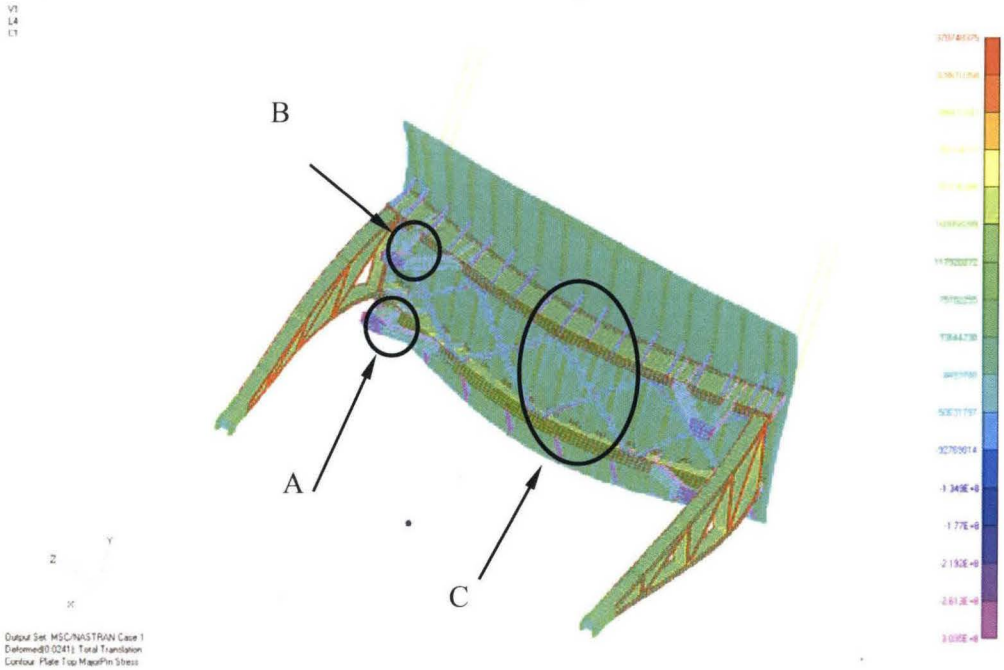

(a) 3-D view

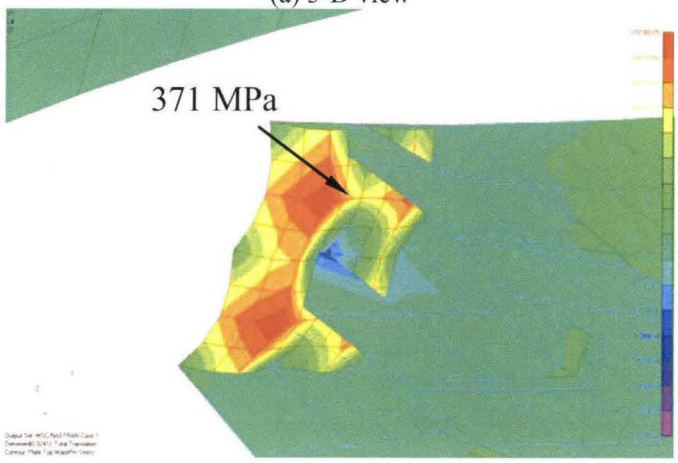

(b) Enlarged A

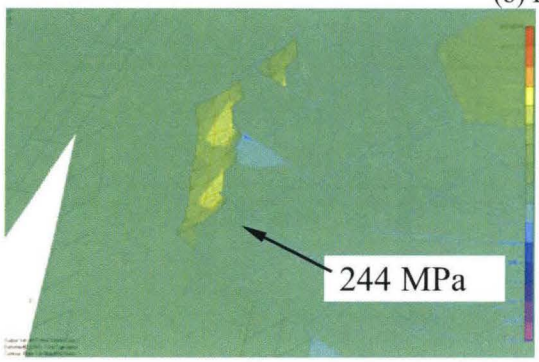

(c) Enlarged B

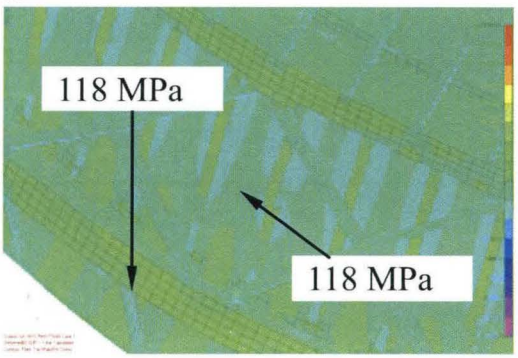

(d) Enlarged C

Figure 12.4: Color contours of stress in the Thermalito gate for a hydrodynamic load twice the hydrostatic load with $d_0 = 5.7$ m.

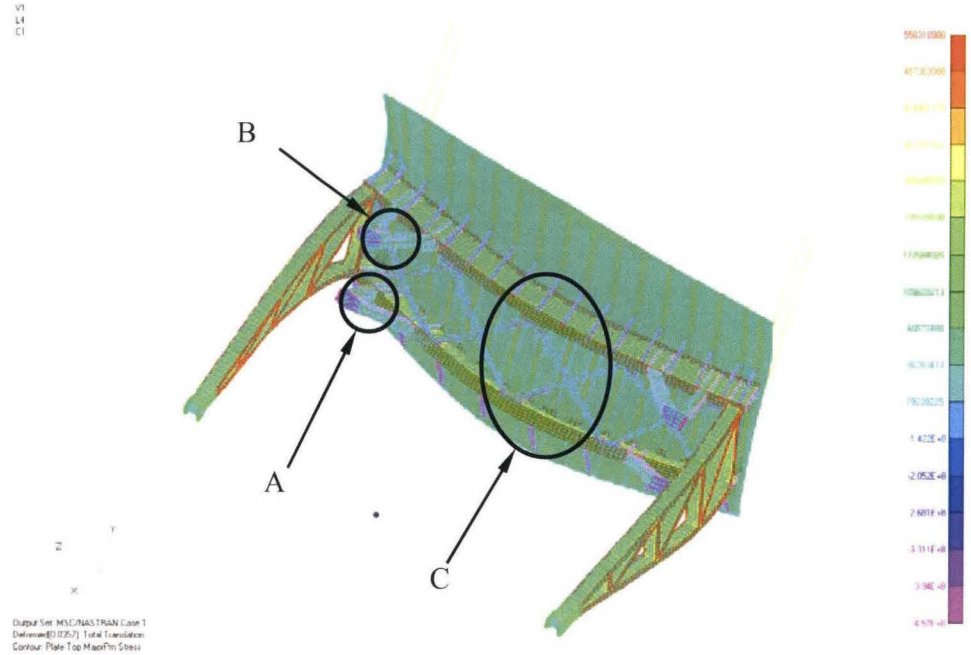

(a) 3-D view

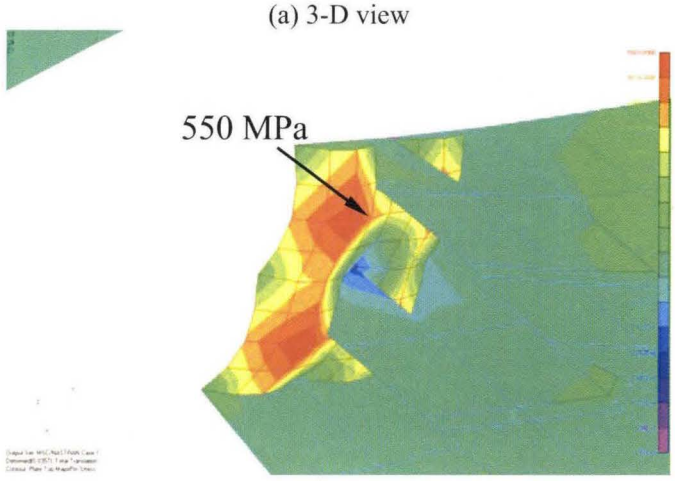

(b) Enlarged A

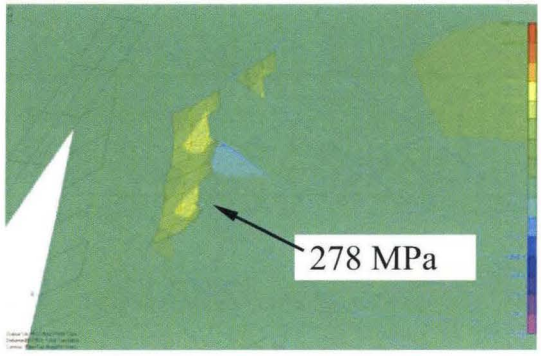

(c) Enlarged B

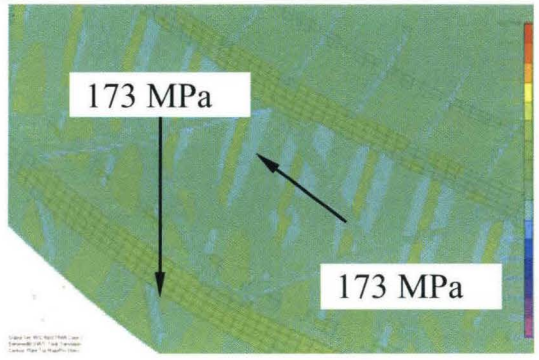

(d) Enlarged

Figure 12.5: Color contours of stress in the Thermalito gate for a hydrodynamic load three times larger than the hydrostatic load with d_0 = 5.7 m.

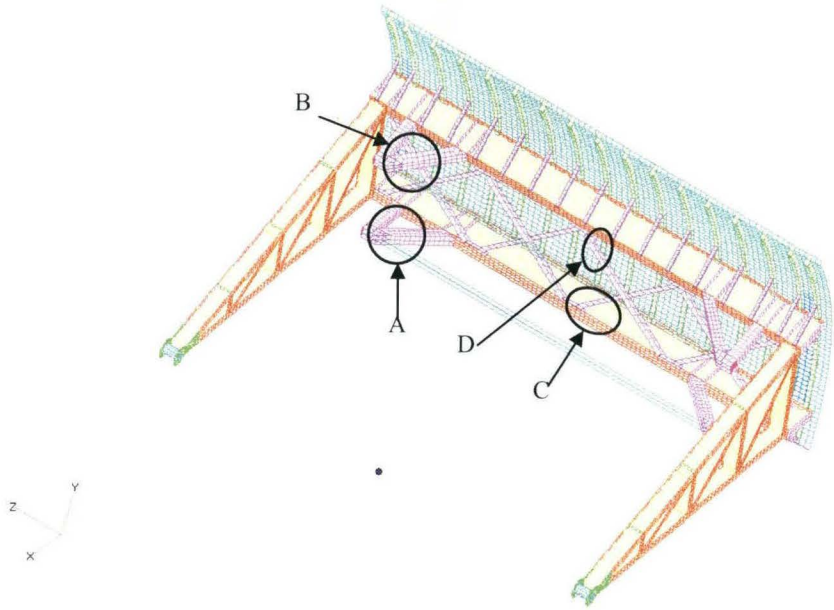

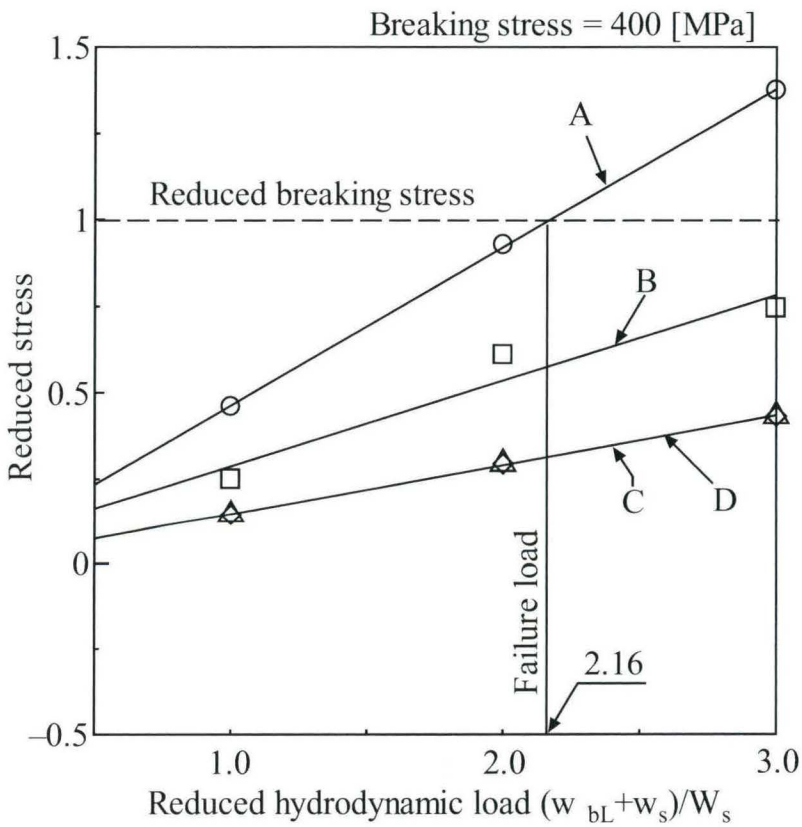

Figure 12.6: Stress vs. hydrodynamic load.

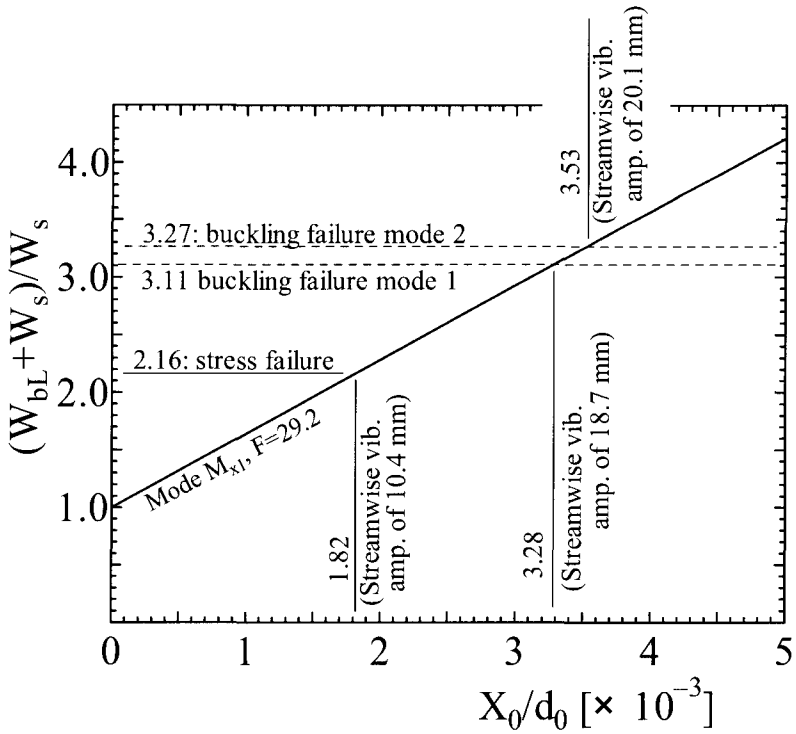

Figure 12.7: Hydrodynamic load vs. streamwise vibration amplitude at the bottom spanwise center of the skinplate.

12.3 High Strength of Welded Joints against Tensile Force

FEM simulation can also be used to calculate the tensile force on strut braces, as shown in Figure 12.8. In this figure the ordinate represents the reduced tensile load, defined by the ratio of the tensile force to the breaking force F_{BL} of welded joint. The strut brace numbered 4 exhibits the largest value of reduced tensile load.

The breaking force F_{BL} of welded joint between the strut braces and the radial strut can be calculated using the following expression:

$$F_{BL} = 0.7S \cdot L \cdot f_W \quad , \tag{12.1}$$

where S [cm] represents the base width of the weld, L [cm] the welded length and f_w [kN/cm^2] the breaking stress of the weld, which takes on a value of 24 kN/cm^2. For the Thermalito gate, as shown in the detail of Figure 12.9, S and L take on the following values:

$$S = \frac{3}{16} inch = 0.47625\,[cm], \qquad L = (2inch \times 4) + \left(5\frac{1}{2} inch \times 2\right) = 48.26\,[cm].$$

With these values, the breaking force F_{BL} takes on a value of 379 kN.

$$F_{BL} = 0.7S \cdot L \cdot f_W = 379\,[kN]$$

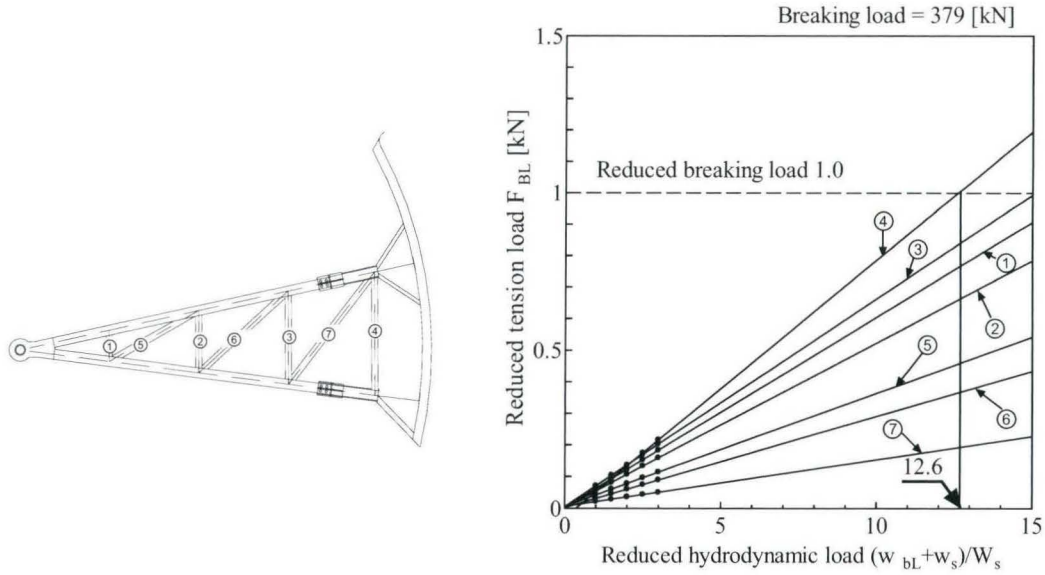

Figure 12.8: Tension load on strut brace vs. hydrodynamic load.

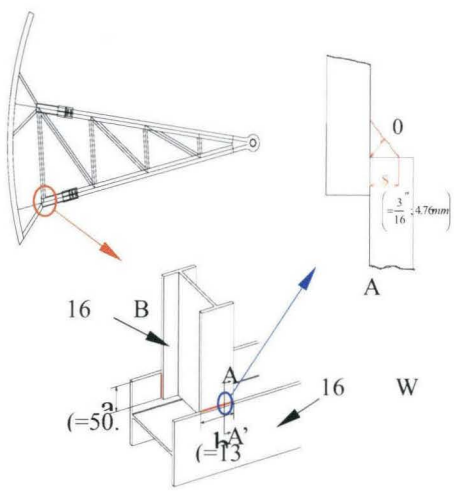

Figure 12.9: Welded joint between the strut brace streamwise radial strut.

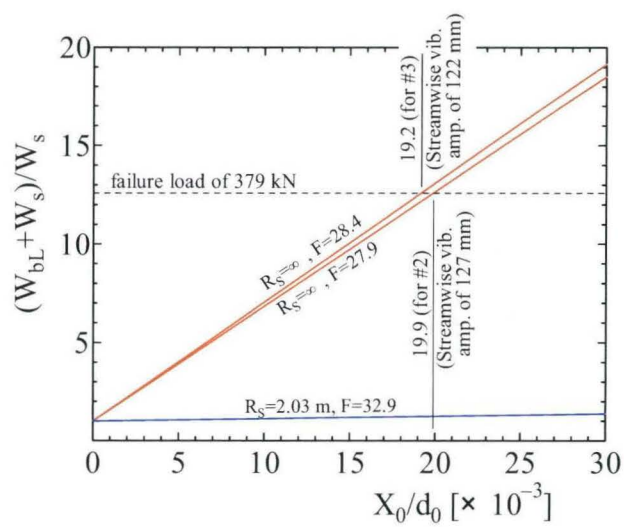

Figure 12.10: Hydrodynamic load vs. and the vibration amplitude.

In Figure 12.8, a reduced tensile load of 1.0 represents the reduced breaking load at which the welded joint between the strut brace and the radial strut breaks. The welded joint of the No.4 strut brace breaks at the reduced hydrodynamic load of 12.6. This value of reduced hydrodynamic load can be shown to correspond to a reduced streamwise vibration amplitude of 19.9×10^{-3}, as shown in Figure 10, or a dimensional streamwise vibration amplitude of X_0 = 127 mm with d_0 = 5.7 m. This amplitude is far too large relative to that for other failure modes and indicates that the welded joints are sufficiently strong.

12.4 Failure due to Buckling

With the FEM model shown in Figure 8.1, a buckling simulation can be made for the Thermalito gate, as shown in Figures 12.11 and 12.12, in which the upstream submergence was set at d_0 = 5.7 m, corresponding to the gate's most dynamically unstable state. The "Eigenvalue" in the figures represents the critical reduced hydrodynamic load at which buckling occurs. The reduced critical hydrodynamic load

is defined as the ratio of the critical resultant hydrodynamic load for buckling to the hydrostatic load. These values are also included in the previously discussed Figure 12.7, showing buckling to occur at far greater loading than failure due to stress.

For the first buckling mode, shown in Figure 12.11, the eigenvalue is 3.11. For the second buckling mode, shown in Figure 12.12, the eigen value is and 3.27. In Mode 1, the rigid stiffener plate holding the tension rods buckles, while in Mode 2, the triangular strut supporting the rigid stiffener plate twists and produces buckling.

The eigenvalues of 3.11 and 3.27, as shown in Figure 12.7 (as mentioned above), correspond to reduced streamwise vibration amplitudes of 3.28×10^{-3} and 3.53×10^{-3}, respectively. These reduced amplitudes represent the dimensional amplitude of 18.7 mm and 20.1 mm, respectively, when $d_0 = 5.7$ m.

These eigenvalues of 3.11 and 3.27 are substantially larger than the critical reduced hydrodynamic load of 2.16 for stress-induced failure. Correspondingly, the vibration amplitudes of 18.7 mm and 20.1 mm needed for a buckling failure are also substantially larger than 10.4 mm needed to produce stress concentration failure.

Figure 12.13 shows that the eigenvalue for buckling decreases linearly with increasing upstream submergence, but even for submergences of more than 6 m remain larger than that reduced loading needed for stress failure.

It can be concluded that buckling would not occur until after failure due to stress concentration had already occurred.

V1
L3
C1

Eigenvalue 3.11

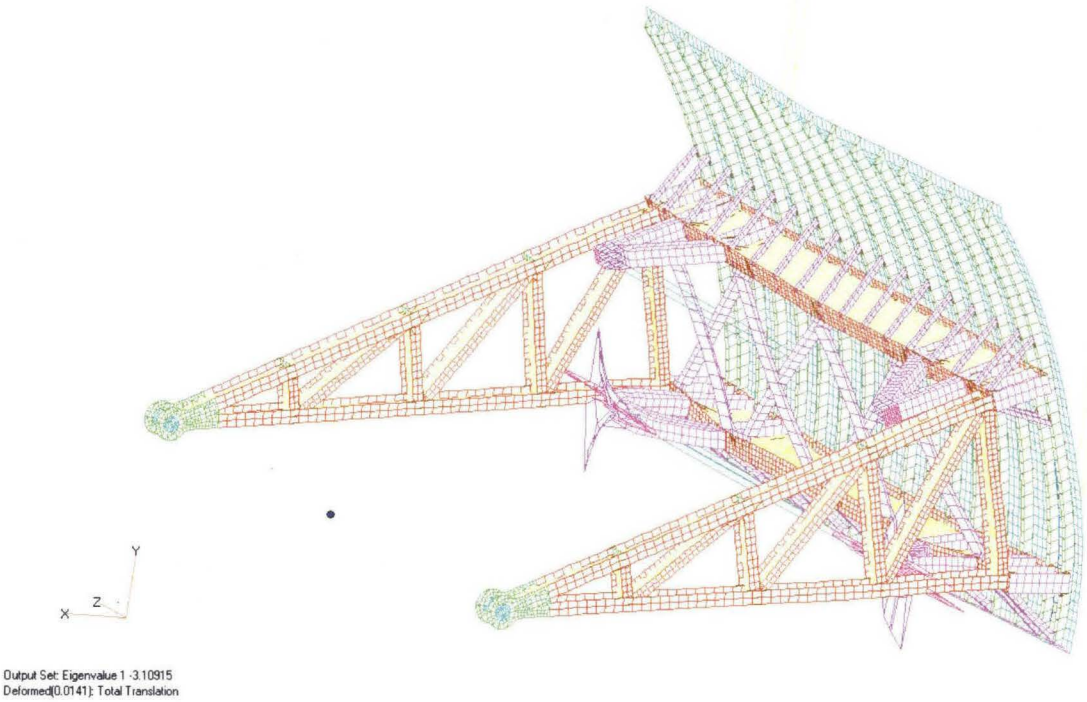

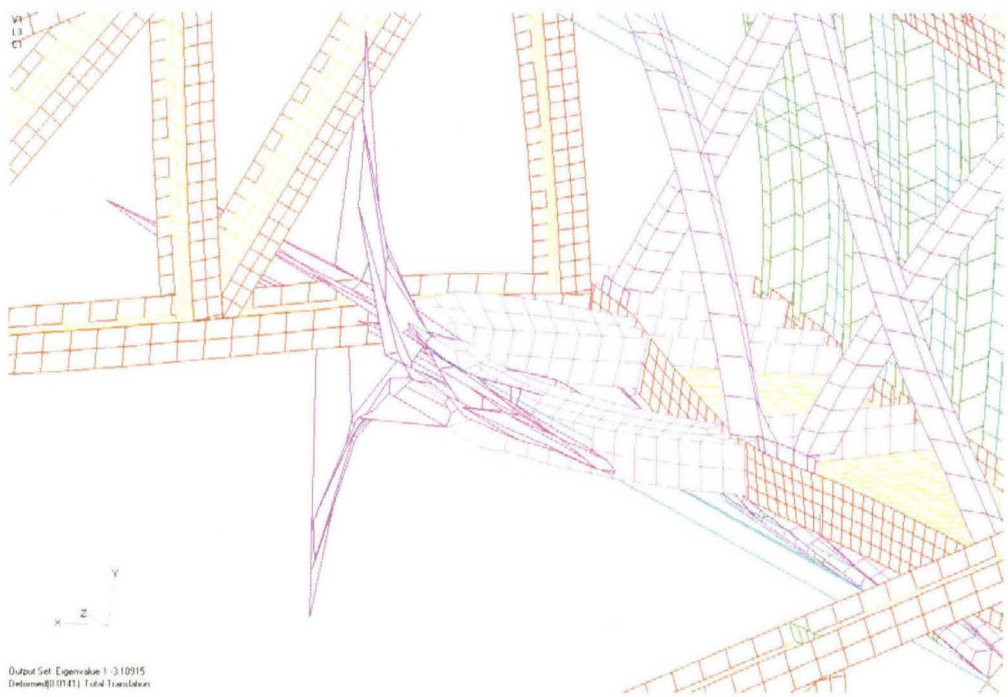

Figure 12.11: Buckling Mode 1 of the Thermalito gate with an eigenvalue of 3.11.

V1
L3
C1

Eigenvalue 3.27

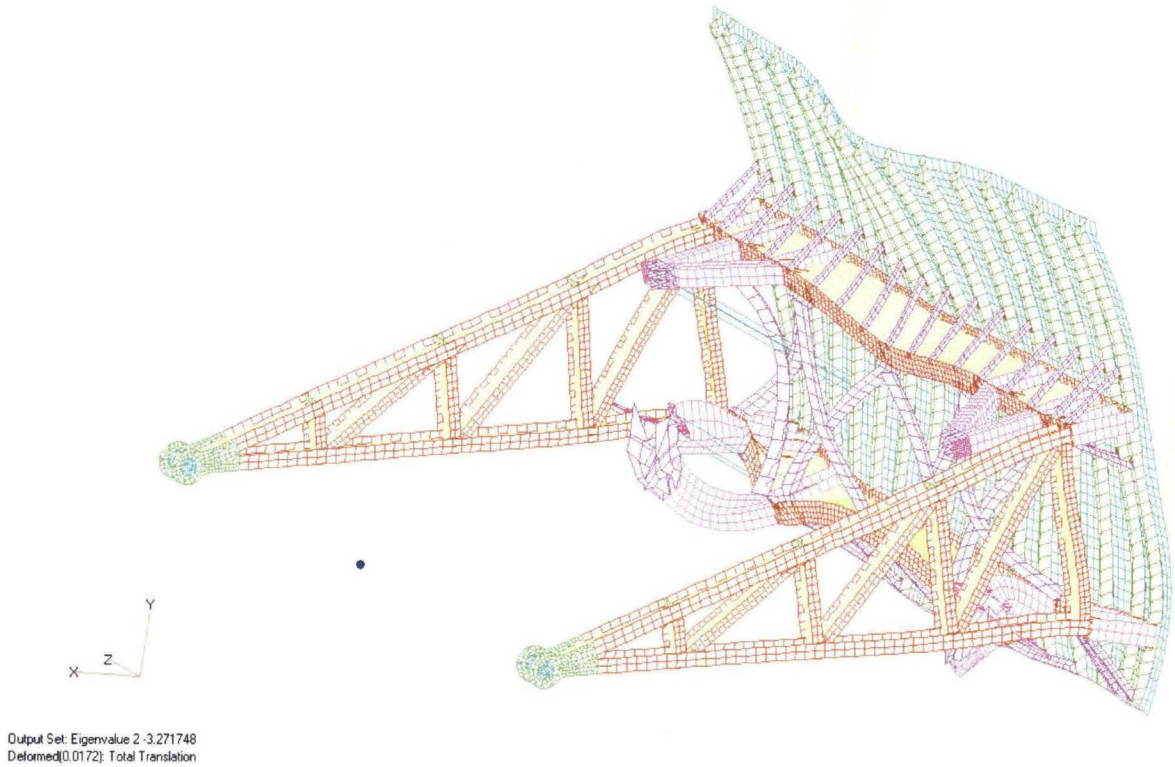

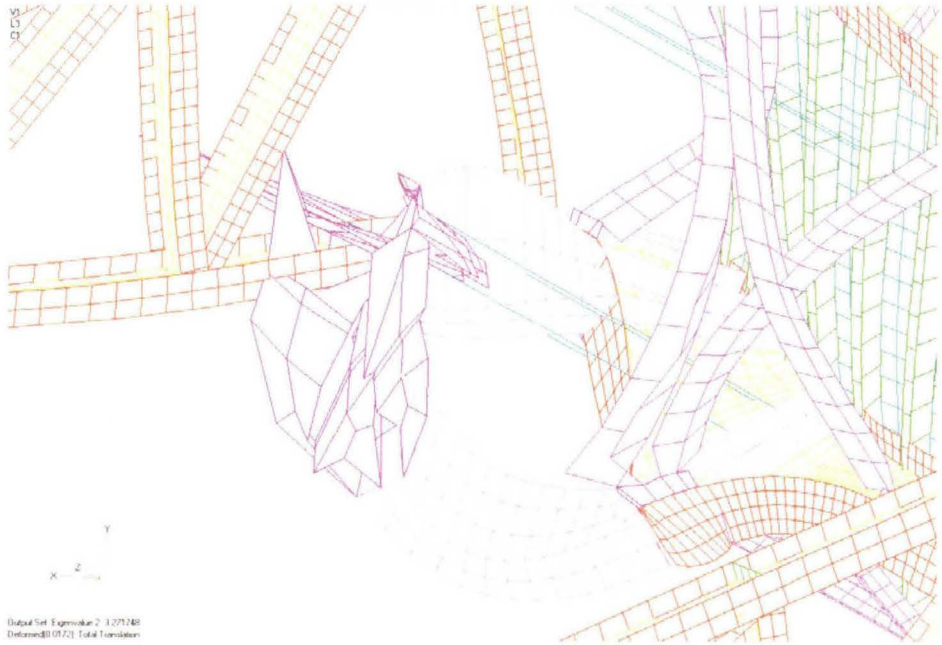

Figure 12.12: Buckling Mode 2 of the Thermalito gate with an eigenvalue of 3.27.

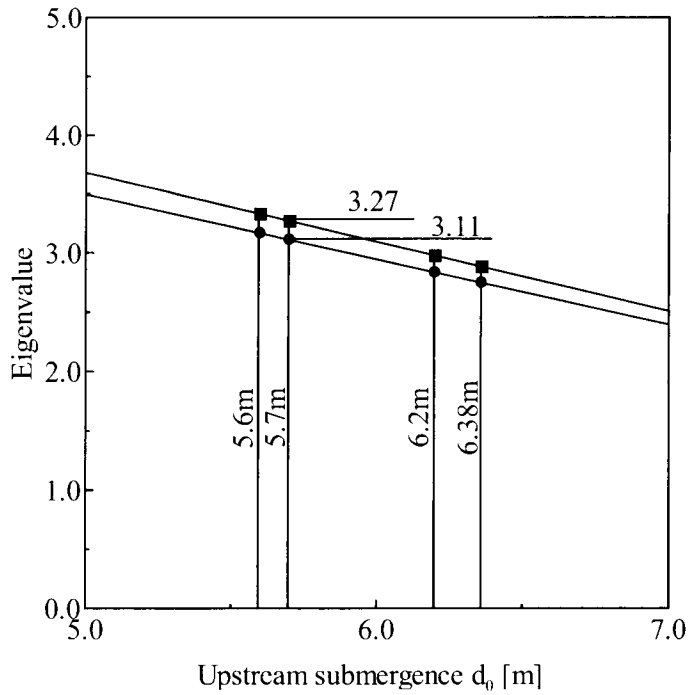

Figure 12.13: Eigenvalue for buckling of the Thermalito gate vs. upstream submergence depth.

REFERENCES

(1) Ishii, N., Anami, K., Knisely, C.W., 2005, "*Lessons from Folsom Dam Tainter-Gate Failure and Future Works for Subsequent Generations*", Final Report of Folsom Dam Gate Failure in 1995, submitted to Mid-Pacific Region, Bureau of Reclamation United States Department of the Interior (Dec. 07, 2005).

(2) Ishii, N., Anami, K., Knisely, C.W., 2006, *Vibration Field Testing Plan for Thermalito Diversion Dam Tainter Gates*, submitted to California DWR, Oroville Field Division (Nov. 13, 2006).

(3) Anami, K., 2002, Flow-Induced Coupled-Mode Self Excited Vibration of Large-Scaled Tainter-Gates (in Japanese), Dissertation submitted to Osaka Electro-Communication University, March 2002. (*Translated into English on Dec. 2005*)

(4) Anami, K., Ishii, N., Knisely, C. W., Oku, T., 2007a, Full-Scale Verification of Coupled-Mode Excitation of A 50-ton Tainter-Gate, Modernization and Optimization of Existing Dams and Reservoirs, Proc. of 27th Annual USSD Conference, pp.647-658, (Philadelphia, USA).

(5) Anami, K., Ishii, N., Knisely, C. W., Oku, T., 2007b, Field Measurement of Dynamic Instability of A 50-Ton Tainter-Gate, Proc. of 2007 ASME Pressure Vessels and Piping Division Conference, CD-ROM, PVP2007-26543, (San Antonio, USA), to be presented.

(6) Ishii, N., Anami, K., Makihata, T., Oku, T., Ohara, T., 2007, Tainter-gate failure in Japan, Journal of Structural Engineering, Vol.53A, pp.589-5961, (in Japanese).

(7) Anami, K., Ishii, N., Knisely, C. W., Todd, R.V., Oku, T., 2006a, Vibration Tests with a 1/13-Scaled 3D Model of Folsom Dam Tainter-Gate and Its Prediction by Theory, Proc. of ASME 6th International Symposium on FSI, AE & FIV+N, Vol. 4, pp.1127-1134, PVP2006-ICPVT-11-93917(CD-ROM), (Vancouver, Canada).

(8) Anami, K., Ishii, N., Knisely, C. W., Todd, R.V., Oku, T., 2006b, Vibration Tests with A 1/13-Scaled 3D Model of Folsom Dam Tainter-gate, Proc. of Hydro Vision 2006, No.179(CD-ROM), (Portland, USA).

(9) Anami, K., Ishii, N., Knisely, C.W., Oku, T., 2005, Hydrodynamic Pressure Load on Folsom Dam Tainter-Gate at Onset of Failure due to Flow-Induced Vibrations, Symposium on Flow-Induced Vibration-2005, Proc. of ASME Pressure Vessels and Piping Conference, CD-ROM, PVP2005-71444, (Denver, USA).

(10) Anami, K., Ishii, N., Knisely, C.W., Matsumoto, Y., 2005, Field vibration tests of a Flap gate undergoing self-excited vibration and its in-water vibration frequency, Transactions of the Japan Society of Mechanical Engineers, Series B, 71-704, pp. 1067-1074, (in Japanese).

(11) Anami, K., Ishii, N., Oku, T., 2005, A design criterion for Dynamic Stability of Eccentric Tainter-gates, Transactions of the Japan Society of Mechanical Engineers, Series C, 71-712, pp. 3375-2280, (in Japanese).

(12) Anami, K., Ishii, N. and Knisely, C.W., 2004a, Validation of Theoretical Analysis of Tainter Gate Instability Using Full-Scale Field Tests, Proc. of 2004 Flow-Induced Vibration Conference, Vol.1, pp.409-414, (Paris, France).

(13) Anami, K., Ishii, N. and Knisely, C.W., 2004b, Field Vibration Tests and Dynamic Stability Analysis of A Full-Scaled Tainter-gate, 2004 ASME Pressure Vessels and Piping Conference, CD-ROM, (San Diego, USA).

(14) Anami, K., Ishii, N., Takano, W., 2004, Theoretical Analysis of Flow-Induced Streamwise Rotating Vibration of Inclined Circular-Arc Rigid Skinplate and Its Verification by Model Tests (in Japanese), Transactions of the Japan Society of Mechanical Engineers, Series C, 70-690, pp. 385-393.

(15) Anami, K. & Ishii, N., 2003, Model Tests for Non-Eccentricity Dynamic Instability Closely Related to Folsom Dam Tainter-Gate Failure, Proc. of ASME Pressure Vessels and Piping Conference, Vol.465, 213-221, (Cleveland, USA).

(16) Anami, K., Ishii, N., Takano, W., 2003, Empirical evaluation method of Hydrodynamic pressures induced by vibrations of inclined circular-arc skinplate of Tainter gates, Journal of Structural Engineering, Vol.49A, pp.645-651, (in Japanese).

(17) Anami, K. and Ishii, N., 2002, Model Tests for Hydrodynamic Pressure Caused by Vibrations of a Vertical Flat Weir Plate and Verification of Theoretical Analysis, Transactions of the Japan Society of Mechanical Engineers, Series B, 68-667, pp. 719-725, (in Japanese).

(18) Anami, K., Ishii, N., Takano, W., 2002, Equivalent Added mass and Wave-Radiation Damping Coefficients for Flow-Induced Rotational Vibrations of Vertical Weir Plate, Transactions of the Japan Society of Mechanical Engineers, Series B, 68-668, pp. 1072-1079, (in Japanese).

(19) Ishii, N. and Anami, K.,2001a, Field and Model Investigations of FIV of Folsom Dam Tainter-Gate, Proc. of Commemorative International Symposium for the 40th Anniversary for the Foundation of the OECU, Vol.2, pp.143-164.

(20) Anami, K. & Ishii, N., 2001,Analyses of FIV of Folsom Dam Tainter Gates and Verifications by Model Tests, Proc. of Commemorative International Symposium for the 40th Anniversary for the Foundation of the OECU, Vol.2, pp.165-181.

(21) Ishii, N. and Anami, K., 2001b, Application of Experiences and of Recent Findings with Tainter Gates in Japan on the Folsom Dam Gate Stability, Proc. of Commemorative International Symposium for the 40th Anniversary for the Foundation of the OECU, Vol.2, pp.193-206.

(22) Anami, K. and Ishii, N., 2000, Flow-Induced Dynamic Instability Closely Related to Folsom Dam Tainter-Gate Failure in California, In: *Flow Induced Vibration* (eds: Ziada S. & Staubli T.), pp.205-212, Balkema.

(23) Anami, K., Ishii, N., Knisely, C.W., Matsumoto, Y., 2000, Measured and Calculated Vibration Characteristics of a Full-Scale Flap Gate Undergoing Self-Excited Vibration, Proc. of ASME Pressure Vessels and Piping Conference, Vol. 414-1, pp.23-29, Seattle, Washington, USA.

(24) Anami, K., Ishii, N. and Yamasaki, M., 2000, Hydrodynamic Pressure Induced by Rotating Skinplate of Folsom Dam Tainter-Gate (in Japanese), Transactions of the Japan Society of Mechanical Engineers, Series B, 68-652, pp. 3116-3123.

(25) Anami, K. and Ishii, N., 1999, Flow-Induced Coupled-Mode- Vibration of Folsom Dam Tainter-Gates in California, Proc. of ASME Pressure Vessels and Piping Conference, Vol. 396, pp.343-350, (Boston, USA).

(26) Anami, K. & Ishii, N., 1998a, In-Water Streamwise Vibration of Folsom Dam Radial Gates in California, Proc. of 1998 ASME PVP Conf., Vol. 363, 87-93, (San Diego, USA).

(27) Anami, K. & Ishii, N., 1998b, In-air and In-Water Natural Vibrations of Folsom Dam Radial Gates in California, In: *Experimental Mechanics 1*(ed. Allison I.M.), 29-34, Balkema.

(28) Ishii, N., 1997, *Dynamic Stability Evaluation for Folsom Dam Radial Gate and Its Inherent Non-Eccentricity Instability*, submitted to Bureau of Reclamation, U.S. Department of the Interior.

(29) Forensic Report, 1996, *Spillway Gate 3 Failure Folsom Dam*, American River Division Central Valley Project California and Bureau of Reclamation Mid-Pacific Regional Office Sacramento, California, (Nov. 18, 1996).

(30) Ishii, N., 1995a, *Folsom Dam Gate Failure Evaluation and Suggestions*, 1st report submitted to U.S. Bureau of Reclamation, (Aug. 24, 1995).

(31) Ishii, N, 1995b, *Folsom Dam Gate Failure Evaluation Based on Modal Analysis and Suggestion*, 2nd report submitted to U.S.B.R., (Nov. 8, 1995).

(32) Ishii, N., 1992, Flow-Induced Vibration of Long-Span Gates (Part I: Model Development), Journal of Fluids and Structures, Vol.6, No.5, pp.539-562.

(33) Ishii, N., Naudascher, E., 1992, A Design Criterion for Dynamic Stability of Tainter Gates, Journal of Fluids and Structures, Vol.6, No.1, pp.67-84.

(34) Ishii, N., Naudascher, E., 1984, Field Tests on Natural Vibration Modes of A Tainter Gates, in K.V.H. Smith, Channels and Channel Control Structures, pp.209-222, Southampton, Springer-Verlag.

(35) Ishii, N., Imaichi, K., Hirose, A., 1980, Dynamic Instability of Tainter-Gates, In: *Practical Experiences with Flow-Induced Vibrations* (Naudascher, E. & Rockwell, D.), pp.452-460, Berlin, Springer- Verlag.

(36) Ishii, N. and Imaichi, K., 1977, Water Waves and Structural Loads Caused by a Periodic Change of Discharge from a Sluice-Gate, Bulletin of JSME, Vol.20, No.146, pp.988-1008.

(37) Ishii, N., Imaichi, K.and Hirose, A., 1977, Instability of Elastically Suspended Tainter-Gate System Caused by Surface Waves on the Reservoir of a Dam, Transactions of the ASME, Journal of Fluid Engineering, Ser.I, Vol.99, No.4, pp.699-709.

(38) Timoshenko, S, Young, D.H., Weaver, W.Jr., 1974, Vibration Problems in Engineering, John Wiley & Sons, p.81.

(39) Creager, W. P. & Justin, J. D., 1927, "Hydro-Electric Handbook", John Wiley & Sons.

Appendix: List of all Measurement Instrumentations from Japan

(a) Carry-on items

Carry-on items							
No.	Weight(kgf) & Size(cm)	Article	Company	Type	Price(¥)	Number of Article	
1 Carrying bag	14.5 55×35×22	Lap top computer	TOSHIBA	Dynabook G7/U24PD DW	420,000	2	
		Power supply Amplifier for Accelerometer	Rion	LF-20	226,600	1	
2 Carrying bag	10 55×35×22	Digital video camera	Panasonic	NV-C2	100,000	1	
				VDR-D300	100,000	1	
				NV-GS250-S	100,000	1	
				NV-GS200	100,000	1	
		Dynamic strain amplifier	KYOWA	DPM-6H	1,262,000	1	
3 Carrying bag	13 55×35×22	Pressure transducer	TOYODA	PMS-5M -1M	131,840	1	
		DC amp for Pressure transducer	TOYODA	AA6200	207,000	2	
		Displacement Transducer	KYOWA	DTP-05 MDS	25,000	2	
		Servo type Accelerometer	Rion	LS-20C	214,000	15	
		Servo type Accelerometer	Rion	LS-10C	105,000	3	
4 Carrying bag	13.0 55×35×22	Digital data recorder	TEAC	LX-10	2,217,000	2	
		Mobile printer	Canon	IP-90	30,000	1	
5 Carry cart	14.4 47×33×21	FFT Analyzer	A & D	AD3525	2,925,000	1	
Hand bag		Power supply Amplifier for Accelerometer	Rion	LF-20	226,600	5	

(b) Checked-in items 1 (continue to next page)

Checked-in items①							
No.	Weight(kgf) & Size(cm)	Article	Company	Type	Price(¥)	Number of Article	
		LCD Monitor	IODATA	LCD-A153V	50,000	1	
		LCD Monitor	ALTRAS ONIC	[illegible]	15,000	1	
		Color Quad processor	DAIWA	SG-202	20,000	1	
1 Suit case 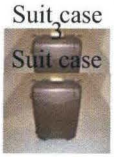	31 72×52×25	TV TUNER	IO DATA	G0013	25,000	1	
		Tool box				2	
		Digital panel meter	OMRON	K3TE-V314	10,000	2	
		Digital video camera	Panasonic	NV-MX5000	100,000	1	
		Magnetic Holder base	KANETEC	MB-PL	8,000	3	
		Digital video camera	Panasonic	NV-DJ100	100,000	1	
		Work glove			-	10	
		Transceiver	Icom		30,000	9	
		Carabineer hook			-	17	
		Aluminum block			-	18	
		Leisure sheet for rain-cover			-	3	
		Mobile Printer ink			-	1	
		Copying paper			-	4	
4 Suit case	32 72×52×25	Signal wire cable (BNC)			2,000	41	
		Signal wire cable			4,000	3	
		Video cable			5,000	4	
2 Suit case	31 72×52×25	Hammer drill	HILTI	TE6-C	100,000	1	
		Magnetic Holder base	KANETEC	MB-PL	8,000	2	
		Magnetic Holder base	KANETEC	MB-PR	6,000	5	
5 Suit case	32 72×52×25	C-Type clamp extended			-	4	
		connecting cable for Accelerometer			-	4	
		Tank Grinder			25,000	1	
		Angle steel			-	3	
		Clothing			-	-	

(c) Checked-in items 2 (continue to next page)

Checked-in items③							
No.	Weight(kgf) & Size(cm)	Article	Company	Type	Price(¥)	Number of Article	
6 Suit case	32 72×52×25	Impact Hammer with force gauge	PCB	GK-086B50	1,051,000	1	
		Power supply amplifier for Hammer	PCB	GK-480M106		2	
		Harnesses				4	
		Self Retracting Lanyards	FUJII DENKO	BB-60-SN	29,700 50,000	3	
		Helmet				5	
		Clothing					
7 Bag	30 60×33×32	Extended connecting cable for Accelerometer	Rion	EC-40D	54,000	6	
8 Bag	30 60×33×32	Extended connecting cable for Accelerometer	Rion	EC-40D	54,000	6	
9 Bag	30 60×33×32	Extended connecting cable for Accelerometer	Rion	EC-40D	54,000	6	

(d) Checked-in items 3.

TOTAL VALUE: ¥18,392,840-
($157,203-)